UV Laser Ablation of Metals

by

George Paul Pinho

A thesis

presented to the University of Waterloo

in fulfillment of the

thesis requirement for the degree of

Doctor of Philosophy

in

Physics

Waterloo, Ontario, Canada, 1998

© George P. Pinho 1998

National Library of Canada
Bibliothèque nationale du Canada

Acquisitions and Bibliographic Services
Acquisitions et services bibliographiques

395 Wellington Street
Ottawa ON K1A 0N4
Canada

395, rue Wellington
Ottawa ON K1A 0N4
Canada

Your file Votre référence

Our file Notre référence

The author has granted a non-exclusive licence allowing the National Library of Canada to reproduce, loan, distribute or sell copies of this thesis in microform, paper or electronic formats.

L'auteur a accordé une licence non exclusive permettant à la Bibliothèque nationale du Canada de reproduire, prêter, distribuer ou vendre des copies de cette thèse sous la forme de microfiche/film, de reproduction sur papier ou sur format électronique.

The author retains ownership of the copyright in this thesis. Neither the thesis nor substantial extracts from it may be printed or otherwise reproduced without the author's permission.

L'auteur conserve la propriété du droit d'auteur qui protège cette thèse. Ni la thèse ni des extraits substantiels de celle-ci ne doivent être imprimés ou autrement reproduits sans son autorisation.

0-612-38265-6

Canada

The University of Waterloo requires the signatures of all persons using or photocopying this thesis. Please sign below, and give address and date.

UV Laser Ablation of Metals

The mechanism of energy transfer between an excimer laser beam (λ = 308 nm, 248 nm), an Al substrate and the environment around the interaction site is investigated for laser intensities 10^{12} - 10^{13} Wm^{-2}. Two energy transfer mechanisms are considered: inverse bremsstrahlung absorption due to plasma formation, and scattering by nanoparticles in the plume.

Imaging and optical spectroscopy experiments show that a plasma forms and that the electron density can reach 10^{26} m^{-3} confirming that inverse bremsstrahlung absorption is present in the plume. This electron density is ~ 100 times larger than can be produced by laser heating of the target indicating that the laser ionizes the plume directly.

Nanoparticles are also shown to be present in the plume. These nanoparticles have sizes in the 2 - 3 nm range and a number density ~ 10^{21} m^{-2}. These nanoparticles appear to be vaporized by the laser resulting in high energy ions.

Measurements on the transmission of the laser pulse through the plume show that nanoparticles are too small to attenuate the laser beam. The attenuation mechanism is strictly inverse bremsstrahlung absorption and electron densities reach 10^{26} m^{-3} in the first 10 ns of the laser pulse.

These high electron densities are shown to be produced by the ionization of nanoparticles in the plume which can generate large electron and ion densities thus ionizing the plume.

Acknowledgements

I would like to thank Prof. Walt Duley for giving me the opportunity to tackle a project that covered everything from plasma physics to nanoparticle physics and along the way took me halfway around the world. I am indebted to him for his patience and knowlegdeable direction during the last three years.

Thanks also go to my committee, Prof. Wing-Ki Liu, Prof. John Hepburn, and Prof. Nick Westwood for taking the time from their busy schedules to answer my questions and guide my research.

Special thanks go to Gert Callies and Henrik Schittenhelm from the IFWS in Stuttgart, Germany who not only significantly contributed to this project but extended a gracious and helping hand during my two month research exchange in Stuttgart.

For loving care and support, I thank my parents, and my brother and sister who all gave me the strength and helped me along when I saw nothing but darkness.

Finally, I would like to thank my soul mate, Serena, for providing the crowning touch on my life.

Table of Contents

1. Introduction **1**

1.1 Applications of Excimer Lasers 1

1.2 Fundamental Problems of Excimer Laser Ablation 3

1.3 Area of Research 5

2. Theory of UV Laser-Metal Interactions **8**

2.1 Absorption and Heating 8

2.2 Melting and Vaporization 13

2.3 Vaporization with Back Pressure 17

2.4 Target Surface Structure 21

2.5 Vapor Expansion into a Gas 23

2.6 Laser-Plume Interactions 31

3. Computer Simulation of Laser Ablation **44**

3.1. Solution to the Euler Equations 44

3.2 The LASADYN Code 55

3.3 Effects of Pulse Shape and Laser Intensity on the Laser Ablation of Metals 62

3.4 Effect of Gas Pressure and Gas Composition on Laser Ablation of Metals 76

4. Experimental System **83**

4.1 High Vacuum Laser Ablation Chamber 83

4.2 Laser Focussing System 86

4.3 Mass Ablation Rates 89

4.4 Dye Laser Resonance Absorption Imaging (DLRAI) 91

4.5 TOF Mass Spectroscopy of Plasma 94

4.6 Optical Spectroscopy and Scattering 98

4.7 Absorption of Laser Pulse in the Plasma 102

5. Results **106**

5.1 Ablation Depth Measurements 106

5.2 Imaging of the Plasma Plume 112

5.3 Mass and Velocity Distributions of the Ablated Material 130

5.4 Scattering and Optical Spectroscopy of the Laser Plume 144

6. Plasma Forming Mechanisms **162**

6.1 Model of the Laser-Plume Interaction 162

6.2 Laser Heating and Ionization of Metal

Nanoparticles 163

6.2.1 Laser Heating 163

6.2.2 Ionization and Vaporization of Metal Nanoparticles....165

6.2.3 Production of Free Electrons and Ions....171

6.2.4 Production of High Energy Ions....176

6.3 Numerical Calculations and Comparison with Results....177

6.3.1 Ionization of the Plume....177

6.3.2 High Energy Ions....186

6.3.3 Discussion....191

7. Conclusions....192

APPENDIX A: XeCl Laser Emission....197

APPENDIX B: Riemann Problem....201

REFERENCES....204

List of Tables

Table 5.1. Initial velocities measured for Al^{+} and Al^{2+} 133

Table 5.2. Neutral component velocities for Al^{0} from figures 5.19 and 5.20 134

Table 6.1. Comparison of electron densities generated by nanoparticle ionization with the measured electron densities in section 5.4 184

Table 6.2. Maximum ejection velocities of ions escaping nanoparticles from figure 6.5 187

Table 6.3 Measured ion velocities for the TOF results 189

List of Illustrations

Figure 2.1. Surface temperature evolution for 308 nm laser heating assuming a Gaussian laser pulse with I = 10^{13} Wm^{-2} and FWHM = 30 ns. No vaporization is assumed 12

Figure 2.2. Temperature evolution when vaporization is included (I=10^{13} Wm^{-2}, FWHM=30 ns) . Conditions are the same as in Figure 2.1 14

Figure 2.3. Sketch showing the target, the Knudsen layer, and the collisionless time-of -flight region that develops during the ablation of a substrate 18

Figure 2.4. Irradiation of a Cu target at 308 nm with 750 pulses from an excimer laser with an intensity of 2.5×10^{13} Wm^{-2}. This view is of the crater rim (Kinsman1991) 22

Figure 2.5. Irradiation of a Cu target at 308 nm by an excimer laser with an intensity of 2.5×10^{13} Wm^{-2}. In this single shot case evidence of melting and vaporization are present (Kinsman 1991) 24

Figure 2.6. A schematic diagram showing the discontinuities observed using Schlieren photography for Cu at 248 nm (Callies et al. 1995) 25

Figure 2.7. Graphical representation of the evolution of the 5 discontinuities in figure 2.6 (Callies et al. 1995) 27

Figure 2.8. Shock wave (x) and plume (+) positions as a function of backing gas pressure for (a) air, (b) argon 2.3 μs after the start of the laser pulse. The laser intensity was 1.75×10^{12} Wm^{-2} (Ventzek et al. 1992) 30

Figure 2.9. Plot of absorbed power per cubic meter for single-photon ionization and inverse bremsstrahlung at a laser wavelength of 308 nm and an Al density and temperature of 10^{26} m^{-3} and 8000 K respectively. Below 10^{25} m^{-3}, single-photon ionization is the dominant absorption mechanism while above 10^{25} m^{-3}, absorption is dominated by inverse bremsstrahlung.....39

Figure 2.10. Laser pulse transmission through the plasma for 248 nm radiation incident on a Cu target (Schittenhelm et al. 1996). The curve labeled "1" is the laser intensity for the unattenuated beam, while the curve below that is the transmitted beam.....40

Figure 2.11. Nanoparticle scattering model of Schittenhelm et al. (1996) showing how nanoparticles of sizes 40 nm and densities of ~ 10^{20} m^{-3} in the plume could attenuate the laser beam.....41

Figure 3.1. Schematic of the shock tube problem showing the backward facing rarefaction wave (1), the contact discontinuity (2), and the shock wave (3), for pressure, density, velocity, and internal energy as a function of displacement z. Both the velocity and pressure are continuous across the contact discontinuity.....46

Figure 3.2. Cell boundaries used in the numerical solution of the Euler equations.....48

Figure 3.3. Illustrations of slope construction in cells to illuminate discontinuities. Here j is the cell number and j+1/2 and j-1/2 are the cell boundaries. W refers to either pressure, density, or velocity in the cells.....51

Figure 3.4. The diagram shows the three constraints imposed on the slope at cell j.....53

Figure 3.5. Laser ablation model for vaporization showing the four different parts of LASADYN....56

Figure 3.6. Boundary conditions used in the simulation of laser ablation. When the vapor pressure is less than the background gas pressure no vaporization occurs....58

Figure 3.7. Shock tube problem showing the smooth transition for the F value at the contact discontinuity....61

Figure 3.8. Simulation of laser ablation of Al in 1 atm of N_2 showing the temperature, density, pressure, and velocity of the plasma and background gas. The laser intensity is 1×10^{13} Wm^{-2}, the wavelength 308 nm, and the FWHM = 30 ns....63

Figure 3.9. Laser ablation of Al at 30 ns into the laser pulse. The conditions are the same as in figure 3.8....65

Figure 3.10. Laser ablation of Al at 50 ns near the end of the laser pulse for the same conditions as in figure 3.8. Notice the well resolved contact discontinuity....66

Figure 3.11. Electron density and inverse bremsstrahlung absorption coefficient in the plasma. The intensity is 1.0×10^{13} Wm^{-2}, λ=308 nm, and FWHM=30 ns....67

Figure 3.12. Laser ablation of Al after 10 ns for and intensity of 1.0×10^{13} Wm^{-2} with a skewed Gaussian pulse of 10 ns rise time and 50 ns fall time. The wavelength is 308 nm....69

Figure 3.13. Laser ablation of Al at 30 ns after the start of the laser pulse. The intensity is 1.0×10^{13} Wm^{-2} and the pulse has a rise time of 10 ns and a fall time of 50 ns. The wavelength is 308 nm....70

Figure 3.14. Laser ablation of Al 50 ns after the start of the laser pulse. The pulse conditions are the same as in figure 3.3 71

Figure 3.15. Laser ablation of Al at three different laser intensities showing the effect of laser power on the gas dynamics. Solid line - 10^{14} Wm^{-2}, short dash line - 10^{13} Wm^{-2}, long dash line - 10^{12} Wm^{-2}. The pulse is a skewed Gaussian with a rise time of 10 ns and a fall time of 50 ns. The figure shows the results at 30 ns 73

Figure 3.16. Composition of the IB absorption coefficient for three different laser intensities. The pulse is a skewed Gaussian with a rise time of 30 ns and a fall time of 50 ns. The time is 30 ns after the start of the laser pulse 74

Figure 3.17. Absorption of the laser pulse by inverse bremsstrahlung in an Al plasma using a laser intensity of $I = 1\times10^{14}$ Wm^{-2}. The dashed line is the unattenuated beam while the solid line represents the transmitted beam 75

Figure 3.18. Effects of N_2 gas pressure on the laser ablation of Al at a laser intensity of 1.0×10^{13} Wm^{-2} with FWHM=30 ns and λ=308 nm. The time is 30 ns after the start of he pulse. The solid line corresponds to an N_2 pressure of 1 atm. The short dash line is for a pressure of 0.1 atm, and the long dash line is for a pressure of 0.01 atm 77

Figure 3.19. Effect of gas pressure on the laser ablation of Al for the same conditions as in figure 3.18 but 50 ns after the start of the laser pulse. Solid line - 1atm N_2. Short dash line - 0.1 atm N_2. Long dash line - 0.01 atm N_2 78

Figure 3.20. Effect of gas composition on the laser ablation of Al with a laser intensity is 1.0×10^{13} Wm^{-2} and FWHM = 30 ns. The time is 30 ns after the start of the laser pulse. The solid line corresponds to 1 atm N_2. The short dash line corresponds to 1 atm Ar, and the long dash line corresponds to 1 atm He.....80

Figure 3.21. Effect of gas composition on the laser ablation of Al for the same conditions as in figure 3.20 but at 50 ns after the start of the laser pulse. Solid line - 1 atm N_2. Short dash line - 1 atm Ar. Long dash line - 1atm He 81

Figure 4.1. Above view of high vacuum laser ablation chamber showing the mini optical board. The chamber is 25 cm in diameter and 20 cm deep.....84

Figure 4.2. Target wheel assembly. Each target is 1 cm long and 0.5 cm high.....85

Figure 4.3. Laser focussing system to obtain uniform energy density on the target.....87

Figure 4.4. Laser beam profile of an excimer laser showing the flat top along the two orthogonal directions (lumonics HyperEX-400 excimer laser manual).....88

Figure 4.5. DLRAI experimental set up for tracking individual species within a laser induced plasma plume (courtesy of IFSW, Stuttgart, Germany).....92

Figure 4.6. TOF set up showing the different components and different regions that the ions travel through.....96

Figure 4.7. Experimental set up for performing optical emission and scattering experiments on the plasma.....99

Figure 4.8. a) Focus of telescope compared to the plasma when the laser spot size is 200 μm. b) Same as a) but with a laser spot size of 350 μm.....101

Figure 4.9. Experiment to measure the absorption of the pulse in the plasma plume.....104

Figure 5.1. Ablation depth measurements for Al in N_2 gas of varying pressure. The wavelength of the laser is 308 nm and the FWHM = 30 ns. The curves are nonlinear indicating attenuation of the laser pulse in the plume.....107

Figure 5.2. Ablation depth measurements for Al in varying Ar pressure. The wavelength of the laser is 308 nm and FWHM = 30 ns. The curves are nonlinear indicating attenuation of the laser pulse in the plume.....110

Figure 5.3. Ablation depth measurements for Al in varying He pressures. The laser wavelength is 308 nm and FWHM = 30 ns. The curves are nonlinear indicating attenuation of the laser pulse in the plume pressures.....111

Figure 5.4. Dye laser resonance absorption images at different times after the laser pulses at a laser intensity of 1.2×10^{13} Wm^{-2} and a N_2 gas pressure of 1 atm. The wavelength of the laser is 248 nm and the beam spot size is 200 μm. No absorption of the dye laser pulse is shown indicating that the plume is ionized.....113

Figure 5.5. Dye laser resonance absorption images of the Al plasma at a laser intensity of 1.2×10^{12} Wm^{-2}, magnification of 20, and N_2 gas pressure of 1 atm. The laser wavelength is 248 nm and the beam spot size is 200 μm The images are reversed because they were taken on the opposite side of the target.....115

Figure 5.6. Dye laser resonance absorption images at an intensity of 4.7×10^{12} Wm^{-2} and a gas pressure of 1 atm N_2. The wavelength of the laser is 248 nm and the beam spot size is 200 μm. At 65 ns, the plasma is beginning to

neutralize.....116

Figure 5.7. Dye laser resonance absorption images at an intensity of 4.7×10^{12} Wm^{-2}, magnification of 20, and an N_2 gas pressure of 1 atm. The wavelength of the laser is 248 nm and the beam spot size is 200 μm . At these late times the plasma is completely neutral.....117

Figure 5.8. DLRA images at a background gas pressure of 0.5 atm of N_2. The laser intensity is 1.2×10^{13} Wm^{-2} and the wavelength is 248 nm. No absorption can be seen.....119

Figure 5.9. DLRA images at a background gas pressure of 0.5 atm of N_2. The laser intensity is 4.7×10^{12} Wm^{-2} and the wavelength is 248 nm. Absorption of the dye laser pulse begins after 30 ns.....120

Figure 5.10. Plasma emission for a laser intensity of 1.2×10^{13} Wm^{-2} and 1 atm N_2. The wavelength of the laser is 248 nm. The filter used was 450 nm. Plasma emission can be seen near the target and behind the shock wave outlined in white.....122

Figure 5.11. Velocity of contact front as a result of acceleration of the ionized vapor near the target. These measurements were taken from figure 5.10.....123

Figure 5.12. Interferometric measurements of the electron density under the conditions of figure 5.10 at 36 ns after the start of the laser pulse. The target is located at r=0.0 and z=0.0 (Schittenhelm et al. 1998). Notice the very high electron density near the target surface.....125

Figure 5.13. Schlieren photographs of the Al plasma structure for a laser intensity of 1.2×10^{13} Wm^{-2} and wavelength 248 nm. Several discontinuities are observed and presented in figure 5.14 127

Figure 5.14. Model of plasma structure for excimer laser ablation of metals in the presence of background gas. ND1 and ND2 are two unidentified discontinuities present in figure 5.13. These are most likely due to refractive index changes in the plume 128

Figure 5.15. Refractive index distribution for the plot in figure 5.12 (Schittenhelm et al. 1998). The changes in the refractive index create the discontinuities observed in figure 5.13 129

Figure 5.16. TOF spectra for the laser ablation of Al in vacuum at laser intensities 9.7×10^{12} Wm^{-2}, 6.3×10^{12} Wm^{-2}, and 4.5×10^{12} Wm^{-2}. The wavelength of the laser is 308 nm. Al^{2+} and Al^{+} are observed 131

Figure 5.17. TOF spectra for ablation of Al in vacuum at laser intensities of 3.2×10^{12} Wm^{-2} and 2.4×10^{12} Wm^{-2}. The wavelength of the laser is 308 nm.... 132

Figure 5.18. TOF as a function of initial ion velocity for Al^{+}, Al^{2+}, and Al_2^{+} using equation 5.1 135

Figure 5.19. TOF of the neutral component accompanying ion emission at laser intensities 9.7×10^{12} Wm^{-2}, 6.3×10^{12} Wm^{-2}, and 4.5×10^{12} Wm^{-2}. The laser wavelength is 308 nm. Neutral peak NP1 is most likely Al^{2+} that has recombined with electrons while NP2 is due to Al^{+} that has recombined with

an electron.....136

Figure 5.20. As in figure 5.19 but at laser intensities of 3.2×10^{12} Wm^{-2} and 2.4×10^{12} Wm^{-2}. Here very little neutral material is observed due to acceleration stack effects.....137

Figure 5.21. Potential well created by photoelectron emission during laser ablation of metals. This well can cause the acceleration of ions as they are emitted from the target.....140

Figure 5.22. TOF spectra produced by laser irradiation of the debris around the ablation site on Al. The laser intensity is 1.7×10^{11} Wm^{-2} and the wavelength is 308 nm. This result shows that nanoparticles can be easily ionized by laser radiation.....143

Figure 5.23a. Scattering and optical emission in the 307 - 395 nm range from an Al plasma in 1 atm N_2. The laser intensity is 10^{13} Wm^{-2} and the wavelength is 308 nm. The peak at 308 nm is scattered laser light. No resonant ground state Al transitions exist for this laser (Appendix A). Al^{2+} at 360.1 nm is observed at 30 ns after the start of the laser pulse.....145

Figure 5.23b. Al plasma emission in the 235 nm to 320 nm range in 1 atm N_2. The laser intensity is 10^{13} Wm^{-2} and the wavelength is 308 nm. Two peaks at 281.6 nm and 263.7 nm are observed. These peaks are due to transitions in Al^{+} 146

Figure 5.24. Transmission of the laser pulse through the Al plasma for a laser intensity of 10^{13} Wm^{-2} and wavelength 308 nm. Since there is no overlap with the Al ground state transition at 308.22 nm, the attenuation is most likely due to inverse bremsstrahlung absorption. Solid line - unattenuated laser pulse. Dashed line - transmitted laser pulse 150

Figure 5.25a. Al plasma emission in the 307 to 395 nm range at a pressure of 1 atm N_2. The laser intensity is 5.6×10^{12} Wm^{-2} and the wavelength is 308 nm. Scattering is still present in the early part of the pulse. The peak at 360.1 nm is due to Al^{2+} 153

Figure 5.25b. Al plasma emission in the 235 to 325 nm spectral range at a pressure of 1 atm N_2. The laser intensity and wavelength are the same as in figure 5.25a. Two peaks at 281.6 nm and 263.7 nm are observed. These peaks are due to transitions in Al^{+} 154

Figure 5.26. Transmission of the laser pulse through the Al plasma plume for an intensity of 5.6×10^{12} Wm^{-2} and wavelength 308 nm. Since there is no overlap with the Al ground state transition at 308.22 nm (Appendix A), the observed transmission must be due to inverse bremsstrahlung absorption. Solid line - unattenuated laser pulse. Dashed line - transmitted laser pulse 155

Figure 5.27a. Al plasma emission in the 307 nm to 395 nm range at a pressure of 1 atm N_2. The laser intensity is 2×10^{12} Wm^{-2} and the wavelength is 308 nm. The scattered signal is observed at 308 nm but very little line emission is

present.....156

Figure 5.27b. Al plasma emission for the 235 to 325 nm spectral range and pressure of 1 atm N_2. The laser intensity and wavelength are the same as in figure 5.27a. Very little emission is observed at 281.6 nm and 263.7 nm. These peaks are due to transitions in Al^+ 157

Figure 5.28. Transmission of the laser pulse through the Al plasma plume for a intensity of 2×10^{12} Wm^{-2} and wavelength 308 nm. The transmission of the laser pulse is nearly 100% as indicated by the dashed line. The solid line is the unattenuated laser pulse.....158

Figure 5.29a. Al plasma emission in the 307 - 395 nm range at a pressure of 10^{-3} atm. The laser intensity is 10^{13} Wm^{-2} and the wavelength is 308 nm. Scattering (308 nm) and line emission from Al^{2+} (360.1 nm) are still observed indicating that the effects of the gas pressure are small.....159

Figure 5.29b. Al plasma emission for the 235 - 325 nm spectral range at a pressure of 10^{-3} atm. The laser intensity and wavelength are the same as in figure 5.29a. Line emission is still observed at 281.6 nm and 263.7 nm due to transitions in Al^+ 160

Figure 6.1. a) Ion emission rate as a function of temperature for an Al nanoparticle 5 nm in size with a charge Q = 15. The vibrational frequency for Al is ~ 1×10^{12} s^{-1} (Kittel 1986). b) Thermal electron emission for the same conditions as in a).....173

Figure 6.2. Ion emission rate as a function of decreasing nanoparticle size. The

temperature is 15000 K and Q = 15 174

Figure 6.3. Results for the ionization of 5 nm Al nanoparticles in an Al vapor plume, at laser intensities of 10^{13}, 5.6×10^{12}, and 2×10^{12} Wm^{-2}. The laser wavelength is 308 nm 178

Figure 6.4. Results for the ionization of 5 nm nanoparticles in an Al vapor plume, for the same conditions as in figure 6.3. Ionization begins at 10 ns 182

Figure 6.5. Ionization rates of the vapor by ejected electrons, and recombination rates of the ejected electrons and ions using the values in figure 6.3 183

Figure 6.6. (a) Charge on nanoparticles that begin ionization at 3 ns. (b) Charge on nanoparticles that begin ionization at 10 ns. These results were obtained from the simulations in figures 6.3 and 6.4 188

Figure A.1. XeCl laser emission measured using a UV-VIS spectrometer with a resolution of 0.11 nm 199

Figure A.2. Mercury calibration spectrum used to calibrate the UV-VIS spectrometer used in figure A.1 200

Chapter 1

Introduction

1.1 Applications of Excimer Lasers

Materials processing with short pulse excimer lasers (10 - 30 ns) is becoming widely used in industry. The high laser intensities (~ 10^{13} Wm^{-2}) and large photon energies (4 - 6 eV) achieved with such lasers results in a unique method of laser interaction with certain materials. The most significant feature is the fact that excimer lasers can remove material by ablation rather than thermal mechanisms such as melting, evaporation, or vaporization usually associated with CO_2 and Nd:YAG lasers. This non-thermal process differs depending on the material. In metals, the photon energy is similar to the work function of many metals and the absorption coefficient can be very large. The ablative process is therefore one of ionization with rapid heating of the lattice within a small volume. Little heat is generated outside the penetration depth of the laser. In organics, the ablation is photo-chemical since the photon energy is often greater than the bond energy in many organic materials. As a result excimer laser ablation of materials produces a much higher

degree of precision than can be achieved with other types of laser processing. This leads to some very significant applications in materials processing. In micromachining, for example, excimer lasers can ablate material with micrometer precision. This allows the formation of complex microstructures in materials for the electronics industry and also allows layered materials to be ablated without affecting the underlying substrate. Some applications are: precision machining of polymers for the electronics industry, marking of materials for identification, surface cleaning of metals and artwork, electrical contact machining in printed circuit boards, and fabrication of micro-components such as exhaust nozzles for micro-satellites (Znotins 1987, Bransden et al. 1990, Hayashi and Miyamoto 1995, Kitagawa et al. 1995, Hansen et al. 1997, Georgiou et al. 1998). Material that is ablated by an excimer laser tends to be hot and ionized which naturally leads into the area of thin film deposition by laser ablation. Many applications exist such as the development of novel thin films for coatings, and for the electronics industry. One of the most important applications is in the formation of superconducting thin films by laser ablation of bulk material. Here, the stoichiometry of the film is important (Habermeier 1992) and depends on the excimer laser being able to ionize and form a plasma from the bulk target. This area is still quite new, however, and has not yet been encompassed by industry.

Micromachining and thin film formation are the two areas in which excimer lasers are now being used. Only a few applications have been briefly mentioned here. Many more exist and each year new applications for excimer laser are found.

1.2 Fundamental Problems of Excimer Laser Ablation

Although the excimer laser has unique applications and is a versatile tool there are undesired effects during laser ablation. For example, the ablation of metals often results in a dense plasma forming above the work piece which can completely absorb the laser energy (Schittenhelm et al. 1996). This can dramatically reduce the laser material coupling efficiency which affects the amount of material ablated per laser shot for micromachining. In addition, nanoparticles can form in the ablation plume which are then redeposited around the interaction site as debris (Miyamoto et al 1994 p240, p249) necessitating further processing for cleaning. Also, nanoparticles can collect on thin films during formation impeding the growth of lattice structures. This is an important factor in superconducting thin films (Zheng et al. 1994).

The successful optimization of these and other applications as well as the development of new ones all depend on a detailed understanding of the UV laser-material interaction process both in vacuum and under ambient processing conditions. In the current model of excimer laser ablation of metals, the laser rapidly heats and ablates the substrate creating a dense plume in front of the target. Shortly after the start of the laser pulse, ~ 10 ns, the plume begins to attenuate the laser pulse (Schittenhelm et al. 1996). The attenuation increases toward the end of the pulse and in cases in which the intensity reaches 10^{13} Wm^{-2} the plume can attenuate most of the laser pulse energy (Schittenhelm et al. 1996). For 248 nm radiation, two attenuation mechanisms have been proposed: inverse bremsstrahlung absorption by free electrons (no resonant absorption bands exist at 248 nm), and scattering and absorption by nanoparticles (Schittenhelm et al. 1996). Inverse bremsstrahlung

absorption varies as λ^3 and is therefore very weak at UV laser wavelengths. This requires that the plume be highly ionized forming a plasma. For example, in the ablation of Al the electron density would need to be ~ 10^{26} m^{-3} (Pinho et al. 1997) in the plume before appreciable absorption of the laser pulse occurs. This is of the same order as the plume density. Attaining such a high electron density by target heating alone is not possible for 248 nm radiation since the target temperature and therefore the plume temperature remain too low, < 10^4 K, giving electron densities which are much too small for absorption of the laser pulse. This has led investigators to consider scattering and absorption by nanoparticles in the plume as an alternate to plasma absorption. Since attenuation by small nanoparticles varies as λ^{-4} in the Rayleigh limit, scattering of the laser beam in the plume can be very efficient. Schittenhelm et al. (1996) have shown that nanoparticles with sizes up to 50 nm and number densities ~ 10^{20} m^{-3} could efficiently attenuate the laser beam. Evidence for nanoparticles formation in the plume, however, is limited. Miyamoto et al. (1994 p240, p249) has shown that nanoparticles are present around the interaction site but that they are formed long after the laser pulse as the plume cools. Nanoparticles formation during the laser pulse has never been experimentally observed. Theoretical models have been proposed by Callies et al. (1996, 1998). They have been able to model nanoparticles formation in the plume using condensation theory for the excimer laser ablation of Al. They found that nanoparticles of sizes 5 - 30 nm and number densities 10^{20} - 10^{21} m^{-3} could be formed near the target surface. However, their model was highly sensitive to the temperature in the plume and the surface tension of the nanoparticles: slight variations in either of the quantities and no nanoparticles would form. Although the model was an

important first step in showing that nanoparticles can form in an excimer laser induced plume and that the nanoparticles may be responsible for the attenuation of the laser beam, the model did not consider the effects of laser heating on the nanoparticles. With laser intensities in the range 10^{12} - 10^{13} Wm^{-2} any nanoparticles formed would be heated and quickly vaporized within a few nanoseconds. The nanoparticles may not survive long enough to effectively scatter the laser beam.

Absorption by a plasma and scattering by nanoparticles are the only two mechanisms that can attenuate the laser beam in the Al plume at 248 nm. At 308, nm a resonant absorption transition in Al exists at 308.22 nm (Reader et al. 1980) and this may explain the ionization of the plume. Without resonance absorption in the ground state of the metal, plasma absorption will be too weak and scattering by nanoparticles may not be possible. Therefore, properly assessing which of these mechanisms is significant is a very important step in understanding the excimer laser ablation of materials since once the mechanism is known, the attenuation can be controlled and laser processing can be optimized.

1.3 Area of Research

In light of the fundamental problems associated with excimer laser ablation, a major theoretical and experimental study was undertaken to evaluate the energy transfer mechanism between an excimer laser operating at 308 nm and 248 nm, a solid substrate, and the environment around the interactions site. The substrate chosen for this will be Al since this is a well characterized metal of industrial importance. The environment chosen

will be N_2. However, the effects of vacuum, He, and Ar on the ablation process will also be examined to study the effects of gas pressure and gas composition on the ablation process.

It will first be shown in Chapters 2 and 3, with a model of laser ablation that if no resonant ground state transitions exist in the metal (see Appendix A), then insufficient ionization occurs in the vapor plume between 10^{12} Wm^{-2} and 10^{13} Wm^{-2} to induce inverse bremsstrahlung absorption. A minimum electron density for inverse bremsstrahlung absorption in the plume will be established and it will be shown that only at intensities greater than 10^{13} Wm^{-2} is inverse bremsstrahlung absorption significant.

In Chapters 4 and 5 a series of experiments will be devised and performed to evaluate the presence of a plasma and nanoparticles in the ablation plume. Dye laser resonance absorption at 248 nm and optical spectroscopy experiments at 308 nm will be primarily used to show that a strong plasma does form in the plume during the laser pulse at the laser intensities of interest. Scattering experiments (at 308 nm) will reveal that nanoparticles are also present in the plume in the early part of the laser pulse. The nanoparticles are independent of the gas atmosphere and appear to originate from the molten surface of the Al before plasma formation. The experiments will show that nanoparticles subsequently disappear as the plasma forms in the laser induced plume. This only depends upon the laser intensity indicating that the nanoparticles are vaporized by the laser.

In Chapter 6, the experimental results will be used to develop a model which will show that strong laser heating and ionization of the nanoparticles does occur. The nanoparticles

become ionized and vaporize producing high energy electrons and ions. This will be confirmed by time of flight mass spectroscopy of the plume. The ionization of the nanoparticles, as will be shown, is primarily responsible for ionizing the plume, since no resonant ground state transitions exist at 308 nm and 248 nm (Appendix A). The level of ionization is sufficient to activate inverse bremsstrahlung absorption. Attenuation of the laser pulse will, therefore, be shown to be a two-step process involving the ionization of nanoparticles followed by inverse bremsstrahlung absorption.

Chapter 2

Theory of UV Laser-Metal Interactions

2.1 Absorption and Heating

Conversion of laser radiation to heat in metals involves the excitation of electrons to states of higher energy. At UV laser wavelengths, the laser photon energy, $h\nu$, is comparable to or larger than the work function of the metal, ϕ. This can result in the electrons being directly ejected from states near the Fermi surface to continuum states. The ejected electrons originate in a skin depth, $\delta(\lambda)$ which is the inverse of the absorption coefficient $\alpha(\lambda)$ given by,

$$\alpha(\lambda) = \frac{4\pi k}{\lambda} \tag{2.1}$$

where k refers to the imaginary part of the complex refractive index $m=n-ik$. At 308 nm, k = 3.74 for Al (Palik 1985) giving $\alpha(\lambda) = 1.5 \times 10^8\ m^{-1}$. In practice, the absorption coefficient is

smaller for metals due to surface irregularities. However, the skin depth is usually no more than 1 μm.

Electrons that are not ejected dissipate their excess energy as heat within this skin depth. Since the quantum efficiency for the production of photoelectrons in metals is on the order of 10^{-4} (Kawamura et al. 1984) for Al, only a very small fraction of the excited electrons will be emitted as photoelectrons. The remaining electrons with energies $\varepsilon = \varepsilon_F + h\nu$ will lose their excess energy through electron-electron and electron-phonon scattering.

Transfer of energy from the electron gas to the lattice occurs over a very short time since the electron and phonon density is very high (on the order of 10^{29} m^{-3}). The timescale for this is typically 10^{-14} s and a rapid conversion of excess electronic energy into lattice heat therefore occurs. For typical excimer lasers, the pulse width is on the order of 10 - 30 ns and therefore decoupling of the electron and lattice temperatures does not occur.

Heating of a solid by a radiative source can then be described by the heat conduction equation (Carslaw and Jaeger 1976),

$$\nabla^2 T(x,y,z,t) - \frac{1}{\kappa}\frac{\partial T(x,y,z,t)}{\partial t} = -\frac{A(x,y,z,t)}{K} \tag{2.2}$$

where T is the temperature as a function of space and time, κ is the thermal diffusivity (m^2s^{-1}) and K is the thermal conductivity ($Wm^{-1}K^{-1}$). $A(x,y,z,t)$ is the rate of heat production per unit volume of material (Wm^{-3}). κ and K are both assumed to be independent of temperature.

As discussed earlier, the skin depth for the penetration of ultraviolet radiation into Al is about 1 μm. This is much less than the lateral spatial extent of a focused excimer laser beam and so one can, therefore, ignore lateral heat conduction and rewrite equation 2.2 as,

$$\nabla^2 T(z,t) - \frac{1}{\kappa}\frac{\partial T(z,t)}{\partial t} = -\frac{A(z,t)}{K} \tag{2.3}$$

where z is the coordinate perpendicular and extending into the sample surface. The usual approximation for the volume heat source is to assume that (Duley 1996),

$$A(z,t) = (1-R)I_o(t)\alpha e^{-\alpha z} \tag{2.4}$$

where R is the surface reflectivity and $I_o(t)$ is the time dependent laser intensity incident on the surface. Equation 2.3 then describes the solution for the temperature profile inside a sample exposed to a uniform heat source of intensity $I_o(t)$.

For certain conditions one can find approximate solutions to equation 2.3. If the material is strongly absorbing such as metals, then the temperature profile is approximately given by (Duley 1976,1996),

$$T(z,t) = T_o + 2\frac{(1-R)I_o(\kappa t)^{1/2}}{K} ierfc\left(\frac{z}{2(\kappa t)^{1/2}}\right) \tag{2.5}$$

where the condition that $(\kappa t)^{1/2} \gg \alpha^{-1}$ is assumed. Equation 2.5 assumes a time independent laser pulse. After the laser pulse, the temperature varies as (Duley 1976, 1996),

$$T(z,t) = T_o + 2\frac{(1-R)\kappa^{1/2}}{K}\left[t^{1/2} ierfc\frac{z}{2(\kappa t)^{1/2}} - (t-t_{off})^{1/2} ierfc\frac{z}{2(\kappa(t-t_{off}))^{1/2}}\right] \quad (2.6)$$

where T_o is the initial temperature, t_{off} is the time at which the laser pulse ends and *ierfc* is the integral of the error function. The temperature decrease after the laser pulse arises from thermal diffusivity. The surface temperature is obtained by solving equation 2.5 for z = 0 which is,

$$T(0,t) = T_o + 2\frac{(1-R)I_o}{K}\left(\frac{\kappa t}{\pi}\right)^{1/2} \quad (2.7)$$

Figure 2.1 shows the temperature profile for a Gaussian laser pulse of intensity 10^{13} Wm^{-2} and 30 ns width incident on Al with $R = 0.8$, $K = 100$ $Wm^{-1}K^{-1}$, and $\kappa = 8.8\times10^{-5}$ m^2s^{-1}. This was obtained by solving equation 2.7 using discrete pulses of intensity $I_o = I(t)$ and width Δt with Δt much smaller than the width of the laser pulse. The temperature rises strongly in the midpart of the laser pulse and is highest toward the end of the pulse as is expected from equation 2.7. However, the maximum temperature reached of over 3×10^5 K is a gross over estimate and occurs since vaporization has not been included. The vaporized material carries away some heat and therefore cools the surface. In the next section melting and vaporization is examined and its effect on the temperature profile will be discussed.

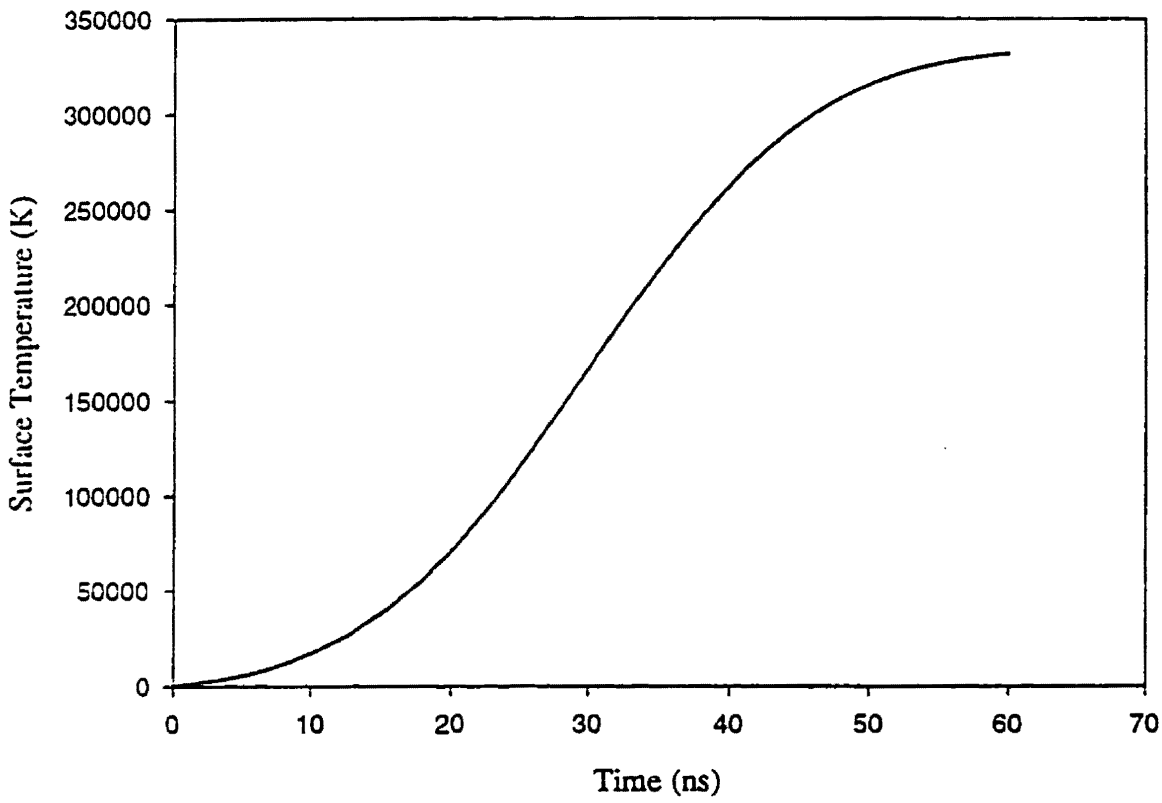

Figure 2.1. Surface temperature evolution in Al for 308 nm laser heating assuming a Gaussian laser pulse with $I = 10^{13}$ Wm^{-2} and FWHM = 30 ns. No vaporization is assumed.

2.2 Melting and Vaporization

When the melting temperature is reached, further heating is required to overcome the latent heat of fusion and the material temperature, therefore, remains constant during melting. In the one-dimensional model above this can be estimated by assigning a temperature equivalent to the latent heat of fusion, $\Delta T = L_f/C$, where C is the specific heat capacity ($JKg^{-1}K^{-1}$) (Rosen et al. 1982). Equation 2.7 is then,

$$T(0,t) = T_o - \Delta T + 2\frac{(1-R)I_o}{K}\left(\frac{\kappa t}{\pi}\right)^{1/2}, T_o \rangle T_{melt} \tag{2.8}$$

where T_o is greater than the melting temperature. This is not a large correction; for example, in Al, ΔT is only 317 K.

Vaporization at the sample surface occurs at all temperatures but is strongest near the boiling point T_b. The vapor pressure may be calculated from the Clausius-Clapeyron equation,

$$P(T) = P(T_b)\exp\left(\frac{L_v}{k_b}\left(\frac{1}{T_b} - \frac{1}{T}\right)\right) \tag{2.9}$$

which assumes a liquid-vapor equilibrium (Sussman 1972). The density of the vapor can be calculated from the ideal gas equation,

$$\rho(T) = \frac{P(T)m_s}{k_b T} \tag{2.10}$$

where m_s is the atomic mass of the sample material. The vaporization speed of the ejected material can also be assumed to occur under thermodynamic equilibrium. Equating kinetic energy to thermal energy gives a vapor speed,

$$u(T) = \sqrt{\frac{2k_b T}{m_s}} \tag{2.11}$$

These quantities strongly depend upon the laser pulse and the sample material.

This ejected material will cool the sample since it carries away some of the heat deposited by the laser. The mass flux out of the surface is $\rho(T)u(T)$ where $\rho(T)$ is the density. The vaporized energy flux of this ejected material is then,

$$EF = \rho(T)u(T)L_v \tag{2.12}$$

where L_v is the latent heat of vaporization. This must be balanced with the energy flux from the incident laser beam. Equation 2.7 must therefore be rewritten as,

$$T(z,t) = T_o + 2\frac{\{(1-R)I_o - \rho(T)u(T)L_v\}}{K}\left(\frac{\kappa t}{\pi}\right)^{1/2} \tag{2.13}$$

to properly account for the material which is ejected and, therefore, give the correct temperature profile. Figure 2.2 shows the temperature profile under the same conditions as in figure 2.1 except that now the mass flux of vaporizing material is included. Notice that now

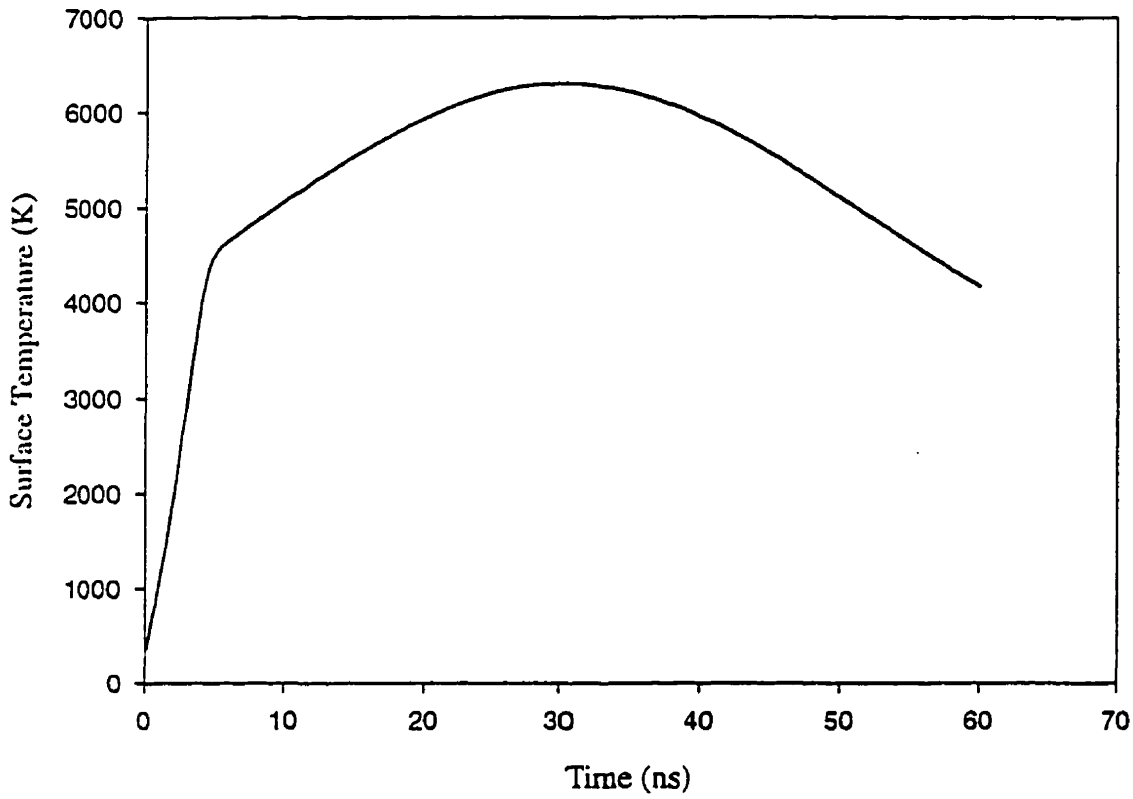

Figure 2.2. Temperature evolution when vaporization is included ($I=10^{13}$ Wm^{-2}, FWHM = 30 ns) . Conditions are the same as in Figure 2.1.

the maximum temperature reached is only ~ 7000 K and that the temperature curve tends to follow the profile of the laser pulse more closely. This is because as the sample becomes hotter equation 2.12 exceeds the flux due to the laser pulse and, therefore, cooling occurs.

As the surface vaporizes it recedes leaving a crater. From the Clausius-Clapeyron equation the mass evaporation rate is,

$$M_{evp}(T) = P(T)\left(\frac{m_s}{2\pi k_b T}\right)^{1/2} \tag{2.14}$$

From this the total ablation depth can be obtained as,

$$Z = \int_0^{\infty} \frac{M_{evp}(T)}{\rho(T)} dt \tag{2.15}$$

since the temperature is time dependent. For typical excimer laser pulses as that used in figure 2.1, this equation predicts ablation depths on the order of 0.1 nm per pulse (Duley 1996) suggesting that less than a monolayer of material is removed. Actual experiments (Kinsman 1991) show that the ablation depth in Al and Cu at 308 nm is on the order of 1 μm which suggests that processes other than thermal equilibrium vaporization occur. Sing et al. (1990) have shown that the heating below the surface in metals due to a finite absorption depth of the laser beam can lead to higher ablation depths. In their calculations, the heating below the surface increased with energy density and absorption coefficient with subsurface temperatures greater than the surface temperatures approximately 0.2 μm into Si targets. This can lead to

explosive removal of material and, therefore, increase the ablation depth. A further consideration is the possibility of forming a molten layer within the skin depth of the sample. Hydrodynamic effects (Kelly and Rothenberg 1985) may then result in more material being removed. Duley (1996) has estimated the depth of melting in Al to be ~ 2.1 μm for an excimer laser pulse of 10^{13} Wm^{-2} and FWHM = 30 ns. This is comparable to results obtained experimentally and suggests that material removal in liquid form dominates the ablation process.

2.3 Vaporization with Back Pressure

As significant vaporization begins after the laser has heated the target sufficiently, vapor will begin to expand outwards (equation 2.11). There are two cases one must consider. The first is vaporization into vacuum where the vapor flow is not impeded and vaporized material can expand without collision. However, when there is a back pressure due to a background gas surrounding the target, vaporized material collides with the background gas over a few mean free paths which alters the velocity distribution of the vapor so that some of the vaporized material returns to the target (Knight 1979, Kelly and Dreyfus 1988, Ytrehus 1976). The region over which collisions occur is known as the Knudsen layer (figure 2.3). Here f_{s+} is a half-range velocity distribution for particles with speeds $v > 0$, f_{k-} is a half-range velocity distribution for particles with speeds $v < 0$ which undergo collisions in the Knudsen layer and return to the surface, and f_{k+-} is a full-range velocity distribution with speeds $-\infty < v < \infty$ for material which escapes the Knudsen layer.

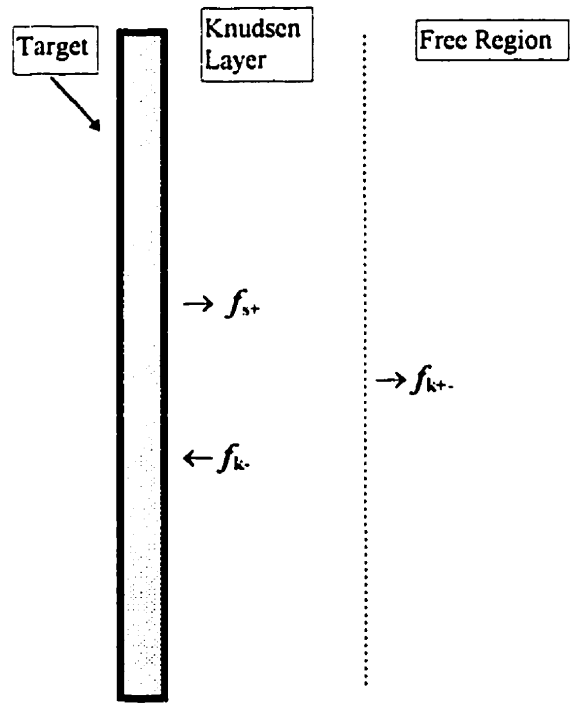

Figure 2.3. Sketch showing the target, the Knudsen layer, and the collisionless time-of-flight region that develops during the ablation of a substrate.

The usual assumption is that particles are emitted thermally. The velocity distributions can then be assumed to be Maxwellian (Anisimov 1968, Ytrehus 1977, Knight 1979, Kelly and Dreyfus 1988). For the initial flux,

$$f_{s+} = \frac{n_s}{(2\pi k_b T_s / m_s)^{3/2}} \exp\left[-\frac{m_s(v_s^2 + v_x^2 + v_y^2)}{2k_b T_s} \right], v_s \geq 0 \qquad (2.16)$$

where n_s the surface number density, v_x and v_y are the particle speeds parallel to the surface, and v_s is the particle speed perpendicular to the surface. Initially, there are no collisions with the gas and so the speed in the z-direction is greater than zero. Collisions, will however, occur after a few mean free paths. In this range, equation 2.16 will develop a negative velocity component as collisional equilibrium is established at the edge of the Knudsen layer. The distribution then becomes a full range Maxwellian (Anisimov 1968, Ytrehus 1977, Knight 1979, Kelly and Dreyfus 1988),

$$f_{k+-} = \frac{n_k}{\left(2\pi k_b T_k\right)^{3/2}} \exp\left[-\frac{m_s\left(\left(v_z - u_k\right)^2 + v_x^2 + v_y^2\right)}{2k_b T_k} \right], -\infty < v_z, v_y, v_x < \infty \qquad (2.17)$$

with plus and minus particle speeds. The number density and temperature are lower outside the Knudsen layer since some of the ejected material recondenses back at the surface. The velocity component u_k is the center of mass velocity of the gas as it leaves the Knudsen layer.

The third distribution function f_{k-} just describes the material that recondenses back at the surface and is identical to equation 2.16 except that $v_s < 0$.

The significance of the Knudsen layer in the laser ablation of metals is the lowering of the temperature, density, and gas speed of ejected material. An exact analytical solution for this decrease, however, does not exist. Instead an approximate solution can be constructed. The first step is the assumption that the Knudsen layer is narrow. Noorbatcha et al. (1987) has shown that a Knudsen layer can form with as few as 3 collisions per particle over approximately 1.5 mean free paths. For UV laser ablation of metals the mean free path for an Al atom in a pressure of 10^5 Nm^{-2} of N_2 is approximately 3×10^{-7} m and the collision frequency is 5×10^9 s^{-1}. This implies that a Knudsen layer is approximately 0.45 μm wide and forms at a time < 1 ns. One can therefore treat a Knudsen layer as a discontinuity with quantities (T_s, ρ_s, v_s) at the surface and (T_k, ρ_k, u_k) at the outer edge of the layer. The solution obtained by Ytrehus (1977), Cercignani (1981), and Frezotti (1986) is to conserve mass, momentum, and energy flux across the layer. With u_k as the speed of sound in the gas the results for temperature and number density for a monatomic vapor in 1 dimension are (Cercignani 1981, Kelly and Dreyfus 1985),

$$\begin{aligned} \frac{T_k}{T_s} &= 0.669 \\ \frac{n_k}{n_s} &= 0.308 \\ \frac{P_k}{P_s} &= 0.206 \\ \frac{u_k}{v_s} &= \sqrt{\frac{\gamma}{2}} = 0.914 \end{aligned} \tag{2.18}$$

These are commonly known as the Knudsen layer jump conditions. Knudsen layer formation is very important when heating targets with a laser as it can control surface heating by reducing the flux of material leaving the surface (equation 2.13). It also provides a necessary correction when calculating the thermodynamics of the vaporized material. Neglecting Knudsen layer formation would result in highly exaggerated temperatures and densities.

2.4 Target Surface Structure

The surface structure of metals irradiated by excimer lasers are typical of melting followed by hydrodynamical sputtering (Kelly and Rothenberg 1985). Figure 2.4 shows an SEM of Cu irradiated at 308 nm with 750 pulses from an excimer laser with an intensity of 2.5×10^{13} Wm^{-2} (Kinsman 1991). The view of the crater rim shows turbulent flow which results from backpressure from the vaporized material which pushes molten material to the edges of the heated zone. The porous areas are regions where vaporization of material has occurred. Kelly and Rothenberg (1985) suggest that these areas may be due to ejection of surface asperites which are accelerated away from the surface. They have also indicated that the volume change caused by ejection of asperites followed by thermal expansion of the liquid may be a cause for the turbulent flow observed in figure 2.4 unlike thermal vaporization which may be too slow to account for turbulent flow.

In a single shot case (figure 2.5) melting is also observed from the smooth structures seen in the figure. The crater-like appearance of the surface suggests that material vaporizes

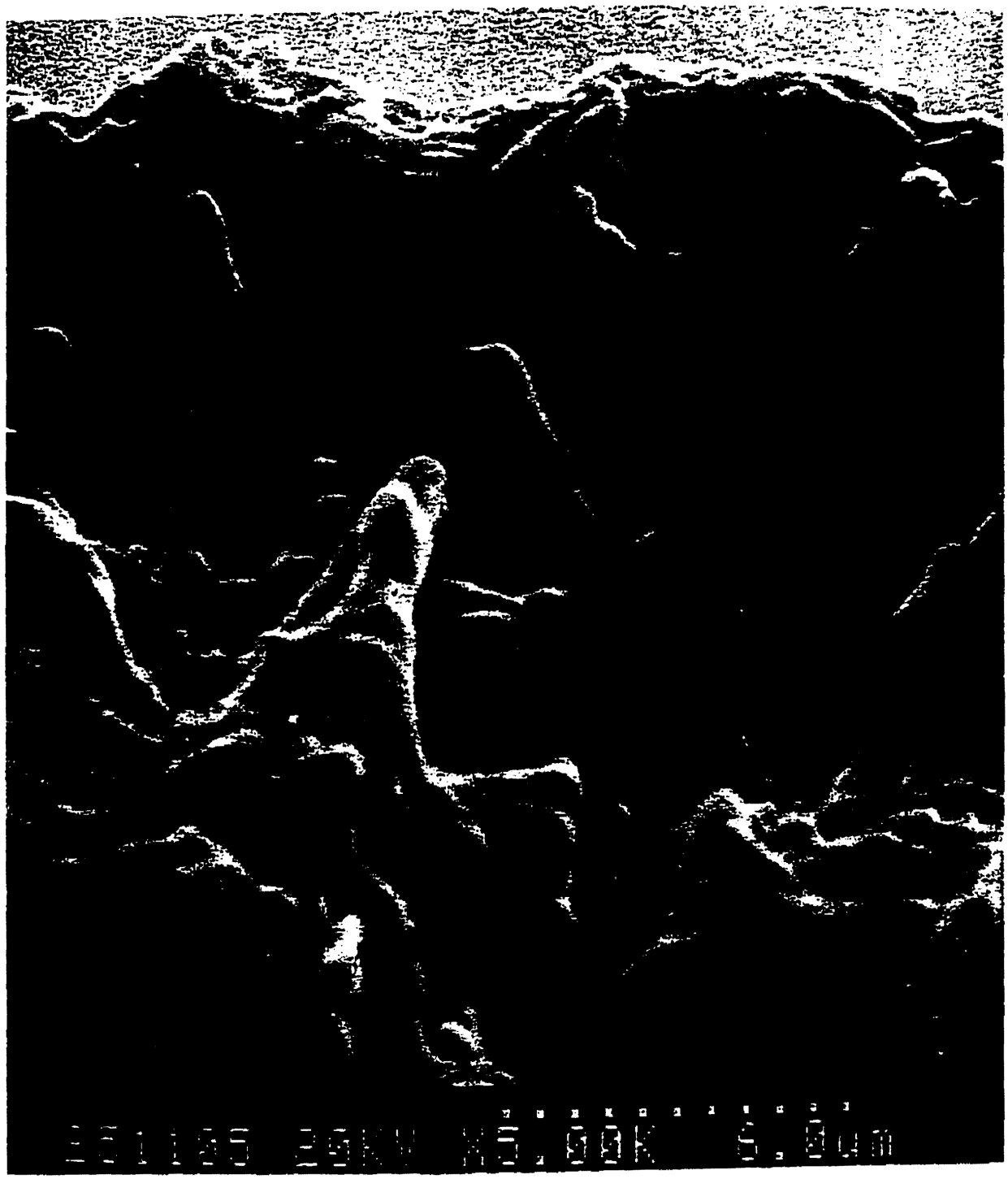

Figure 2.4. Irradiation of a Cu target at 308 nm with 750 pulses from an excimer laser with an intensity of 2.5×10^{13} Wm^{-2}. This view is of the crater rim (Kinsman 1991).

violently otherwise a totally smooth surface would be expected. The formation of asperites in these areas explains the surface craters but also suggests that ablation of metals can produce a large quantity of particulate matter.

2.5 Vapor Expansion into a Gas

The process of rapid surface heating with short pulse UV lasers results in strong vaporization of the target. Vapor expansion velocities usually range from 10 ms^{-1} at low laser intensity (~ 10^{10} Wm^{-2}) (Sell et al. 1991) to over 5000 ms^{-1} at intensities of 10^{13} Wm^{-2} and higher (Guo et al.1993, Sell et al. 1991, Cappelli et al. 1990, Dreyfus et al. 1986) when a background gas is present. These vapor speeds, which are much greater than the local sound speed, result in the compression of the gas to form a shock wave. This is similar to a piston compressing a gas as the diffusion rate is much smaller than the rate of expansion of the vapor. In other words there is not enough time for the vaporized material and the background gas to undergo significant mixing. As the density and speed of the vapor are much higher than that of the gas, compression of the background gas results.

Studies of shock waves in laser-induced plasmas have been conducted by many workers (Grun et al. 1991, Otis et al. 1993, Ventzek et al. 1992, 1993, Callies et al 1995, Gilgenbach et al 1991, Geohegan 1992, Gupta et al 1991, Sappey and Gamble 1992). The morphology and evolution of shock waves from metal surfaces irradiated with excimer laser pulses is very complex. The structure of an evolving shock is shown in figure 2.6 (Callies et al. 1995).

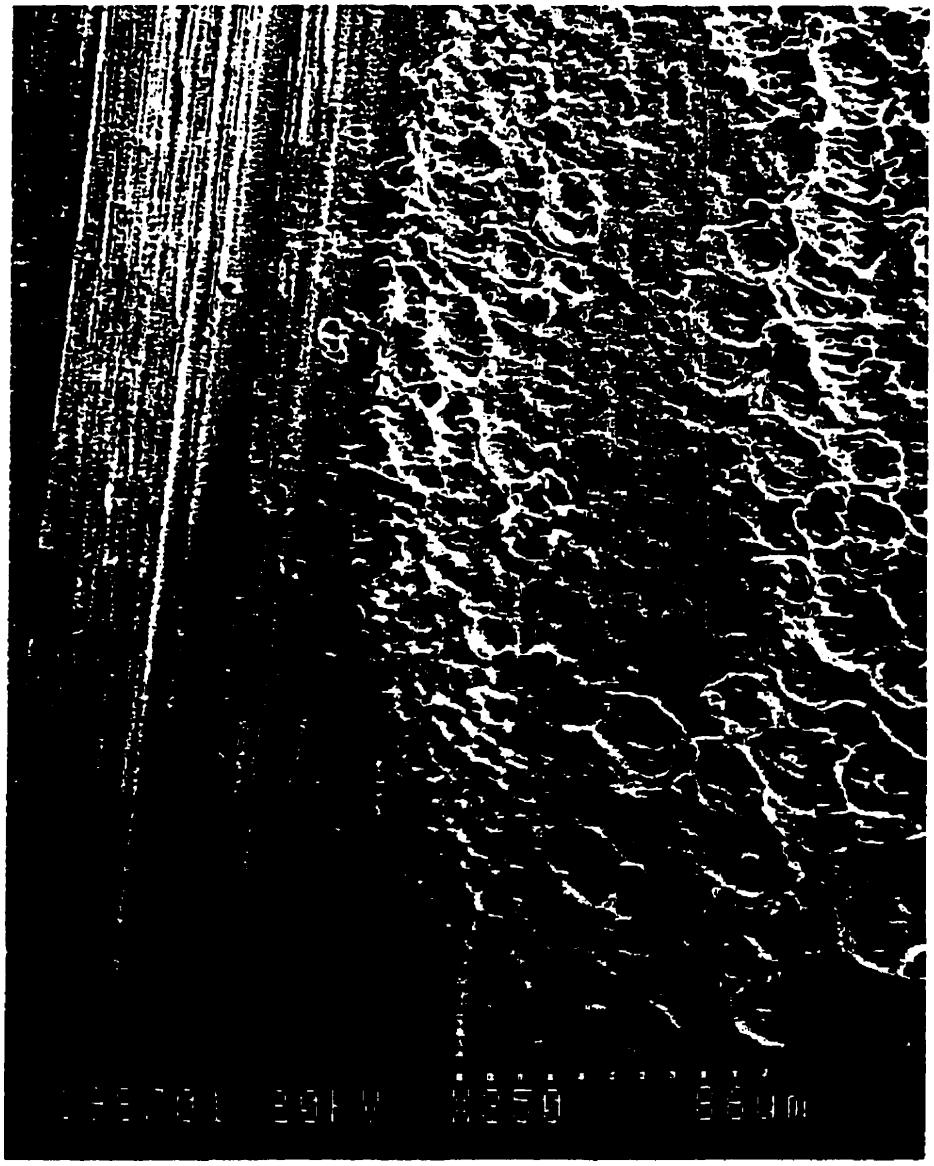

Figure 2.5. Irradiation of a Cu target at 308 nm by an excimer laser with an intensity of 2.5×10^{13} Wm^{-2}. In this single shot case evidence of melting and vaporization are present (Kinsman 1991).

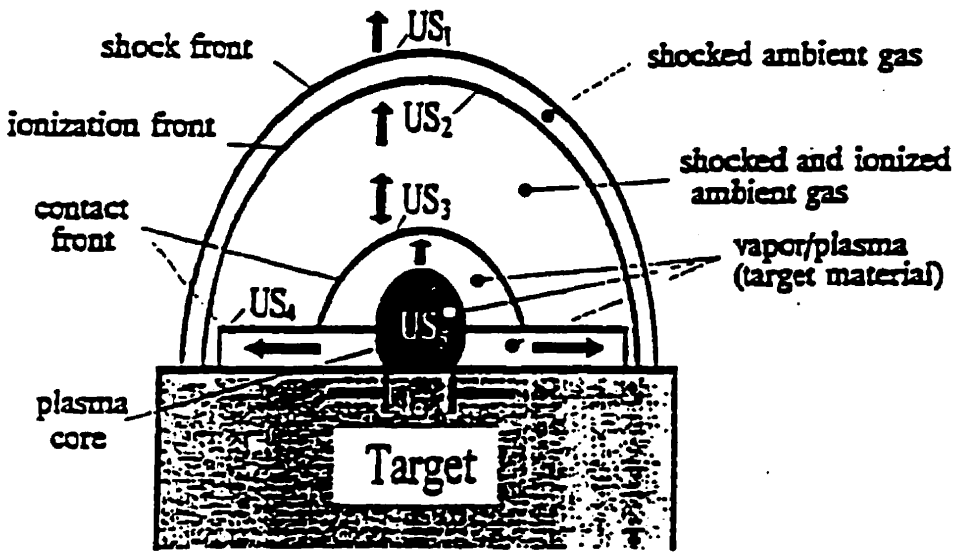

Figure 2.6. A schematic diagram showing the discontinuities observed using Schlieren photography for Cu irradiated at 248 nm (Callies et al. 1995).

A shock front leads an ionization front and is followed by a contact front separating the ambient gas from the vaporized material. There is also a laterally expanding front US_4 which is probably due to stagnation from the other discontinuities, and a plasma core representing a high temperature plasma (Callies et al. 1995).

Callies et al. (1995) have modeled the shock wave and the contact front. The shock wave can be described by the Taylor-Sedov blast wave theory (Sedov 1959) which gives the radius of the shock front as,

$$r(t) = C\left(\frac{E_o}{\rho}\right)^{1/(2+\xi)} t^{2/(2+\xi)} \tag{2.19}$$

where C is a constant, ξ gives the dimensionality of the propagation which is $\xi = 3$ for a spherical wave , E_o represents the fluence deposited in the explosion (Jm^{-2}), and ρ is the density of the ambient gas. Equation 2.19 accurately models the expansion of the shock wave for times greater than the laser pulse since it assumes a point explosion. Callies et al. (1995) obtained better agreement by having E_o follow the temporal behavior of the laser pulse. The contact front position can be related to that of the shock front for times during the laser pulse by (Callies et al. 1995),

$$r_{cf}(t) = \frac{2}{(\gamma+1)} r\left(\frac{t}{t_o}\right)^{2(1-\gamma)/(5(1+\gamma))} \tag{2.20}$$

where γ is the adiabatic constant and t_o is the time at which the contact front changes from a planar discontinuity to a spherical discontinuity.

There is much uncertainty as to why some of these discontinuities form. Figure 2.7 shows an evolution plot of the five discontinuities. The ionization front closely follows the shock front and contains ionized ambient gas indicating that ionization is the result of the compression produced by the shock wave. There are some doubts, however, as to how much

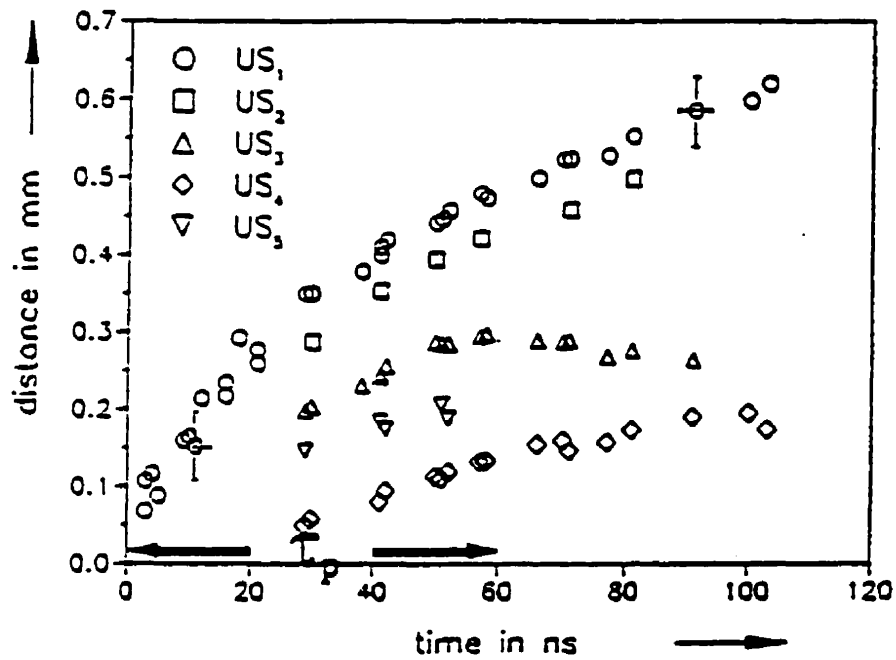

Figure 2.7. Graphical representation of the evolution of the 5 discontinuities in figure 2.6 (Callies et al. 1995).

ionization could be produced by the shock wave. US_4, and US_5 only seem to appear part way through the laser pulse and recede back to the surface shortly after the laser pulse. Callies et al. (1995) have discussed this effect in terms of the ignition of a plasma in the region behind the ionization front, which leads to a strong gas flow towards the target. This pushes down on the evaporating material creating a strong radial outflow. The plasma core has also been interpreted as a region of plasma ignition.

The discontinuities discussed by Callies et al. (1995) cannot be observed in the excimer laser ablation of metals into vacuum or at low pressures (Ventzek et al. 1992) as the shock wave produced is too weak to ionize or affect the pressure and density of the vaporized material. This suggests that the laser ablation of metals can be strongly affected by the background gas pressure. Ventzek et al 1992 have examined the excimer laser ablation of Al in different gases (argon, air, nitrogen) and pressures (10^{-5} Torr - 760 Torr) using a KrF (248 nm, FWHM = 40 ns) laser pulse at intensities up to 1.75×10^{12} Wm^{-2}. Using dye laser resonance absorption, they observed that ablating Al in vacuum produced material that remained near the surface for much longer than the laser pulse. This behavior is expected and is consistent with a 1 dimensional rarefaction wave model (Ventzek et al. 1991) in which the ablated material is required to reflect off the surface as it expands into vacuum. This model predicts that the density of the ablated material remains highest near the target and decreases as $\sim z^{-3}$ power for $z > 0$. An interesting observation made by Ventzek et al. (1992) was that expansion of the Al vapor exceeded 30 kms^{-1} for laser intensities greater than 1.75×10^{12} Wm^{-2}. This is very unusual since the kinetic energy of the vapor is ~ 130 eV which is greater than the laser photon energy by a factor ~ 26. They were unable to offer any explanation for their

observations. This, however, is not an uncommon phenomenon. Unusually high vapor speeds have been observed in the excimer laser ablation of other materials in vacuum including polyimide (Ventzek et al. 1992) and superconductors such as $YBa_2Cu_3O_7$ (Cheung et al 1991). In these cases, species tend to ablate with a range of velocity indicating some sort of preference for the ablation of one species over another. This is an indication that the understanding of the excimer laser ablation process is too simplistic.

With backing gases, Ventzek et al. (1992) observed the laser plume to closely follow the shock wave at lower pressures, but at higher pressures, substantial separation between the plume and shock wave occurred, as shown in figure 2.8 for air and argon. Below approximately 20 Torr of air, the plume closely follows the shock wave. As the pressure was increased to 100 Torr separation began to occur as the plume receded behind the shock. Above 100 Torr, Ventzek et al. (1992) determined that the plume remained close to the target. With argon, the plume and shock wave traveled less distance since argon is a heavier gas. This is consistent with equation 2.19 since shock radius is inversely proportional to gas density. As a result the plume speed is decreased and is therefore dependent on the backing gas pressure and composition. The separation between plume and shock wave in figure 2.8b occurs above 10 Torr. An interesting observation made by Ventzek et al. (1992) is the sharp change between regions A, B, and C in the figure that they have labeled "the kink". They have suggested that condensation (particulate formation) within the plume as it cools slows the expansion by conservation of momentum. If the background gas is heavier, then the saturation pressure in the plume can be reached at lower pressures which explains the observations in figure 2.8b.

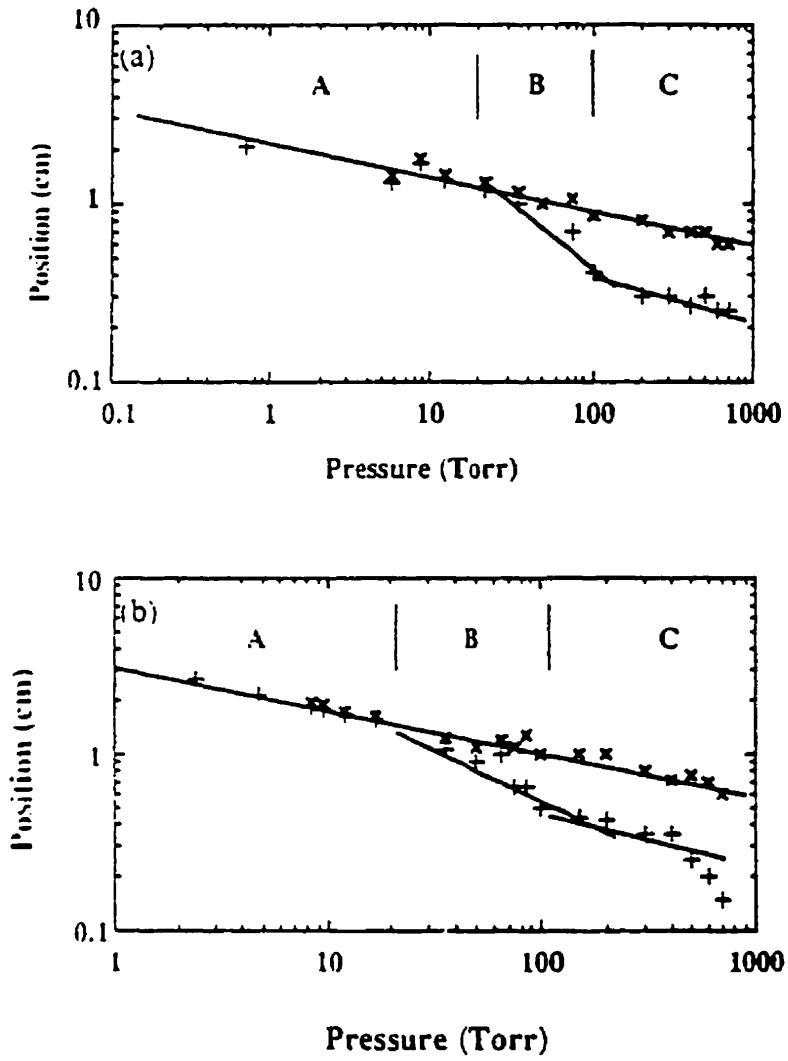

Figure 2.8. Shock wave (x) and plume (+) positions as a function of backing gas pressure for (a) air, (b) argon 2.3 μs after the start of the laser pulse. The laser intensity was 1.75×10^{12} Wm^{-2} (Ventzek et al. 1992).

The effects of gas composition and pressure are significant not only to plume speed but also to the pressure, density and, therefore, the plume temperature. A high backing gas pressure or large gas density would slow down the expansion of the plume but surface heating would remain unchanged so that the vapor pressure and density in the plume would increase.

2.6 Laser - Plume Interactions

For excimer lasers with intensities higher than 10^{12} Wm^{-2}, the laser beam is attenuated in the vapor/plasma (Schittenhelm et al. 1996) and can interact with the plume in three ways. Absorption of the laser pulse can occur by line absorption, inverse bremsstrahlung (IB), or through scattering and absorption by particulate matter such as nanoparticles.

In the case of line absorption, if the photon energy is greater than the ionization energy of the vapor, then rapid ionization can occur as the photons are absorbed. The excess energy will appear in the electrons. When the photon energy is less than the ionization energy of the vapor as is the case with metals (e.g. Al ionization potential 6 eV, XeCl laser 4 eV), a resonant ground state transition must exist near the laser wavelength. If this occurs, then rapid excitation of the vapor to an intermediate state lowers the ionization potential of the vapor so that absorption of another photon can result in ionization and plasma formation. This depends on the laser wavelength and type of material being ablated. Ablating Al with an excimer laser at 248 nm, for instance, produces no line absorption since no resonant ground state transitions in Al exist at 248 nm. At 308 nm, however, a resonance absorption band in Al at 308.22 nm due to a 3p-3d transition (Reader et al. 1980) can overlap with the laser line resulting in absorption of the laser pulse energy and the excitation of Al atoms. Absorption of a second

photon can then ionize the Al since ionization from the excited state only requries 2 eV and the photon energy is 4 eV. This can be of major significance for the UV laser ablation of metals since a resonant ground state transition in the metal can result in a highly ionized plasma. If the overlap is insufficient, however, then absorption will not occur as shown in Appendix A.

The formation of a plasma when no resonant ground state transitions exist in the vapor initially depends on there being a sufficient electron density to initiate an avalanche ionization or vapor breakdown. Such electrons originate from photoelectric emission on the metallic surface. With excimer laser radiation, the photon energy is comparable to the work function of the metal target. The electron current density emitted from a laser illuminated surface can then be very high. For example, a 308 nm excimer laser of pulse length 30 ns focussed on an Al target with an intensity of 1×10^{13} Wm^{-2} can produce ~ 5×10^{19} electrons per square meter (Duley 1996). Another process is thermal ionization of ablated atoms. Assuming thermodynamic equilibrium, the Saha equation,

$$\frac{N_e N_i}{N_a} = \frac{2Q_i}{Q_a}\left(\frac{2\pi m_e k_b T}{h^2}\right)^{3/2} \exp\left(-\frac{\chi_i}{k_b T}\right) \tag{2.21}$$

gives the electron and ion density dependence on the atomic species, density, and the temperature of the plume. At an Al vapor temperature of 10^4 K, the electron density is about $0.001N_a$. Typical vapor densities are in the range of 5×10^{26} m^{-3} calculated using the ablation rate equations so that the electron density is ~ 10^{24} m^{-3}. This number is quite small compared to the vapor density indicating that plasma formation for excimer laser ablation of metals

cannot occur from thermal vaporization alone and it is necessary that the laser beam interact with the vapor. This leads to photoionization. For Al, the Al atom ionization energy is 6 eV which is larger than the laser photon energy (KrF Laser ~ 5 eV, XeCl Laser ~ 4 eV) so that photoionization must proceed from excited states (if no resonant ground state transitions exist, Appendix A). The first excited state in Al is the $3s^2 4s\ ^2S$ state, 3.1 eV above the ground state. Ionization from this state then only requires 2.9 eV. The amount of ionization produced depends directly on the number of excited atoms. In addition to single photon ionization, multiphoton ionization can also occur at high laser intensity which allows ionization to occur directly from the ground state. However, this process is relatively weak compared to single-photon ionization at the laser intensities reached (Tozer 1965, Poprawe et al. 1985).

The initial free electrons produced by the above mechanisms can absorb laser radiation as they oscillate in the Coulomb field of an ion in a process known as inverse bremsstrahlung (IB) absorption and is very important in the production of a plasma. The inverse of this process is one in which an electron loses energy as it is decelerated in the Coulomb field of the ion. Inverse bremsstrahlung can also occur in electron-atom scattering, however, absorption of laser radiation by this process is relatively weak. Mulser et al. (1973) gives the inverse bremsstrahlung absorption coefficient as,

$$\alpha_{IB} = \frac{2\omega}{c_o}\left[\frac{1}{2}\left(\sqrt{\left\{1-\left(\frac{\omega_p}{\omega}\right)^2\frac{1}{1+(\nu_c/\omega)^2}\right\}^2+\left\{\frac{\nu_c}{\omega}\left(\frac{\omega_p}{\omega}\right)^2\frac{1}{1+(\nu_c/\omega)^2}\right\}^2}-\left\{1-\left(\frac{\omega_p}{\omega}\right)^2\frac{1}{1+(\nu_c/\omega)^2}\right\}\right)\right]^{1/2} \tag{2.22}$$

where ω_p is the plasma frequency, ω is the laser frequency, and ν_c is the electron ion/atom collision frequency. The electrons that absorb the laser energy are heated and can then ionize atoms by collisional ionization. This proceeds by two mechanisms: ionization of the ground state and ionization of the excited state. For ground state Al, an electron with 6 eV is required (Rosen et al. 1982, Zel'dovich and Raizer 1966 p383),

$$Al + e + 6.0\ eV \leftrightarrow Al^{+} + 2e$$

The reverse of this reaction is dielectronic recombination in which one electron acts as a third body absorbing the emitted photon. For Al in the ground state, two steps are required. The first is electron impact excitation (Rosen et al. 1982, Zel'dovich and Raizer 1966 p383),

$$Al + e + 3.1\ eV \leftrightarrow Al^{*} + e$$

where Al^{*} is the $3s^2 4s\ ^2S$ state of the Al. Ionization of this excited state then requires less energy (Rosen et al. 1982, Zel'dovich and Raizer 1966 p383),

$$Al^{*} + e + 2.9\ eV \leftrightarrow Al^{+} + 2e$$

Since the electrons will always have less than the photon energy (KrF Laser ~ 5 eV, XeCl Laser ~ 4 eV) ionization would most likely proceed by the latter mechanism since only half the energy is required. Another process which may contribute to these reactions is a heavy-body

collision between two Al atoms. Some important reactions are (Rosen et al 1982, Zel'dovich and Raizer 1966 p383),

$$Al + Al + 3.1\ eV \leftrightarrow Al^{*} + Al$$

$$Al + Al + 6.0\ eV \leftrightarrow Al^{+} + Al + e$$

$$Al + Al^{*} + 2.9\ eV \leftrightarrow Al^{+} + Al + e$$

$$Al^{+} + Al + 3.1\ eV \leftrightarrow Al^{*} + Al^{+}$$

$$Al^{+} + Al + 6.0\ eV \leftrightarrow Al^{+} + Al^{+} + e$$

$$Al^{+} + Al^{*} + 2.9\ eV \leftrightarrow Al^{+} + Al^{+} + e$$

Electrons created by the above reactions can also be heated by inverse bremsstrahlung absorption and can then participate in further collisions. The result is a cascade in which the increasing electron density increases the ionization rate until all the vapor is ionized in an avalanche process.

The transition from a thermal vapor to a plasma, however, is not easily accomplished due to processes such as dielectronic and three-body recombination. These decrease the free electron density and the ionization rate which can actually drive the plasma back into a vapor. To understand this, consider the time constant for dielectronic recombination as originally derived by Zel'dovich and Raizer (1966 p 390),

$$\tau_{DR}^{-1} = 2.199 \times 10^{-36} N_e N_+ T_e^{-1} (s^{-1}) \qquad (2.23)$$

For an electron density of 3×10^{24} m^{-3} and an electron temperature of 8000 K which is typical of photoionization for an Al vapor at a density of 5×10^{26} m^{-3}, the recombination time is 0.4 ns resulting in rapid electron loss. On the other hand if $T_e = 2\times10^4$ K then τ_{DR} = 10 ns and ionization can be rapid. This implies that inverse bremsstrahlung absorption must large so that sufficient electron heating is generated from the initial free electrons to produce a plasma. At long wavelengths such as that of the CO_2 laser (Pirrr et al. 1977, Weyl et al. 1980, Phipps et al. 1988, Aden et al 1993) this is not a problem as inverse bremsstrahlung is very strong and plasmas easily form. However, at UV laser wavelengths inverse bremsstrahlung is quite weak since equation 2.22 is proportional to the cube of the wavelength. This requires that the initial electron density be quite large to induce plasma formation. To see this, one can compare how much energy is absorbed by photoionization and inverse bremsstrahlung by calculating the absorbed power per cubic meter for each. For photoionization from an excited state the absorbed power density is $P_{SP} = N^* \sigma I$ (Rosen et al. 1982) where N^* is the density of atoms in the excited state, σ is the photoionization cross-sectior and I is the laser intensity. For inverse bremsstrahlung, the absorbed power density is $P_{IB} = \alpha_{IB} I$. A plot P_{IB}, and P_{SP} versus the electron density is shown in figure 2.9 for a laser intensity of 10^{12} Wm^{-2} with a laser wavelength of 308 nm, and an aluminum vapor density of 10^{26} m^{-3} at a temperature of 8000 K. Photoionization is independent of the electron density. For inverse bremsstrahlung absorption, the absorbed power density and, therefore, electron heating is quite small compared to photoionization and so this only becomes significant when the absorbed power density exceeds that due to single-photon ionization at an electron density ~ 10^{25} m^{-3}. At the initial free electron densities produced by single-photon ionization, the amount of heat

deposited in the electrons by inverse bremsstrahlung is insignificant. Plasma formation could therefore not occur. For a plasma to form at UV laser wavelengths then the initial electron density in the plume must be much >> 10^{23} m^{-3}. This is the mechanism of plasma formation when no resonant ground state transitions exist such as is the case with 248 nm excimer lasers interacting with an Al vapor. A special case for the 308 nm excimer laser is also possible (Appendix A).

The λ^3 dependence of α_{IB} has led some researchers (Callies et al. 1994, Schittenhelm et al. 1996) to suggest that inverse bremsstrahlung may not be the dominant absorption mechanism in a UV laser-induced plume at laser wavelength of 248 nm. Schittenhelm et al. (1996) performed an experiment to measure the fraction of laser energy transmitted through its own plasma. This was done by machining exceptionally small holes in Cu and Al targets and then measuring the amount of laser energy that passed through the plasma and pin hole to a detector at the back of the target. Their results for the ablation of Cu in air using 248 nm at various intensities is shown in figure 2.10. The results were similar for Al. At a maximum intensity of ~ 5×10^{12} Wm^{-2}, the transmission decreases to ~ 10% after 15 ns into the laser pulse. They modeled the results for the laser ablation of Cu and Al and found that inverse bremsstrahlung absorption only produced 0.5 % attenuation of the laser beam. This was due to the small electron density, ~ 10^{24} m^{-3}, in the plume. Complete attenuation of the laser beam by inverse bremsstrahlung would require an electron density greater than 10^{26} m^{-3} (Pinho et al. 1997).

Since inverse bremsstrahlung absorption appeared to be weak for their experiments, Callies et al. (1994) and Schittenhelm et al. (1996) both concluded that the attenuation of the laser

pulse in figure 2.10 must be due to some other mechanism. A possible process proposed by Schittenhelm et al. (1996) is scattering by small nanoparticles condensed in the plasma. They were able to model the results of figure 2.10 using Rayleigh scattering with a scattering coefficient (Bohren and Huffman 1984),

$$\alpha_{sca} = \frac{128\pi^5 a^6 N}{3\lambda^4}\left|\frac{m^2-1}{m+2}\right|^2 \tag{2.24}$$

where m is the complex index of refraction of the medium, a is the nanoparticle radius, and N the number density of nanoparticles. This is very effective at excimer laser wavelengths because of the λ^{-4} dependence. Nanoparticles were assumed to grow in the plasma by effusion where the nanoparticle radius is (Schittenhelm et al. 1996),

$$r_{cl} = \left(\frac{m_a}{2\pi k_b T}\right)^{1/2} \frac{P}{\rho_{cl}} t \tag{2.25}$$

P is the vapor pressure and ρ_{cl} is the density of the nanoparticles. This requires knowledge of the vapor temperature and pressure as a function of time. Schittenhelm et al. (1996) obtained these from a gasdynamic code which was capable of simulating laser ablation and results for a Cu nanoparticle density of ~ 1.5×10^{20} m^{-3} are shown in figure 2.11. The fit of the data is good although the attenuation tends to zero as nanoparticle size increases. This was not evident in the data for which there was some transmission. Schittenhelm et al. (1996) did neglect any nanoparticle dissociation so that nanoparticles could only grow in time. They found that to

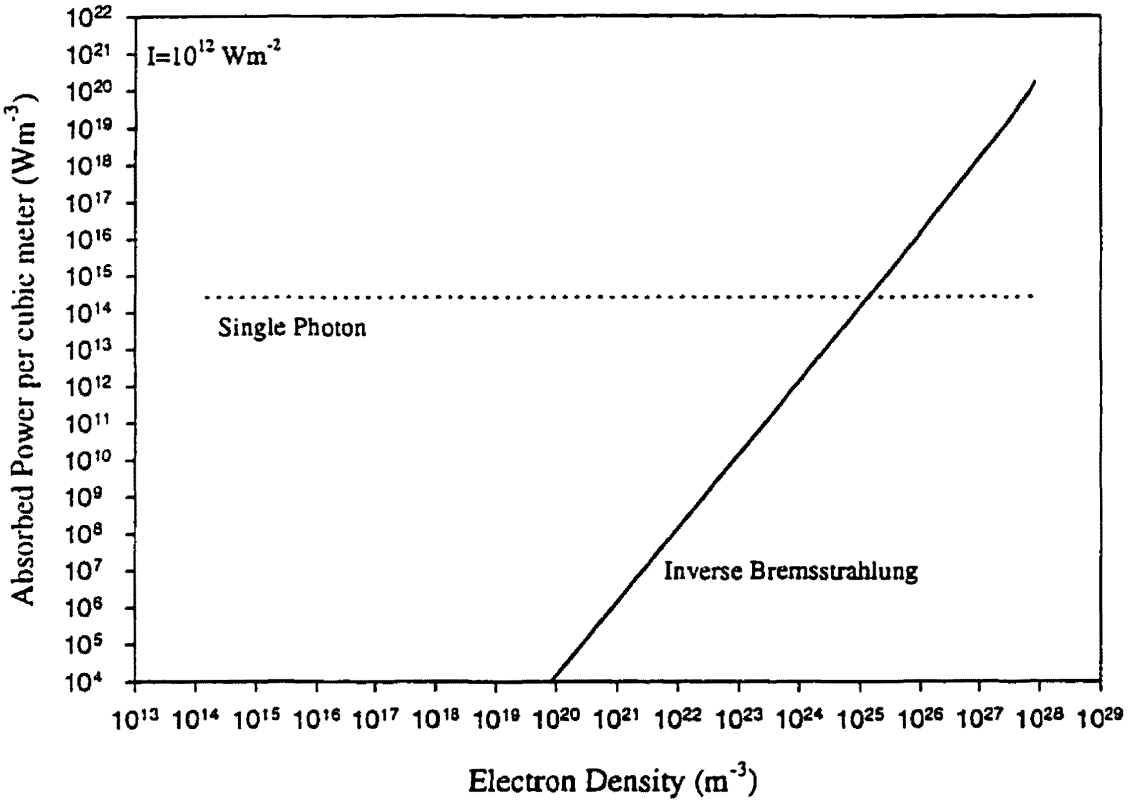

Figure 2.9. Plot of absorbed power per cubic meter for single-photon ionization and inverse bremsstrahlung at a laser wavelength of 308 nm and an Al vapor density and temperature of 10^{26} m^{-3} and 8000 K respectively. Below 10^{25} m^{-3}, single-photon ionization is the dominant absorption mechanism while above 10^{25} m^{-3}, absorption is dominated by inverse bremsstrahlung.

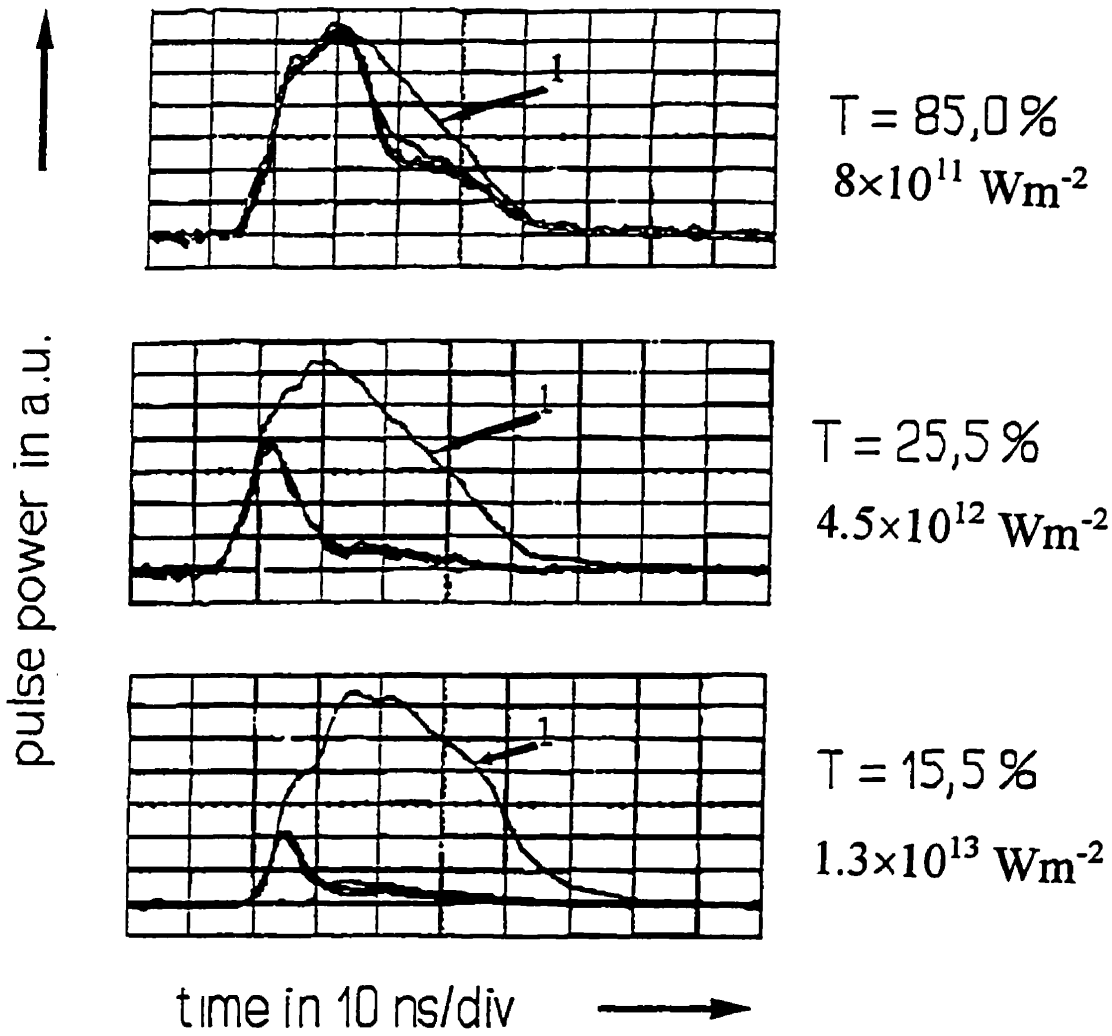

Figure 2.10. Laser pulse transmission through the plasma for 248 nm radiation incident on a Cu target (Schittenhelm et al. 1996). The curve labeled "1" is the laser intensity for the unattenuated beam, while the curve below that is the transmitted laser intensity.

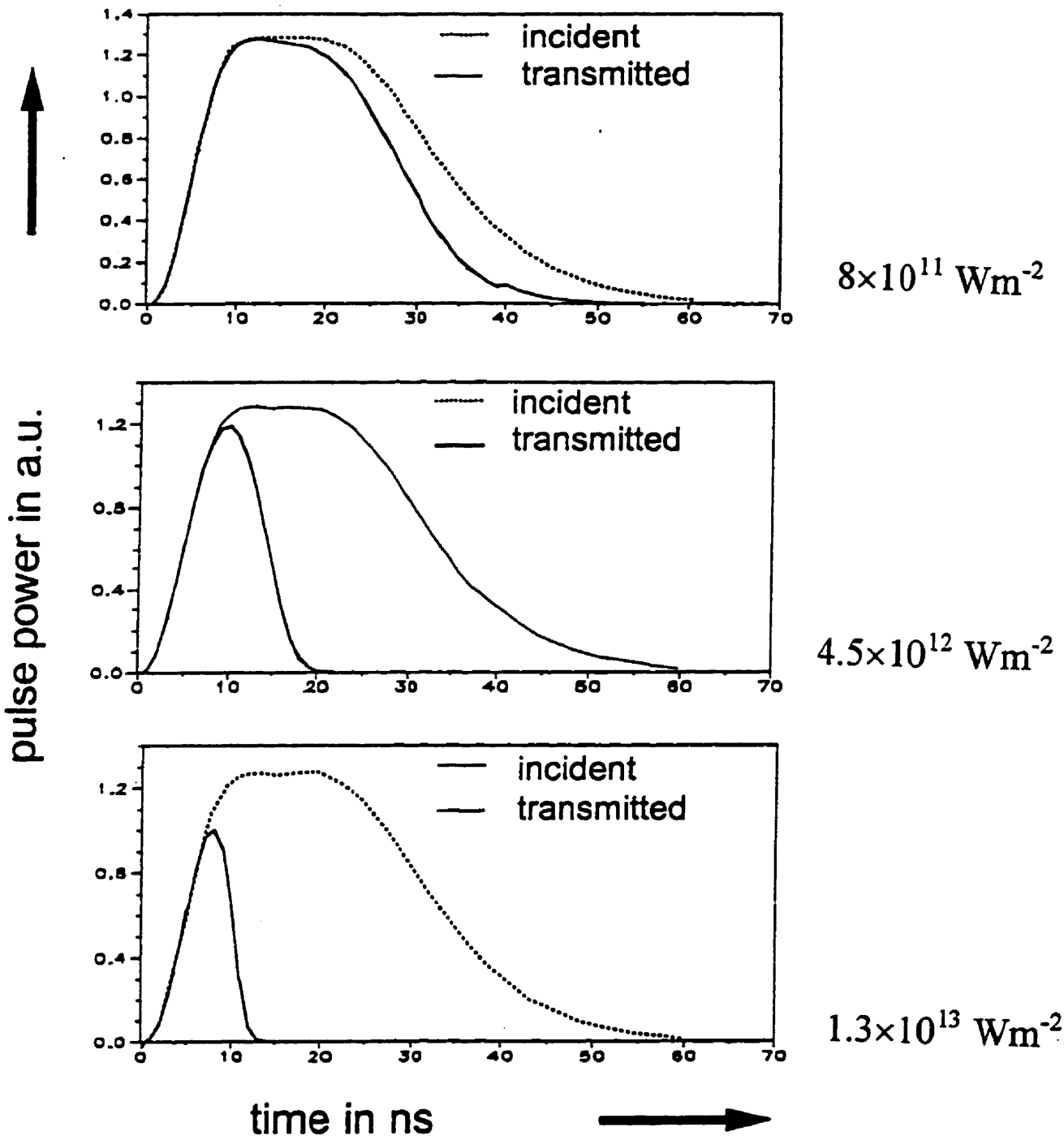

Figure 2.11. Nanoparticle scattering model of Schittenhelm et al. (1996) showing how nanoparticles of sizes 40 nm and densities of ~ 10^{20} m^{-3} in the plume could attenuate the laser beam.

attenuate the laser beam to 0% transmission required nanoparticles with a size of ~ 40 nm. Callies et al. (1997, 1998) later developed the nanoparticle theory further using the condensation theory of Lifshitz and Sloyozov (1961). This theory has the advantage of being more accurate than the simple effusion theory since it does not rely on an initial nanoparticle radius. Instead nanoparticles are formed by fluctuations in a supersatured medium. These nanoparticles can then grow by nucleation from the surrounding vapor. In this theory, the number of particles formed per cubic meter per second is given by,

$$s = \sqrt{\frac{2\sigma\pi}{m_a}} N\rho \exp\left[-\frac{16\pi\sigma^3}{3(k_b T)^3 \Delta_s^2}\right] \tag{2.26}$$

and is strongly dependent on the surface tension σ of the nanoparticle, the vapor temperature T, and the amount of supersaturation Δ_s. The problem with this theory is that the surface tension must be temperature dependent and a 20% change in σ represents a change in s from 10^{10} $m^{-3}s^{-1}$ to 10^{-10} $m^{-3}s^{-1}$ (Callies et al 1997). This makes the condensation theory difficult to work with since the surface tension of metals are not very well known at high temperatures. Callies et al. (1998) was able to model the results of Schittenhelm et al. (1996) with a judicious choice of σ, however, this theory also predicts that nanoparticles may not form at all in laser induced metal vapor/plasmas.

Although one cannot definitely determine whether nanoparticles form in laser induced plasmas, there is a substantial amount of indirect evidence to indicate otherwise. Sappey and Gamble (1991,1992), and Miyamoto et al. (1994, p240, 249) have shown experimentally that

nanoparticles are present in the plasma plume in the excimer laser ablation of Cu and ceramics. The times for this to occur are ~ 1 μs after initiation of the laser pulse indicating that nanoparticles are formed as a result of cooling of the vaporized material which differs from the model proposed by Schittenhelm et al.(1996) in which nanoparticles would have to form during the laser pulse when the plasma is quite hot (~ 8000 K). Direct evidence for nanoparticle formation during the laser pulse is sparse. Dreyfus (1991) has shown using laser induced fluorescence that Cu_2 is present during the plasma formation in the excimer laser ablation of Cu. This would be the starting point for further nanoparticle growth via the process $Cu_2 \rightarrow Cu_3 \rightarrow Cu_4$. To date no other direct evidence has been presented for nanoparticle formation in the plume leaving inverse bremsstrahlung absorption as the most likely attenuation mechanism.

Chapter 3

Computer Simulation of Laser Ablation

3.1 Solution to the Euler Equations

As a laser beam heats up a substrate such as aluminum, vaporization ensues as the temperature of the material approaches the boiling point. The vaporized material expands away form the surface as discussed in the previous chapter. The expansion of the vapor into a surrounding gas can be described by the Euler flow equations describing the flow of an inviscid compressible fluid (Zel'Dovich and Raizer 1966 pg 48),

$$\begin{aligned} &\frac{\partial \rho}{\partial t} + \frac{\partial(\rho u)}{\partial z} = 0 \\ &\frac{\partial(\rho u)}{\partial t} + \frac{\partial}{\partial z}(P + \rho u^2) = 0 \\ &\frac{\partial}{\partial t}(\rho E) + \frac{\partial}{\partial z}(\rho u E + uP) = Q \end{aligned} \tag{3.1}$$

Here, ρ is the density of the vapor, u is the vapor speed, P is the vapor pressure, E is the sum of the internal energy and kinetic energy of the vapor in J/Kg, and Q is the amount of laser power per unit mass deposited in the expanding vapor in W/kg. The first equation describes the conservation of mass, the second is the conservation of momentum and the third, conservation of energy. The Euler equations can be used to compute the flow of any vapor into another provided its thermodynamic properties are known. These equations also include the formation of shock waves although no dissipation mechanism is present so that at a shock wave interface a discontinuity arises. This can be seen by integrating the flow equations for a layer of infinitesimal thickness. The temporal parts will vanish along a discontinuity since no mass momentum or energy accumulates there. The spatial parts give the difference between the mass, momentum, and energy on either side of the discontinuity. The result is,

$$\begin{aligned} &\rho_1 u_1 = \rho_o u_o, mass \\ &P_1 + \rho_1 u_1^2 = P_o + \rho_o u_o^2, momentum \\ &e_1 + \frac{P_1}{\rho_1} + \frac{u_1^2}{2} = e_o + \frac{P_o}{\rho_o} + \frac{u_o^2}{2}, energy \end{aligned} \tag{3.2}$$

where e is the internal energy. Other discontinuities are present in the density as well where the expanding vapor meets the backing gas. Figure 3.1 shows the behavior of the pressure, density, velocity, and internal energy of the vapor as predicted by equations 3.1 for a shock tube problem in which a high pressure gas is allowed to expand into a lower pressure gas. The pressure and gas speed show two waves of propagation, a backward facing rarefaction wave

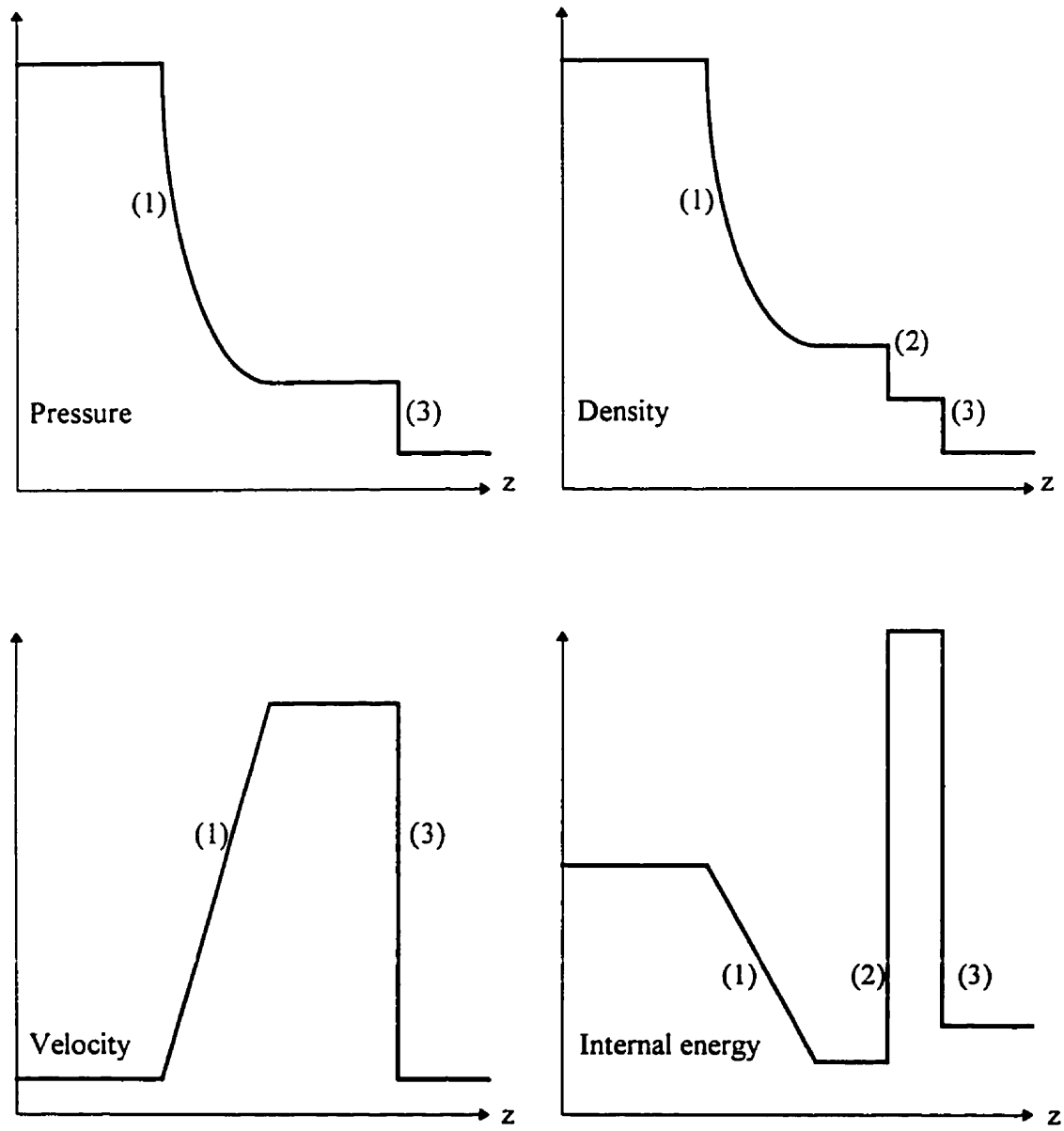

Figure 3.1 Schematic of the shock tube problem showing the backward facing rarefaction wave(1), the contact discontinuity(2), and the shock wave(3) for pressure, density, velocity, and internal energy as a function of displacement z. Both the velocity and pressure are continuous across the contact discontinuity

(1), and the shock wave discontinuity (3). In the density and internal energy, a third discontinuity, the contact front (2) is observed. The cooling effect observed behind the contact front is due to the increase in the density as the vapor "bunches" up at the contact discontinuity. The pressure remains constant to sustain the shock wave otherwise another flow region would occur at the contact discontinuity. This is known as isentropic cooling.

The three different waves 1,2 and 3 all propagate at different speeds. From equations 3.2 the particle speed on either side of the shock front with respect to the local sound speed is (Zel'Dovich and Raizer, 1966, p 53),

$$u_o = c_o\sqrt{\frac{(\gamma - 1) + (\gamma + 1)P_1 / P_o}{2\gamma}} \tag{3.3}$$

in the undisturbed gas (γ is the gas constant) which equals the speed of the shock and,

$$u_1 = c_1\sqrt{\frac{(\gamma - 1) + (\gamma + 1)P_o / P_1}{2\gamma}} \tag{3.4}$$

behind the shock in the compressed gas. If $P_1 > P_o$ then the shock front propagates at supersonic speed into the undisturbed gas but the compressed gas leaves the shock at subsonic speed with respect to the compressed gas. The other discontinuities therefore propagate at slower speeds since they cannot overtake the shock wave. Over time the shock wave will outrun the contact front and the rarefaction wave.

The presence of discontinuities makes solving this system of equations 3.1 for a flowing vapor non-trivial. No analytical solutions exist thus requiring numerical techniques. Many different methods of solving equations 3.1 exist. Sod (1978) gives a review of some finite difference methods and their comparative stabilities. A simple and accurate method is the direct Eulerian MUSCL (monotonic upstream scheme for conservation law code) scheme developed by Colella (1985). The space in front of the target is divided into zones as shown in figure 3.2.

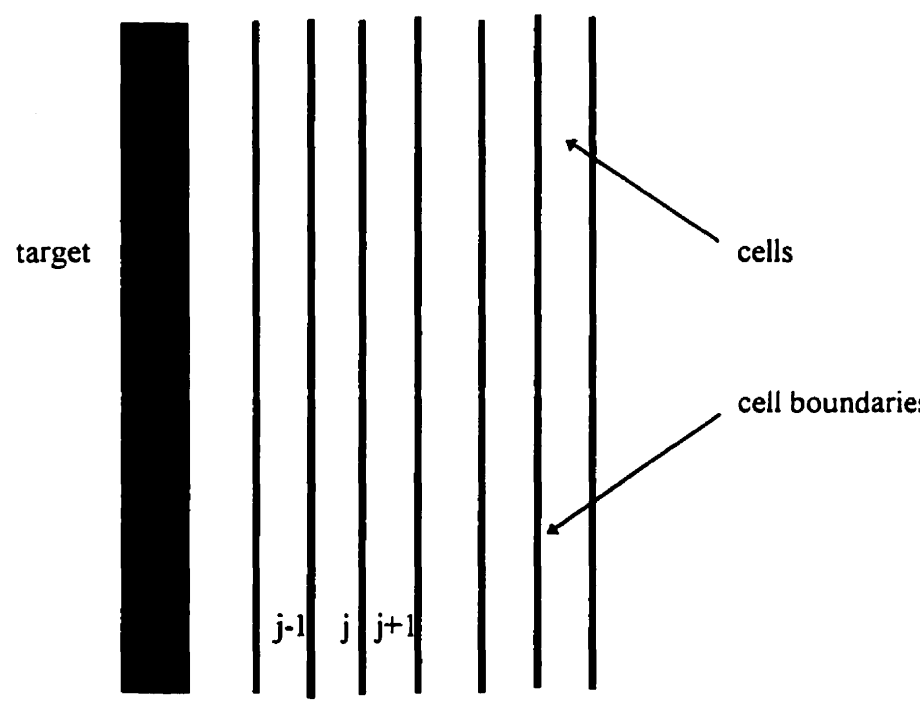

Figure 3.2. Cell boundaries used in the numerical solution of the Euler equations.

Each cell j has a cell boundary j+1/2 and j-1/2. The positions of the cells from the target are given by Z_j and the spacing between the cells is $\Delta Z_j = Z_{j+1/2} - Z_{j-1/2}$. Z_j can also be defined in terms of the cell boundaries as $Z_j = 1/2(Z_{j+1/2} - Z_{j-1/2})$. The assumption is made that the conserved quantities,

$$U(t)_j = \begin{pmatrix} \rho \\ \rho u \\ \rho E \end{pmatrix}$$
$$F(t)_j = \begin{pmatrix} \rho u \\ \rho u^2 + P \\ \rho u E + uP \end{pmatrix} \tag{3.5}$$

in equations 3.1 are known at time t across a zone ΔZ. The solution requires computing $U(t+\Delta t)_j$ and $F(t+\Delta t)_j$ at the new time step. In the MUSCL scheme (Colella 1985) this is accomplished by calculating $F(t)_{j+1/2}$ and $F(t)_{j-1/2}$ at the cell boundaries for the old time and for the new time $t+\Delta t$. The average of these is then computed,

$$F^{avg}_{j+1/2} = \frac{F(t)_{j+1/2} + F(t+\Delta t)_{j+1/2}}{2}$$
$$F^{avg}_{j-1/2} = \frac{F(t)_{j-1/2} + F(t+\Delta t)_{j-1/2}}{2} \tag{3.6}$$

The conserved quantities (equations 3.1) at the new time step are then given by,

$$U(t+\Delta t)_j = U(t)_j - \frac{\Delta t}{\Delta Z}(F^{avg}_{j+1/2} - F^{avg}_{j-1/2}) \tag{3.7}$$

This is a fairly reliable and fast scheme. The most difficult part of this method is calculating $F(t+\Delta t)_{j\pm 1/2}$ which requires tracing approximate solutions from $F(t)_{j\pm 1/2}$.

The first step in solving equation 3.6 is to calculate linear profiles of the pressure, density, and vapor speed $w=(P, \rho, u)$ in each cell by interpolating slopes at the centers of the cells. The values within each cell are written as (Colella 1985),

$$w(z) = w_j + \delta w_j \frac{(z - z_j)}{\Delta z_j}, z_{j-1/2} < z < z_{j+1/2} \tag{3.8}$$

where δw_j is the slope. This provides a smoother transition between cells instead of the usual step and allows for handling of discontinuities by providing dissipation where needed. This is illustrated in figure 3.3. The slope in cell j depends on the values of the conserved quantities in cells $j+1$ and $j-1$ (Colella 1985) and are given by the following algorithm (van Leer, 1979),

$$\delta_{\lim} w_j = \begin{cases} \min 2(|w_{j+1} - w_j|, |w_j - w_{j-1}|), (w_{j+1} - w_j)(w_j - w_{j-1}) > 0 \\ 0, otherwise \end{cases} \tag{3.9}$$

and,

$$\delta w_j = \min\left(\frac{|w_{j+1} - w_{j-1}|}{2}, \delta_{\lim,j}\right) sign(w_{j+1} - w_{j-1}) \tag{3.10}$$

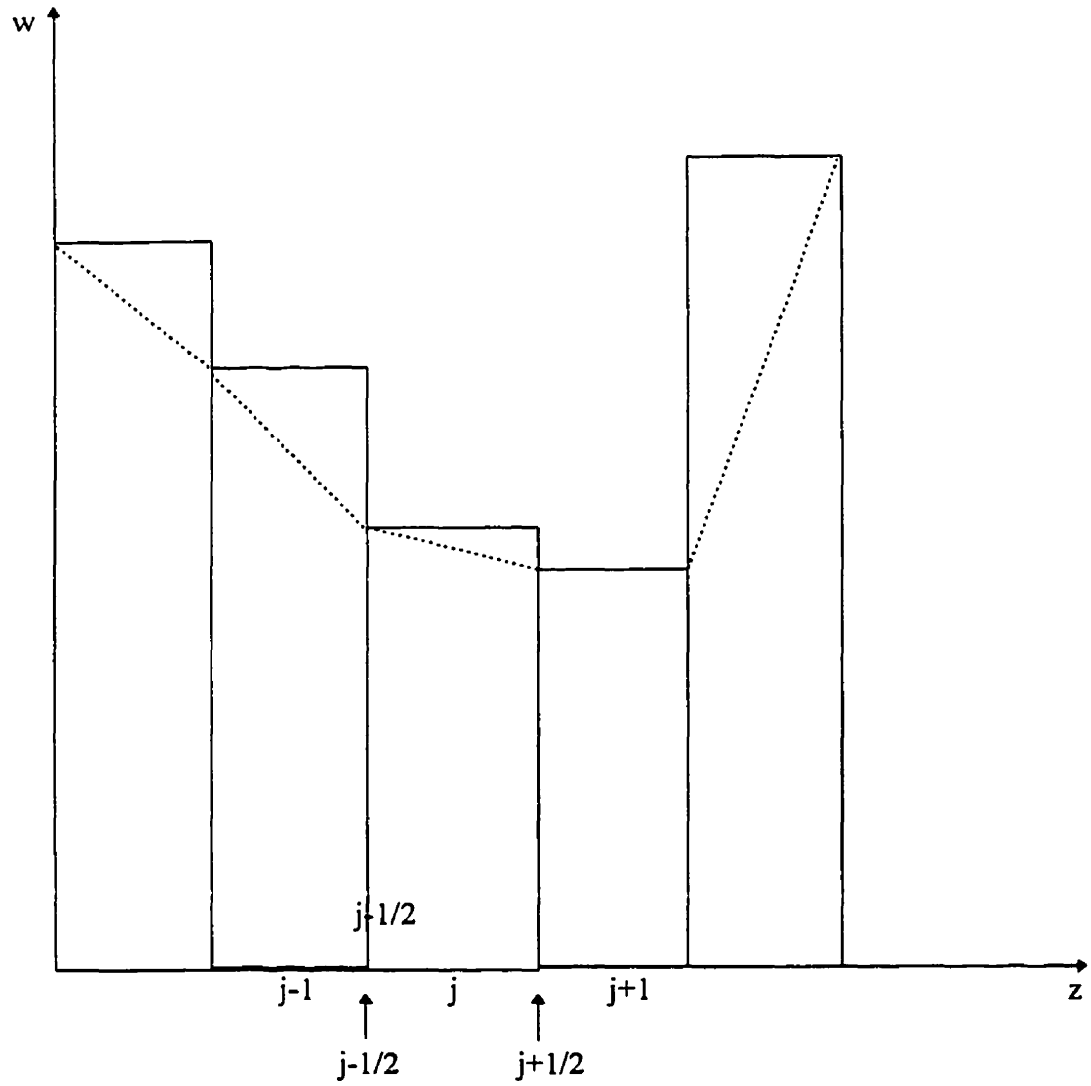

Figure 3.3. Illustration of slope construction in cells to eliminate discontinuities. Here j is the cell number and j+1/2 and j-1/2 are the cell boundaries. W refers the either pressure, density or velocity in the cells.

The slope is not allowed to exceed the average values of the slopes in the neighbouring cells as indicated in 3.10, to prevent oscillations from cell to cell. Also, conditions in which extremum exist forces the slope to zero. This is also the case if the sign of the slope is not the same as that of the neighbouring cells. The three cases are shown in figure 3.4.

The variables $w=(P, \rho, u)$ are piece-wise linear in each cell but are discontinuous at the cell boundaries as indicated in figure 3.4. For example, the cell boundary $j+1/2$ can have two different values. On the left side of the boundary the value is,

$$w_{j+1/2,L} = w_j + 1/2\delta w_j \tag{3.11}$$

where δw_j is the slope in cell j, and on the right side of the boundary the value is,

$$w_{j+1/2,R} = w_{j+1} - 1/2\delta w_{j+1} \tag{3.12}$$

which depends on the slope in cell $j+1$. This is known as a Riemann problem and is especially important in the vicinity of shock waves.

In the second step the Riemann problem must be solved at each cell boundary. The choice of which state to use is not straightforward if the vapor expands into another gas due to the formation of discontinuities. To maintain a smooth flow, the solution to the Riemann problem must therefore be able to introduce sufficient dissipation in the neighbourhood of shocks. The problem is knowing how to identify the different discontinuities where dissipation is needed. Colella (1982) has shown that each discontinuity has a characteristic speed associated with it.

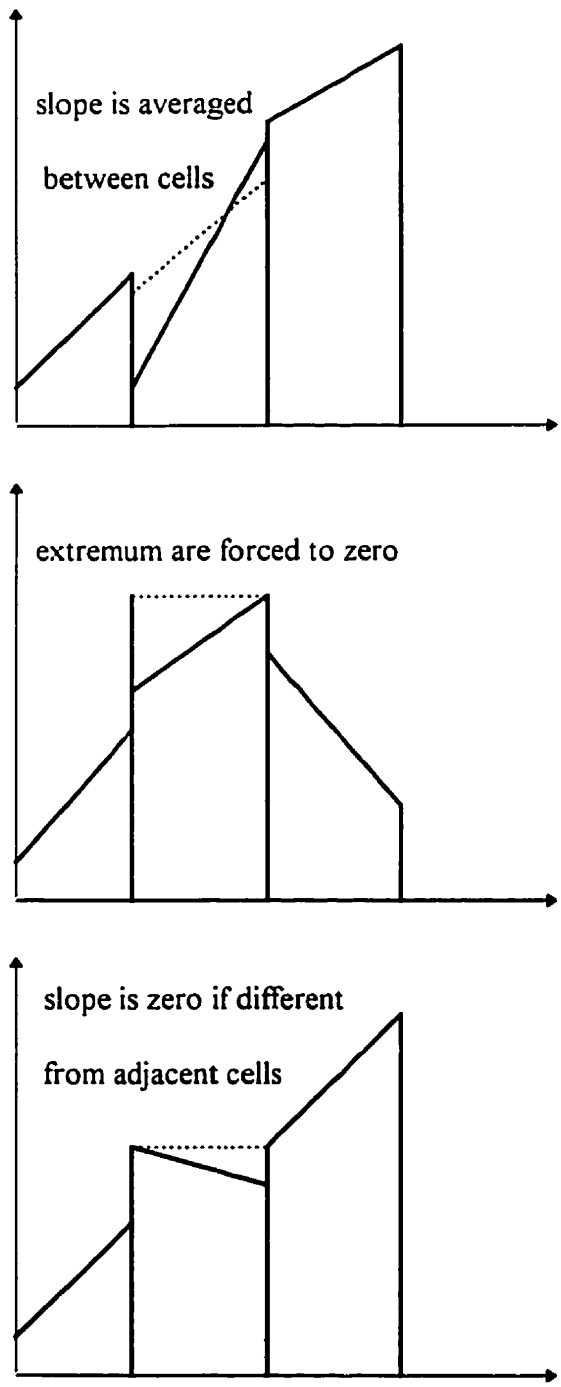

Figure 3.4. The diagram shows the three constraints imposed on the slope at cell j.

The rarefaction wave has a characteristic speed u-c, the contact discontinuity has a characteristic speed u and the shock wave has a characteristic speed $u+c$. Once the discontinuity is identified, equations 3.2 and 3.4 can be used to determine the degree of dissipation in a rather complex and long procedure. The solution will be either one of the states, or an intermediate value between the two states. This of course depends on the characteristic wave speeds. In this way, shock waves can be easily handled in equations 3.1. An iterative approach developed by van Leer (1979) and Colella (1982) is discussed in Appendix B.

Once suitable global cell boundary values are established, the next step is to calculate the cell boundary values at the new time step. To do this, the characteristic wave velocities must once again be considered. Each wave near a shock has a different speed given by (Colella 1985),

$$\frac{dr_{\pm,0}}{dt} = v_{\pm,0} \tag{3.13}$$

where the plus and minus refer to wave speeds $u+c$ and u-c, and the zero is the contact wave speed. For each of the waves, characteristic flow equations can be derived from equations 3.1 and 3.2 assuming that the discontinuous changes in the pressure are small. When this happens the Lagrangian shock speed in Appendix B can be written as ρc which is approximately equal to u_I and u_o on either side of the discontinuity. The results given by (Colella 1985, van Leer 1979) are,

$$\frac{1}{\rho c}\frac{dP}{dt_{\pm}} \pm \frac{du}{dt_{\pm}} = 0$$
$$\frac{d}{dt_0}\left(\frac{1}{\rho}\right) = -\frac{1}{(\rho c)^2}\frac{dP}{dt_0} \tag{3.14}$$

These approximate equations describe the change in the conserved quantities as a function of time. The first one neglects the contact discontinuity since both the pressure and velocity are continuous across this interface as indicated in figure 3.1. The second equation must take the contact discontinuity into consideration. The characteristic equations are usually solved using finite difference methods. However, when the discontinuity is large, further approximations must be made to provide values which are well behaved.

Having obtained the conserved quantities at all the cell boundaries for the old and new times, one can then proceed to calculate the conserved quantities (using equation 3.7) at the new time step in each cell. This procedure is repeated for as much time as is necessary.

3.2 The LASADYN Code

The numerical approach of solving the Euler equations was used to develop a 1D Laser Ablation Dynamics (LASADYN) code for studying the laser-plasma interaction. The code is divided into four parts. The first is the interaction of the laser with the metal. This induces melting and vaporization as discussed in chapter 2. Once vaporization has begun, the Knudsen layer effect must be considered. The vapor that escapes the Knudsen layer then causes gas motion and the Euler equations are solved to obtain the flow of the vapor. Finally the electron and ion density is calculated and the laser is allowed to interact with the intervening vapor via

inverse bremsstrahlung absorption. It is assumed that no line absorption occurs (appendix A). Figure 3.5 shows the model of the code with the different parts.

For the code to operate successfully correct parameters and boundary conditions must first be established. This is done in view of the numerical scheme in section 3.1. The space in front

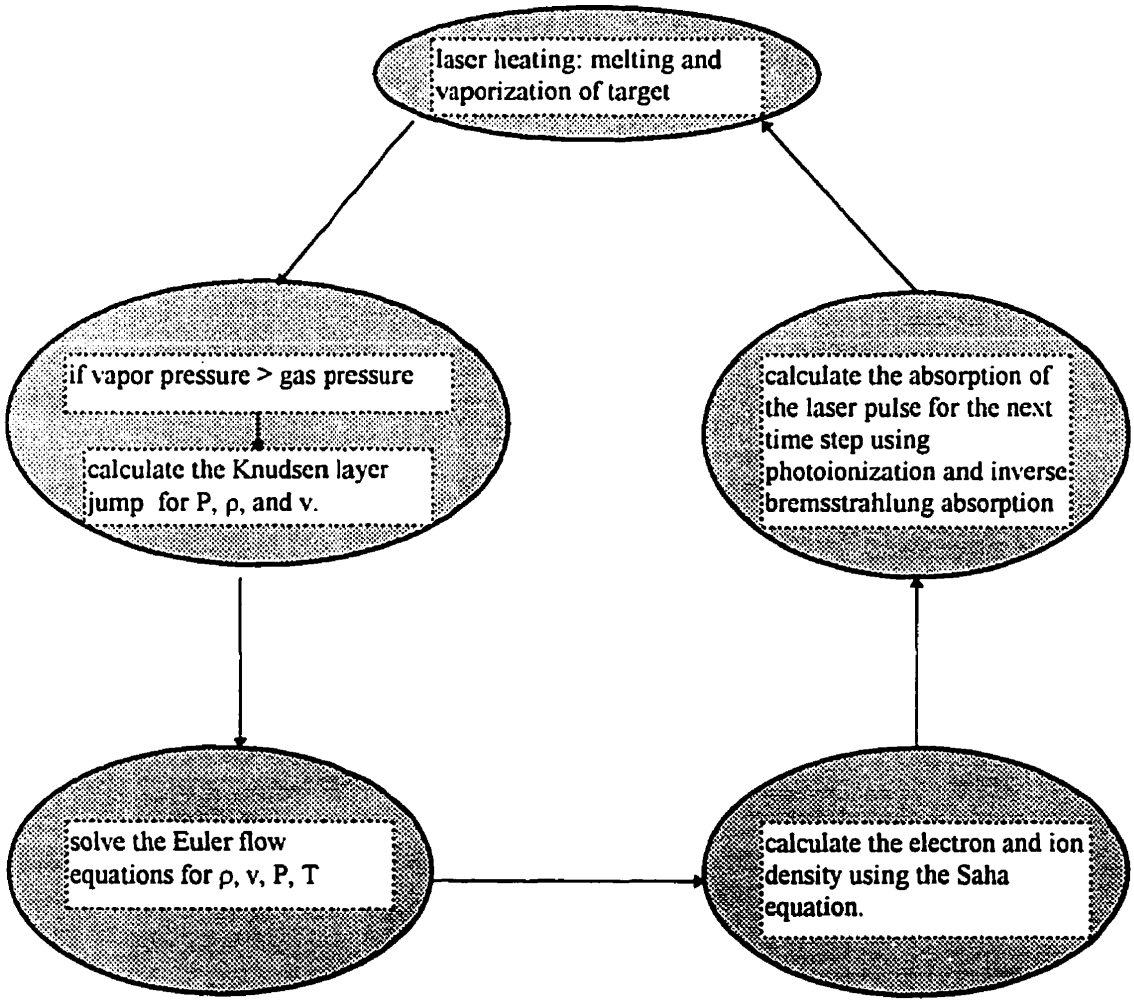

Figure 3.5. Laser ablation model for vaporization showing the four different parts of LASADYN.

of the target is divided into equally spaced zones. The number of zones depends on how much distance the vapor flow is to be computed over. The boundary of this space must be larger than the total distance of computation since the numerical scheme requires parameters for the background gas ahead of the current computational cell. At the target surface the thermodynamic state of the metal must be specified at each time step. There are two important cases here. In the first case, the temperature of the target is below the vaporization temperature. Although some material vaporizes the assumption is made that the metal vapor pressure is lower than the background gas pressure so that no vapor flow occurs. When the target temperature exceeds the vaporization temperature, vapor flow begins and the pressure, density, and velocity of the vapor emerging from the Knudsen layer are treated as the first computational cell. In the same time step the laser is allowed to interact with the plasma via inverse bremsstrahlung absorption and photoionization. The amount of heat deposited in each cell as a result of this is the heat Q in equations 3.1. In this way plasma heating can be followed. As well the amount of laser energy absorbed in each cell is considered and the appropriate attenuation of the laser beam at the target surface is calculated. The Euler equations are then solved for the entire specified space and the procedure is repeated at the next time step. The boundary conditions for the computational domain are shown in figure 3.6

The gas chosen as the background gas usually has a different specific heat and a different gas constant than the vaporized material. This is an important consideration since the pressure cannot be directly calculated in equations 3.1. The numerical scheme presented provides the density, velocity, and the total energy. The pressure must be calculated from the ideal gas

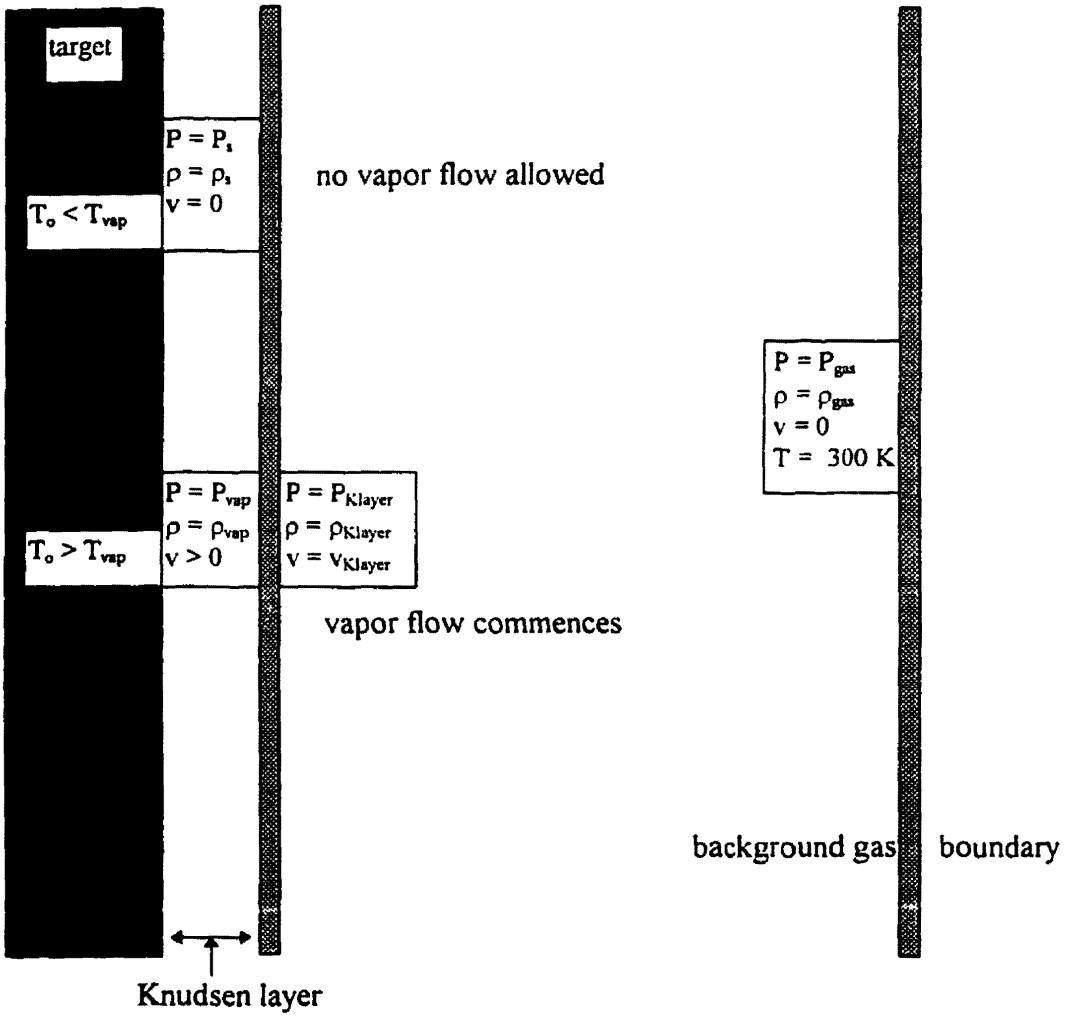

Figure 3.6. Boundary conditions used in the simulation of laser ablation. When the vapor pressure is less than the background gas pressure no vaporization occurs.

equation,

$$P(t)_j = \frac{\rho(t)_j}{m} k_b T(t)_j \tag{3.15}$$

Since the internal energy is $C_v T$ and equations 3.1 calculate the total energy, equation 3.15 can be rewritten as,

$$P(t)_j = \rho(t)_j (\gamma - 1)(E(t)_j - 1/2u(t)_j^2) \tag{3.16}$$

If the gas constant γ changes from the vapor to the background gas, then a discontinuity will occur in the pressure. This can pose problems for the stability of the Euler equations. A solution to this is to have a smooth transition from one gas constant to the other. If the vaporized material is assigned the value $F=1$ and the background gas the value $F=0$ then a continuity equation describing the flow of the vapor can be written as,

$$\frac{dF}{dt} + u\frac{dF}{dZ} = 0 \tag{3.17}$$

The derivative of u with respect to Z is taken to be zero. This implies that the fluid is incompressible. This will give only one discontinuity at the contact point between the two vapors since the fluid simply moves with one velocity. Equation 3.17 is solved along with the Euler equations making use of the MUSCL scheme. The result is that a smooth transition will

exist between 1 and 0 for the two vapors at the contact discontinuity. Using this, the gas constant and specific heat for cell j can be written as,

$$\begin{aligned} \gamma_j &= (1-F_j)\gamma_{gas} + F_j\gamma_{vapor} \\ C_{v,j} &= (1-F_j)C_{v,gas} + F_j C_{v,vapor} \end{aligned} \tag{3.18}$$

giving a smooth transition for the pressure and for the temperature. Figure 3.7 shows how equations 3.17 is applied for a shock tube problem. The smooth transition between 1 and 0 is fairly steep due to the MUSCL scheme but occurs right at the contact discontinuity as discussed. Equation 3.18 varies accordingly.

The amount of computation involved in gasdynamic codes is enormous and increases with the number of cells. The choice of cell spacing must be small enough that the shock wave produced is well resolved. For laser induced plasmas good resolution is obtained with a cell spacing of 1μm or less. If the plasma is to be followed for 1mm, 1000 cells would be required for the computation. This would not be a problem if the time step could be chosen arbitrarily. However, for stability, the time step must satisfy the following condition (Colella 1985),

$$\Delta t \leq \sigma \max\left(\frac{\Delta Z}{u_j + c_j}\right) \tag{3.19}$$

where u is the vapor speed. This correlates with equation 3.7 where the step $\Delta t/\Delta Z$ must be small enough that the change in $U(t)_j$ is small. If $u = 4000$ ms^{-1} then Δt would be 10^{-10} s. For

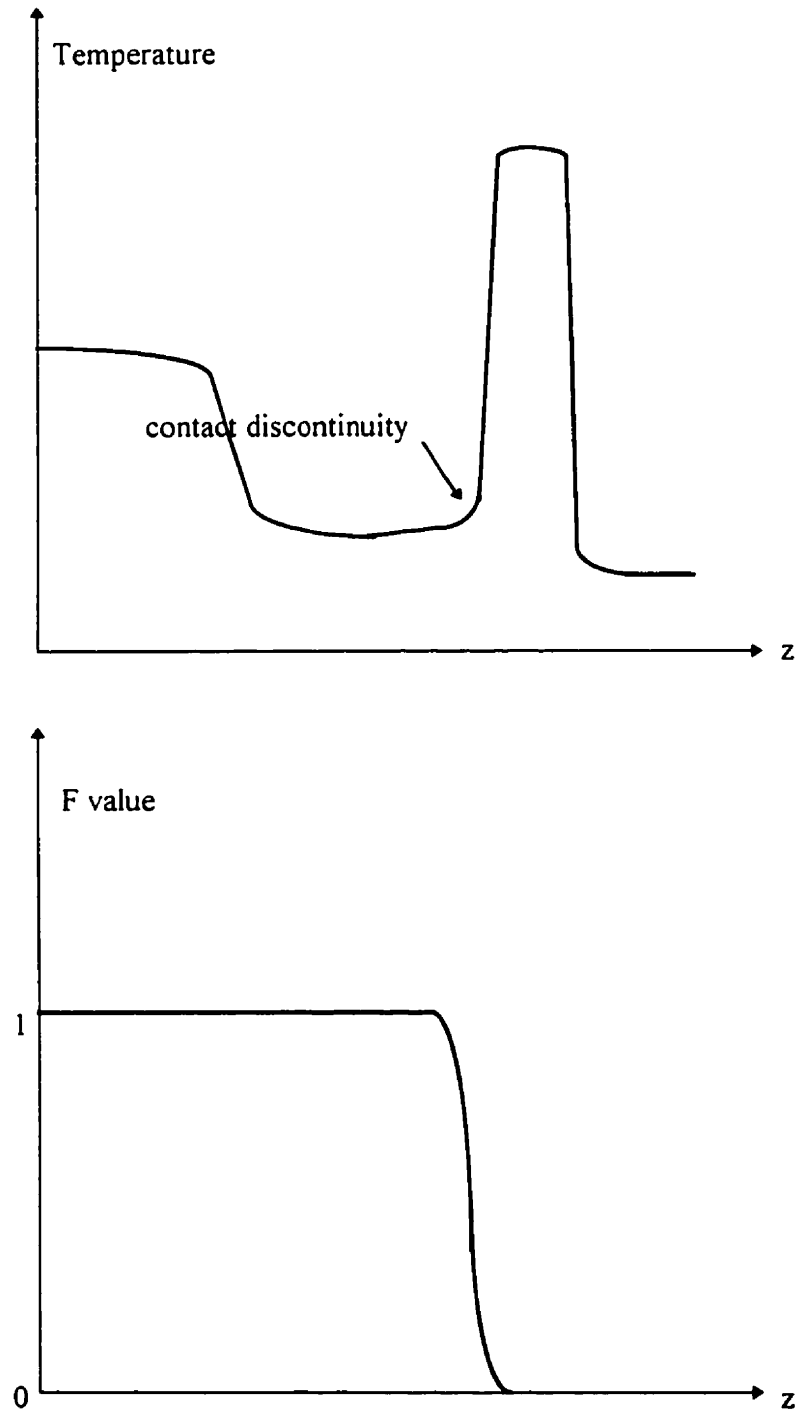

Figure 3.7. Shock tube problem showing the smooth transition for the F value at the contact discontinuity.

1mm this would require ~ 2000 time steps. Depending on the number of computations required at each cell the computer time necessary can greatly increase.

3.3 Effects of Pulse Shape and Laser Intensity on the Laser Ablation of Metals

The pulse shape and laser intensity have significant effects on the laser-induced plasma due to the rate at which heat is deposited in the target. This also depends on when the heat is deposited into the target. In figure 3.8 the simulation for the laser ablation of Al in 1 atm of N_2 with an excimer laser is shown. The laser intensity is 1×10^{13} Wm^{-2} and the wavelength is 308 nm (line absorption is neglected, Appendix A). The pulse shape is Guassian with a FWHM=30 ns and a pulse length of 60 ns. The results are for 10 ns after the start of the laser pulse. The temperature in the vaporized material starts at ~ 4500 K and drops until the shock wave in the backing gas. This is the isentropic cooling effect. The contact front in the plasma is not yet resolved in the density indicating that the shock front and the plasma are connected. This is also indicated in the slope of the density and pressure at the contact discontinuity. A slope greater than zero indicates that the plasma is pushing on the vapor as the plasma "bunches up" at the contact discontinuity. Once the shock separates from the plasma the slope should go to zero. The velocity of the plasma increases initially from 2500 m/s since the pressure is decreasing. As the plasma begins to "bunch up" at the contact discontinuity the speed decreases as the plasma is slowed and the shock wave is formed. As in the above case, once the shock wave separates from the plasma, the gas speed will assume a flat top between the rarefaction wave and the shock wave. In the undisturbed gas the speed is zero. The electron density is quite small since the plasma temperature is low.

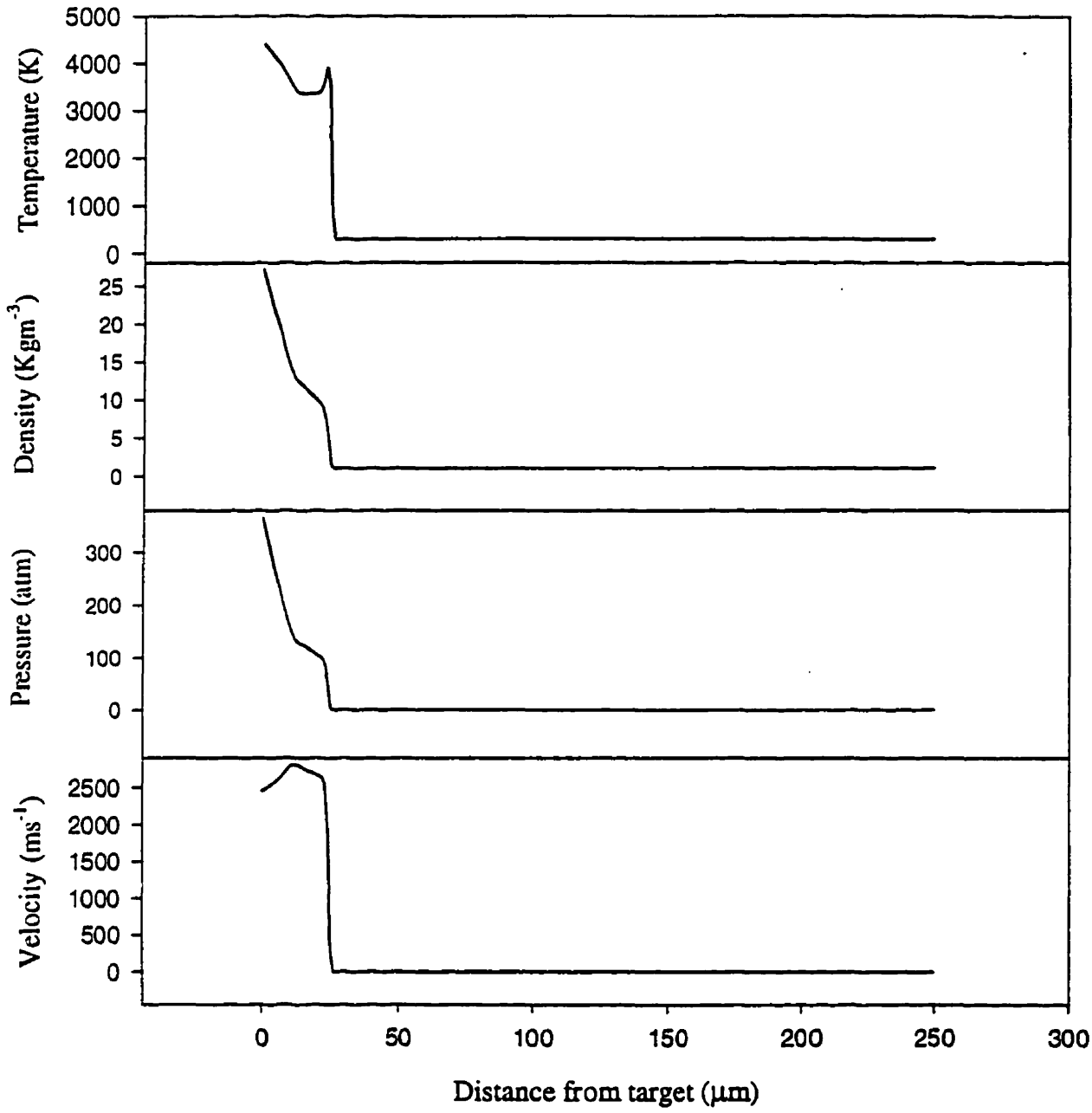

Figure 3.8. Simulation of laser ablation of Al in 1 atm of N_2 showing the temperature, density, pressure, and velocity of the plasma and background gas. The laser intensity is 1×10^{13} Wm^{-2}, the wavelength 308 nm, and the FWHM = 30 ns

As a result, laser absorption at these early times is essentially zero.

In figure 3.9 the same results are presented at 30 ns, the peak of the laser pulse. Here, the contact discontinuity is beginning to become resolved indicating that the shock wave is starting to separate from the plasma. The slope on the pressure and density curve near the contact discontinuity are still greater than zero implying that the shock wave is still being accelerated.

The contact discontinuity occurs in what appears to be the shock. This is due to the "bunch up" of the plasma at the contact discontinuity which increases its temperature since the pressure must be continuous. This is typical of ablation into background gases. The temperature of the plasma directly behind the shock wave is always highest due to the energy required to push the gas. This correlates with the results of Callies et al. (1995) where an ionization front is located directly behind the shock wave. No step in the temperature is observed due to the smooth transition in the specific heat.

At later times as shown in figure 3.10 for 50 ns after the laser pulse, the contact discontinuity is well resolved. The pressure and density are beginning to drop at the surface due to cooling since less laser energy is available and the plasma and shock wave are approaching a steady state propagation indicated by the flat top on the velocity curve.

The laser absorption in the plasma remains quite small due to the low electron density and small absorption coefficient as shown in figure 3.11 at 30 ns. The highest absorption occurs at the target surface since the temperature and density are highest there but the rest of the plasma absorbs very little.

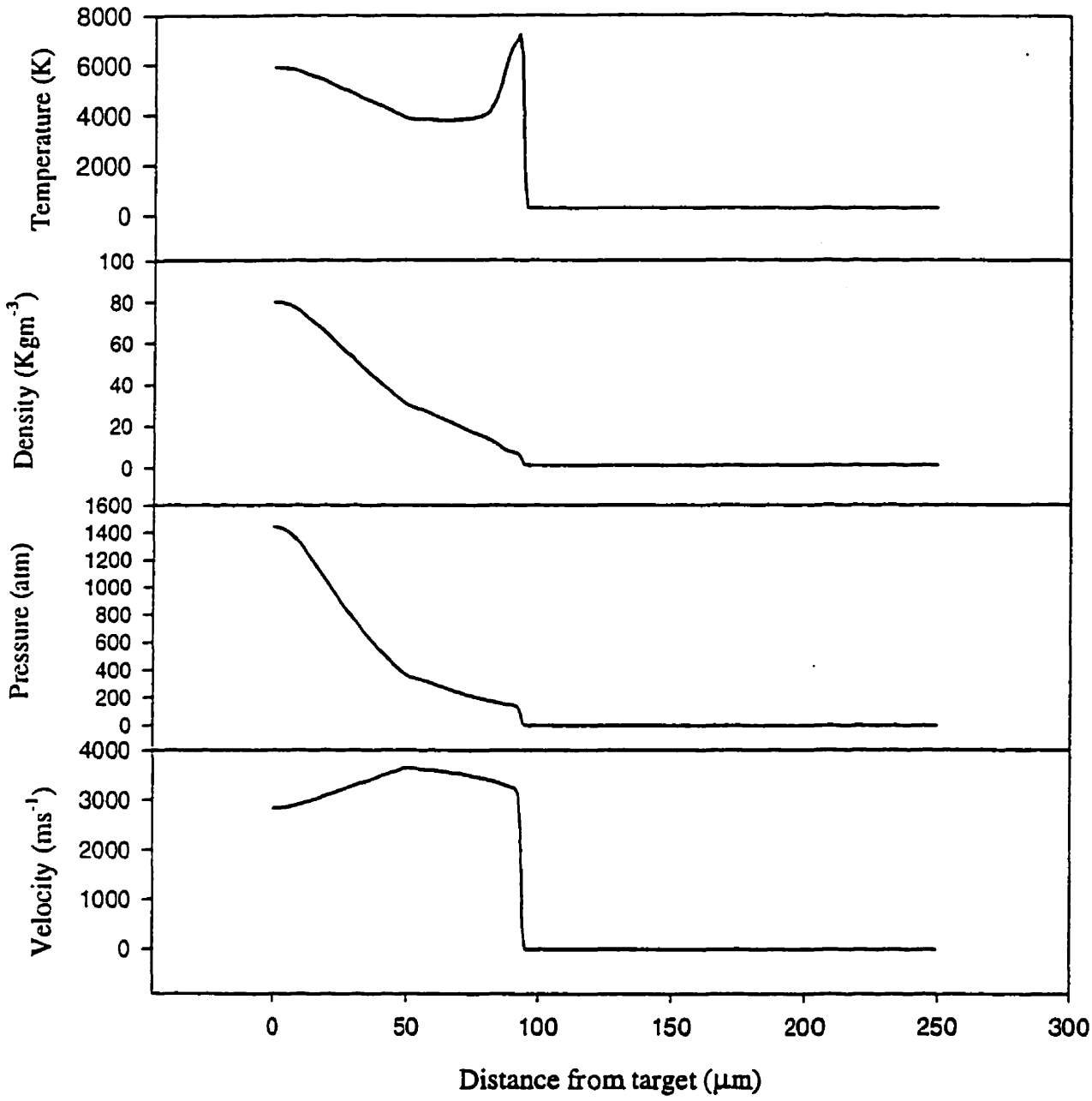

Figure 3.9. Laser ablation of Al at 30 ns into the laser pulse. The conditions are the same as in figure 3.8.

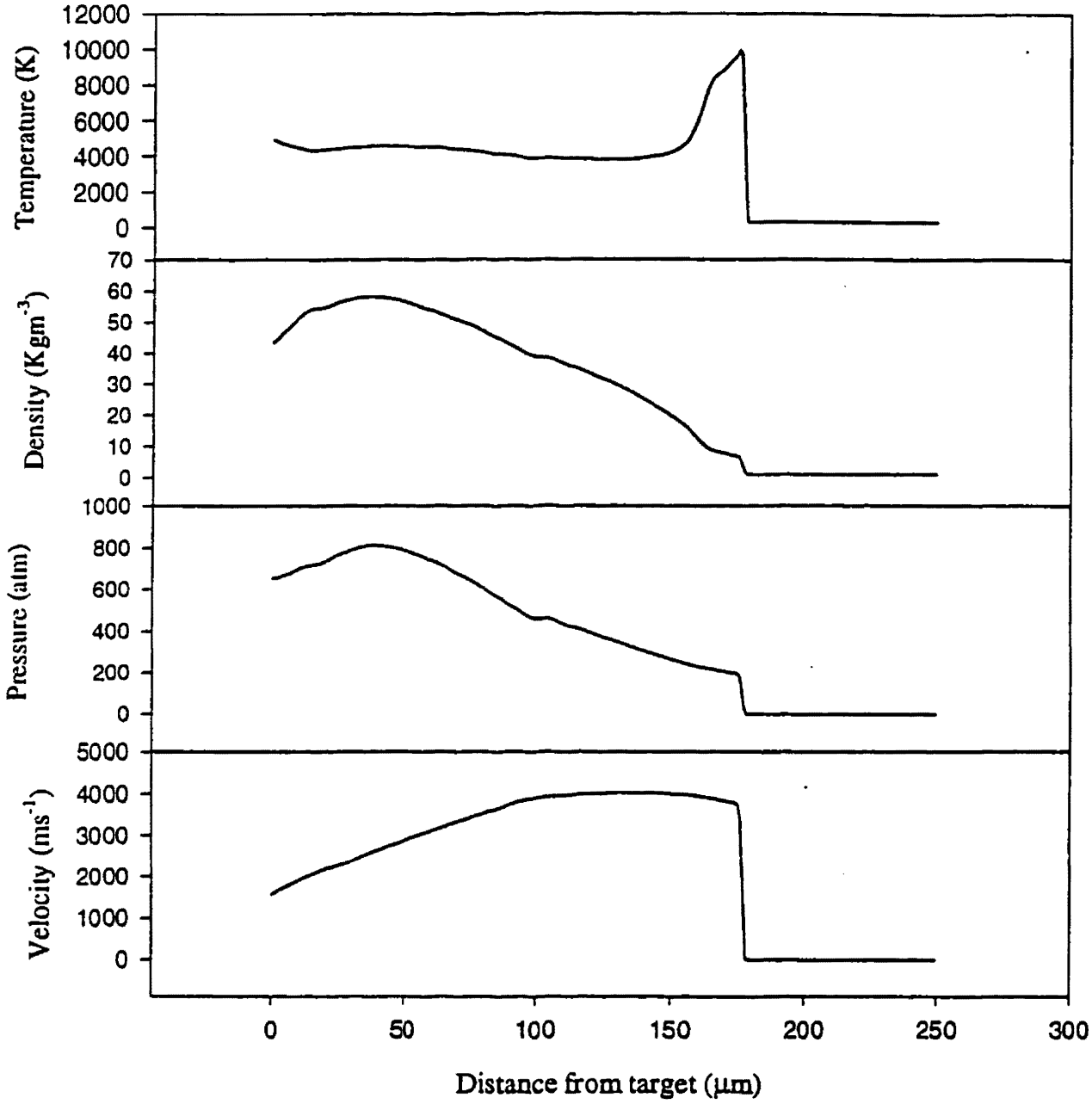

Figure 3.10. Laser ablation of Al at 50 ns near the end of the laser pulse for the same conditions as in figure 3.8. Notice the well resolved contact discontinuity.

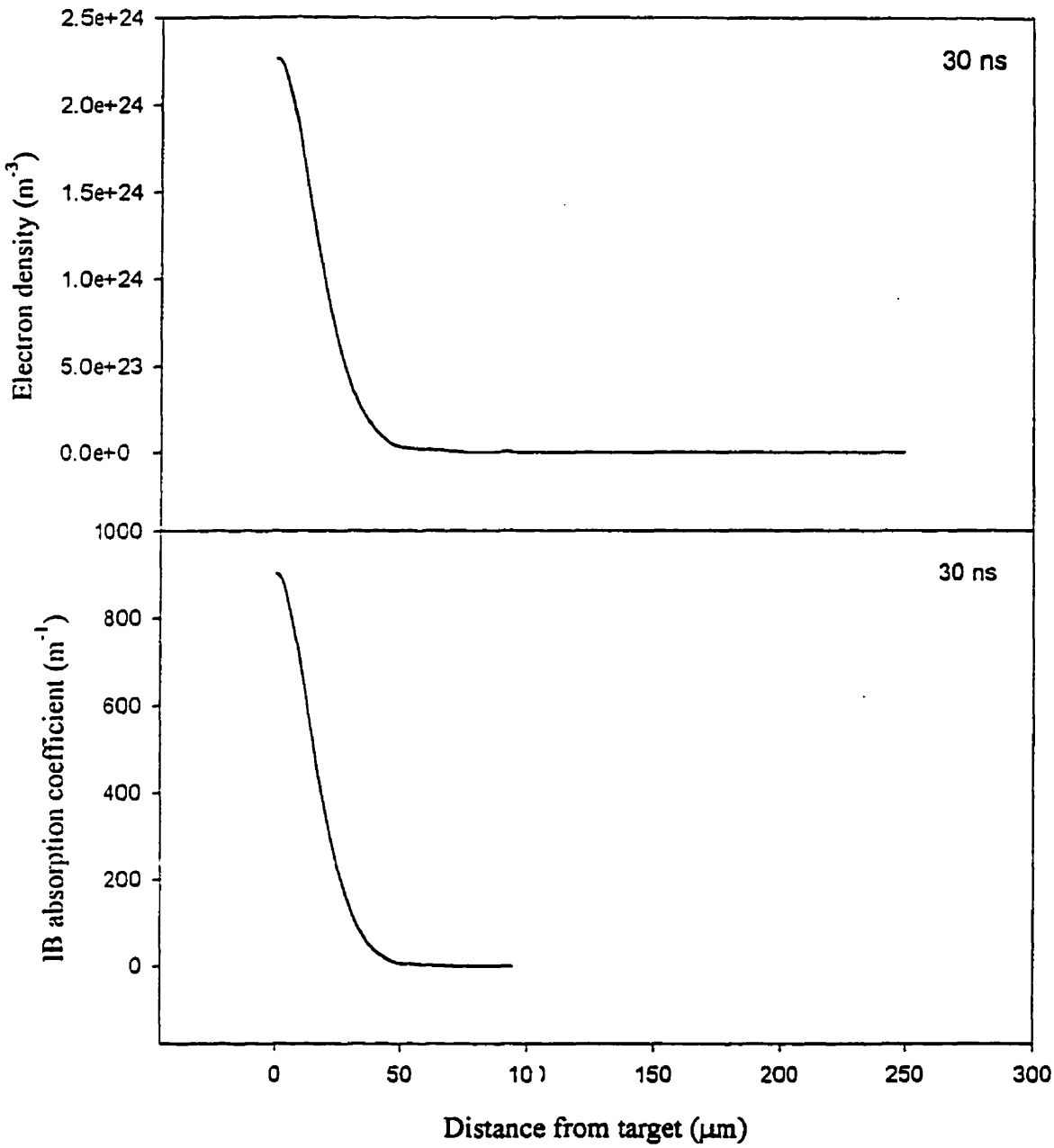

Figure 3.11. Electron density and inverse bremsstrahlung absorption coefficient in the plasma. The intensity is 1.0×10^{13} Wm^{-2}, λ=308nm, and FWHM = 30 ns.

The pulse shape can have a dramatic effect on laser absorption since the rate at which energy is deposited in the target material is different but this also depends at what time the energy is deposited in the target. In figure 3.12 the same simulation as in figure 3.8 is done except that the laser pulse is now a skewed Gaussian with a rise time of 10 ns and a fall time of 50 ns and represents a pulse shape typical of excimer lasers. The results are similar to figure 3.8 except that the peak of the laser pulse has already been reached and the conserved quantities are therefore much larger. The stronger vaporization produces a shock with a higher temperature as shown in figure 3.13 at 30 ns. The vapor temperature behind the shock wave is also higher and reaches 13000 K as compared to ~ 7000 K in figure 3.9.

The propagation velocity of the plasma is also greater reaching 4500 ms^{-1}. Since the shock wave was generated so quickly, the expansion has already approached steady state and the shock is beginning to separate from the plasma.

At 50 ns (figure 3.14) the laser pulse energy is lower than for figure 3.10 and the conserved quantities, density, pressure, and velocity, near the target are smaller, but near the shock they are still larger due to the higher pressure produced in the expansion. The greater expansion velocity has resulted in the plasma travelling a much larger distance than for figure 3.10 at the end of the laser pulse.

The electron density and absorption coefficient remain small. Although the shock temperature and plasma density behind the shock are greater, the temperature of the plasma is insufficient to increase the electron density to values necessary to activate inverse bremsstrahlung.

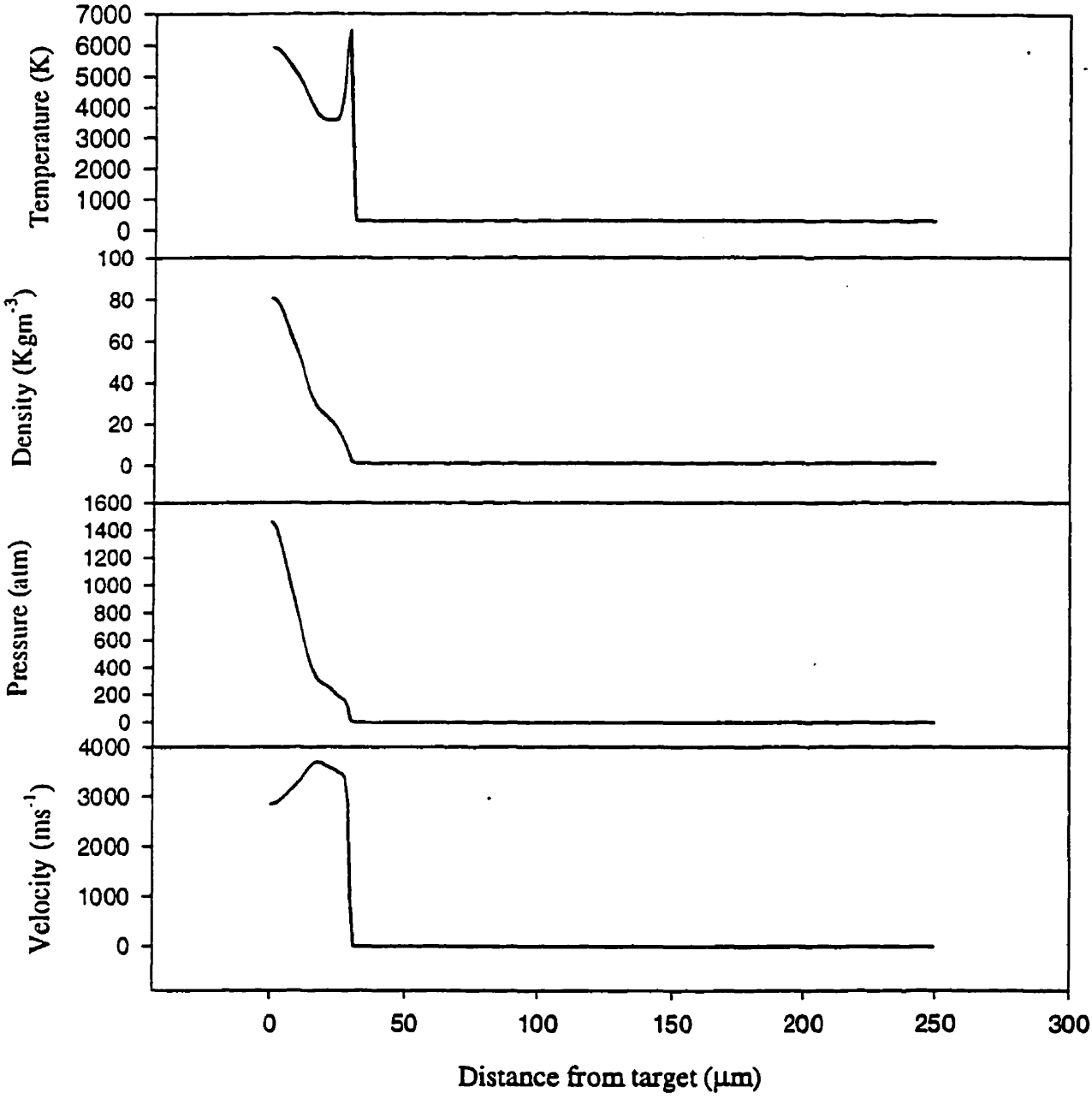

Figure 3.12. Laser ablation of Al after 10 ns for an intensity of 1.0×10^{13} Wm^{-2} with a skewed Guassian pulse of 10 ns rise time and 50 ns fall time. The wavelength is 308 nm.

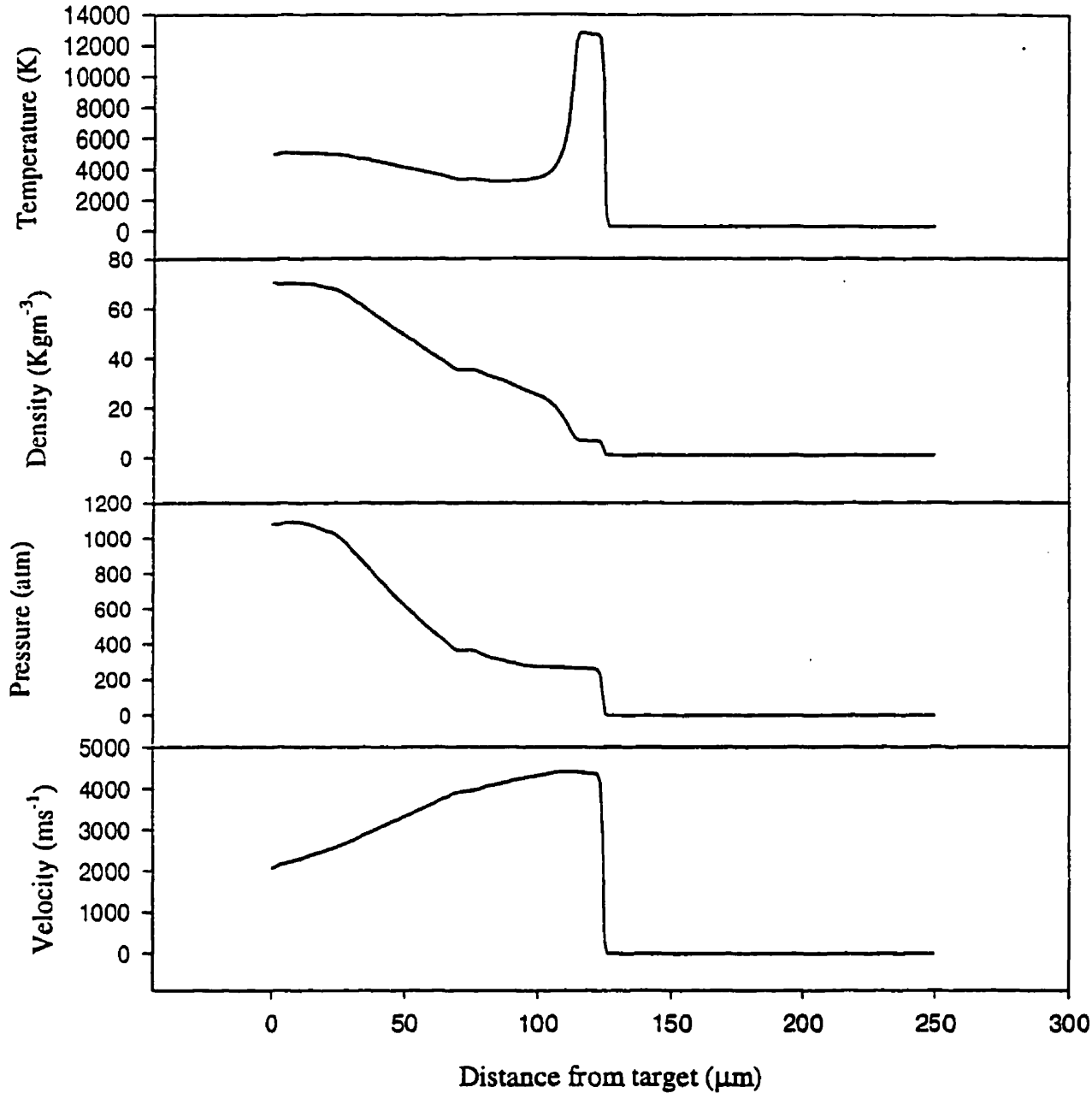

Figure 3.13. Laser ablation of Al at 30 ns after the start of the laser pulse. The intensity is 1.0 $\times 10^{13}$ Wm^{-2} and the pulse has a rise time of 10 ns anf a fall time of 50 ns. The wavelength is 308 nm.

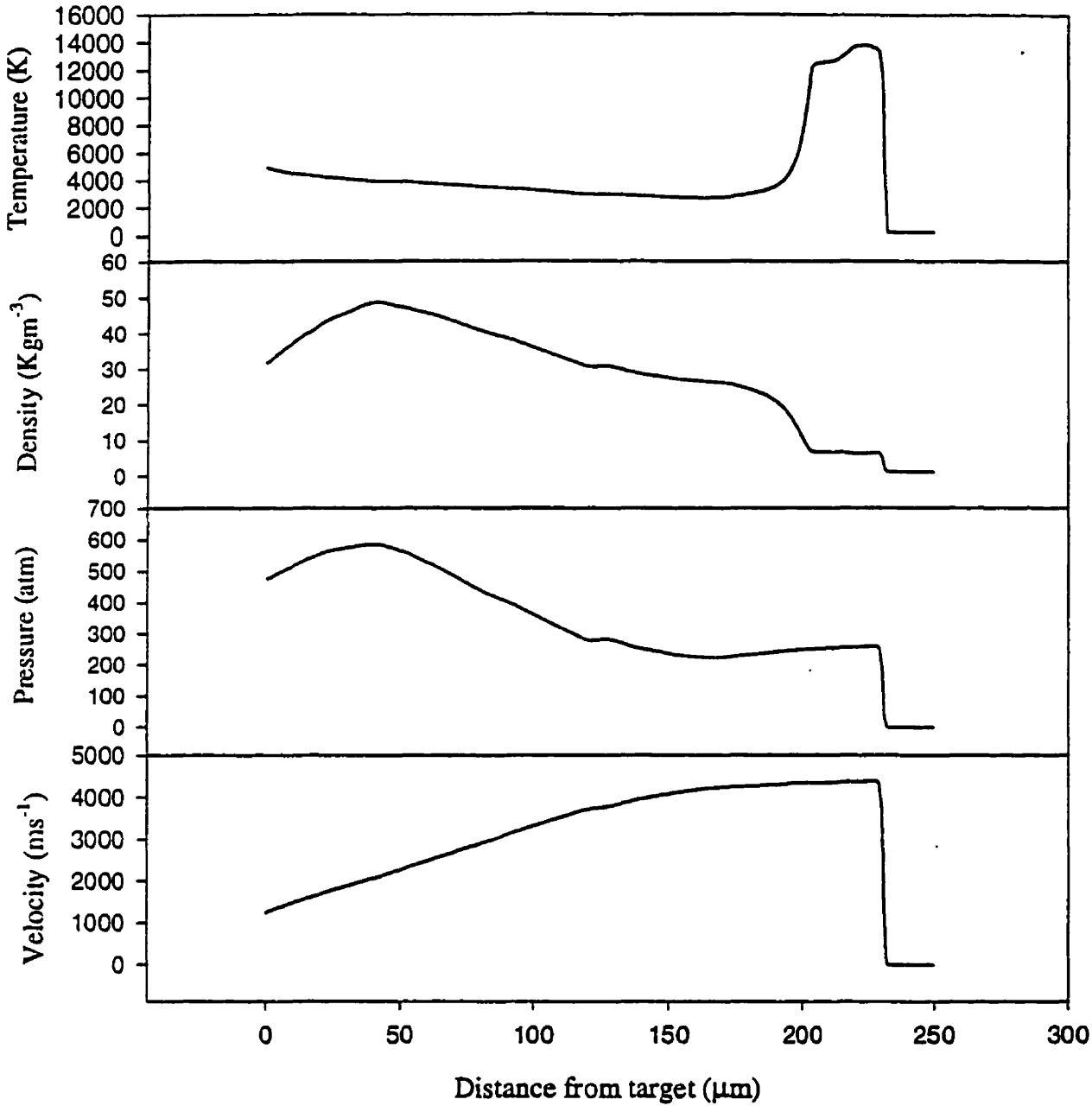

Figure 3.14. Laser ablation of Al 50 ns after the start of the laser pulse. The pulse conditions are the same as in figure 3.13.

Shortening the laser pulse will further increase the conserved quantities since the target surface temperature can be increased dramatically. The propagation of the plasma will be similar to that which has been observed above, however, the plasma temperature can be much higher thus increasing the electron density sufficiently to activate inverse bremsstrahlung absorption.

The effect of the laser intensity on the target is to increase or decrease the rate of energy deposition. If the laser intensity is low enough, the shock pressure approaches the surface pressure of the plasma as shown in figure 3.15 at 30 ns for a laser intensity 1×10^{12} Wm^{-2} with the same 10 ns rise time and 50 ns fall time as in figure 3.13. Here the laser intensity is so low that the expanding vapor can no longer affect the shock wave and shock acceleration has ceased. With high laser intensities, 1×10^{14} Wm^{-2}, the rate of energy deposition is a factor of 10 larger than for $I=1\times10^{13}$ Wm^{-2}. This results in larger conserved quantities at the target surface and the plasma, therefore, has a higher expansion speed at higher laser intensities. The buildup of the pressure and density at the contact front is so large that the temperature reaches 25000 K for $I = 1\times10^{14}$ Wm^{-2} compared with only 12000 K for $I = 1\times10^{13}$ Wm^{-2}.

The high plasma temperature and density produced at $I=1\times10^{14}$ Wm^{-2} results in a much larger electron density and absorption coefficient than at lower laser intensities (figure 3.16). For $I = 1\times10^{14}$ Wm^{-2}, the absorption coefficient is large enough over the plasma that inverse bremsstrahlung absorption can effectively absorb the laser pulse as shown in figure 3.17. This is not the case at lower laser intensities. However, these results assume no line absorption which can dramatically affect the rate of vapor heating.

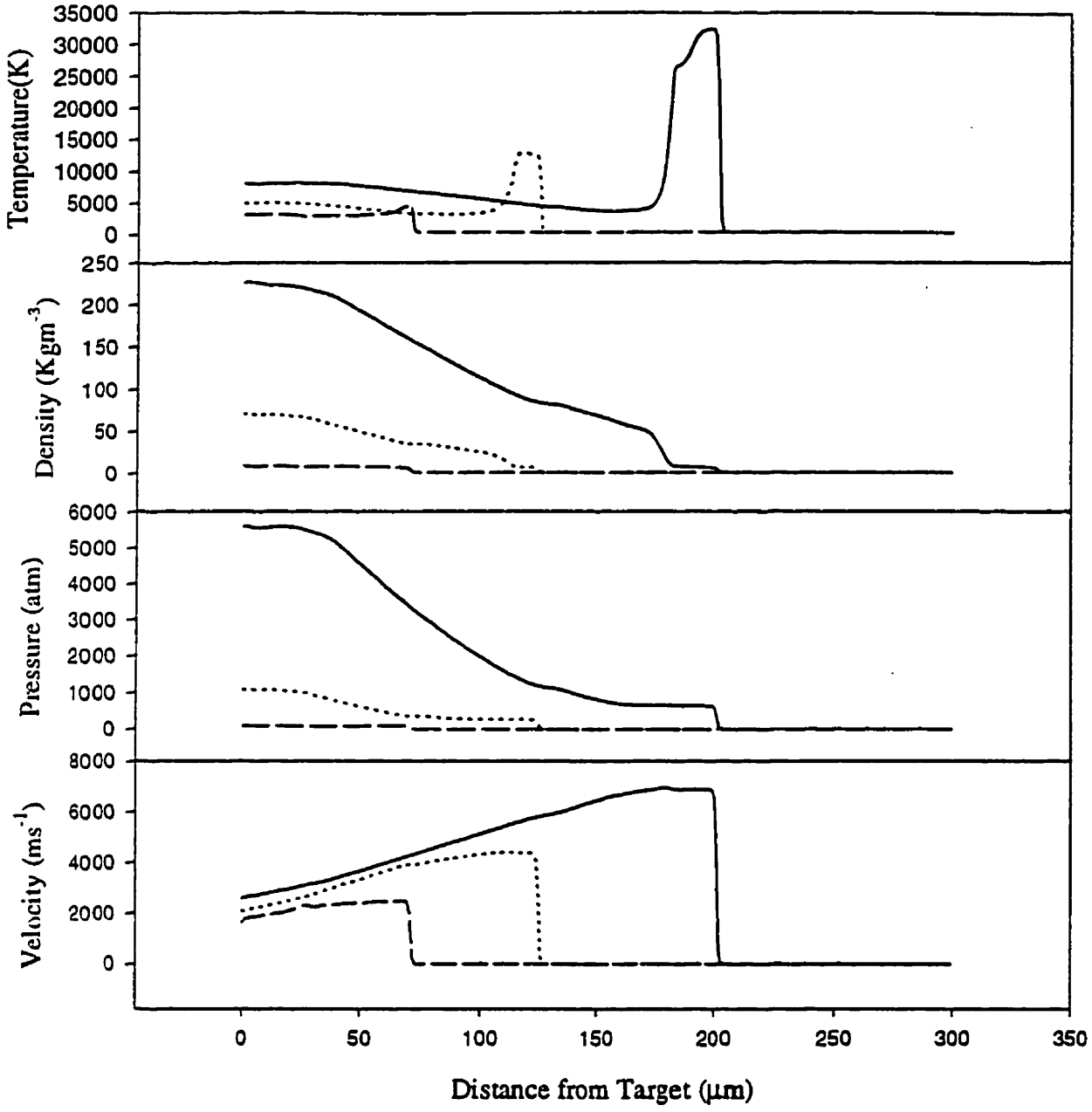

Figure 3.15. Laser ablation of Al at three different laser intensities showing the effect of laser power on the gas dynamics. Solid line - 10^{14} Wm^{-2}, short dash line - 10^{13} Wm^{-2}, long dash line - 10^{12} Wm^{-2}. The pulse is a skewed Gaussian with a rise time of 10 ns and a fall time of 50 ns. The figure shows the results at 30 ns.

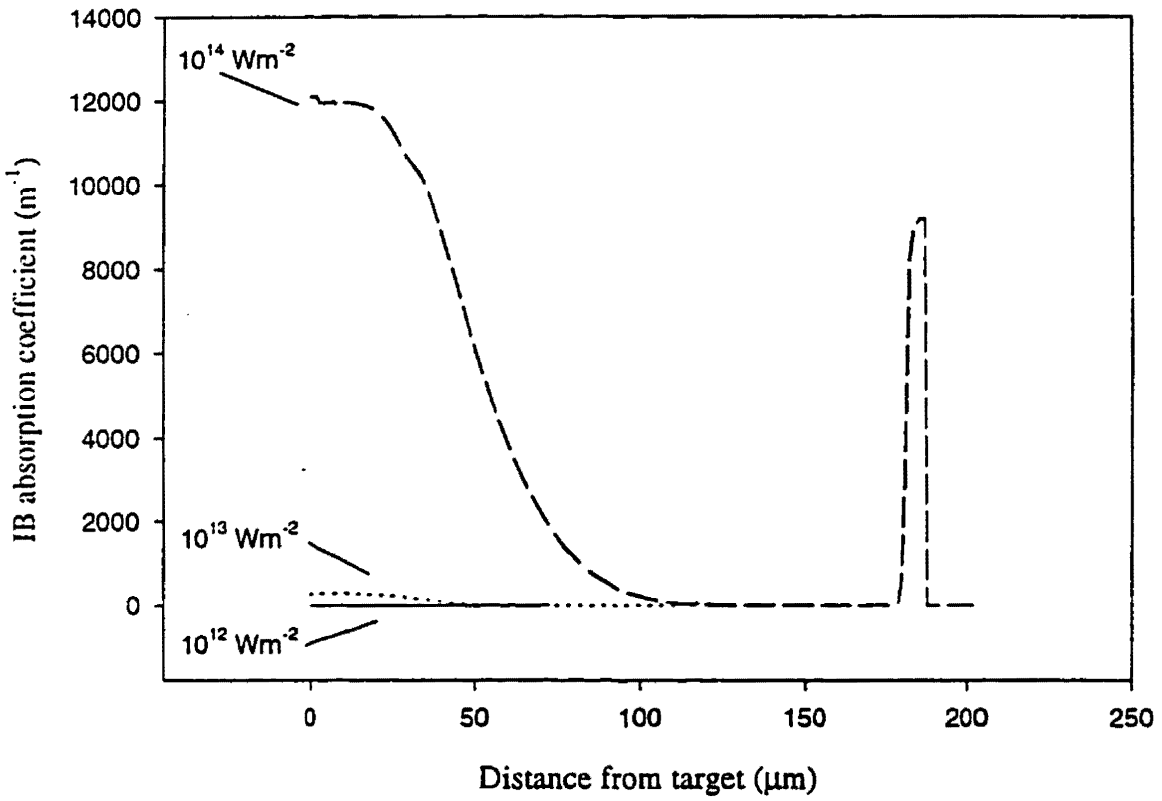

Figure 3.16. Comparison of the IB absorption coefficient for three different laser intensities. The pulse is a skewed Gaussian with a rise time of 30 ns and a fall time of 50 ns. The time is 30 ns after the start of the laser pulse.

The laser intensity and pulse shape have a strong effect on the conserved quantities in the plasma mainly due to the rate of energy deposition and when the energy is deposited. With high enough laser intensities, inverse bremsstrahlung absorption can be effective at attenuating the laser beam.

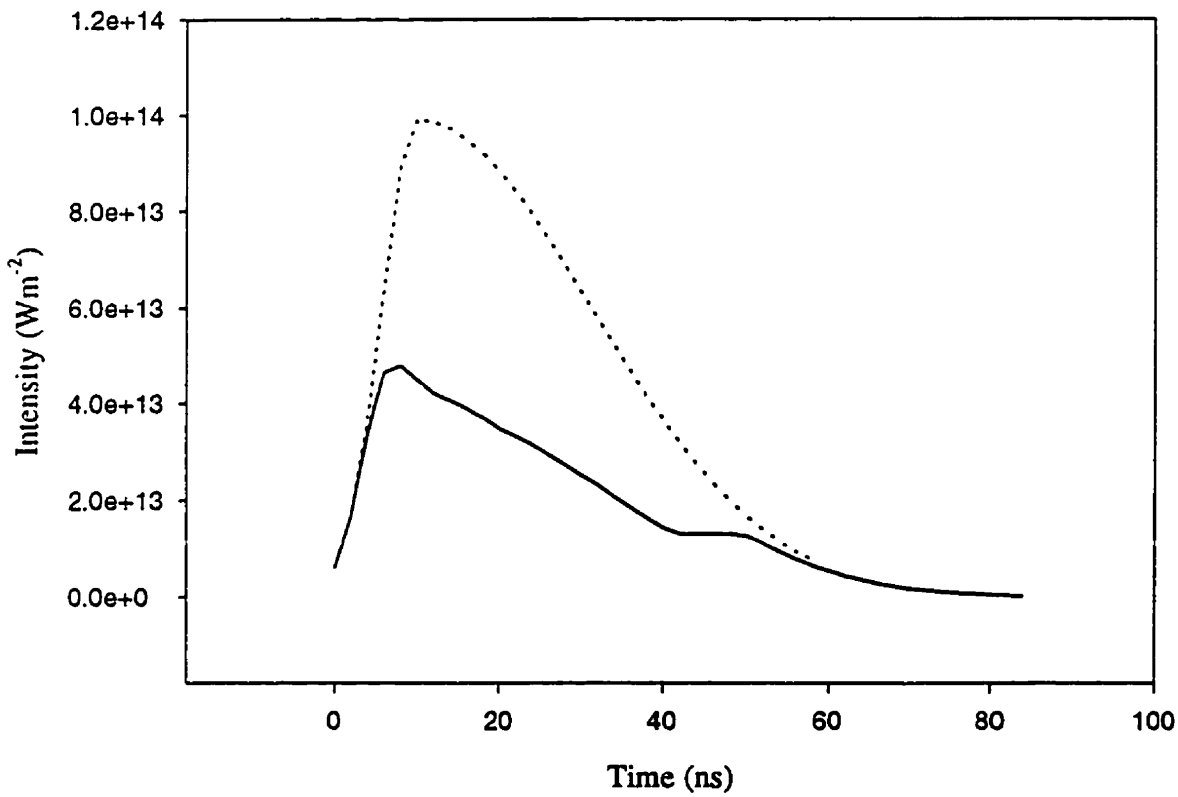

Figure 3.17. Absorption of the laser pulse by inverse bremsstrahlung in an Al plasma using a laser intensity of $I = 1\times10^{14}$ Wm^{-2}. The dashed line is the unattenuated beam while the solid line represents the transmitted beam.

3.4 Effect of Gas Pressure and Gas Composition on Laser Ablation of Metals

Gas pressure will determine the speed of plasma expansion. If the gas pressure is high, the plasma expands slowly whereas a low gas pressure results in a fast expansion. This also affects the temperature and density of the plasma and gas. Results for Al in three different N_2 gas pressures are shown in figure 3.18 for a laser intensity 1×10^{13} Wm^{-2} with a FWHM = 30 ns. The results are for 30 ns after the start of the laser pulse. At 1 atm, the plasma expands least and the shock temperature is lowest. This is due to the pressure differential and the speed of the plasma at the contact front. A low pressure differential results in less compression and a slower plasma speed due to the higher density gas. Since it is more difficult to compress the higher density gas, the plasma pressure, density, and temperature tend to be higher behind the contact front. As the pressure decreases, the gas is more easily compressed, and the shock temperature increases as well as the plasma speed since the expansion is faster. This results in less pressure and density buildup behind the shock front but a higher temperature of the plasma at the contact discontinuity as the hump near the shock wave indicates. This is because the plasma has had time to expand further and increase its energy relative to the high pressure case. Although the plasma temperature is higher at the contact front, the density is lower so that the electron density is quite small.

At 50 ns, near the end of the laser pulse, the plasma and shock wave are well separated at all three pressures (figure 3.19). However, the shock pressure and density are still largest for the 1 atm case implying that the shock is still building. In the lower pressure cases the shock is propagating in a steady state as indicated by the flat slopes in the pressure and density curves.

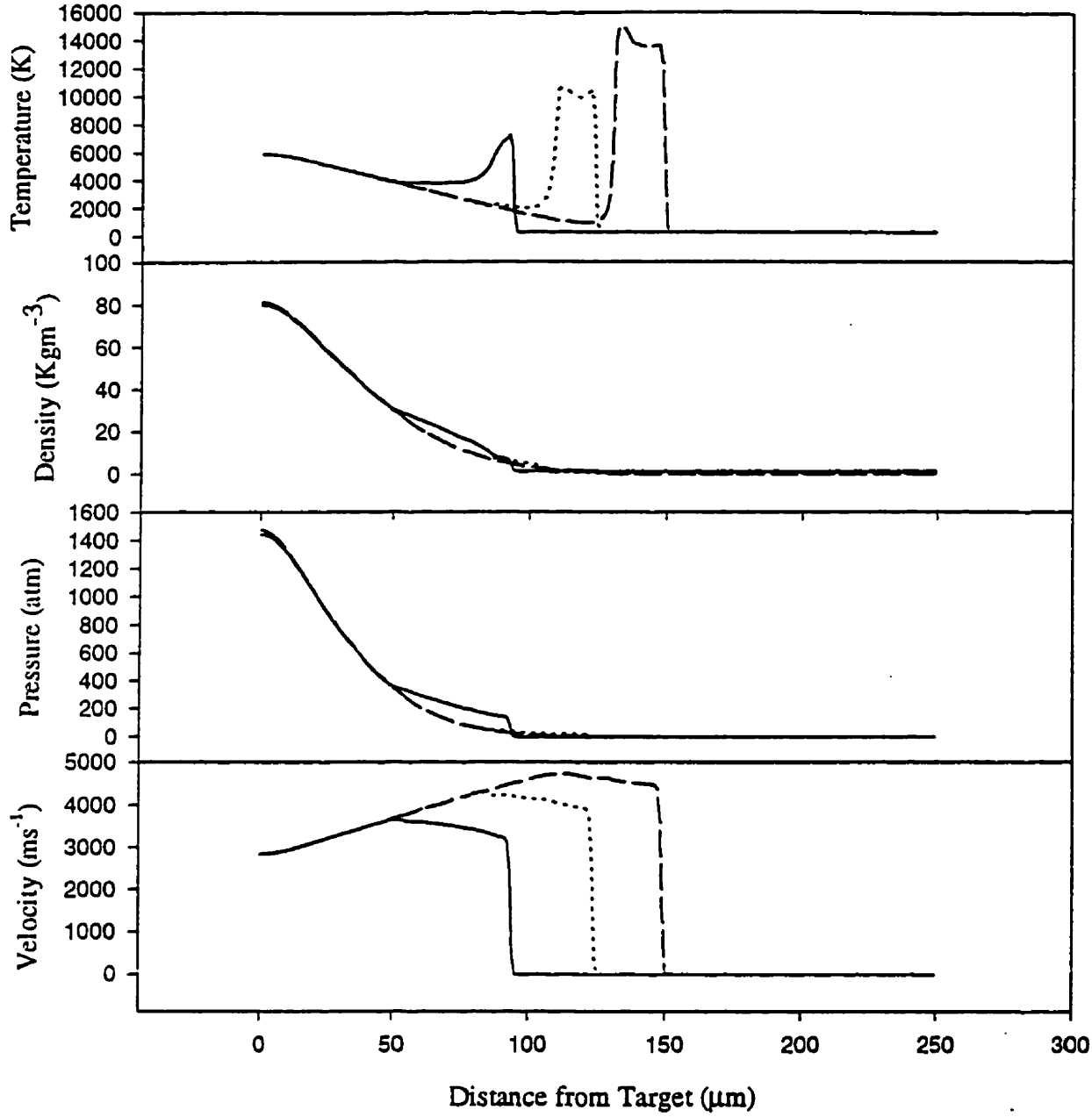

Figure 3.18. Effect of N_2 gas pressure on the laser ablation of Al at a laser intensity of 1.0×10^{13} Wm^{-2} with FWHM = 30 ns and λ = 308 nm. The time is 30 ns after the start of the pulse. The solid line corresponds to an N_2 pressure of 1 atm. The short dash line is for a pressure of 0.1 atm, and the long dash line is for a pressure of 0.01 atm.

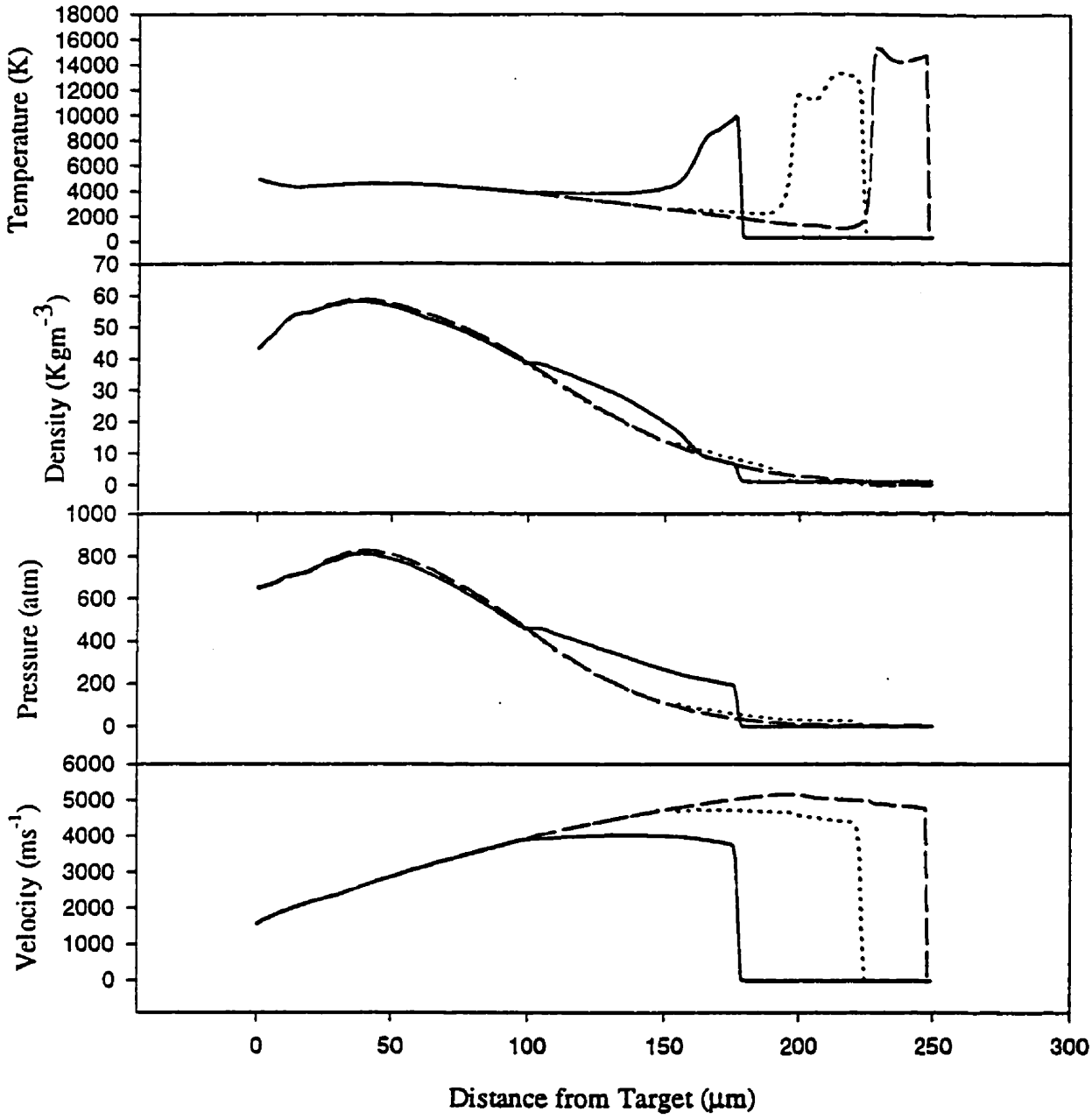

Figure 3.19. Effect of gas pressure on the laser ablation of Al for the same conditions as in figure 3.18 but 50 ns after the start of the laser pulse. Solid line - 1 atm N_2. Short dash line - 0.1 atm N_2. Long dash line - 0.01 atm N_2.

The composition of the background gas can affect the hydrodynamics of the plasma in two ways. The first is through the mass of the gas since a heavier gas is more difficult to compress than a lighter gas. The second is due to the thermodynamic properties of the gas itself such as specific heat and specific gas constant.

In figure 3.20, results for the laser ablation of Al in three different gases, N_2, Ar, and He at 1 atm are shown. The laser intensity and pulse shape are the same as in figure 3.18. He is the lightest gas and is easily compressed and thus does not slow down the vapor expansion as much as for heavier gases. This results in a relatively fast expansion rate in which the shock wave quickly outruns the plasma. The shock temperature is small since the specific heat of He is large due to its smaller mass. With a heavy gas such as Ar, the shock speed is slightly faster than the N_2 case due to a different gas constant which affects the pressure. However, due to the mass of the gas, the expansion rate behind the shock front is slower than in N_2. This results in a higher pressure, density, and temperature in the regions behind the shock as was found for the pressure variation discussed above. Also, the shock temperature is much larger due to the small specific heat of Ar. Even though the plasma temperature is higher for ablation into Ar, the electron density is still too small to activate inverse bremsstrahlung absorption.

At 50 ns after the start of the laser pulse, the difference between the three gases is clear as shown in figure 3.21. The step near the shock wave for Ar is the contact discontinuity and the pressure and density vary dramatically behind the shock wave.

These results give a good indication of how pressure and gas composition affect the thermodynamics of the plasma. If one wants to confine the plasma close to the target

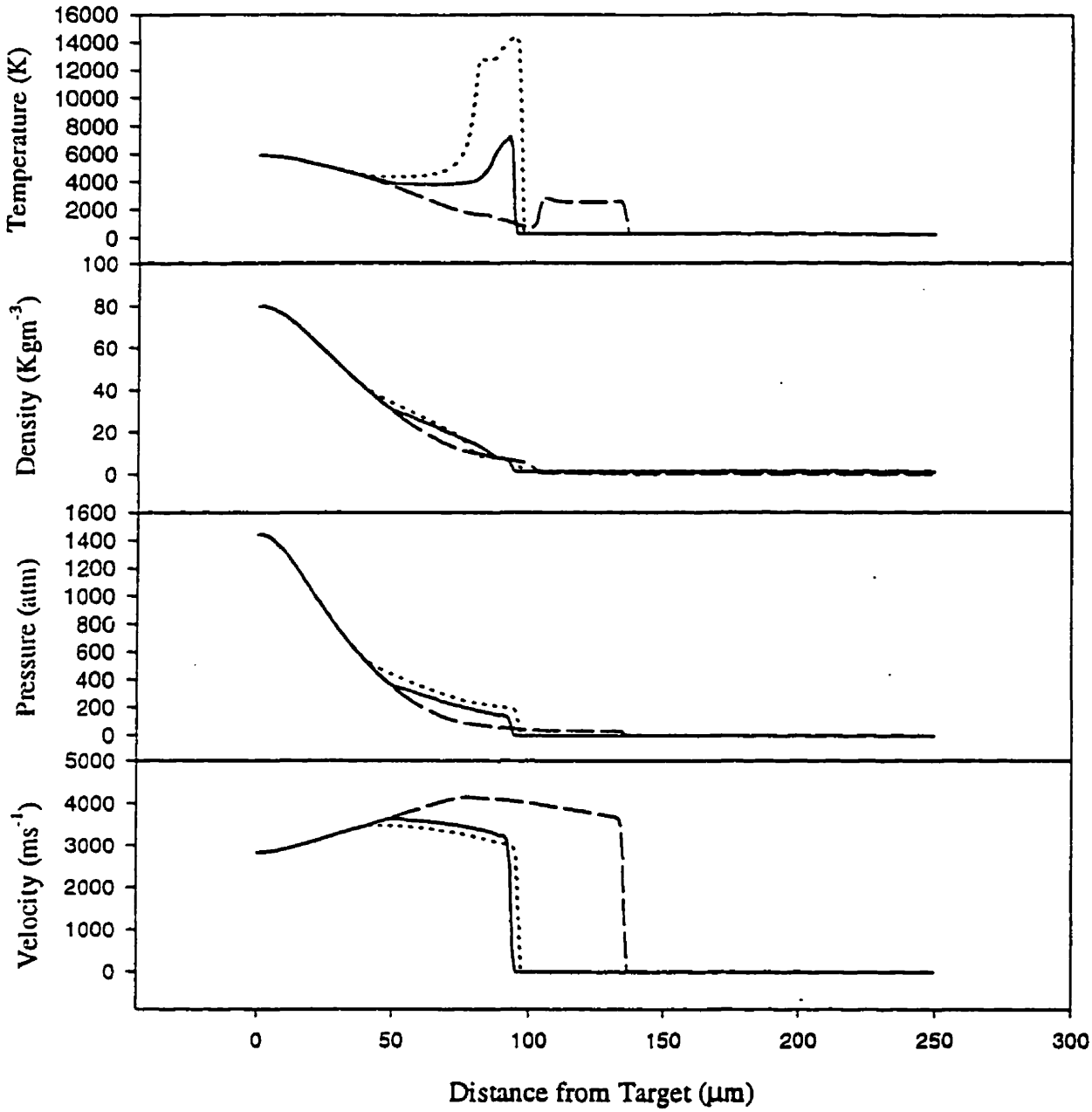

Figure 3.20. Effect of gas composition on the laser ablation of Al with a laser intensity 1.0 $\times 10^{13}$ Wm^{-2} and FWHM = 30 ns. The time is 30 ns after the start of the pulse. The solid line corresponds to 1 atm N_2. The short dash line corresponds to 1 atm Ar, and the long dash line corresponds to 1 atm He.

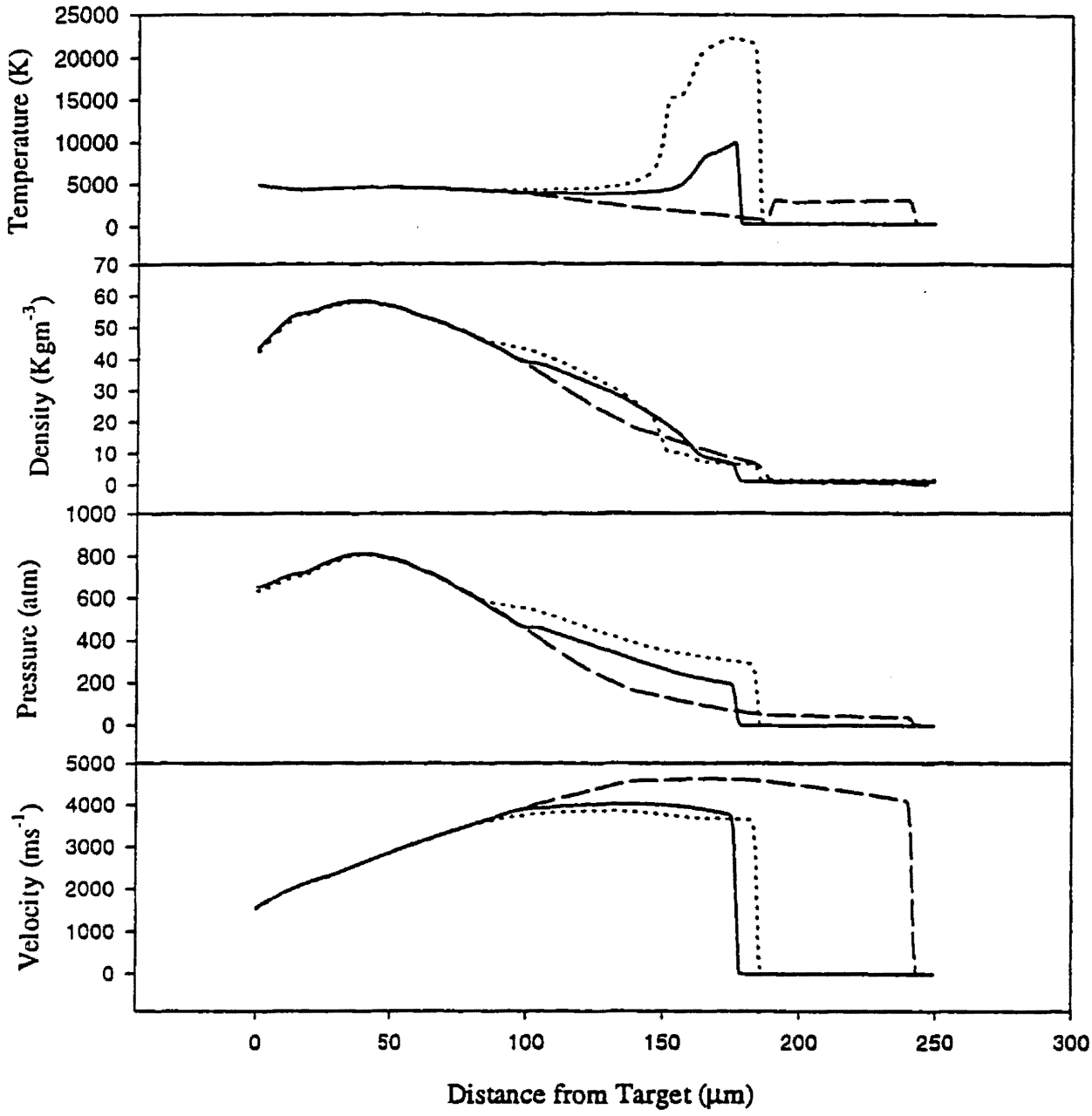

Figure 3.21. Effect of gas composition on the laser ablation of Al for the same conditions as in figure 3.20 but at 50 ns after the start of the laser pulse. Solid line - 1atm N_2. Short dash line - 1 atm Ar. Long dash line - 1 atm He.

effectively increasing its pressure, density, and temperature, then a high gas pressure is necessary and heavy gases are favored. If the pressure is very low then no shock wave is observed and the plasma would just expand as a rarefaction wave into vacuum. The effect on the electron density is minimal. Although the electron density behind the shock is larger for increased pressure or heavier gases, it is not enough to increase the inverse bremsstrahlung absorption coefficient for appreciable laser absorption in the plasma. The most effective method of increasing laser absorption in the plasma appears to be by using high intensity short laser pulses as discussed in section 3.3 or longer wavelength lasers so that inverse bremsstrahlung absorption becomes efficient.

The role of line absorption in Al vapor at 308 nm has been neglected. If sufficient overlap between the laser wavelength and an absorption band occurs, then very strong vapor heating can occur as the photons are absorbed (see section 2.6). This can result in a much hotter plume than predicted in simulations. Absorption of the laser pulse energy can, therefore, occur at low laser intensities, $< 10^{13}$ Wm^{-2}, depending on the amount of overlap. If there is no overlap (Appendix A), then inverse bremmstrahlung absorption is the only effective way of heating the plasma and this will require high laser intensities, $> 10^{13}$ Wm^{-2}.

Chapter 4

Experimental System

4.1 High Vacuum Laser Ablation Chamber

To systematically study how excimer laser radiation interacts with metal surface under a variety of atmospheres, a versatile high vacuum (10^{-7} Torr) stainless steel target chamber was constructed as shown in figure 4.1. This chamber was cylindrical with various sized ports located at 45 deg intervals around its circumference. This allows the laser beam to enter either normal or at a 45 deg angle to the target located in the center of the chamber. This chamber is large enough to accommodate a mini optical board inside it which allows mounting of optical equipment or diagnostic instruments close to the target. For maximum experimental throughput, a target assembly was designed that could hold eight targets (figure 4.2). This target wheel was mounted in the centre of the chamber and connected throughout a shaft to a rotational vacuum feedthrough so that multiple targets could be studied without having to change the gas atmosphere.

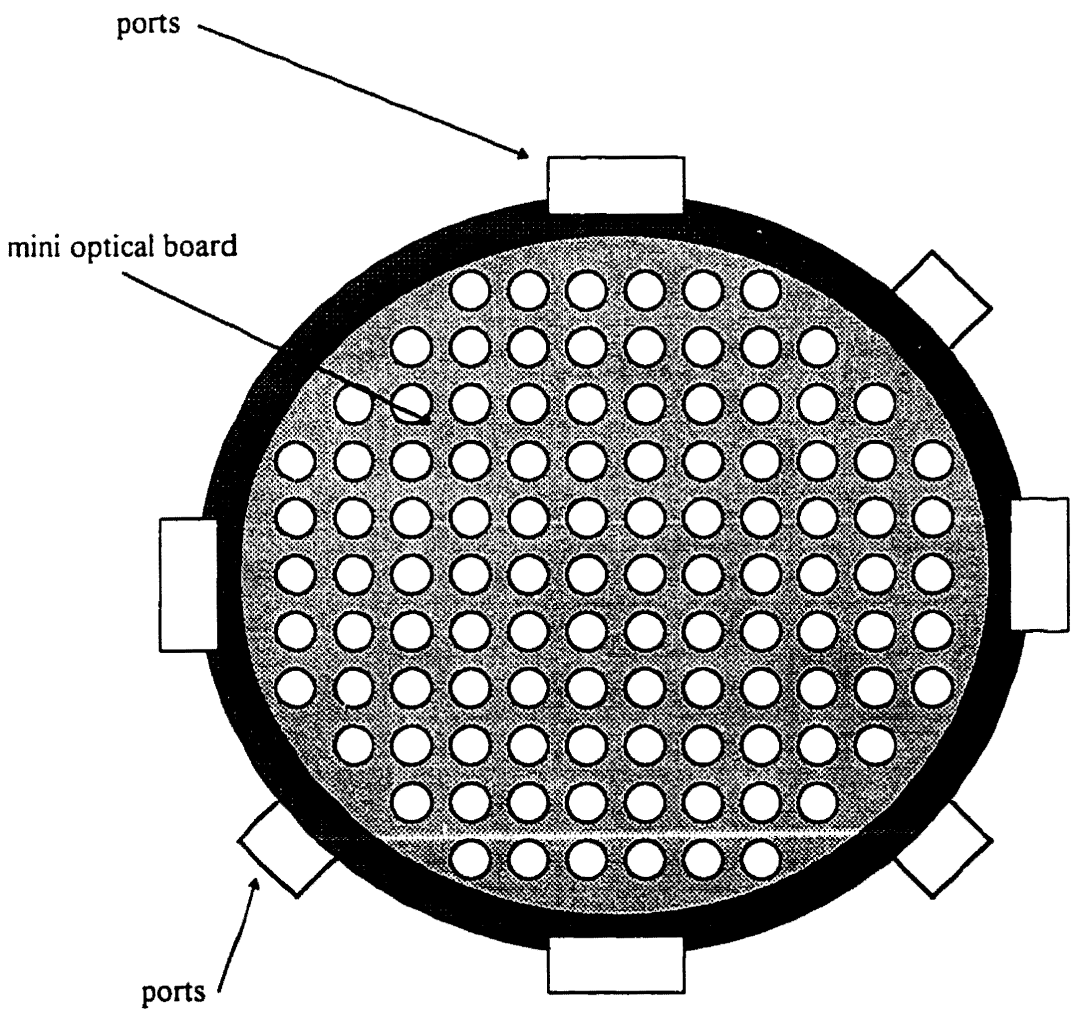

Figure 4.1. Above view of high vacuum laser ablation chamber showing the mini optical board. The chamber is 25 cm in diameter and 20 cm deep.

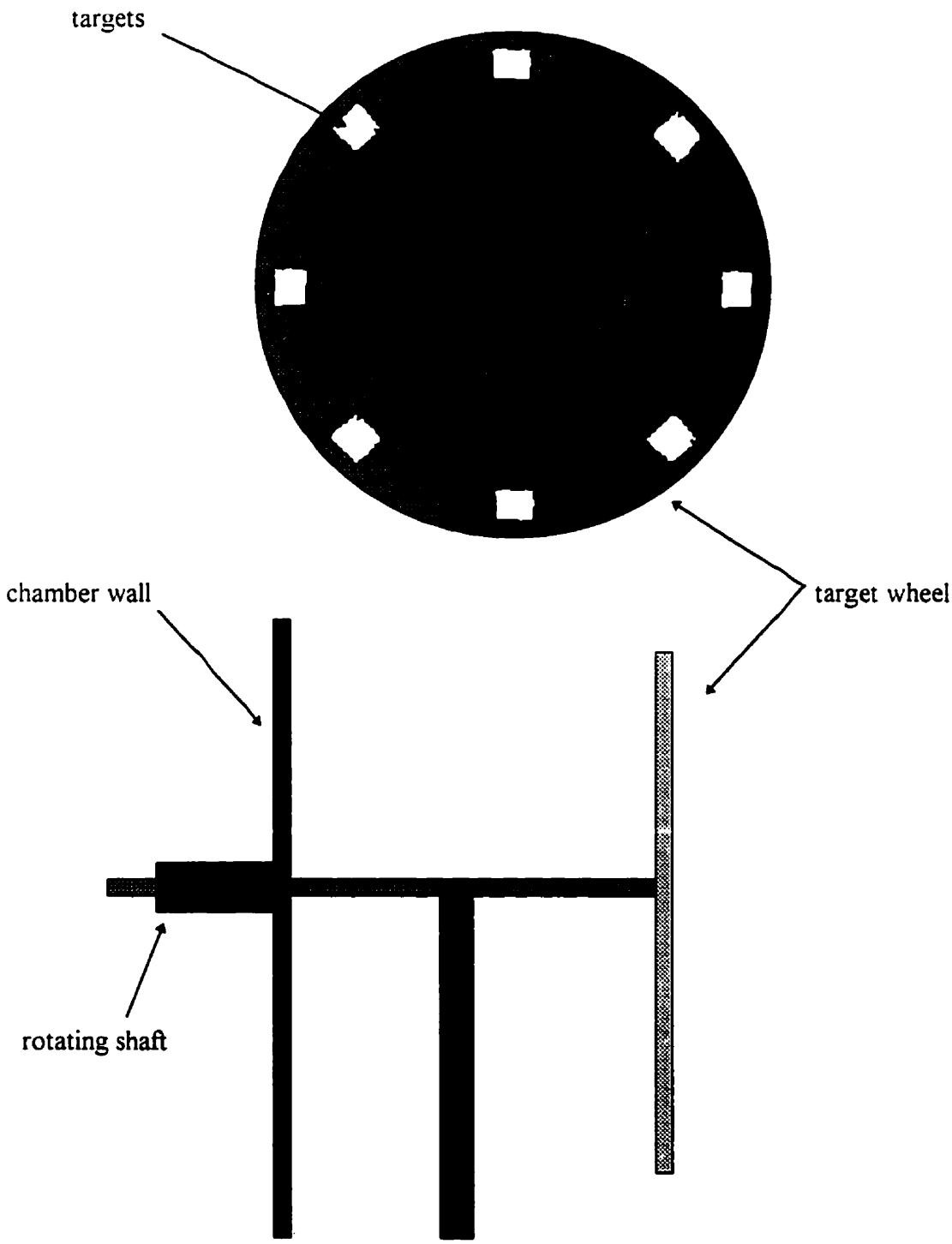

Figure 4.2. Target wheel assembly. Each target is 1 cm long and 0.5 cm high.

4.2 Laser Focussing System

Any experiments performed require knowing the laser intensity and also require a uniform laser intensity on the target. If this intensity is not uniform then the ablated material in the centre of the laser spot would have different thermodynamic properties than the ablated material at the edges of the spot. This could affect the outcome of time of flight or optical spectroscopic experiments on the plasma and is also an important consideration in the accurate determination of ablation rates since less material would be removed at the edges of the laser spot.

Figure 4.3 shows the focussing system used for the experiments. The excimer laser is first passed through an aperture of known size which isolates the part of the laser beam which has uniform intensity. Normally this is the central part of the beam as shown in figure 4.4 for a Lumonics Hyper-Ex 400 laser. The idea is then to image the aperture on the target by reducing the image size of the aperture as much as possible. From the lens equation, image location, i, and magnification, m, are,

$$\frac{1}{i} = \frac{1}{f} - \frac{1}{o}$$
$$m = \frac{i}{o} \tag{4.1}$$

where f is the focal length of the lens and o is the object distance from aperture $A1$ to the lens. A small m requires that the object distance be as large as possible. The image will then be located near the focus of the lens and be substantially reduced in size. In figure 4.3 the object distance is increased to 3.83 metres using two mirrors to bend the beam. The

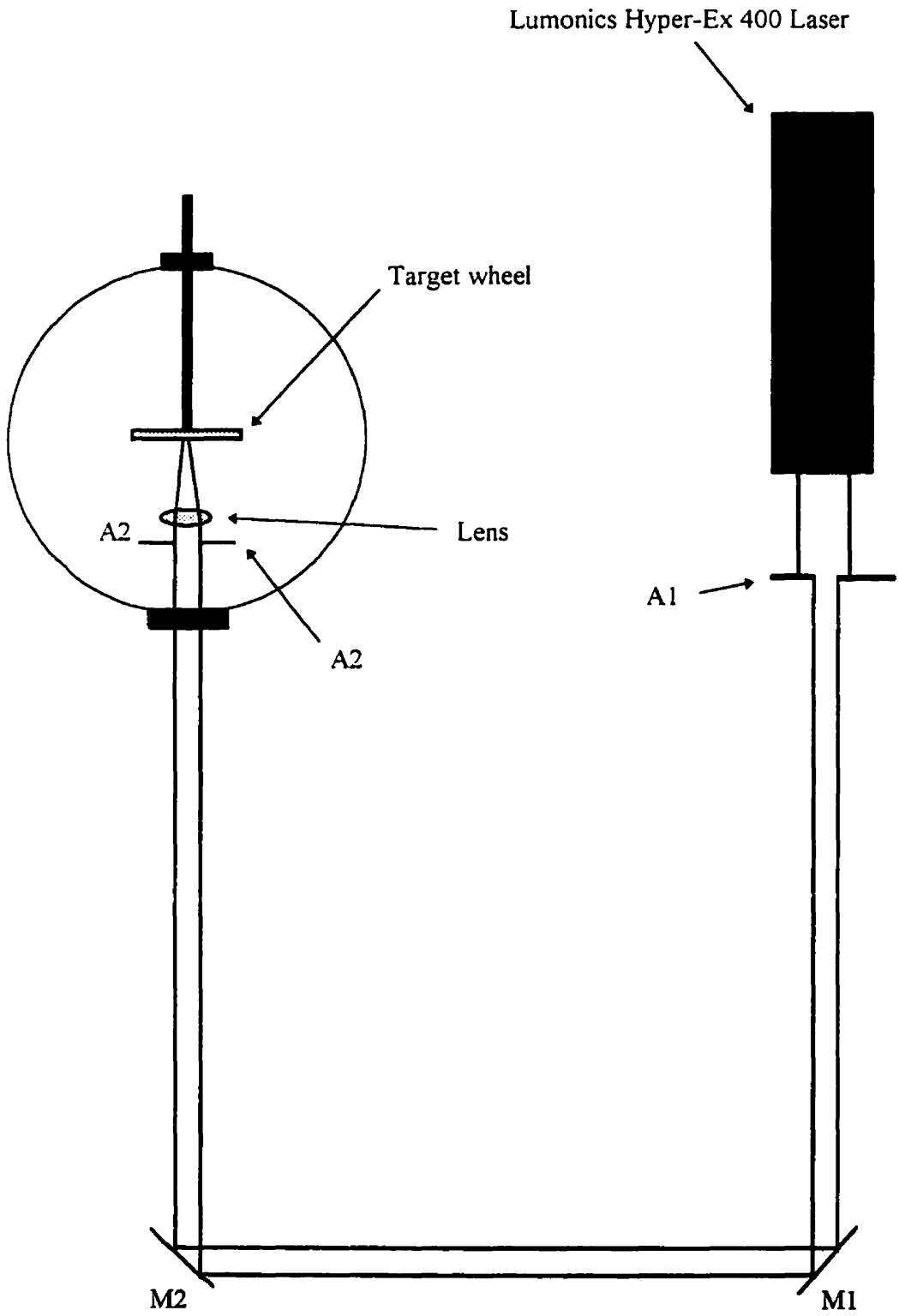

Figure 4.3. Laser focussing system to obtain uniform energy density on the target.

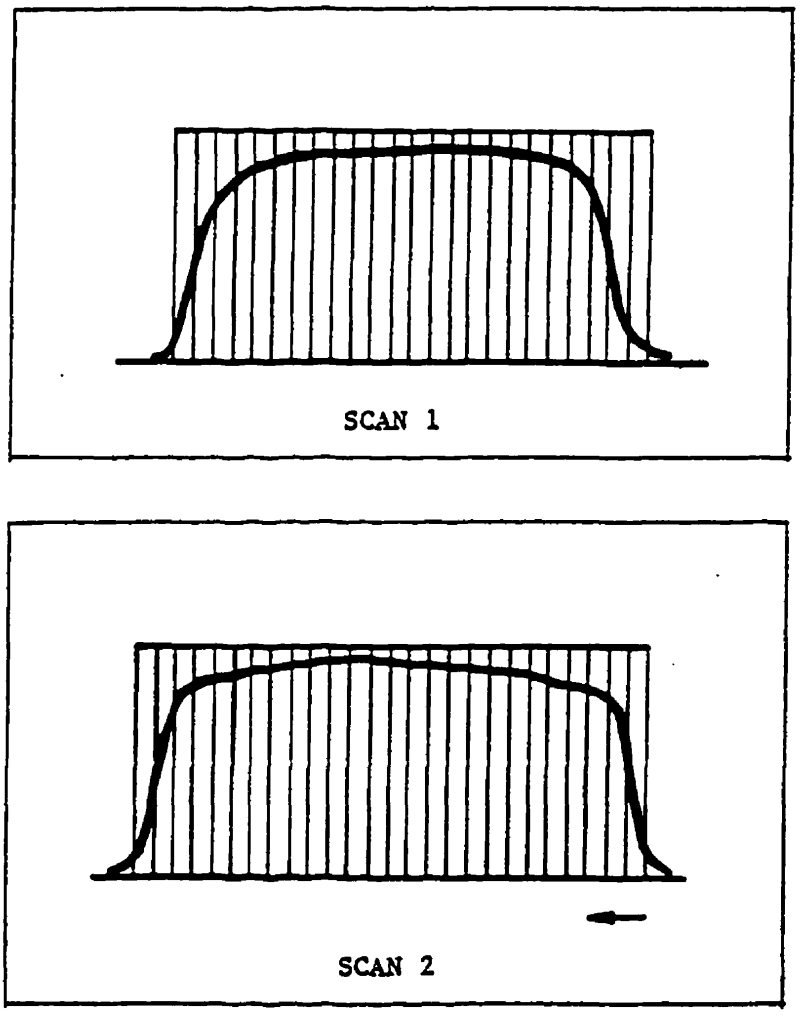

Figure 4.4. Laser beam profile of an excimer laser showing the flat top along the two orthogonal directions (Lumonics HyperEX-400 excimer laser manual).

image distance produced with a lens of focal length 9.5 cm is 9.7 cm which gives m= 0.025. The size of the aperture, A1, is 7 mm so that the spot size is reduced to 175 μm at the target. A second aperture, A2, located directly behind the focussing lens removes any inhomogenieties suffered by the beam as a result of diffraction at the first aperture or due to divergence of the laser beam.

The maximum energy transmitted through the optical system was found to be 10 mJ (Lumonics HyperEx-400 excimer laser operating at 308 nm). Given the spot size determined above, this corresponds to a maximum intensity on the target of 1.38×10^{13} Wm^{-2} with a pulse FWHM = 30 ns. The actual laser intensity is slightly lower since the beam does diverge and creates a spot at the target larger than that calculated above. The measured value of the spot size was found to be ~ 200 μm and this reduces the laser intensity to 1.0×10^{13} Wm^{-2}. The laser intensity was varied using an attenuator stack made up of individual quartz plates located before the lens.

4.3 Mass Ablation Rates

The mass ablation rates were one of the most difficult experiments to perform since the amount of material removed per laser shot was very small. For example, the ablation depth in Al using 308 nm excimer laser radiation is ~ 1μm (Kinsman, 1991). The typical spot area is ~ 5×10^{-8} m^2 giving a volume of 5×10^{-14} m^3. Multiplying by the density of Al gives 1.35×10^{-10} Kg of material removed per laser shot. Since typical microgram scales have resolutions of $\pm$ 10^{-9} Kg a difficulty arises in accurately measuring the ablation rate. The simplest way to overcome this difficulty is to strike each target with a sufficient number of

laser shots so that the amount of material removed exceeds the scale resolution by at least a factor of 10. The quantity of material removed is then on the order of 10^{-8} Kg and can be measured.

The experimental procedure was follows: Al targets 250 μm thick and 99.999% purity (Alfa AESAR) were first cleaned in an ultrasonic acetone bath to remove any debris or accumulated oxides on the surface. Each target was then carefully weighed with a microgram balance and transferred to the target holder in the high vacuum chamber. The targets were irradiated with 600 - 1000 laser shots depending on the laser intensity. The shots were evenly spaced on the targets and no more than 100 laser shots were allowed in the same spot. The reason is that the focus of the laser may be significantly affected due to the depth produced by more than 100 laser shots thus affecting the laser intensity. Also, if the hole produced approaches the thickness of the target then plastic deformation may occur in the target which can affect the ablation depth.

Once the targets had been processed they were removed from the chamber and cleaned again to remove debris deposited around the spot area by the background gas action on the plasma as discussed in chapter 2. Removal of debris was found to be necessary to arrive at an accurate measure of ablation depth and rate.

Detaching the debris, however, was a problem since ultrasonic cleaning not only removed the debris but also any oxides that built up after the first cleaning as well as some of the aluminum itself. This was found to introduce an error in the measurement of the amount of material ablated from each target. As a result, some targets lost more mass than others at the same laser intensity due to variations in the action of the ultrasonic bath on

each target. To overcome this problem each target was separately cleaned by hand using a swab and acetone. The targets were then examined under a microscope to ensure they were free of debris.

The targets were reweighed and the ablation depth was calculated as follows,

$$A.D. = \frac{\Delta m}{A\rho} \tag{4.2}$$

where Δm is the change in the mass of the target per laser shot, A is the area of the ablation and ρ is the target density .

Experiments were carried out as a function of laser intensity at different gas pressures and gas atmospheres. This allowed the effect of the laser intensity on the target to be observed under different processing conditions.

4.4 Dye Laser Resonance Absorption Imaging (DLRAI)

DLRAI allows one to image specific absorbing atoms by shining a laser, tuned to an absorption band, in the atom and then monitoring the transmitted laser light. This is especially useful in imaging the temporal evolution of a laser-induced plasma as it propagates away from the target since individual species within the plasma can be followed (Gilgenbach et al. 1991, Ventzek et al. 1992).

Figure 4.5 shows the experimental set up (Pinho et al. 1997) for imaging individual species ablated from an aluminum target using a KrF (248 nm) excimer laser. (The experimental set up was part of our German-Canadian collaboration program and is

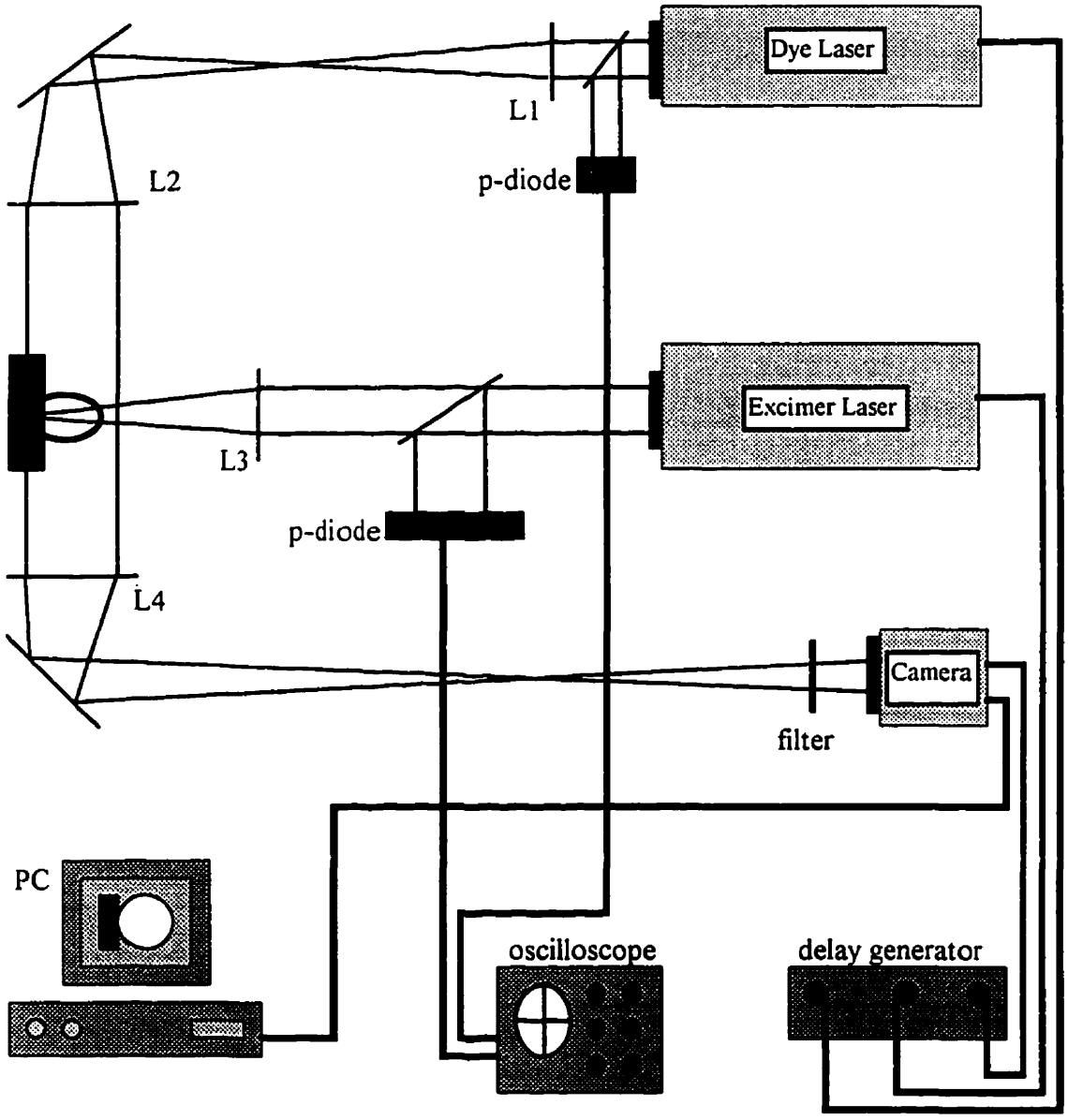

Figure 4.5. DLRAI experimental set up for tracking individual species within a laser induced plasma plume (courtesy of IFSW, Stuttgart, Germany).

owned by the IFSW in Stuttgart, Germany). The beam from the excimer laser (EMG 203 MSC λ = 248 nm, FWHM = 30 ns) was first masked and then projected onto an Al target by an imaging lens L3. This is similar to the laser focussing system in section 4.2 and is necessary for obtaining a symmetrical plasma formation. The magnification of the mask produced a 190μm spot at the target while the laser intensity could be varied from 1.0×10^{12} Wm^{-2} to 1.5×10^{13} Wm^{-2} with a dielectric plate. The imaging system consisted of a nitrogen laser pumped dye laser (LTB UDL301) whose output was expanded and collimated with lenses L1 and L2 to uniformly illuminate the plasma as shown in the figure. Since this was a Schlieren configuration both absorption of the dye laser and also discontinuities such as shock waves and contact fronts due to density changes could be detected. A third lens imaged the centre of the plasma on a high speed CCD camera with a resolution of 5 ns. The camera image was then stored in a PC.

The dye laser had a spectral width of 0.05 nm and a pulse FWHM of 500 ps. The wavelength could be varied from 390 nm to 690 nm but was usually set at 394.4 nm which corresponds to the aluminum ground state transition $3^2P_{1/2}$-$4^2S_{1/2}$. This transition was chosen since most of the neutral Al vapor was in its ground state. Detection of other species such as ions was difficult due to continuum emission since even with a narrow bandpass filter in front of the detector plasma emission was greater than any absorption by ions. This limited this type of experiment to neutral particles only.

To control the delay between the excimer laser and the dye laser, a digital delay generator was used to trigger the lasers and the CCD camera. With appropriate delay times, the time interval between the excimer and the dye laser pulse could be varied with a

minimum delay of 5 ns after the start of the laser pulse. Accurate measurements of delay time was obtained using a pair of photodiodes in conjunction with an oscilloscope. The delay was typically between 30 ns and 1 μs. Difficulties arose in going to shorter times since the plasma was too small to be imaged while increasing the magnification just decreased the intensity so that the images were too dark. Also, the plasma emission intensity was too large to observe any absorption by neutral material.

4.5 TOF Mass Spectroscopy of Plasma

In order to study the mass distribution of different species in the plasma as well as their respective energies, a TOF mass spectrometer was designed and constructed to fit on the high vacuum chamber as discussed in section 4.1.

A typical TOF mass spectrometer consists of an ionization source, an ion acceleration stack, and deflector plates to deflect them if necessary. Accelerated ions enter a field free region of known length over which they travel to a microchannel plate detector. This detector measures the particle flux which can be observed on an ocsilloscope as a function of time. If qV is the energy acquired by an ion where q is the charge and V the voltage of the acceleration stack, then the kinetic energy of the ion of mass m is,

$$\frac{1}{2}mv^2 = qV \tag{4.3}$$

If the field free region has a length D then the time-of-flight is related to the mass of the ion by,

$$t_{TOF} = \sqrt{\frac{m}{2qV}}D \tag{4.4}$$

Including the time that the ion spends in an acceleration stack with length d gives the total flight time as,

$$T_{TOF} = (D + 2d)\sqrt{\frac{m}{2qV}} \tag{4.5}$$

and is the basic method of determining ion mass. Different masses correspond to different times and thus a mass spectrum is produced.

For the experiment, the ions were formed by ablation of a metal target as shown in figure 4.6. The laser pulse irradiated the target at a 45 deg angle as not to interrupt the flow of material into the acceleration stack. The acceleration stack consisted of the target holder and 4 additional wire mesh plates. The bias on each plate differed from the next by 1 KV with a total acceleration potential of 4 KV over a length of ~ 6.5 cm. Following the acceleration stack are 2 deflector plates which can be used for steering the ions toward the detector or deflecting them away from the detector. After acceleration, ions enter the drift tube which has a length of 88.8 cm and strike the MCP detector. The MCP is a dual chevron type with one end at -2 KV and the other end grounded. The gain of the MCP is 10^7. The output of the MCP was recorded on a 150 Mhz LeCroy digital scope. The entire system must be kept at high vacuum due to the large fields and the nature of MCP

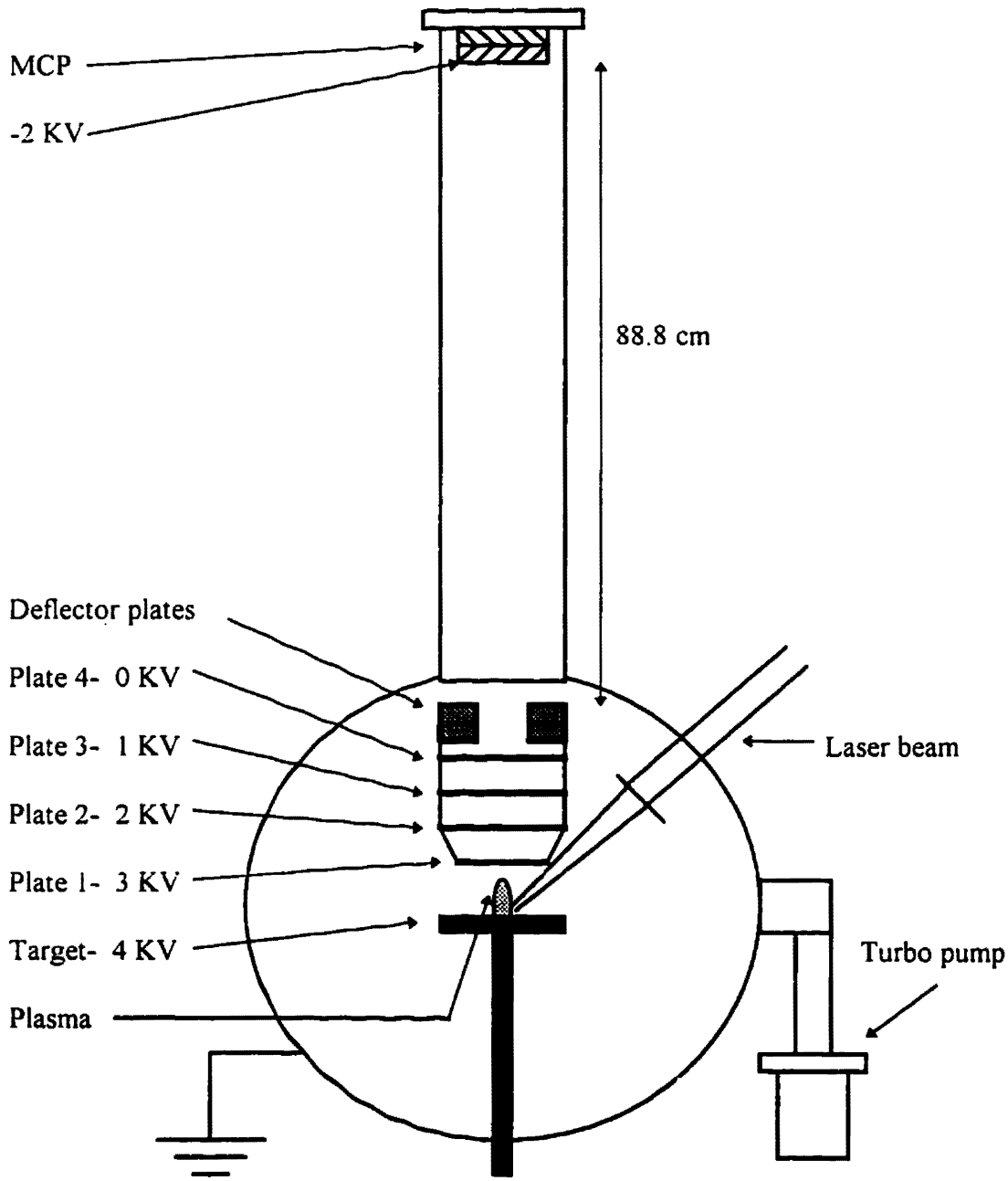

Figure 4.6. TOF experiment set up showing the different components and different regions that the ions travel through.

detectors. This was provided by a 250 Ls^{-1} turbo pump which could pump the high vacuum chamber and the TOF tube to ~ 5×10^{-7} Torr.

The design of the TOF mass spectrometer with the target at 4 KV ensures that ions formed in the plasma do not recombine with electrons which would degrade the signal. Any ions formed will be rapidly accelerated toward the detector while electrons will be accelerated back to the target. Since the MCP operates at -2 KV this will further prevent the detection of any stray electrons that drift into the field free region. The spectra recorded will then consist only of ions and neutral particles.

To find the mass of an ion, equation 4.5 can be used after several assumptions. However, several assumptions were made in deriving 4.5. The first assumption is that all ions are formed at the target surface. Since the ablation is very rapid (the length of the laser pulse is 60 ns), it is safe to assume that all ions will form in a region very near the target surface during the laser pulse. This region is typically < 1 mm based on measured expansion velocities of excimer laser ablated metals (Gilgenbach et al. 1991) and is much smaller than the acceleration stack length d so that this will introduce little error into the time-of-flight. The second assumption is that all the ions form at the same time but this is not true since the laser pulse is 60 ns long. Since typical flight times are in the microsecond range, however, this assumption is valid. The third assumption is that the initial energy of the ions gained from the interaction with the laser is much smaller than that gained by acceleration. Typical ion energies upon laser ablation of metals are 1 - 5 eV (Dreyfus et al. 1986) while the acceleration stack accelerates ions to 4000 eV so that the

effect on time-of-flight is minimal. The final assumption is that the field is uniform in the acceleration stack which may not be entirely accurate.

These four effects will produce broadened peaks as well as slight peak shifts, and will therefore limit the resolution of the TOF mass spectrometer. From equation 4.5 the resolution of the TOF is,

$$\frac{\Delta m}{m} = \frac{2\Delta t}{t} \tag{4.6}$$

where Δt is any shift in flight time due to the above uncertainties. Analysis of these errors yields a limiting resolution of ~ 0.02 so that for Al with an atomic mass of 27, $\Delta m = 0.54$. Therefore a resolution of less than 1 AMU can be obtained.

4.6 Optical Spectroscopy and Scattering

The optical spectrum of the plasma was important in identifying species not observed in TOF spectra and also for determining the amount of ionization present in the plasma. As well, in situ scattering experiments were incorporated to examine the presence of clusters in the plasma.

Figure 4.7 shows a block diagram of the experiment. Light is gathered from the plasma at a 90° to the laser axis with a 5 cm Schmidt telescope and coupled into a fiber-optic cable. The use of a telescope eliminates chromatic aberrations at the fiber-optic cable. The focal spot size of the telescope was 200 μm which approaches the dimensions of the

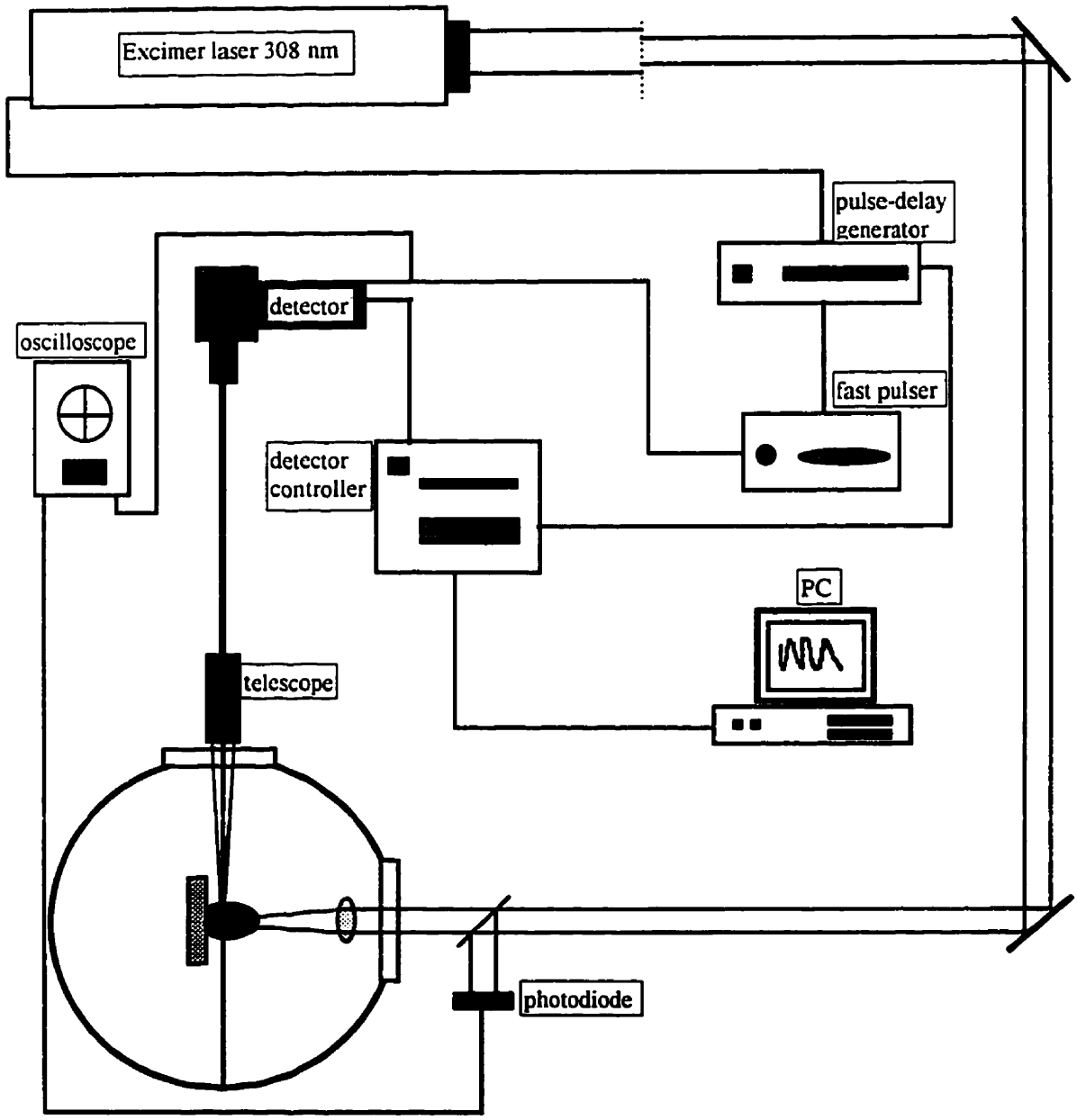

Figure 4.7. Experimental set up for performing optical emission and scattering experiments on the plasma.

plasma (see chapter 3) and precludes any attempt to obtain emission from different parts of the plasma. This could not be avoided due to constraints on the mirrors in the telescope. Another problem is that the telescope cannot view a homogeneous part of the plasma as the edges of the plasma are in the field of view as shown schematically in figure 4.8a. This problem can be partially rectified through increasing the laser spot size on the target to 350 μm. This also allows for better positioning of the telescope focus in the center of the plasma. Focussing of the telescope in the plasma is achieved using a He-Ne laser to align the focus with the plasma.

The light gathered by the telescope is coupled fiber-optically into a gated (10 ns) optical multichannel analyzer (OMA) consisting of a detector controller (EG&G M1461) and a detection unit (EG&G M1420) telescope. The detection unit uses a grating to select wavelengths between 200 and 700 nm. The diffracted light cone strikes a silicon photodiode array converting the photons to electrons which are then amplified by a MCP intensifier and transmitted to a fiber-optic coupled phosphor screen with 1023 channels. Each channel corresponds to a different wavelength. In this way, the detector can sample more than 1 wavelength at a time unlike the conventional method of scanning with the grating. The maximum allowable wavelength range ~ 100 nm.

The detection system operates in a gated mode and is controlled by a pulse/delay generator and a pulsing unit. In operation the pulse/delay generator fires the laser and then after a user selected delay, switches on the fast pulser and the detector controller. The

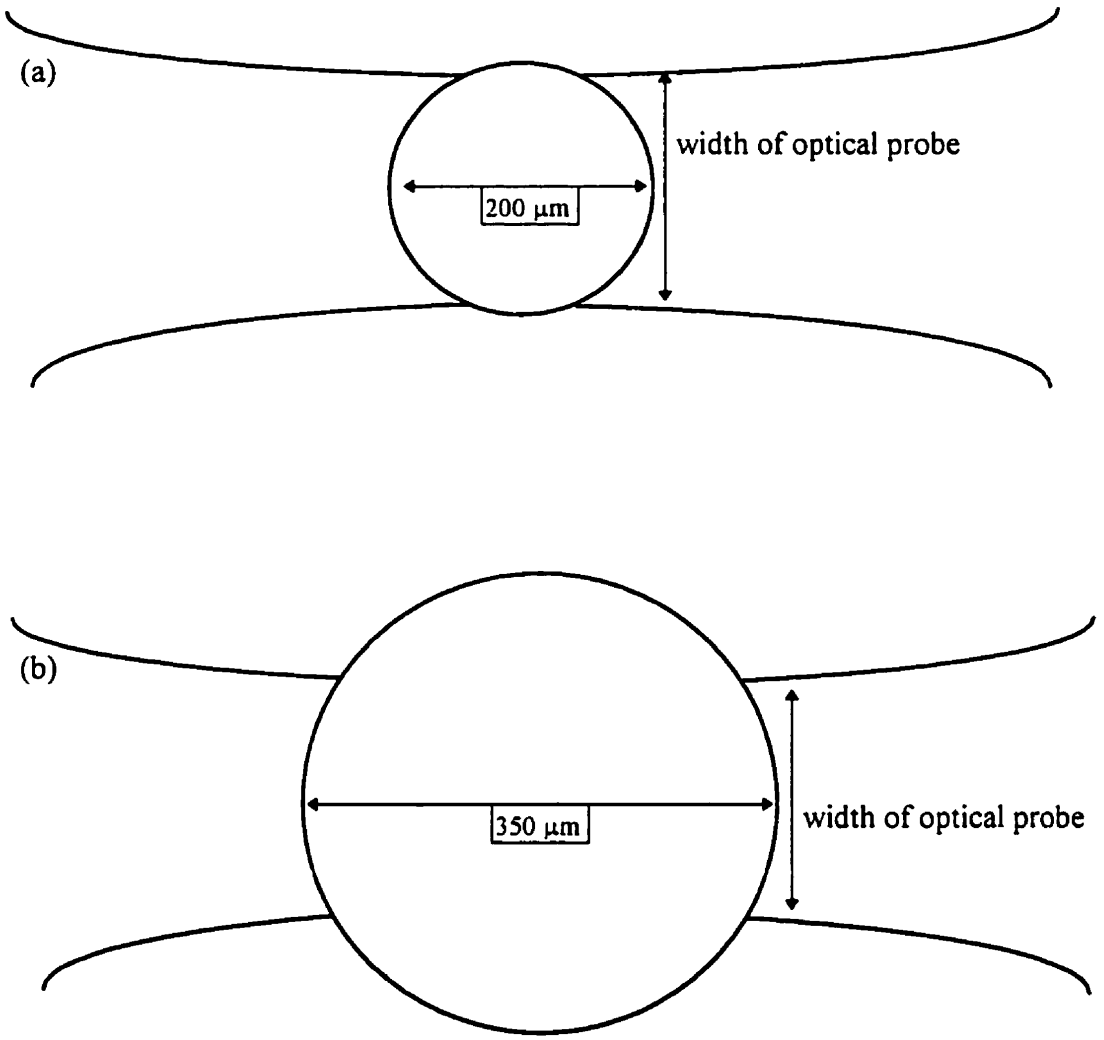

Figure 4.8. a) Focus of telescope compared to the plasma when the laser spot size is 200 μm. b) Same as a) but with a laser spot size of 350 μm.

pulse generated by the fast pulser activates the detector unit for 10 ns. The detector controller then downloads the detector output and plots it on a computer. The delay between the laser and the activation of the detector is measured on a 150 Mhz LeCroy digital scope. This method of operation allows spectra of the plasma to be recorded at 10 ns intervals during and after the laser pulse. The evolution of the plasma emission can therefore be followed for the entire laser pulse. In addition, the orientation of the telescope allows laser light scattered at 90° to be detected since the laser wavelength falls within the this range. This provides a unique method of performing two experiments in one and allows direct correlation between scattered light and plasma emission.

The output of the detector was wavelength calibrated using a mercury lamp. Two peaks of the mercury spectrum were used to calibrate each 100 nm section of the wavelength range 200 nm - 700 nm. In addition, the responsivity of the detector and the associated optics in the ultraviolet and visible range was recorded for a deuterium lamp (Hamamatsu ML1361) which had a known wavelength response. The detector response curve was then used to calibrate peak intensities in plasma spectra. After calibration, excitation temperature and electron densities in the plasma at different times could be calculated under different processing conditions.

4.7 Absorption of Laser Pulse in the Plasma

The most direct method of observing absorption of the laser pulse in the plasma plume is to physically measure the transmission of the laser pulse through the plasma. The difficulty in performing such an experiment is that the transmission of the laser pulse must

be measured along the laser axis normal to the target since this is the direction in which the laser normally interacts with the plasma plume. The procedure, developed by Schittenhelm et al. (1996), is to design a target with a small pinhole in the laser spot as shown in figure 4.9. When the laser fires, the material around the pinhole is ablated creating a plasma that envelopes the pinhole. The transmission of the laser pulse is then measured using a photodiode with 1 ns rise time located behind the target.

For this experiment to be successful, several constraints must be met (figure 4.9). First, the pinhole must be much smaller than the laser spot size. If it is too large then not enough ablation occurs around the pinhole and no laser absorption is observed. Second, the alignment of the laser beam directly over the pinhole is crucial. If the pinhole is too far to one side of the laser spot, then only the edge of the plasma, which is inhomogeneous, is over the pinhole. The transmission can be severely affected by this due to the decreased path length in the plasma. Third, a narrow bandpass filter must be used in front of the detector to isolate the laser line since continuum emission in the plasma can saturate any signal recorded by the detector making it impossible to detect absorption of the laser pulse.

For the experiment, the pinhole size used was 130 μm and was made in 100 μm Al foil using a micro-drill. The corresponding laser spot size was 300 μm leaving sufficient material around the pinhole to be ionized. Alignment of the laser beam was achieved by making the laser beam spot size the dimensions of the pinhole. The laser power was then attenuated so that no plasma would form. With the laser firing at a continuous rate the energy transmitted through the target was detected with a photodiode and

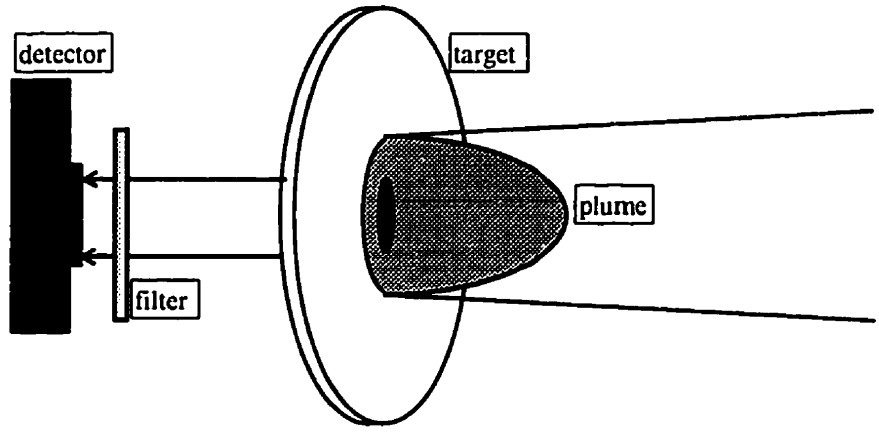

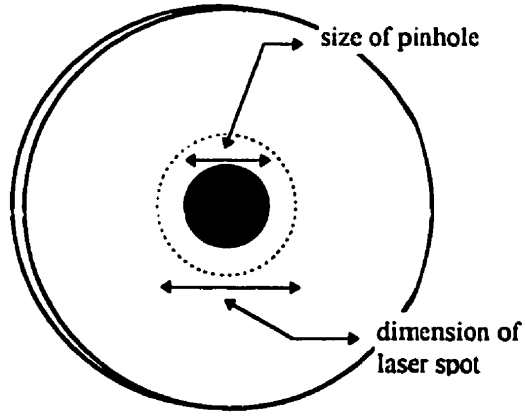

Figure 4.9. Experiment to measure the absorption of the laser pulse in the plasma plume.

monitored on a 150 Mhz LeCroy oscilloscope. The target was then moved until the transmitted energy reached a maximum. This ensured that the laser beam was centered on the pinhole.

To measure the transmitted laser energy the following procedure was used. First the laser beam (Lumonics HyperEX-400 laser, $\lambda = 308$ nm) was attenuated by a known amount in front of the target so that no plasma would form. This beam was used to measure the transmission characteristics of the pinhole and establish a baseline against which absorption of the laser pulse would be measured. The laser was then fired again unattenuated so that a plasma would form and absorb the laser energy. The transmitted beams were recorded on an oscilloscope and the amount of absorption was determined.

The experiments were performed for different laser powers and background gas pressures ranging from 1 atm N_2 to vacuum.

Chapter 5

Results

5.1 Ablation Depth Measurements

Ablation depths were measured for Al as a function of laser intensity for an excimer laser operating at 308 nm. The effects of the backing gases, N_2, Ar, and He and the background gas pressure on the ablation depth were also examined.

Figure 5.1 shows the first set of ablation depth measurements for Al with N_2 as the background gas at pressures from 1 atm to 0.001 atm. The threshold-like behavior of the laser intensity near 1.7×10^{12} Wm^{-2} arises since the laser energy must overcome thermal conduction and the latent heat of vaporization in the target before vaporization occurs. If the intensity is too low the target will remain below the vaporization point and no material is removed. The ablation depth measured reaches a maximum of 0.8 μm for an intensity of 8.3×10^{12} Wm^{-2} which is similar to that found by Kinsman (1991) and is much larger than that predicted from equation 2.15 since substantial melt removal occurs in the target. The

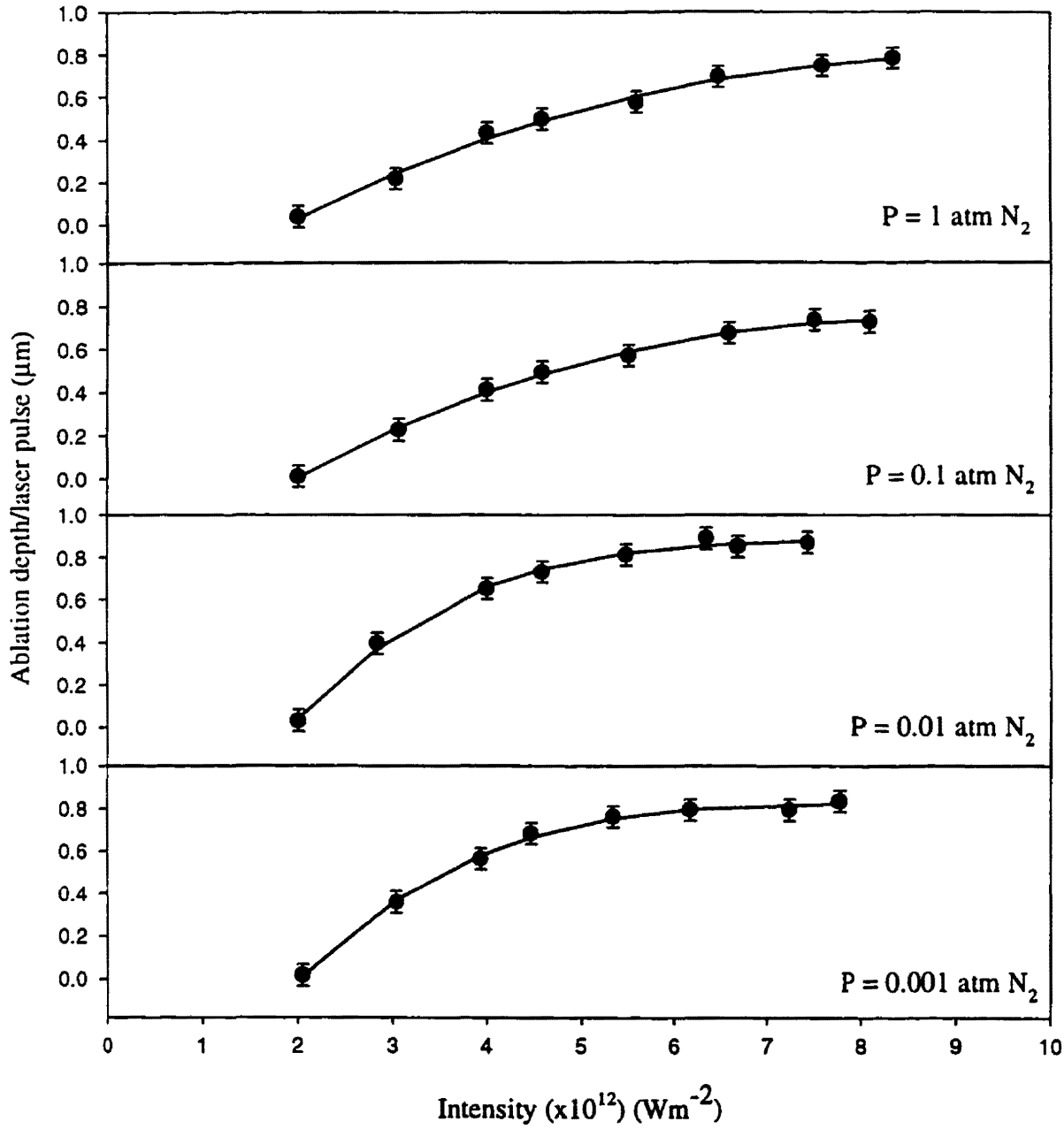

Figure 5.1. Ablation depth measurements for Al in N_2 gas of varying pressure. The wavelength of the laser is 308 nm and the FWHM = 30 ns. The curves are nonlinear indicating attenuation of the laser pulse in the plume

curves are non-linear and plateau at the maximum intensity reached of ~ 8.3×10^{12} Wm^{-2} for all four gas pressures. The increased non-linearity in the ablation depth at 0.01 and 0.001 atm is due to the difficulty in removing the debris. At high background gas pressure large amounts of debris were produced and after cleaning some debris remained affecting the ablation depth, while at the low background gas pressures almost no debris was left on the targets so that the effects of debris formation were insignificant. This resulted in increased accuracy for low pressure measurements.

The deviation from the expected linear increase in the ablation depth with intensity is a result of a decrease in the laser-target coupling efficiency due to plasma interaction. At laser intensities > 10^{13} Wm^{-2}, which were not attainable in the experiment, the ablation depth decreases as has been shown by Herziger and Kreutz (1984), and Poprawe et al. (1984). They found that the drilling efficiency for Al and Cu at 248 nm, which is proportional to the ablation depth, decreased towards a limiting value for intensities greater than 10^{13} Wm^{-2}.

At these high laser intensities (> 10^{13} Wm^{-2}), the interaction is expected to be absorption of the laser pulse by inverse bremsstrahlung processes as discussed in section 2.6 and 3.3. (line absorption at 308.22 nm due to the 3p-3d transition in Al was not present as discussed in Appendix A). The decrease in the ablation depth results from increased absorption in the plasma. At intermediate laser intensities (5×10^{12} - 10^{13} Wm^{-2}), the attenuation mechanism in the plasma is not very clear. The results of section 3.3 indicate that no inverse bremsstrahlung absorption occurs for this intensity range. This suggests that the attenuation might be produced by nanoparticle formation in the plasma

as proposed by Schittenhelm et al. (1996). The debris found around the targets contained particulate matter which suggests nanoparticle formation (4-10 nm). However, this was most likely produced long after the laser pulse (~ 2-10 μs) when the plasma had sufficiently cooled (Kelly et al. 1992, Kuper and Brannon 1992, Miyamoto et al. 1994). During the laser pulse, nanoparticle formation is sensitive to density and temperature fluctuations as discussed in section 2.6 and small changes in either of these quantities can severely affect the rate of nanoparticle growth (Lifshitz and Slyozov 1961, Callies et al 1997). A decrease in the background gas pressure decreases the plasma density and temperature as shown in section 3.4 thereby reducing the amount of supersaturation, Δ_s, in the plasma. The number of surviving nanoparticles (equation 2.26) would then be drastically reduced since nanoparticle formation exponentially depends Δ_s and T. A smaller nanoparticle growth rate in the plasma for lower background gas pressures would result in less attenuation of the laser beam due to scattering. The results shown in figure 5.1 indicate otherwise. The ablation depth reaches a maximum for a gas pressure of 0.001 atm indicating that the attenuation mechanism is quite effective at low gas pressures. This would seem to imply that the attenuation of the laser beam in the plasma is due to absorption.

Changing the gas composition had little effect on the ablation depth. The effect was to change the maximum ablation depth attained as shown in figures 5.2 and 5.3 for Ar and He respectively. Ar gas will increase the plasma pressure behind the shock wave due to its higher mass as shown in figure 3.20. This has the effect of increasing the amount of debris formation on the surface since the vaporized material is held closer to the target and the

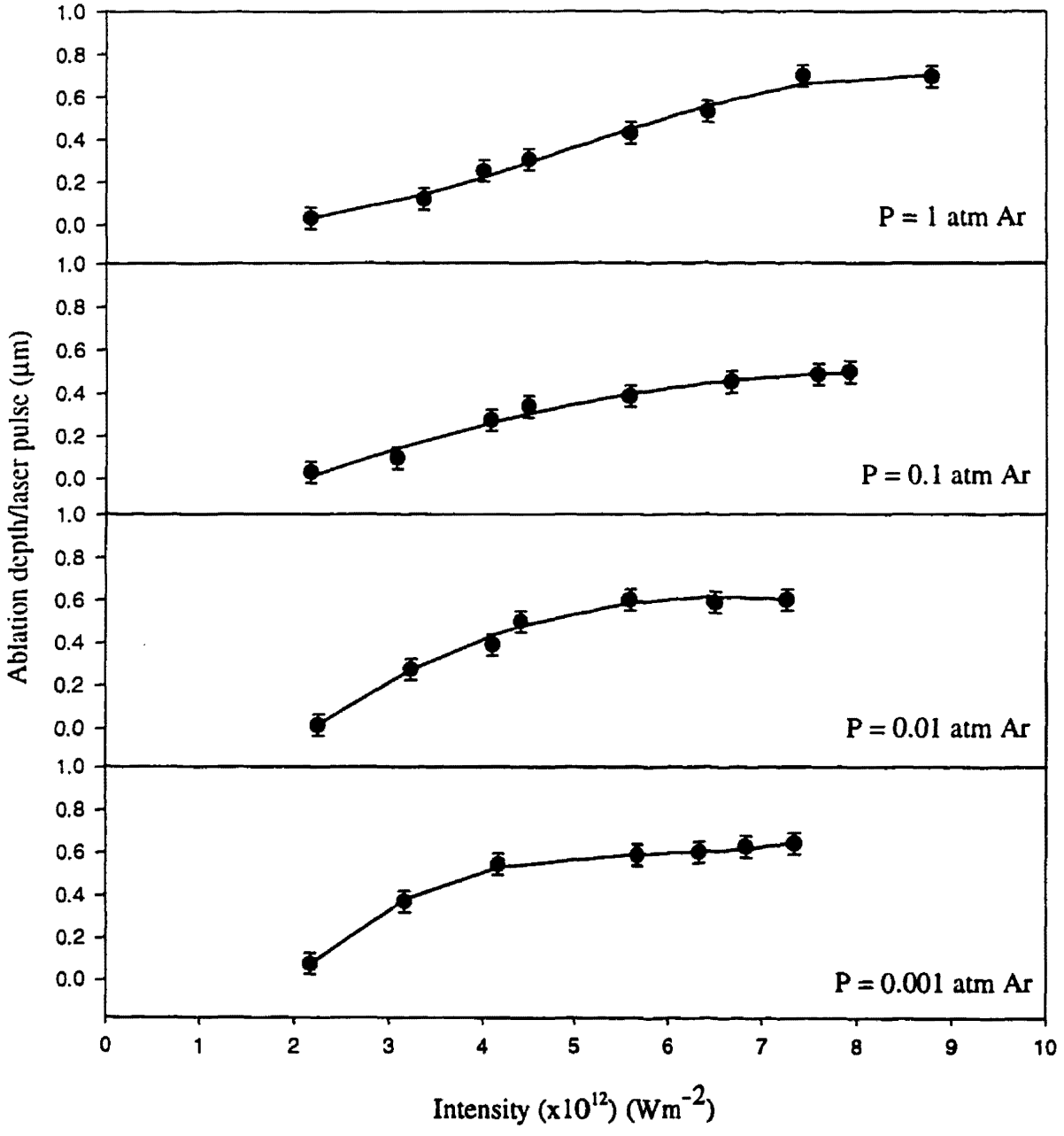

Figure 5.2. Ablation depth measurements for Al in varying Ar pressures. The wavelength of the laser is 308 nm and FWHM = 30 ns. The curves are nonlinear indicating attenuation of the laser pulse in the plume.

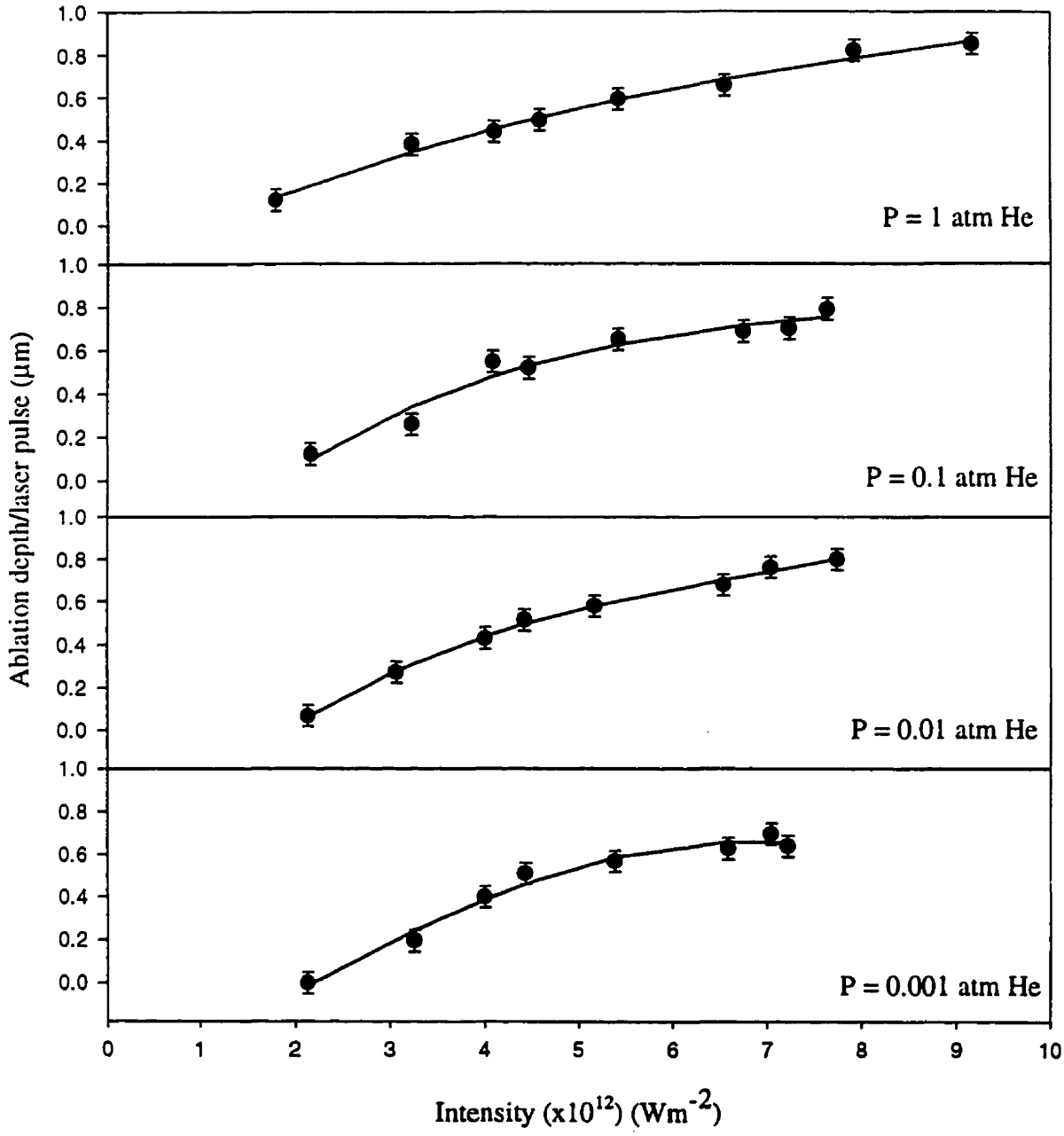

Figure 5.3. Ablation depth measurements for Al in varying He pressures. The laser wavelength is 308 nm and FWHM = 30ns. The curves are nonlinear indicating attenuation of the laser pulse in the plume.

ablation depth, therefore, decreases. In the case of He, the ablation depth is larger than in figure 5.2 since He has a lower mass resulting in less debris. In both cases, attenuation of the laser pulse was observed at the lowest gas pressure of 0.001 atm indicating that scattering by nanoparticles may not be very significant at attenuating the laser beam.

5.2 Imaging of the Plasma Plume

The Al plasma plume created using 248 nm laser radiation was imaged using dye laser resonance absorption imaging (DLRAI). This method allows a particular species in the plume to be followed and also allows the structure of the plasma plume to be studied. The species imaged was neutral Al. Images were obtained as a function of laser intensity and N_2 gas pressure.

Figure 5.4 shows the evolution of the plasma plume at a laser intensity of 1.2×10^{13} Wm^{-2} and a background gas pressure of 1 atm. The dye laser was tuned to the 394.4 nm absorption line for ground state Al. These images are dark because the magnification of the plume had to be set to 75 in order to resolve detail which decreases the intensity of the dye laser on the camera and results in the dark images. For times shorter than 50 ns the images were simply too small or too dark to be useful. This limits DLRAI times in excess 50 ns which is near the end of the laser pulse.

No absorption can be seen in the figure and the only feature present is the shock wave. The lack of absorption, which would be represented by a dark area behind the shock wave, indicates that the vapor/plasma must be sufficiently ionized, otherwise most of the vapor would be in the ground state and absorption would occur.

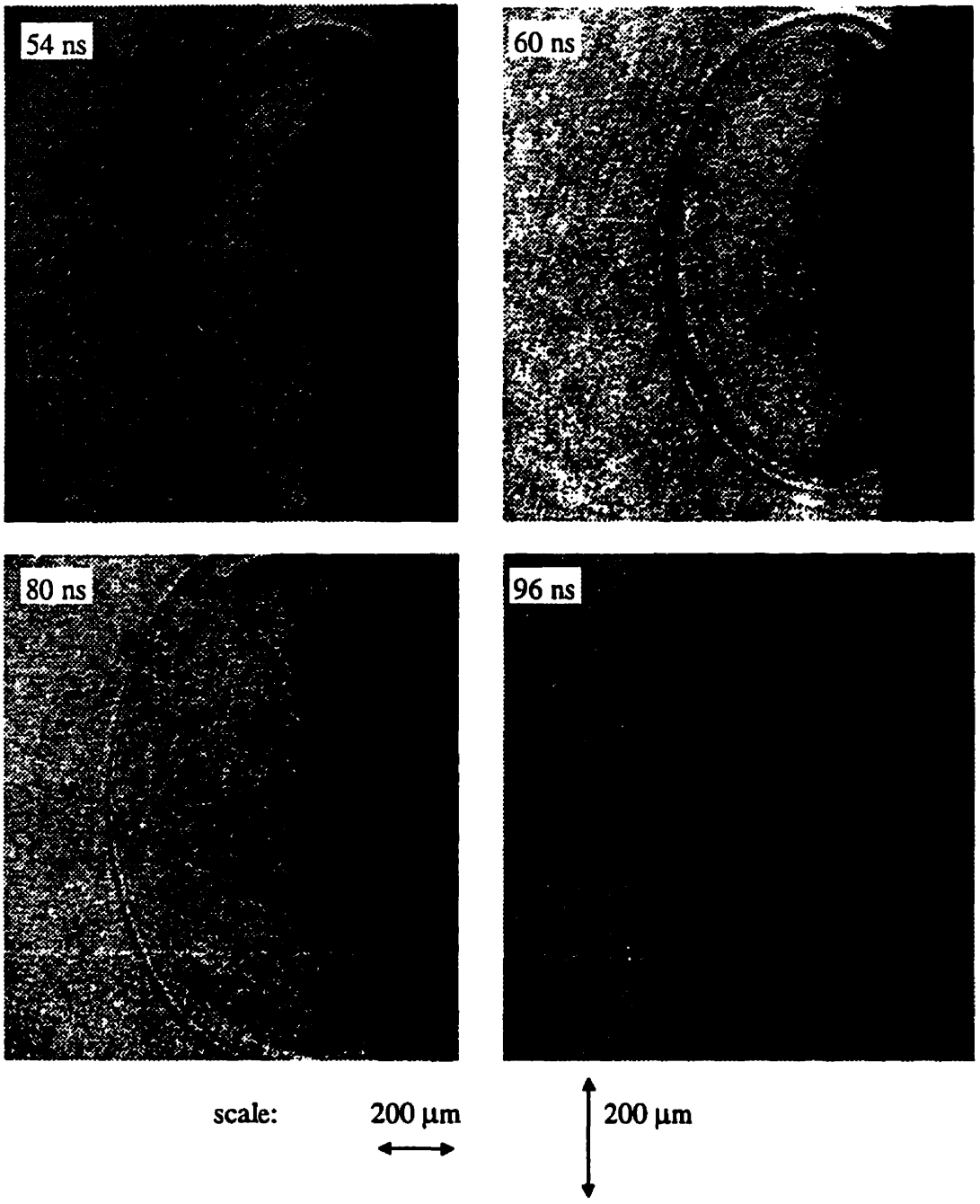

Figure 5.4. Dye laser resonance absorption images at different times after the laser pulse at a laser intensity of 1.2×10^{13} Wm^{-2} and a N_2 gas pressure of 1 atm. The wavelength of the laser is 248 nm and the beam spot size is 200 μm. No absorption of the dye laser pulse is shown indicating that the plume is ionized

Plasma emission is not easily seen since the dye laser intensity is greater than the plasma emission intensity at this magnification. If the magnification is reduced to 20 then the intensity of the dye laser on the camera increases (figure 4.5). This allows the intensity of the dye laser to be decreased relative to that of the plasma emission without sacrificing the illumination of the plasma. Results for delays $\geq$ 140 ns are shown in figure 5.5 at the lower magnification. At 140 ns the lower magnification indicates clearly that the plasma is emitting and no absorption is observed. As time increases, the plasma begins to cool and absorption is observed around the edges of the plume indicating the presence of neutral Al. The plasma does not completely neutralize until ~ 730 ns after the excimer laser pulse.

At a laser intensity of 4.7×10^{12} Wm^{-2}, the plasma neutralizes more quickly (figure 5.6) for the high magnification case. At 65 ns after the start of the excimer laser pulse, the dye laser is beginning to be absorbed suggesting the presence of neutral Al vapor. At earlier times no absorption was noticed although the plume was difficult to distinguish. This implies that the plasma is still sufficiently ionized during the laser pulse that absorption of the dye laser is not observed. After 93 ns, absorption has increased as indicated by the increased darkening. At later times (figure 5.7), the evolution of the plume is similar to figure 5.5 but the shock wave is closer to the plume and has a slower propagation speed.

These results are in agreement with ablation depth measurements. At low laser intensity (figure 5.6), the plasma neutralizes by the end of the laser pulse whereas at high laser intensity (figures 5.4 and 5.5), the plasma remains ionized until ~ 300 ns after the laser pulse. This implies that the plasma is much hotter at 1.2×10^{13} Wm^{-2} than at 4.7×10^{12}

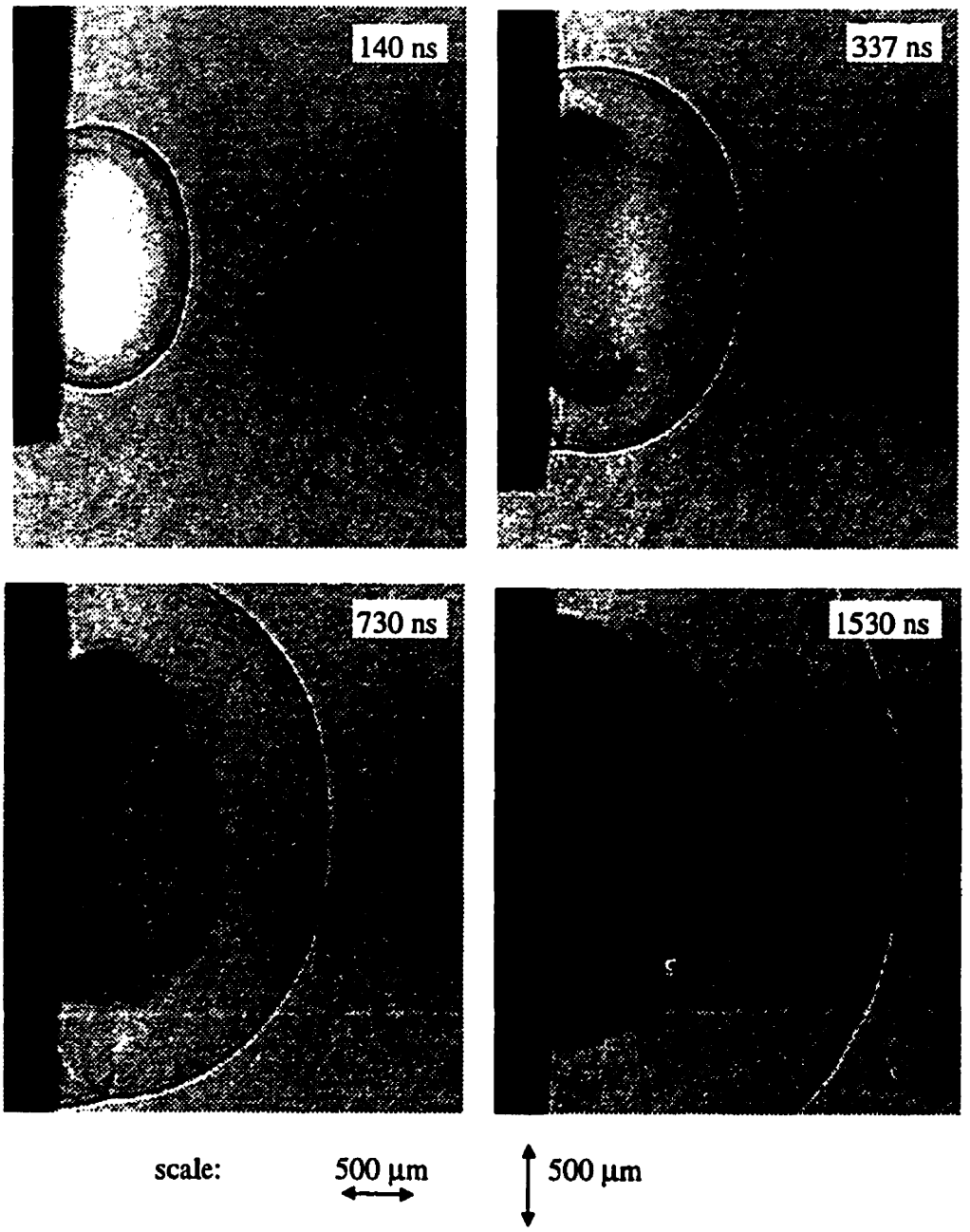

Figure 5.5. Dye laser resonance absorption images of the Al plasma at a laser intensity of 1.2×10^{13} Wm^{-2}, magnification of 20, and N_2 gas pressure of 1 atm. The laser wavelength is 248 nm and the beam spot size is 200 μm. The images are reversed because they were taken on the opposite side of the target.

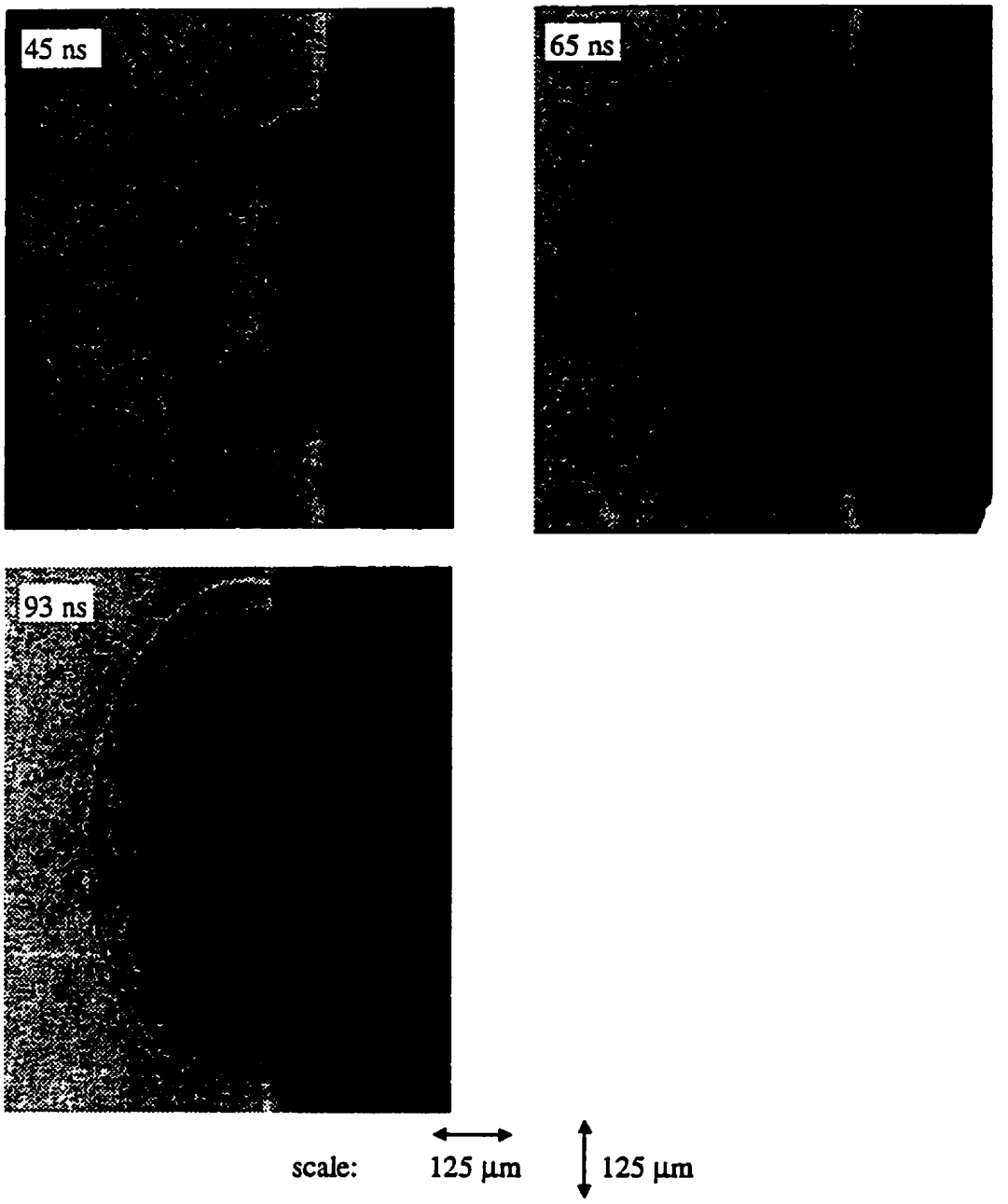

Figure 5.6. Dye laser resonance absorption images at an intensity of 4.7×10^{12} Wm^{-2} and a gas pressure of 1 atm N_2. The wavelength of the laser is 248 nm and the beam spot size is 200 μm. At 65 ns the plasma is beginning to neutralize.

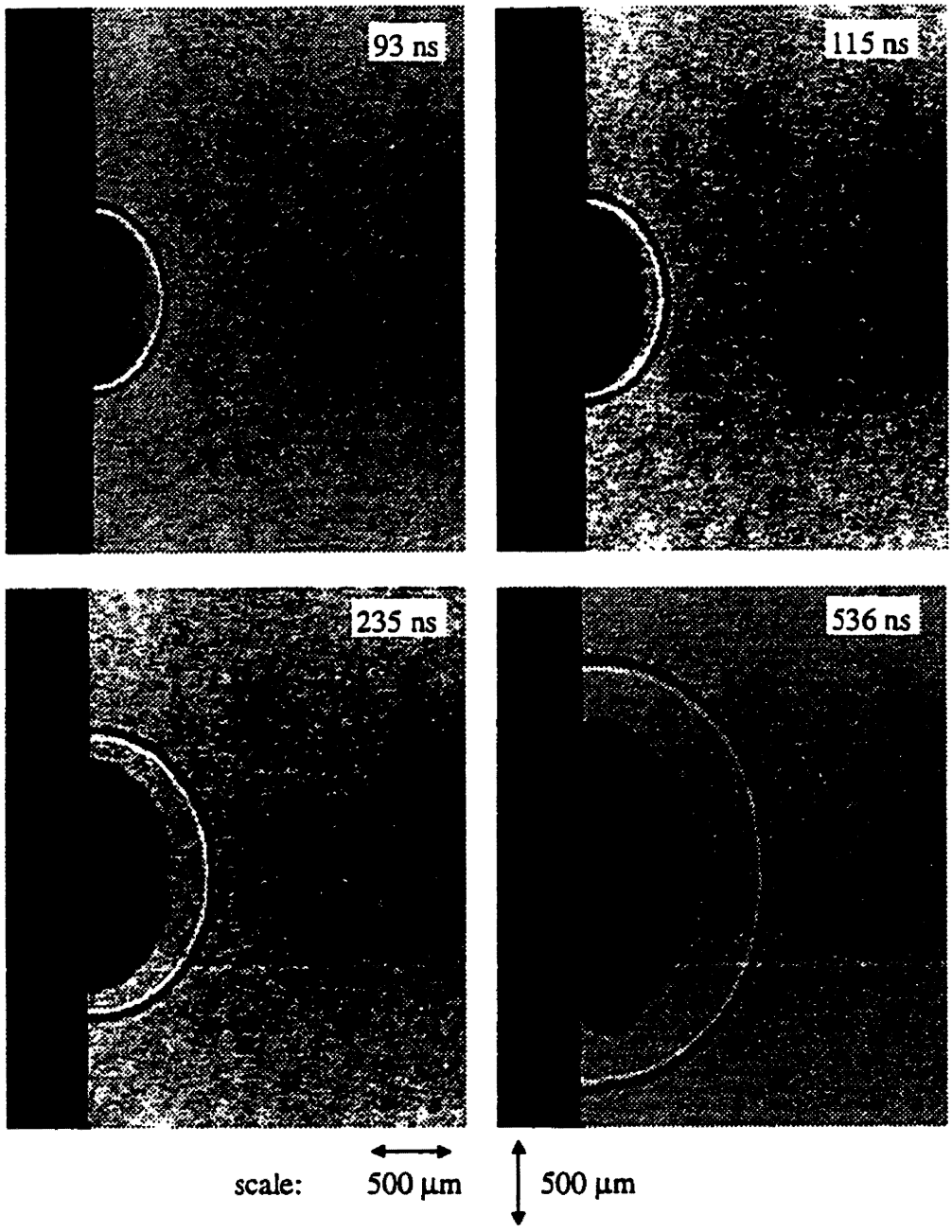

Figure 5.7. Dye laser resonance absorption images at an intensity of 4.7×10^{12} Wm^{-2}, magnification of 20, and an N_2 gas pressure of 1atm. The wavelength of the laser is 248 nm and the beam spot size is 200 μm. At these late times the plasma is completely neutral.

Wm^{-2} and, therefore, can absorb the excimer laser more efficiently due to the higher electron density.

The same experiment was performed at a gas pressure of 0.5 atm to determine the effect of the background gas on the plasma. Figure 5.8 shows some results at an intensity of 1.2×10^{13} Wm^{-2}. The shock wave is not visible since it is weak and lies close to the expanding vapor as discussed in chapter 3. This results in a smaller vapor density in the plume and, therefore, a lower temperature. A plasma is, however, still formed but the images are very dark due to a low dye laser intensity. No absorption occurs at the times shown and neutral vapor was not detected until ~ 115 ns after the end of the excimer laser pulse. At 4.7×10^{12} Wm^{-2}, the vapor is neutral after ~ 34 ns as shown in figure 5.9.

Comparing these results to figures 5.4 and 5.6 indicates that at higher gas pressures the vapor is more easily ionized due to an increased vapor density and higher temperature behind the shock wave. This is in agreement with the simulations in chapter 3 and also agrees with the ablation depth measurements which show that, at low gas pressures, the laser pulse was still attenuated.

To gain insight into how the vapor/plasma becomes ionized, the DLRAI system was used to examine plasma luminescence. This was accomplished by switching off the dye laser and using narrow bandpass filters ($\Delta\lambda$ = 10 nm) to isolate specific wavelengths in the range 415 - 690 nm. Figures 5.10 shows the emission of the plasma at laser intensity of 1.2×10^{13} Wm^{-2} and for 1 atm of N_2 at times from 29 to 80 ns after the start of the laser pulse. The wavelength of the filter used was 450 nm, however, the plasma emission was

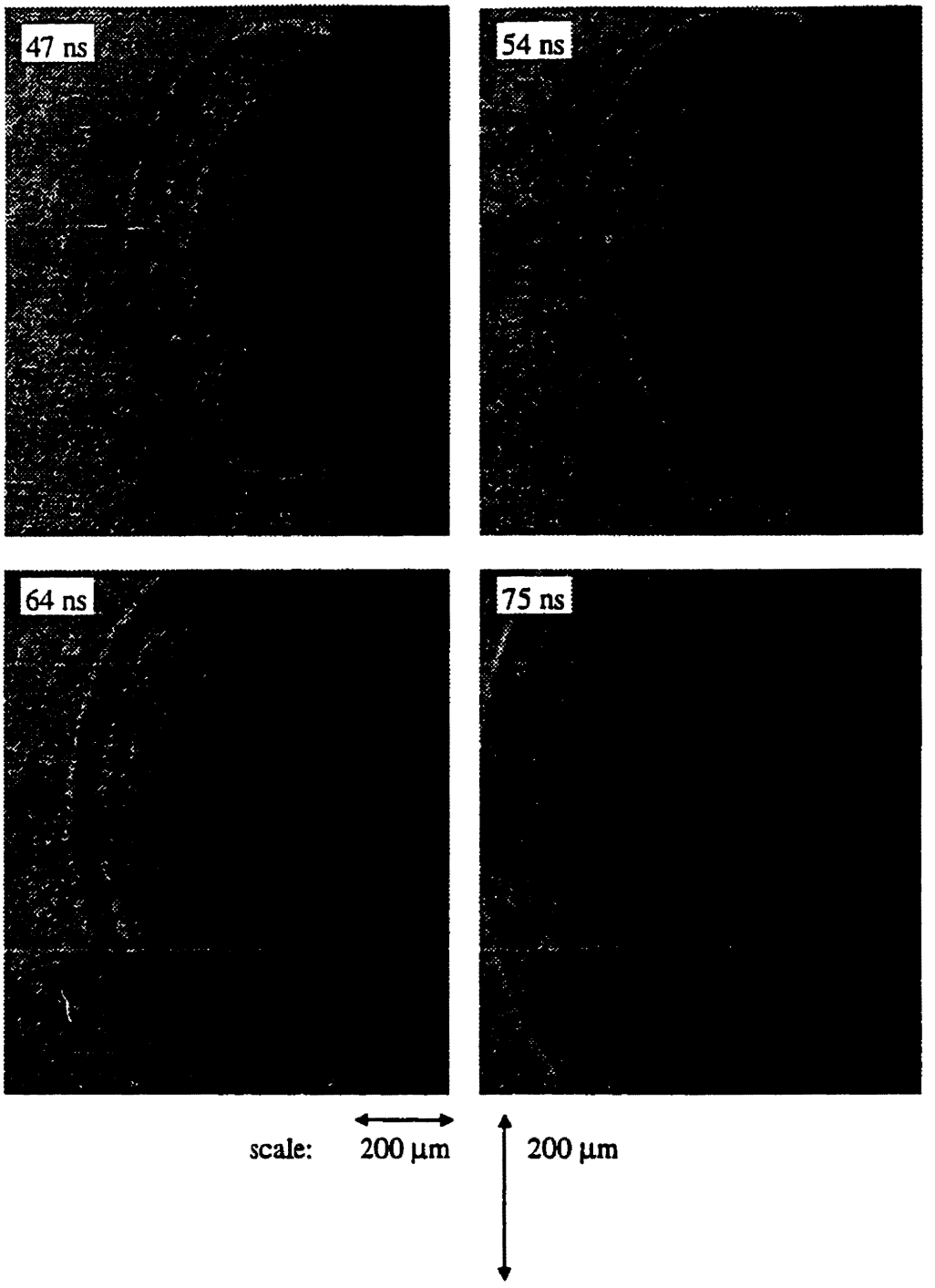

Figure 5.8. DLRA images at a background gas pressure of 0.5 atm of N_2. The laser intensity is 1.2×10^{13} Wm^{-2} and the wavelength is 248 nm. No absorption can be seen.

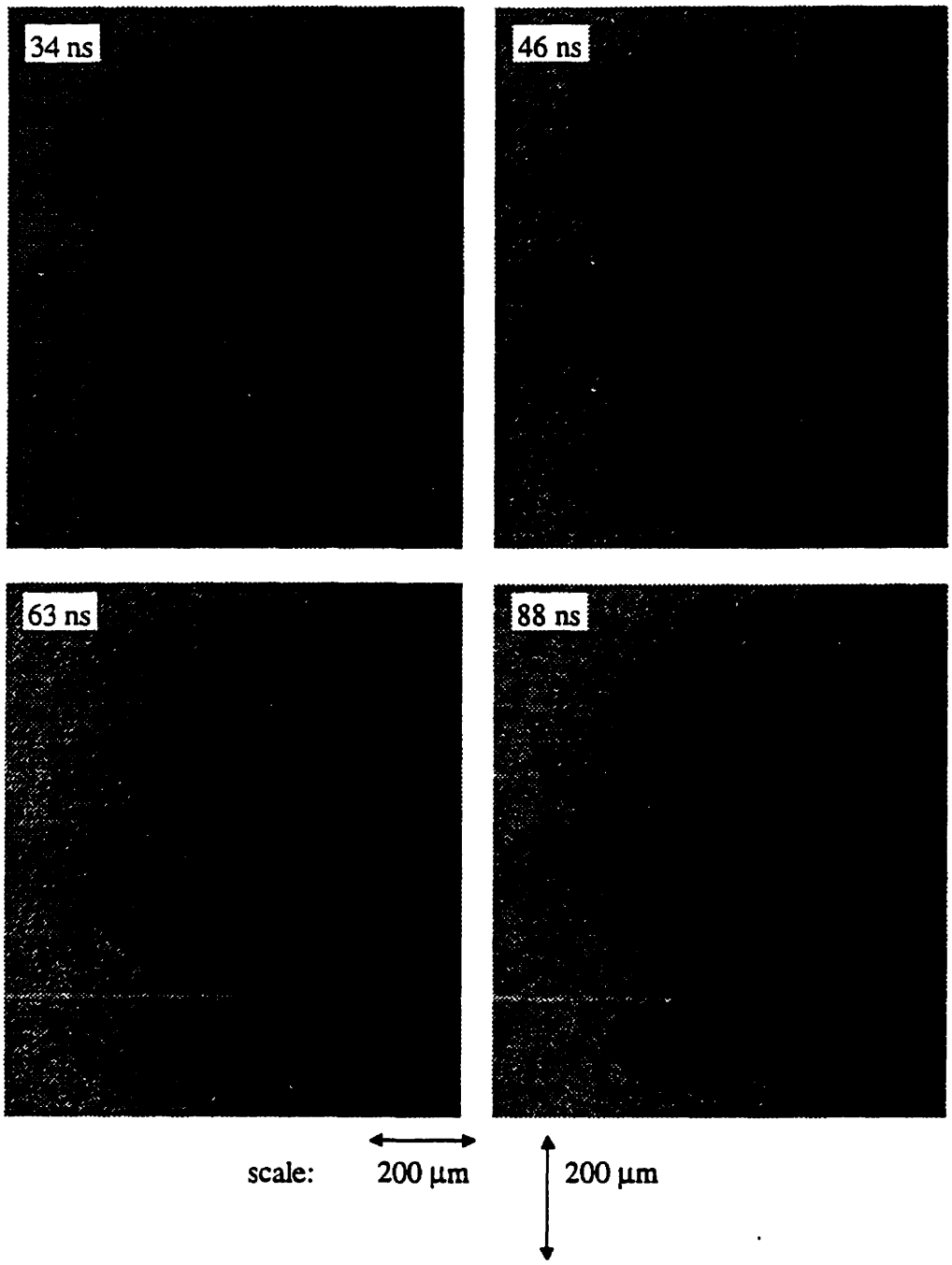

Figure 5.9. DLRA images at a background gas pressure of 0.5 atm of N_2. The laser intensity is 4.7×10^{12} Wm^{-2} and the wavelength is 248 nm. Absorption of the dye laser pulse begins after 30 ns.

observed throughout the entire filter range up to 120 ns after the laser pulse indicating the presence of continuum emission and therefore ionization of the vapor. The emission is concentrated in two regions: near the target surface and behind the contact front. The emission in front of the target is strongest at 29 ns corresponding to the peak of the laser pulse and completely vanishes at 63 ns at the end of the laser pulse. This suggests that the laser is capable of ionizing the vapor since the emission depends on the laser pulse length. The emission in the rest of the vapor appears as a "mushroom cloud" and extends out to the contact front. This can result from the ionized vapor at the target. The electrons have a much higher velocity than the corresponding ions and can, therefore, travel quite a distance in the plasma before collision. Since their thermal energy can be quite high, collisions can result in ionization and excitation of the vapor in the outer regions near the contact front. This is confirmed by measurement of the speed of the contact front in figure 5.10 as shown in figure 5.11. The front has a higher velocity during than after the laser pulse. The velocity is also much higher than predicted in the simulations for similar conditions which is due to acceleration of the contact front by the heated and ionized vapor near the target. The shock wave contains the plasma resulting in the hemispherical shape and this shock wave can also produce a high enough temperature at the contact front to sufficiently ionize the vapor (see chapter 3). After the laser pulse, emission is concentrated near the shock where the pressure and temperature are highest. Without any energy input the emission decreases and dissipates ~ 120 ns after the laser pulse.

Schittenhelm et al. (1998) have recently measured electron density under the conditions of figure 5.10 using interferometric techniques. They showed that the electron density in a

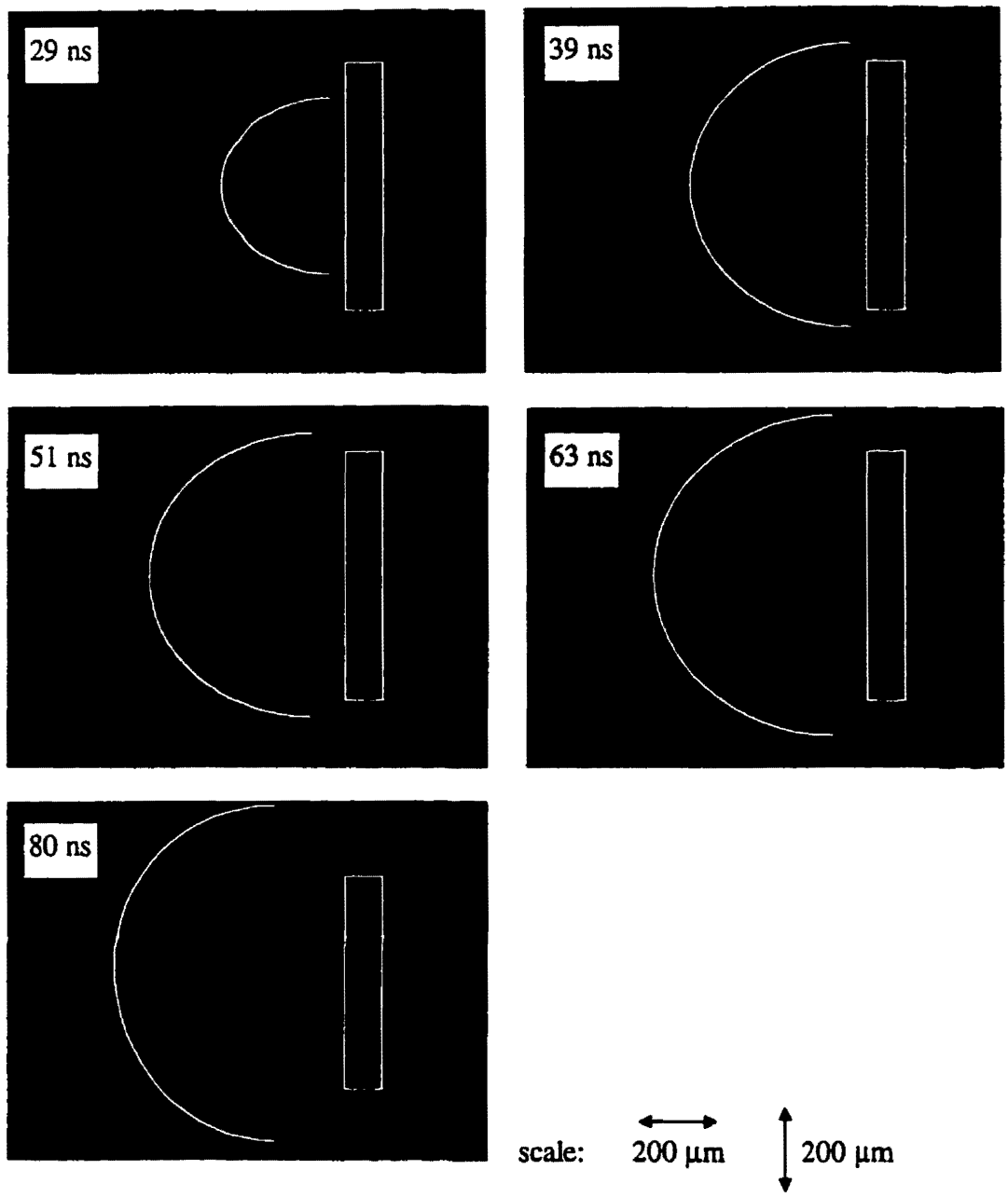

Figure 5.10. Plasma emission for a laser intensity of 1.2×10^{13} Wm^{-2} and 1 atm N_2. The wavelength of the laser is 248 nm. The filter used was 450 nm. Plasma emission can be seen near the target and behind the shock wave outlined in white.

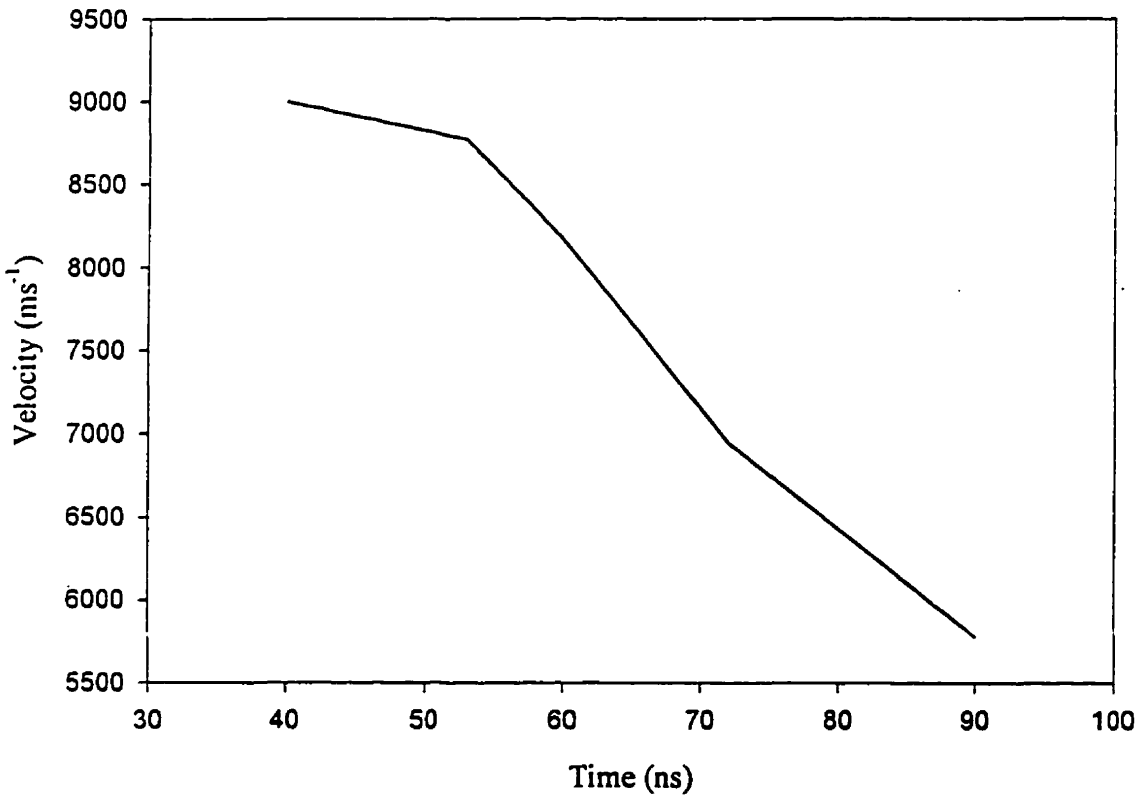

Figure 5.11. Velocity of contact front as a result of acceleration of the ionized vapor near the target. These measurements were taken from figure 5.10.

248 nm induced Al plasma exceeds 10^{26} m^{-3} near the target surface and is about 8×10^{25} m^{-3} in the contact front region at a laser intensity of 1.2×10^{13} Wm^{-2} and 1 atm of air as shown in figure 5.12. This corresponds to a strongly ionized plasma since the atomic vapor density is also ~ 10^{26} m^{-3}. If one assumes thermodynamic equilibrium with an atomic vapor density of 5×10^{26} m^{-3}, the corresponding electron temperature derived from the Saha equation (equation 2.21) using the values from figure 5.12 give T_e ~ 16000 K. To generate such a high temperature and electron density in the plume requires that the laser pulse directly heat the vapor/plasma. Since no resonant ground state transitions exist in Al at 248 nm (Section 2.6 and Appendix A), ionization must take place from excited Al as discussed in chapter 2. This process cannot initially create enough electrons for inverse bremsstrahlung absorption to absorb the laser pulse and heat the vapor/plasma (figure 2.9 and chapter 3), since the maximum electron density produced from these effects is only ~10^{24} m^{-3} at 10^{13} Wm^{-2} as shown in chapter 3. In addition, the shock does not produce enough compression to generate the degree of ionization required for significant inverse bremsstrahlung absorption (see chapter 3). This implies that a different laser heating mechanism must be present at 248 nm which heats the vapor sufficiently to produce the electrons required for inverse bremsstrahlung absorption. This should also be the case for the 308 nm laser used since there is not sufficient overlap with the 308.22 nm transition in Al (Appendix A).

The results obtained here suggest a different interpretation of the plasma structure observed by Callies et al. (1995). Originally it was assumed that the contact front was far back from the shock wave and was separated from the shock front by a region of ionized

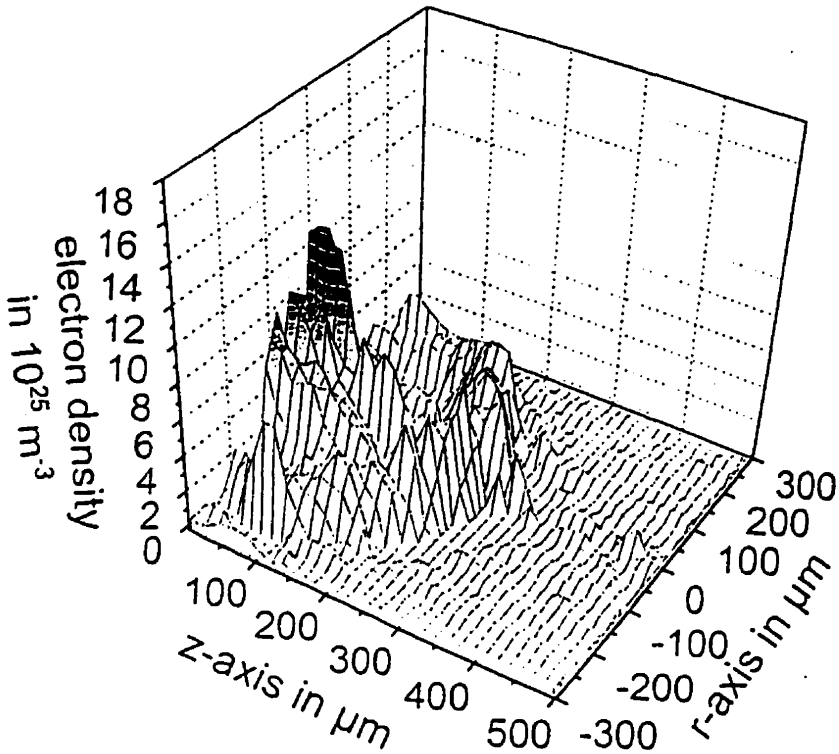

electron density in 10^{25} m^{-3}

16.8 -- 18.0		8.2 -- 9.5	
15.6 -- 16.8		7.0 -- 8.2	
14.4 -- 15.6		5.8 -- 7.0	
13.2 -- 14.4		4.6 -- 5.8	
11.9 -- 13.1		3.4 -- 4.6	
10.7 -- 11.9		2.1 -- 3.4	
9.5 -- 10.7		0.9 -- 2.1	
		0.0 -- 0.9	

Figure 5.12. Interferometric measurement of the electron density under the conditions of figure 5.10 at 36 ns after the start of the laser pulse. The target is located at r =0.0 and z=0.0 (Schittenhelm et al. 1998). Notice the very high electron density near the target surface.

background gas discussed in chapter 2. Figure 5.13 shows Schlieren photographs of the results in figure 5.10. When compared to images from DLRAI experiments, the contact front is seen to closely follow the shock wave. The turbulence at the shock front arises from absorption of the laser pulse at the contact front where the electron density is high. The two other discontinuities observed are within the vapor/plasma. A new schematic representation of the plasma structure based on the above results is presented in figure 5.14 and shows two new discontinuities, ND1 and ND2. ND1 is in the region of ionization just above the target surface where the strongest ionization occurs while the second discontinuity, ND2, occurs parallel to the target surface where there is little ionization (figures 5.12 and 5.13). The maximum ionization in this region is just 0.1 of that in the center over the target. Since these discontinuities correspond to a change in the index of refraction of the vapor/plasma, it is likely they are due to regions of the vapor/plasma that have a different vapor or electron density. This is confirmed by the corresponding refractive index plot of figure 5.12 (Schittenhelm et al. 1998) shown in figure 5.15. The sharp change in the refractive index at a distance of ~ 180 μm corresponds to ND1 and this is most likely produced by heated vapor in the laser spot which accelerates toward the contact front. Ionization in the contact front then causes expansion in two directions: radially and axially to the target. Along the laser axis, the contact front pushes up against the shock and pushes back down on the target causing the radial expansion ND2. The radial expansion of the contact front forming the "mushroom-like" emission in figure 5.10 creates a region above the target that has higher ionization than in intermediate layers creating a jump in the electron density and therefore the

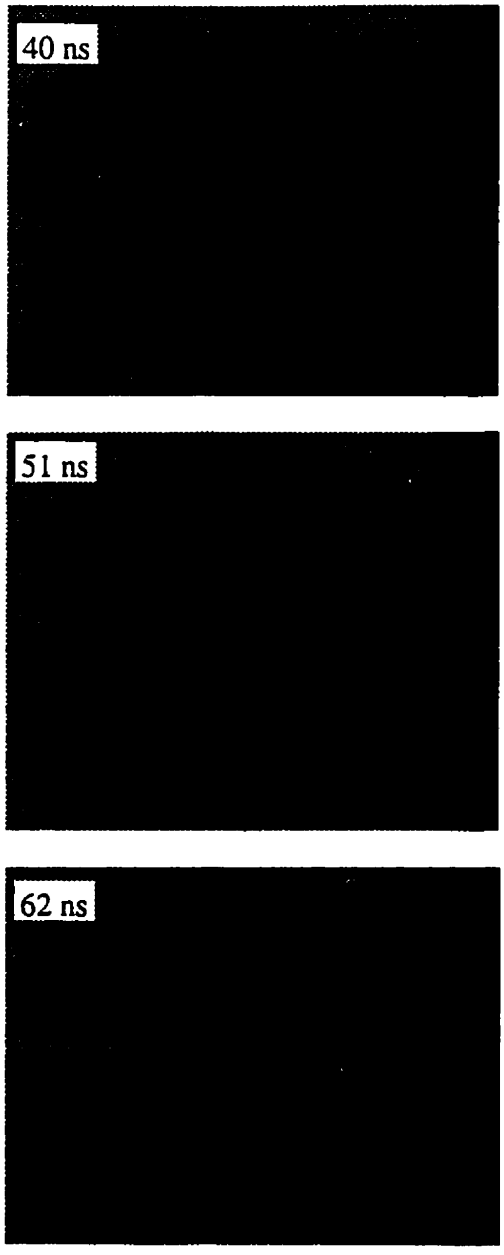

Figure 5.13. Schlieren photographs of the Al plasma structure for a laser intensity of 1.2×10^{13} Wm^{-2} and wavelength 248 nm. Several discontinuities are observed and presented in figure 5.14.

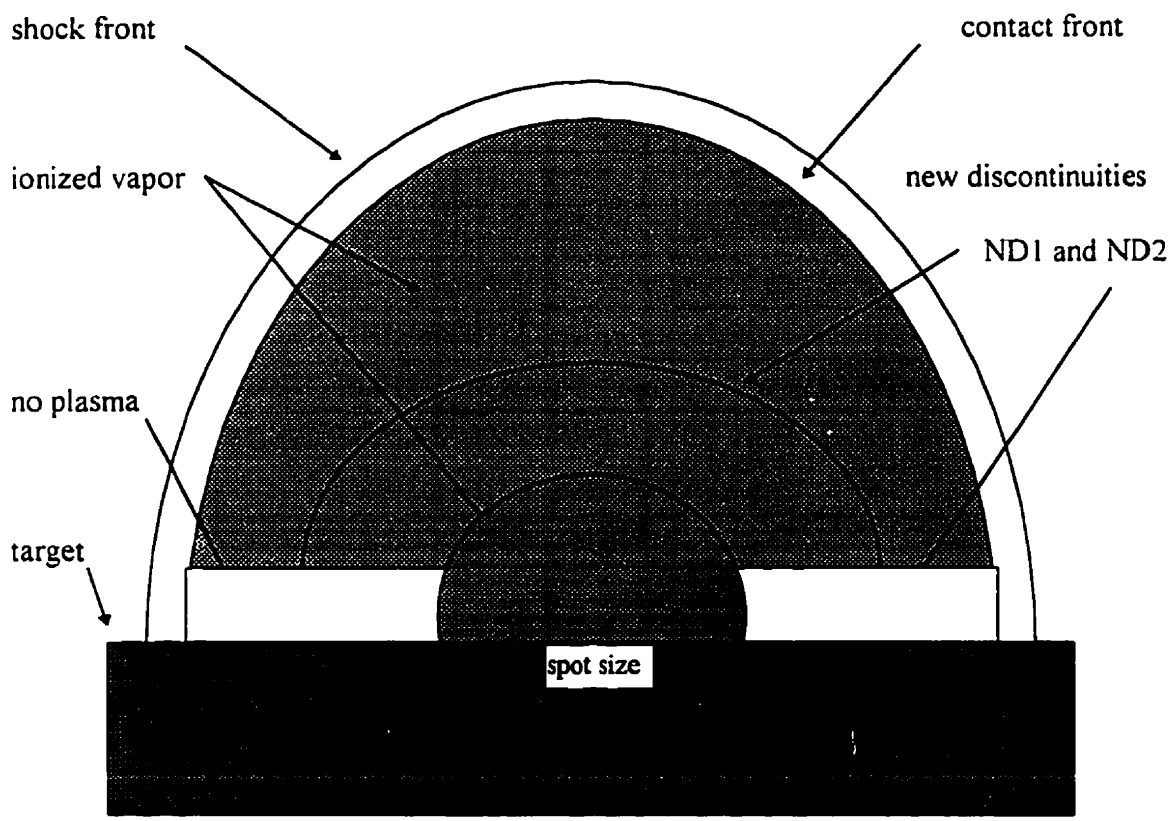

Figure 5.14. Model of plasma structure for excimer laser ablation of metals in the presence of background gas. ND1 and ND2 are two unidentified discontinuities present in figure 5.13. These are most likely due to refractive index changes in the plume.

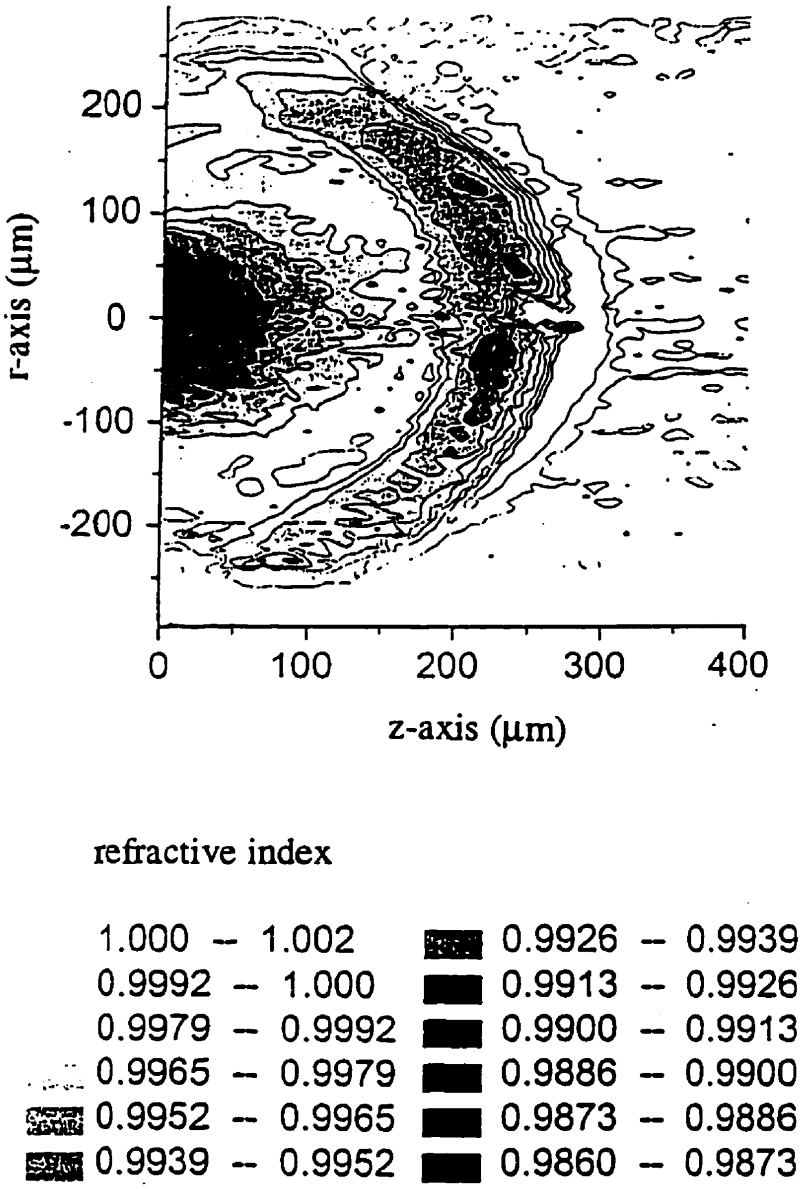

Figure 5.15. Refractive index distribution for the plot in figure 5.12 (Schittenhelm et al. 1998). The changes in the refractive index create the discontinuities observed in figure 5.13.

refractive index resulting in the discontinuity ND1. ND1 is not observed in weaker shocks since the propagation velocity is higher and the contact front density is lower resulting in a much smaller electron density behind the shock.

5.3 Mass and Velocity Distributions of the Ablated Material

Time of flight (TOF) mass spectroscopy was used to study the composition of ablated Al vapor using 308 nm laser radiation. This experiment required high vacuum conditions (section 4.5) and, therefore, the effects of background gases could not be examined. However, the information gained on mass and velocity distributions in the plume is important to how laser radiation interacts with the ablated material.

Figures 5.16 and 5.17 show TOF mass spectra for Al at 5 different laser intensities ranging from 2.4×10^{12} Wm^{-2} to 9.7×10^{12} Wm^{-2}. Each target was first cleaned with a few laser shots to remove any oxide and then 10 laser shots were averaged for each spectrum to eliminate the effects of fluctuations in the laser intensity. The first peak observed at 1.2 μs is due to atomic hydrogen which is present since Al is hydrophilic. This peak vanishes as the laser intensity decreases. These spectra also show aluminum oxide (AlO), water, oxygen, and magnesium which may be due to an impurity in the chamber.

The peaks of interest that are observed are due to Al^{2+}, Al^{+}, Al_2^{+}, and Al_3^{+}. At 9.7×10^{12} Wm^{-2}, Al^{+} and Al^{2+} have shorter flight times than predicted from equation 4.5. As the intensity decreases, the Al^{2+} peak decreases in intensity as expected and shifts to longer time. The Al^{+} peak, however, increases in intensity as it shifts to the theoretical flight time.

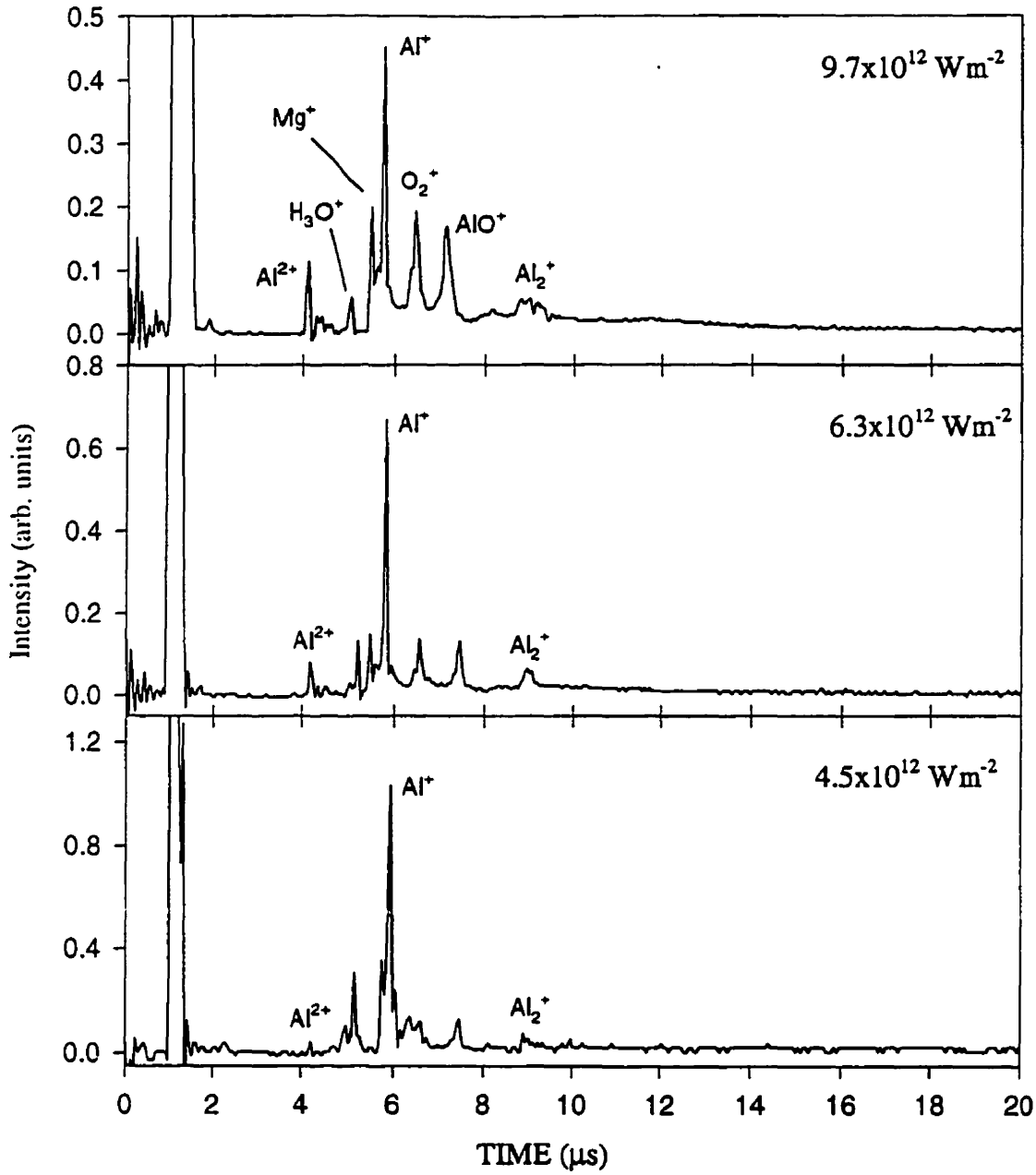

Figure 5.16. TOF spectra for the laser ablation of Al in vacuum at laser intensities 9.7×10^{12} Wm^{-2}, 6.3×10^{12} Wm^{-2}, and 4.5×10^{12} Wm^{-2}. The wavelength of the laser is 308 nm. Al^{2+} and Al^{+} are observed.

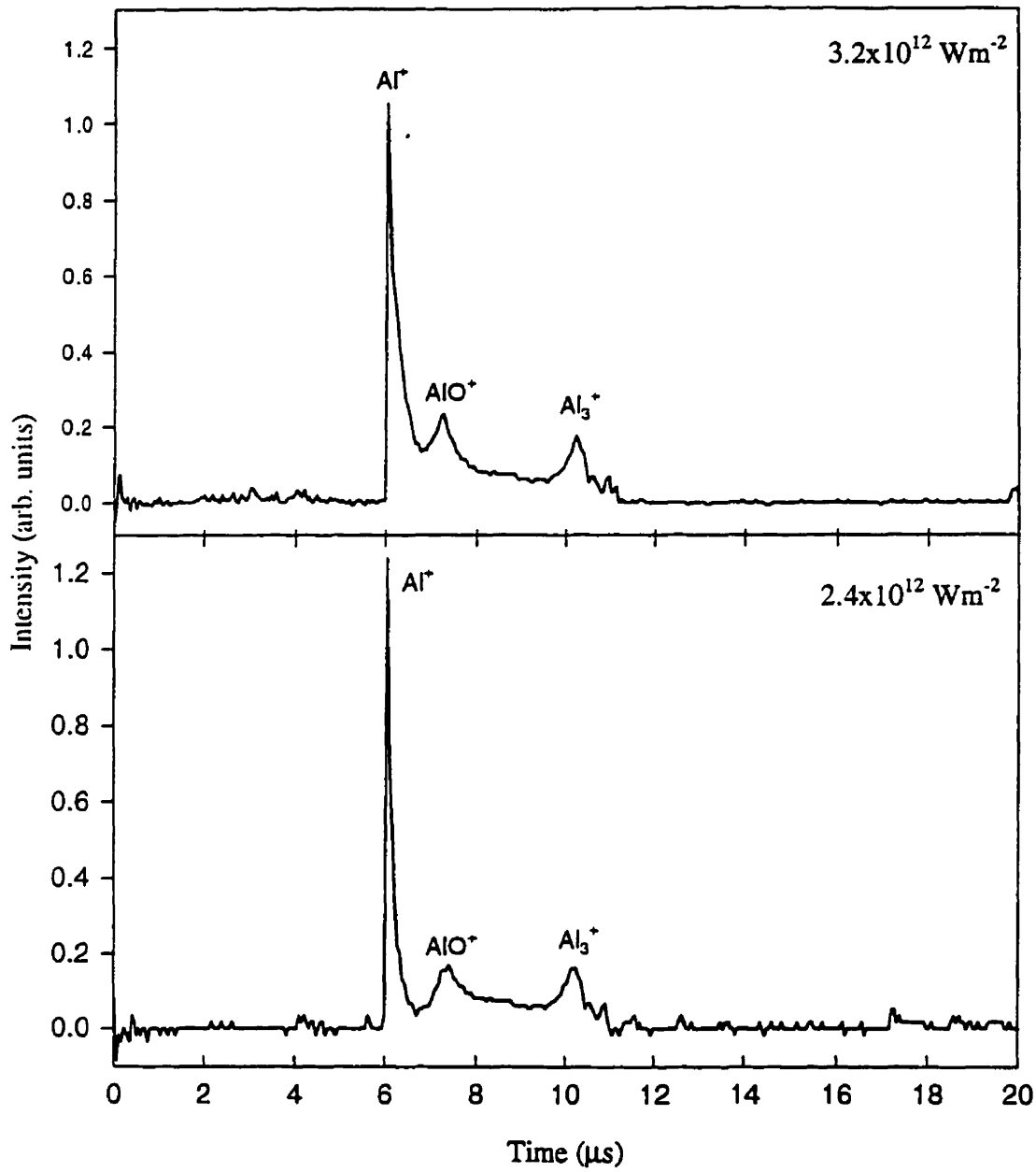

Figure 5.17. TOF spectral for ablation of Al in vacuum at laser intensities of 3.2×10^{12} Wm^{-2} and 2.4×10^{12} Wm^{-2}. The wavelength of the laser is 308 nm.

The shift in the flight time must be due to the initial kinetic energy possessed by the ions. From equation 4.5 an initial energy term can be included to give,

$$T_{TOF} = \frac{D}{\sqrt{v_o^2 + 2qV/m}} + d\frac{m}{qV}(\sqrt{v_o^2 + 2qV/m} - v_o) \qquad (5.1)$$

A graph of this equation for different initial velocities, v_o, of Al^+, Al^{2+}, and Al_2^+ is shown in figure 5.18. The initial velocity corresponding to a 0.25 μs shift in the Al^+ peak at 9.7×10^{12} Wm^{-2} is ~ 38 Kms^{-1}. For Al^{2+}, this velocity increases to ~ 43 Kms^{-1}. As the intensity decreases, the Al^+ velocity decreases to 30 Kms^{-1} at 6.3×10^{12} Wm^{-2}, 23 Kms^{-1} at 4.5×10^{12} Wm^{-2} and finally begins to approach the predicted thermal velocity. A summary of the initial velocities for Al^+ and Al^{2+} is shown in table 5.1.

Table 5.1. Initial velocities measured for Al^+ and Al^{2+}

Intensity ($\times10^{12}$) (Wm^{-2})	Al^+ Velocity (Kms^{-1})	Al^{2+} Velocity (Kms^{-1})
9.7	34	43
6.3	30	34
4.5	23	26
3.2	16	-
2.4	10	-

A strong neutral component was also detected at these high velocities as shown in figures 5.19 and 5.20. These results were obtained with the acceleration stack grounded. The first peak decreases in intensity following the behavior of the Al^{2+} peak while the second peak shifts to lower velocities and eventually vanishes. The velocities of the two peaks are similar to those obtained for Al^{+} and Al^{2+} and are summarized in table 5.2. The similarity in these velocities suggests that these peaks occur as the result of electron recombination with Al^{+} and Al^{2+} to form neutral Al. The differences in velocities may relate to the way in which the recombination occurs.

Table 5.2. Neutral component velocities for Al^{0} from figures 5.19 and 5.20.

Intensity ($\times 10^{12}$) (Wm^{-2})	Neutral peak 1 (Kms^{-1})	Neutral peak 2 (Kms^{-1})
9.7	39.2	33.2
6.3	36.5	30.3
4.5	-	27.4
3.2	-	17.8
2.4	-	14.5

These results can explain why the Al^{+} peak in figures 5.16 and 5.17 increases in size at low laser intensity. At the higher laser intensities, the electrons generated must have a high enough energy that they are not affected by the field of the acceleration stack and

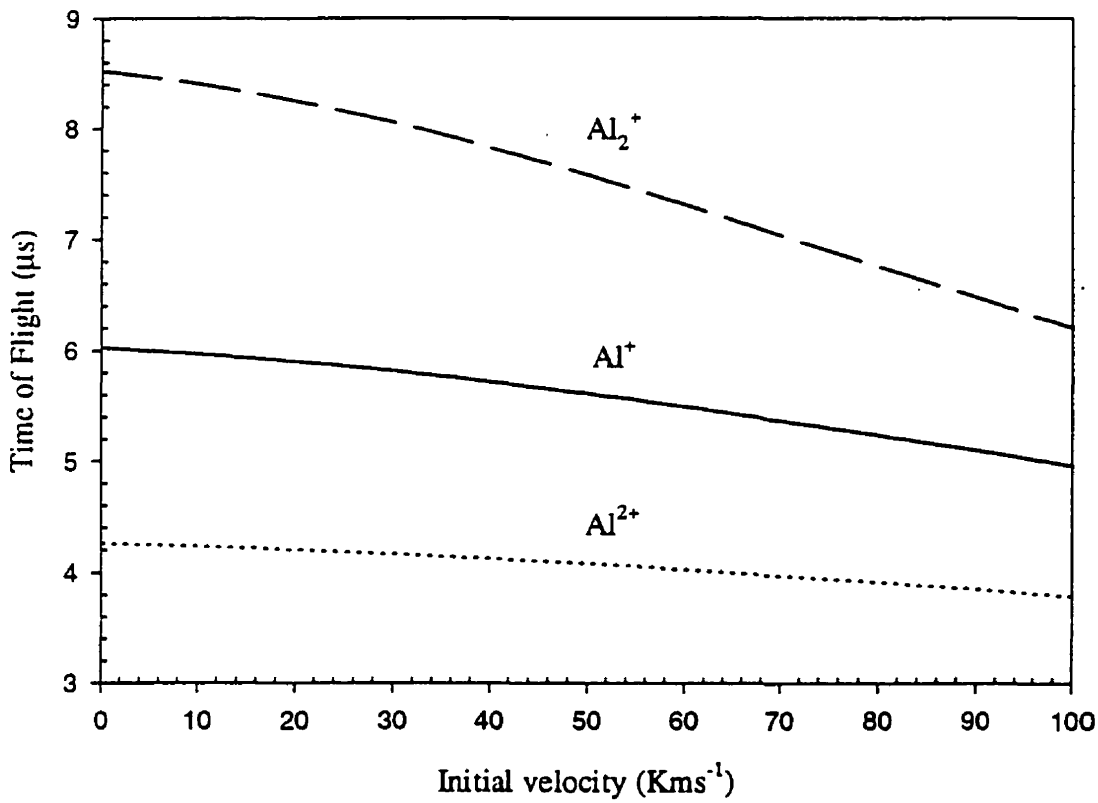

Figure 5.18. TOF as a function of initial ion velocity for Al^+, Al^{2+}, and Al_2^+ using equation 5.1.

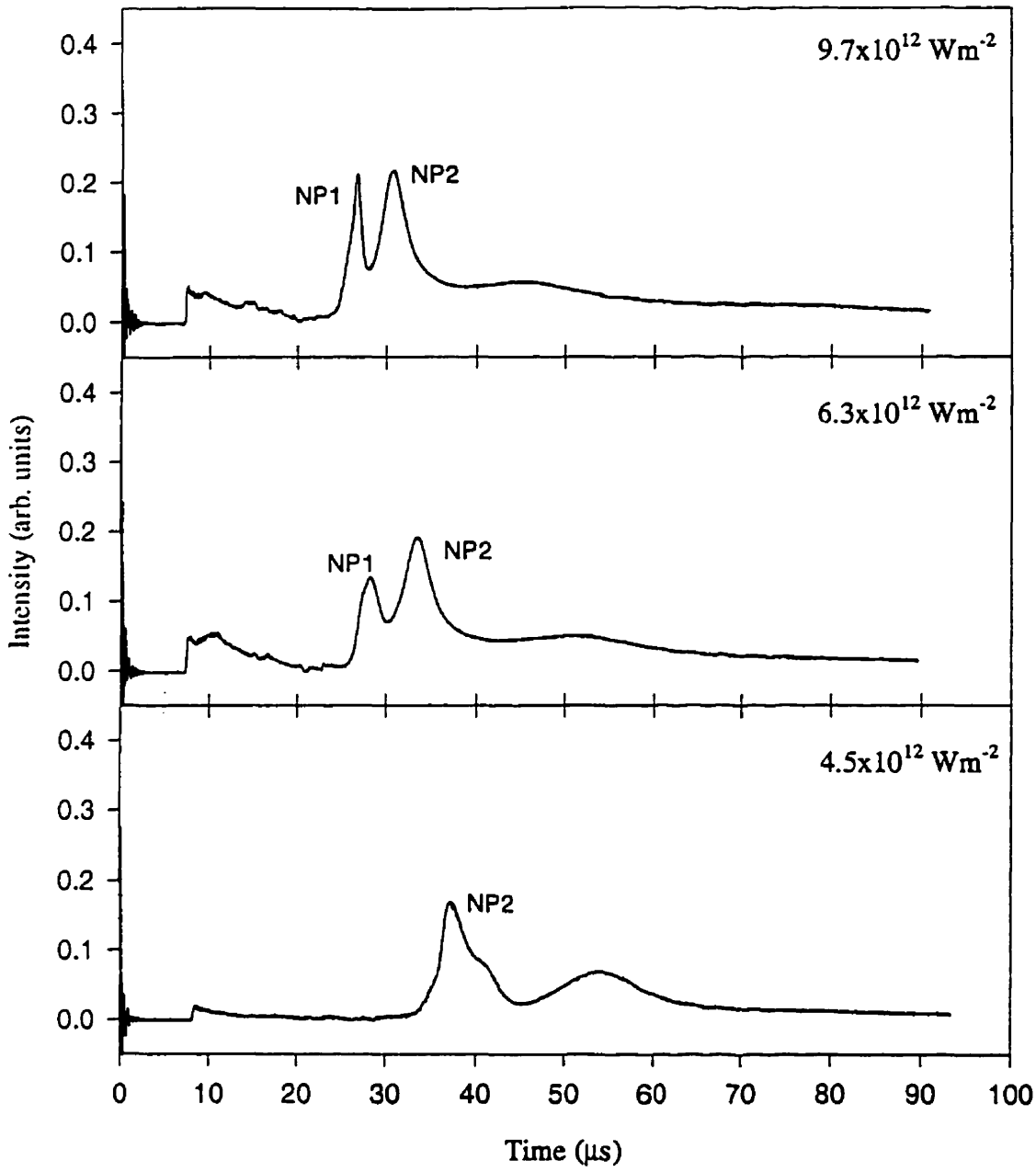

Figure 5.19. TOF of the neutral component accompanying ion emission at laser intensities 9.7×10^{12} Wm^{-2}, 6.3×10^{12} Wm^{-2}, and 4.5×10^{12} Wm^{-2}. The laser wavelength is 308 nm. Neutral peak NP1 is most likely Al^{2+} that has recombined with electrons while NP2 is due to Al^{+} that has recombined with an electron.

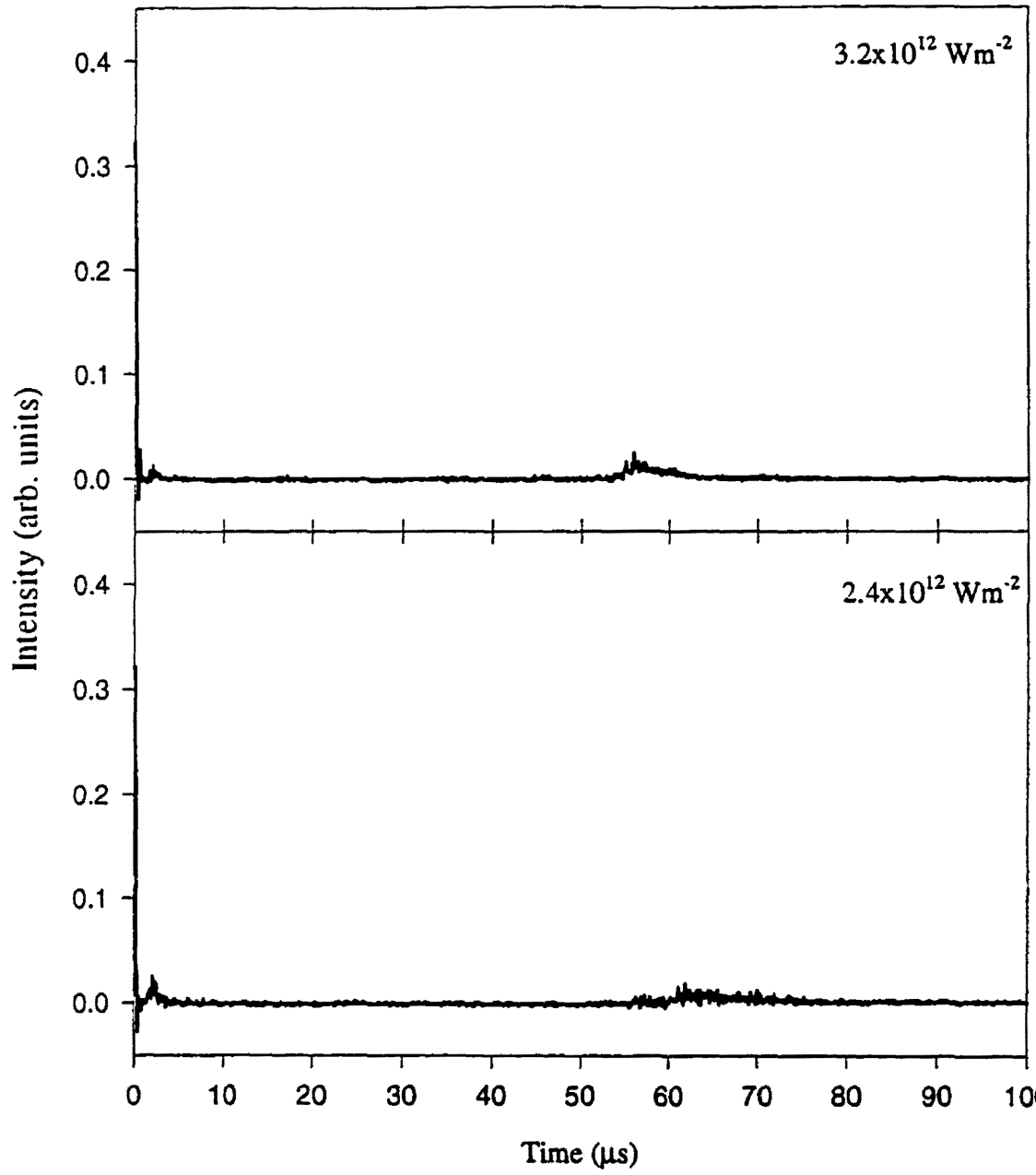

Figure 5.20. As in figure 5.19 but at laser intensities of 3.2×10^{12} and 2.4×10^{12} Wm^{-2}. Here very little neutral is observed due acceleration stack effects.

recombine with the high energy ions which are then not accelerated. This results in a reduced ion component and two neutral peaks, one due to $2e^+$ - Al^{2+} recombination and the other from e^+ - Al^+ recombination. As the intensity decreases to 6.3×10^{12} Wm^{-2} and 4.5×10^{12} Wm^{-2}, the electron energy decreases and electrons are trapped in the stack while ions are accelerated away thus increasing the ion component and decreasing the neutral component (figures 5.19 and 5.20). Only one peak is observed at 4.5×10^{12} Wm^{-2} since the Al^{2+} density decreases. At lower intensity, recombination is minimal as seen in the figures and the ion component is large (figure 5.17).

Similar results have been observed before for the laser ablation of metals with high intensity short laser pulses. Dyer (1989), Wang et al. (1991), von Gutfeld and Dreyfus (1989), and Brosda et al. (1989) have found that Cu, Al, and Zr ion velocities can exceed 20 Kms^{-1} at high excimer laser intensities (> 3×10^{12} Wm^{-2}) while Bykovskii et al. (1987) studied Al, Co, Cd, Pb, and C with a Q-switched CO_2 laser delivering up to 10^{14} Wm^{-2}. They found ion velocities exceeded 80 Kms^{-1} at the highest laser intensities for the metals. Wiedeman and Helvajian (1991), Lubben et al. (1985), Fukushima et al (1993), Estler et al. (1991), Izumi et al. (1991), Saenger (1989) have shown similar results for the excimer laser ablation of high temperature superconductors where Cu and Ba ions had velocities exceeding 20 Kms^{-1}.

The high velocities in figures 5.16 and 5.17 correspond to large kinetic energies. For example, for Al^+ the maximum kinetic energy is ~ 156 eV while Al^{2+} has a kinetic energy of ~ 250 eV. Energies of this magnitude cannot be produced by target heating and expansion alone since not enough heating occurs. The maximum surface temperature

would only be ~ 7000 K in vacuum corresponding to a thermal energy of 0.9 eV. Photoionization of an excited state can only produce 1 or 2 eV excess energy since the laser photon energy which is 4 eV at 308nm and 5 eV at 248 nm, is not much larger than the 3 eV ionization potential for excited Al. An alternative explanation has been suggested by Dyer (1989) and Bykovskii et al. (1987) who propose that recombining ions could produce high kinetic energies. From Puel (1970), the ion expansion energy is given by,

$$E_i = 5(Z+1)k_b T_e \tag{5.2}$$

where Z refers to the charge. For Al at 200 eV this would require an initial ionization state of Z=4 and an electron temperature of 88000 K. This is not possible at the laser intensities used and is much higher than the temperature predicted from the results of Schittenhelm et al. (1998) (section 5.2). In addition, no higher ionization states than Al^{2+} were observed.

Space-charge effects have been examined by Gilton et al (1990) and Orlando et al (1994). In this case, surface photoemission of electrons can lead to a net space-charge density in front of the target which produces a potential that varies with distance as given by the Poisson equation. Slower ions can then be accelerated through attraction to the much faster electrons. The potential depends on how the electrons interact with one another. Electrons that are just being emitted from the surface are repelled by the electrons that were emitted before and are also attracted to their image potentials in the target (Gilton et al 1990). This creates a point where the potential is at a minimum and the rate of change of the electron density is largest as shown in figure 5.21. Electrons at this point

are reflected back to the surface (Orlando et al. 1994). The location of the minimum potential depends on the current density of the photoelectrons and their energy. A large electron energy will push the minimum point further away from the target whereas a large current density will bring the minimum point closer since the attraction to the image

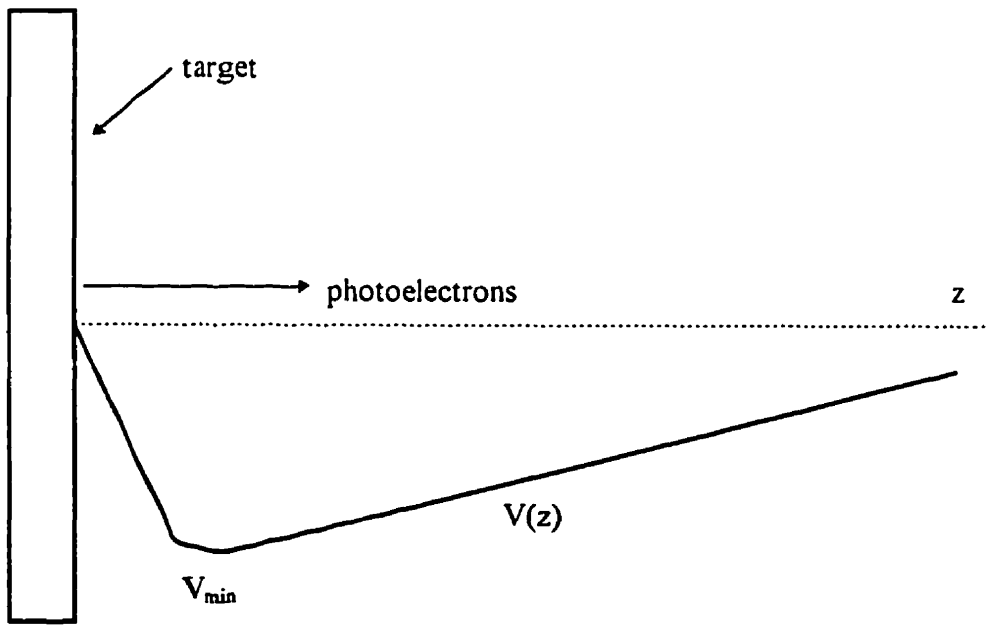

Figure 5.21. Potential well created by photoelectron emission during laser ablation of metals. This well can cause the acceleration of ions as they are emitted from the target.

potential will be large. The depth of the well will be approximately equal to the energy required to reflect the electrons back to the surface. For photoemission from Al excited with excimer laser radiation, the maximum electron energy will be ~ 1eV and this will correspond to a potential of 1 V. The maximum energy gained by an ion in such a potential can only be 1 eV which is the maximum supplied by the field. In fact, once ions pass the minimum point they will decelerate since the potential increases. This implies that space-charge effects are negligible in producing high energy ions unless the electron energy is high.

All of the above mechanisms require that the laser heat the target or the vapor/plasma to produce the high energy ions. This implies that the laser radiation must be efficiently absorbed either in the target or in the vapor/plasma. Murnane et al. (1993) has shown that laser radiation can efficiently couple into metal nanoparticles and found that the coupling efficiency can be more than an order of magnitude greater for nanoparticles than for flat bulk surfaces due to lower reflectivity and an enhanced electric field inside a nanoparticle arising from surface modes. Thus far, direct evidence for nanoparticle formation in UV laser-induced plasmas has not been obtained but figures 5.16 and 5.17 show that Al_2^+ and Al_3^+, which could initiate nanoparticle formation, are present. One reason why nanoparticles are not observed is that they are neutralized before being accelerated which may explain the long tails observed in figures 5.19 and 5.20. Unfortunately, a method of ionizing the vapor before acceleration was not available and this limited the detectability of neutral nanoparticles. Alternatively, nanoparticles may be ionized but then dissociate due to efficient coupling with laser radiation (Murnane et al. 1993) so that all that is observed

are simple diatomic and triatomic molecules. We have examined this by ablating the debris area around the interaction site in Al which is known to contain nanoparticles (Miyamoto et al. 1994). At very low laser intensities of ~ 1.7×10^{11} Wm^{-2}, nanoparticles were ejected (figure 5.22) but were small and of varying size. The bulk Al surface was unaffected by ablation as this intensity is below the ablation threshold for Al. As the intensity was increased to 6.7×10^{11} Wm^{-2} larger nanoparticles began to disappear until all that was left was diatomic and triatomic ions as observed in figures 5.16 and 5.17. This result shows how an increase in the laser energy can ionize and dissociate nanoparticles and may explain why no appreciable nanoparticles were observed in the TOF spectra.

If nanoparticles do exist in large quantities in the plasma plume then the ionization and dissociation of the nanoparticles may represent a mechanism by which the high energy ions are formed at 308 nm. This may also occur at 248 nm. The strong heating provided by the laser could ionize such nanoparticles. Subsequent Coulomb repulsion in the nanoparticles can then generate the high energy ions observed. This may also explain the large electron densities observed by Schittenhelm et al. (1998) at 248 nm. If nanoparticles exist in the plume then the ionization of the nanoparticles may generate enough electron and ions in the plume that inverse bremsstrahlung absorption can become effective.

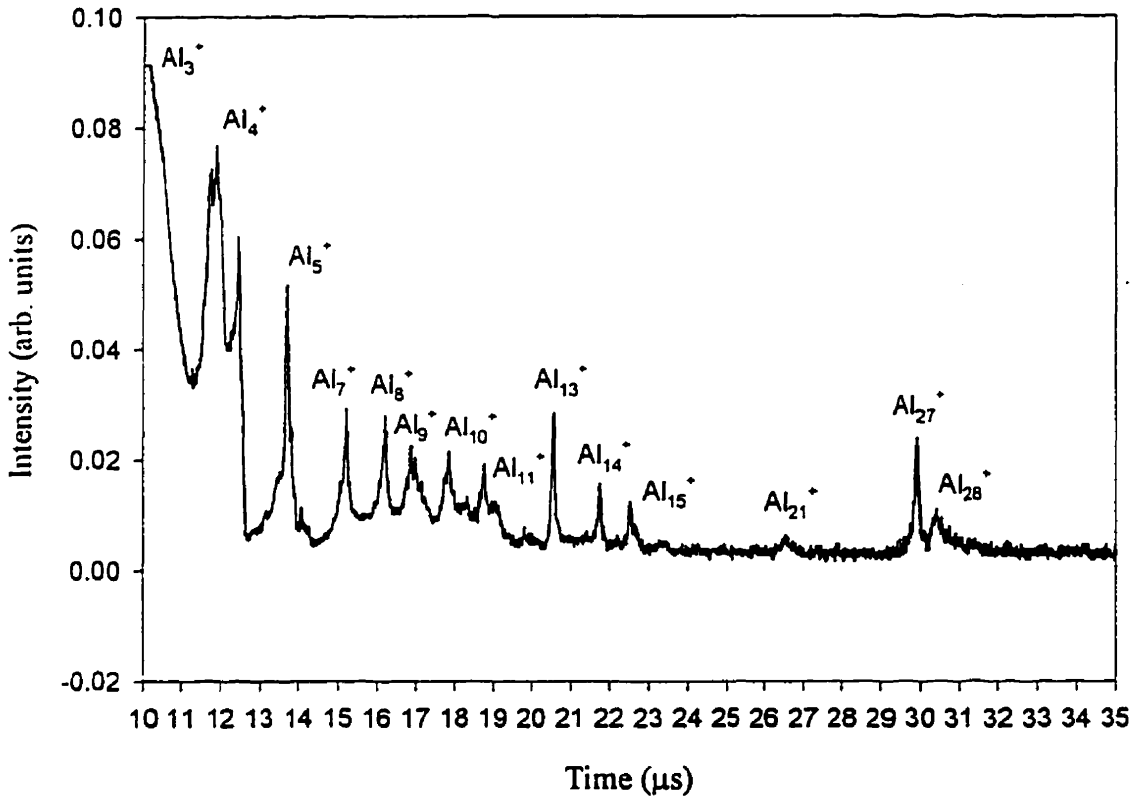

Figure 5.22. TOF spectra produced by laser irradiation of the debris around the ablation site on Al. The laser intensity is 1.7×10^{11} Wm^{-2} and the wavelength is 308 nm. This result shows that nanoparticles can be easily ionized by the laser irradiation.

5.4 Scattering and Optical Spectroscopy of the Laser Plume

Scattering and optical emission from the laser plume were used to investigate the presence of nanoparticles in the plasma and how they relate to optical emission. Such experiments make it possible to correlate nanoparticle formation and electron density in the plasma plume.

In this experiment, scattering and plasma emission from Al vapor were simultaneously observed at 90° to the laser beam (see section 4.5) as a function of laser intensity, gas pressure and composition. Targets were first cleaned with several laser pulses and then spectra were averaged over 10 laser pulses to smooth out any fluctuations in intensity. Figures 5.23a and 5.23b show scattering and emission spectra at different times at a laser intensity of 10^{13} Wm^{-2} and a gas pressure of 1 atm N_2 for a 308 nm excimer laser. The wavelength ranges are from ~ 307 - 395 nm and 235 - 320 nm respectively. Between 10 and 30 ns in figure 5.23a, no emission is observed from the plume which indicates that the vapor must be mostly neutral. The only peak observed is the scattered 308 nm light from the incident laser beam. No resonance absorption occurs since there is no overlap with the 308.22 nm transition in Al vapor for this laser (see Appendix A). The peak at 308 nm is, therefore, scattered laser radiation. With the intensity of the peak corrected for the time dependence of laser pulse, one can see that the peak initially grows in intensity and then decreases at ~ 30 ns as the plasma emission begins to increase as shown by the rise of continuum emission at 35 ns. This is an indication that nanoparticles are present in the plume. Such particles should be efficiently heated by the laser (see section 5.3). The size

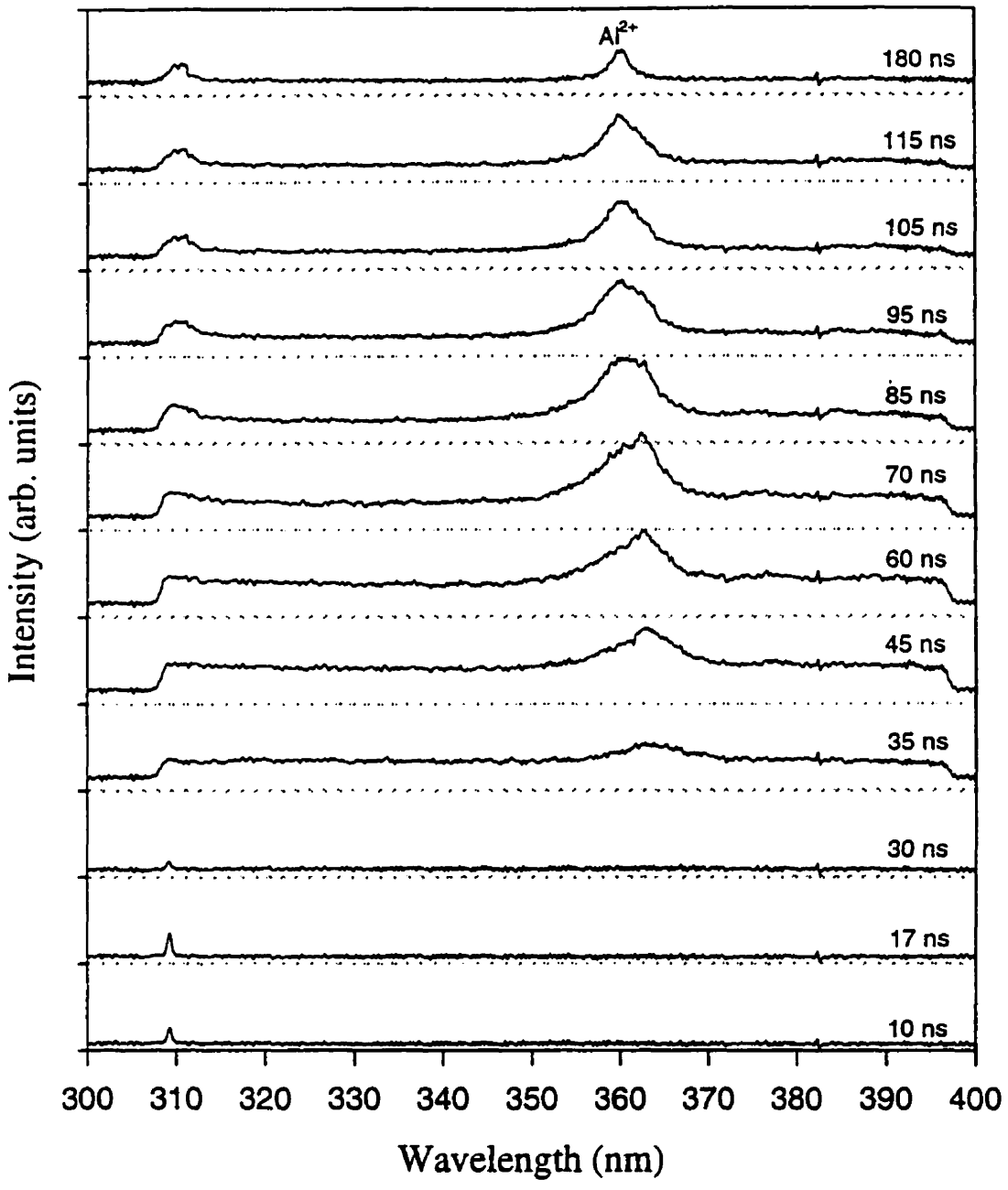

Figure 5.23a. Scattering and optical emission in the 307 - 395 nm range from an Al plasma in 1 atm N_2. The laser intensity is 10^{13} Wm^{-2} and the wavelength is 308 nm. The peak at 308 nm is scattered laser light. No resonant ground state Al transitions exist for this laser (Appendix A). Al^{2+} at 360.1 nm is observed at ~ 30 ns after the start of the laser pulse.

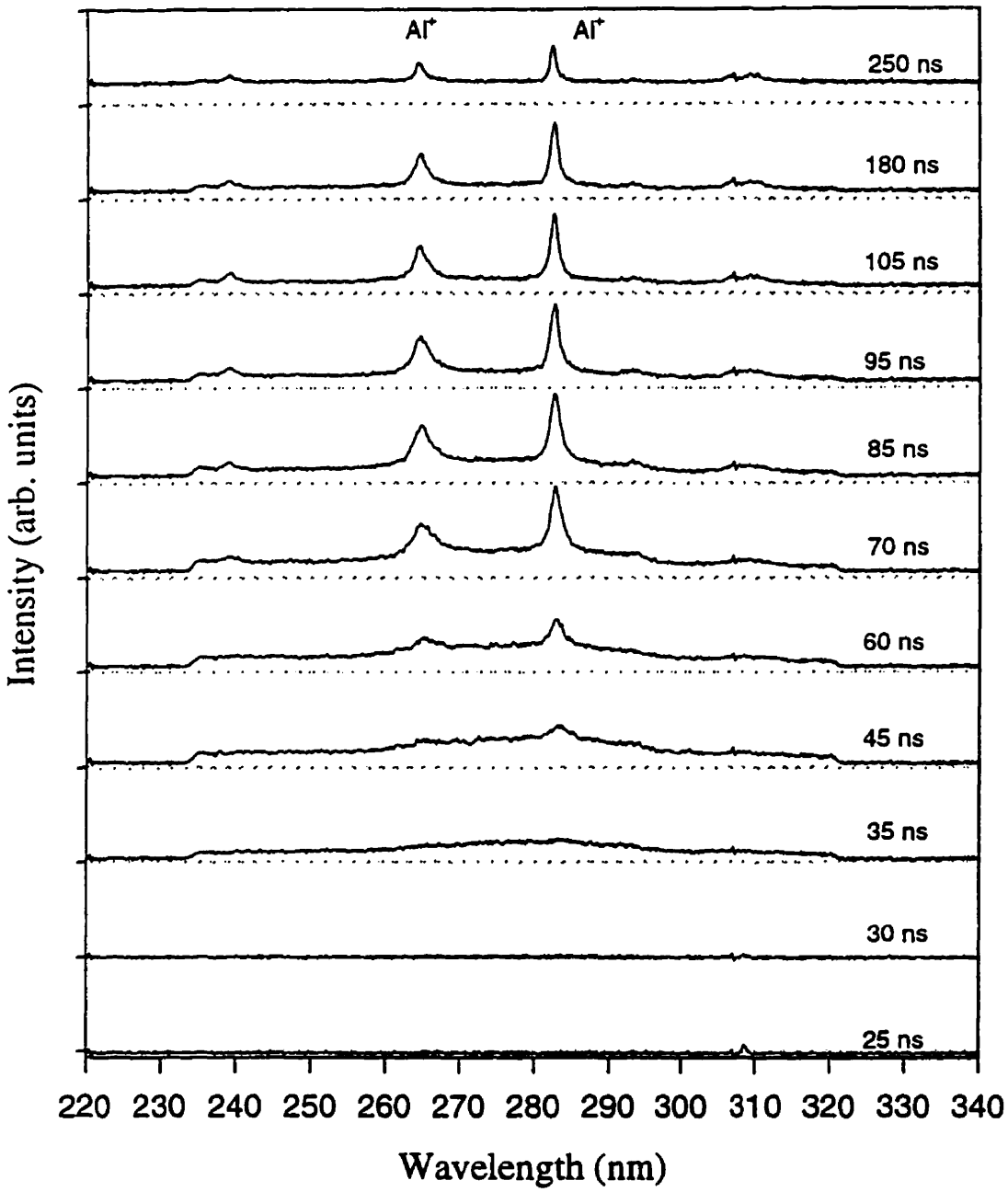

Figure 5.23b. Al plasma emission in the 235 nm to 320 nm range in 1 Atm N_2. The laser intensity is 10^{13} Wm^{-2} and the wavelength is 308 nm. Two peaks at 281.6 nm and 263.7 nm are observed. These peaks are due to transitions in Al^+.

of the nanoparticles are quite small. From Mie theory (Bohren and Huffman 1983) the scattered intensity is given by,

$$\frac{I_s}{I_o} = \frac{8\pi^4 NVa^6}{\lambda^4 r^2}\left|\frac{m^2-1}{m^2+2}\right|^2\left(1+\cos^2\vartheta\right) \tag{5.4}$$

as a function of the incident intensity where N is the nanoparticle number density in m^{-3}, a is the nanoparticle radius, θ the scattering angle, and V is the volume in which the nanoparticles are contained. This assumes that the nanoparticles scatter independently from one another and that the incident intensity is uniform over the nanoparticles. From figure 5.23a, the scattered laser intensity can be calculated since the responsivity of the detector which is known. At 17 ns, the vapor is predicted to expand approximately 50 μm which is much smaller than the detector focal spot size of 200 μm. Assuming that the nanoparticles are contained within this volume gives a scattered laser intensity of ~ 4×10^6 Wm^{-2} in the focal spot of the detector. The incident laser intensity in the focal spot is ~1×10^{13} Wm^{-2}. Substituting these values into equation 5.4 gives a nanoparticle size of 2 nm with a nanoparticle density of 6.1×10^{20} m^{-3}. This is in agreement with the nanoparticle sizes calculated by Callies et al. (1998) for the laser ablation of Al. At 30 ns the scattered laser intensity decreases to 3.3×10^5 Wm^{-2} since the plasma has expanded to ~ 100 μm. Assuming a constant nanoparticle density, the nanoparticle size decreases to 1.3 nm.

As the scattered signal decreases, continuum emission increases rapidly near 35 ns. This is followed by line emission from Al^{2+} and Al^{+} with no emission from Al^{0}. The peak at

~ 360 nm is due to line emission from the 3p ^{2}D-4p ^{2}P multiplet in Al^{2+}. No ground state Al^{2+} was observed since this would occur at $\lambda < 200$ nm, below the detection range of the OMA. The Al^{2+} peak consists of three lines at 360.16, 360.1, and 361.23 nm (Reader et al. 1980) and is broadened by Stark effects produced by the large electron density. A shift from 361.23 nm to 360.16 nm is observed at late times after the laser pulse (> 60 ns). The Al^+ lines are from excited state transitions at 281.6 nm (3s3p ^{1}P-3s4p ^{1}S) and 263.7 nm (3s3d ^{3}D-5f ^{3}F) (Reader et al. 1980, Wiese et al. 1969). The line at 263.7 nm consists of 6 lines which are not resolved due to Stark effects and the resolution of the spectrometer. As the plasma emission begins to subside after the laser pulse, excited Al^0 spectral lines appear at 237.2 nm ($3s^23p$ ^{2}P-$3s^25d$ ^{2}D), and 308.2 nm ($3s^23p$ ^{2}P-$3s^23d$ ^{2}D) (Reader et al. 1980). The emission persists until approximately 250 ns after the laser pulse after which the transition to the Al ground state at 394.6 nm ($3s^23p$ ^{2}P-$3s^24s$ ^{2}S) appears. These were the only lines observed in the spectra since most transitions in Al^+ and Al^{2+} are in the deep UV below 200 nm. In addition, only the most intense emission lines could be observed since the OMA was gated for 10 ns. The apparent overlap between scattered laser light and the 308.22 nm Al ground state transition in figure 5.23a results from using relatively large slits (50-100 μm) in the OMA to increase the amount of light transmission. This causes the peaks to broaden considerably and gives the mistaken impression that overlap occurs.

These results show that the vapor is highly ionized. This may be due to heating and ionization of nanoparticles as no other mechanism can explain the high ionization levels observed (no resonance absorption for the 308 nm excimer laser used, Appendix A).

Calculation of the temperature is impossible since the plasma is in a non-equilibrium state due to heating which can be seen by the low level of line emission and large continuum during the laser pulse as compared to after the laser pulse.

To relate extinction by nanoparticles to inverse bremsstrahlung absorption, the transmission of the laser pulse through the plasma was measured and is shown in figure 5.24. The maximum transmission is ~ 50% at 10 ns and decreases to zero toward the end of the pulse. Although nanoparticles are presumed present, extinction by the nanoparticles is too small to produce the observed results. This is obvious when one calculates the extinction for small particles (Bohren and Huffman 1983),

$$\alpha_{ext} = \frac{8\pi^2 a^3}{\lambda} N \operatorname{Im}\left\{\frac{m^2 - 1}{m^2 + 2}\right\} \tag{5.5}$$

With $a = 2$ nm and $N = 6.1\times10^{20}$ m^{-3}, $\alpha_{ext} = 50$ m^{-1}. Substituting into Beer's equation,

$$\frac{I}{I_o} = \exp(-\alpha_{ext} z) \tag{5.6}$$

and using $z = 50$ μm gives a transmission of 99.7% suggesting that nanoparticles are too small and of insufficient density to produce any attenuation of the laser beam. The interaction of the laser pulse with the plume is, therefore, strictly by inverse bremsstrahlung absorption (assuming no resonant ground state transitions are present, Appendix A). The electron density required for this can be calculated from Beer's

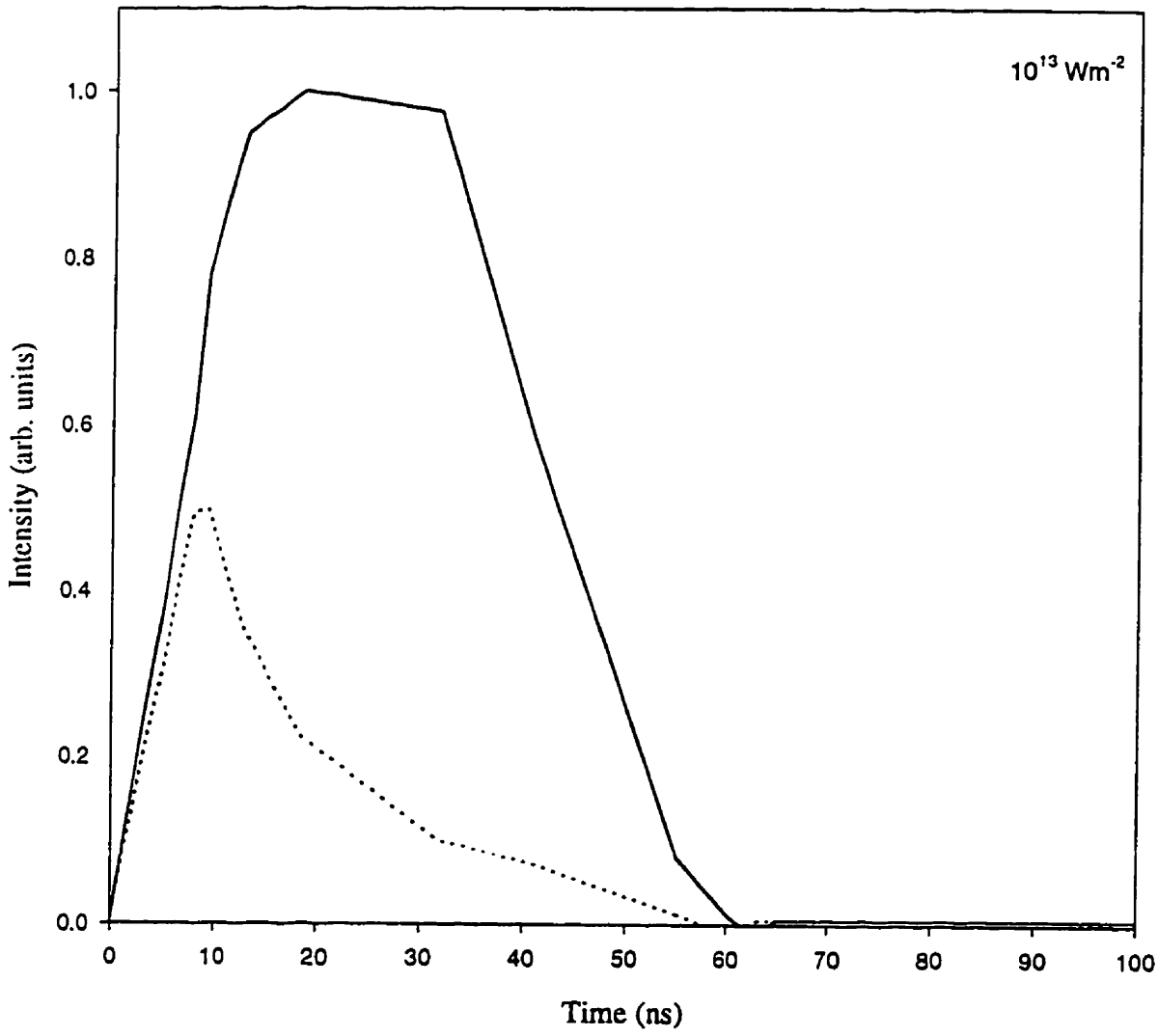

Figure 5.24. Transmission of the laser pulse through the Al plasma for a laser intensity of 10^{13} Wm^{-2} and wavelength 308 nm. Since there is no overlap with the Al ground state transition at 308.22 nm, the attenuation is most likely due to inverse bremsstrahlung absorption. Solid line-unattenuated laser pulse. Dashed line-transmitted laser pulse.

equation. For 50% transmission and a plasma extent of 50 μm, α_{IB} = 13863 m^{-1} which corresponds to an electron density of ~ 1.5×10^{26} m^{-3} and a temperature of ~ 16000 K (section 5.2) in the first 10 ns of the laser pulse.

Comparing to figure 5.23a, and assuming no resonance ground state transitions, this result suggests that nanoparticles must heat rapidly and begin to ionize in the first 10 ns of the laser pulse (no plasma emission is observed since the plasma may not be present throughout the entire detection area). Inverse bremsstrahlung absorption then becomes significant and the laser pulse begins to heat the plasma directly which can then produce the high ionization levels.

Since the nanoparticles are observed until 30 ns, this suggests that nanoparticles originate from the surface (Kelly and Rothenberg 1985) so that as nanoparticles are ionized they are replaced by new ones and the decrease in the scattered signal may, therefore, be due to absorption of the laser pulse in the plume. Eventually, however, the surface temperature may become too hot and nanoparticles are no longer formed. Nanoparticle growth in the vapor may not be possible, since the initial ionization would destroy them and no scattered signal would be observed.

The same results were observed at lower laser intensity except that the nanoparticles were larger and persisted longer before the plasma formed as shown in figure 5.25a for 5.6×10^{12} Wm^{-2}. With the same nanoparticle density as before, the nanoparticle size at 17 ns is ~ 2.5 nm and is larger than in figure 5.23a which may be due to less heating and ionization. The nanoparticles may also be larger as they are emitted from the cooler surface. At 37 ns, nanoparticle scattering is still observed and the nanoparticle size is ~ 1.2

nm. The plasma emission intensity decreases in comparison to figure 5.23a and the line emission from Al^{2+} and Al^{+} (figure 5.25b) is less indicating a smaller electron density and, therefore, less inverse bremsstrahlung absorption which results from less ionization of the nanoparticles. This can be seen in figure 5.26 in which the transmission has increased to 70% at 10 ns. In this case α_{IB} = 7133 m^{-1} and the corresponding electron density is ~ 1×10^{26} m^{-3} assuming a plasma temperature of 16000 K. At 2×10^{12} Wm^{-2} in figure 5.27a, the scattered intensity from the nanoparticles is larger and the nanoparticles are ~ 3 nm at a density of 6.1×10^{20} m^{-3}. In this case, the scattered signal is observed to persist until 37 ns since less nanoparticle heating occurs. The cooler surface may also produce nanoparticles for a longer period of time. The ionization of the nanoparticles is (figure 5.27b), therefore, less and the plasma emission and electron density are smaller. The transmission of the laser pulse (figure 5.28) in this case is ~ 100% indicating that the electron density generated by nanoparticle ionization is too small for inverse bremsstrahlung absorption. Here the electron density would have to be below ~ 3×10^{25} m^{-3}.

Similar results were observed for the ablation of Al at lower N_2 gas pressures. It was found that as the gas pressure decreased, the continuum emission decreased but the line emission and nanoparticle scattering were still present as shown in figures 5.29a and 5.29b for 10^{-3} atm and 10^{13} Wm^{-2}. The decrease in the continuum emission results from a lack of a shock wave to contain the plasma so that the electron density will be low throughout most of the detection area. However, the plasma extent can be larger as the speed of the expansion is quite fast, so that the distance over which absorption occurs is greater and absorption of the laser pulse energy can still occur.

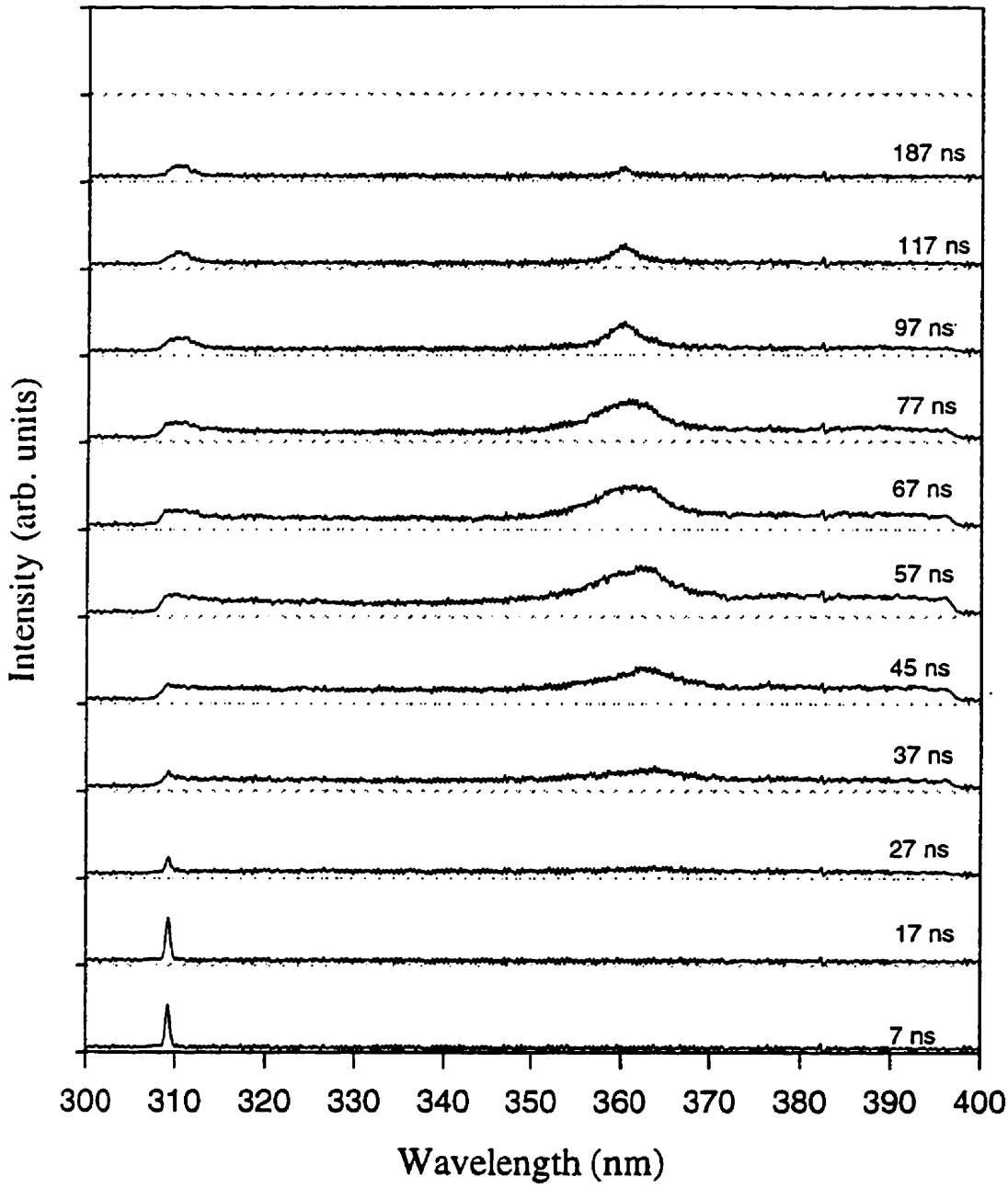

Figure 5.25a. Al plasma emission in the 307 to 395 nm range at a pressure of 1 atm N_2. The laser intensity is 5.6×10^{12} Wm^{-2} and the wavelength is 308 nm. Scattering is still present in the early part of the pulse. The peak at 360.1 nm is due to Al^{2+}.

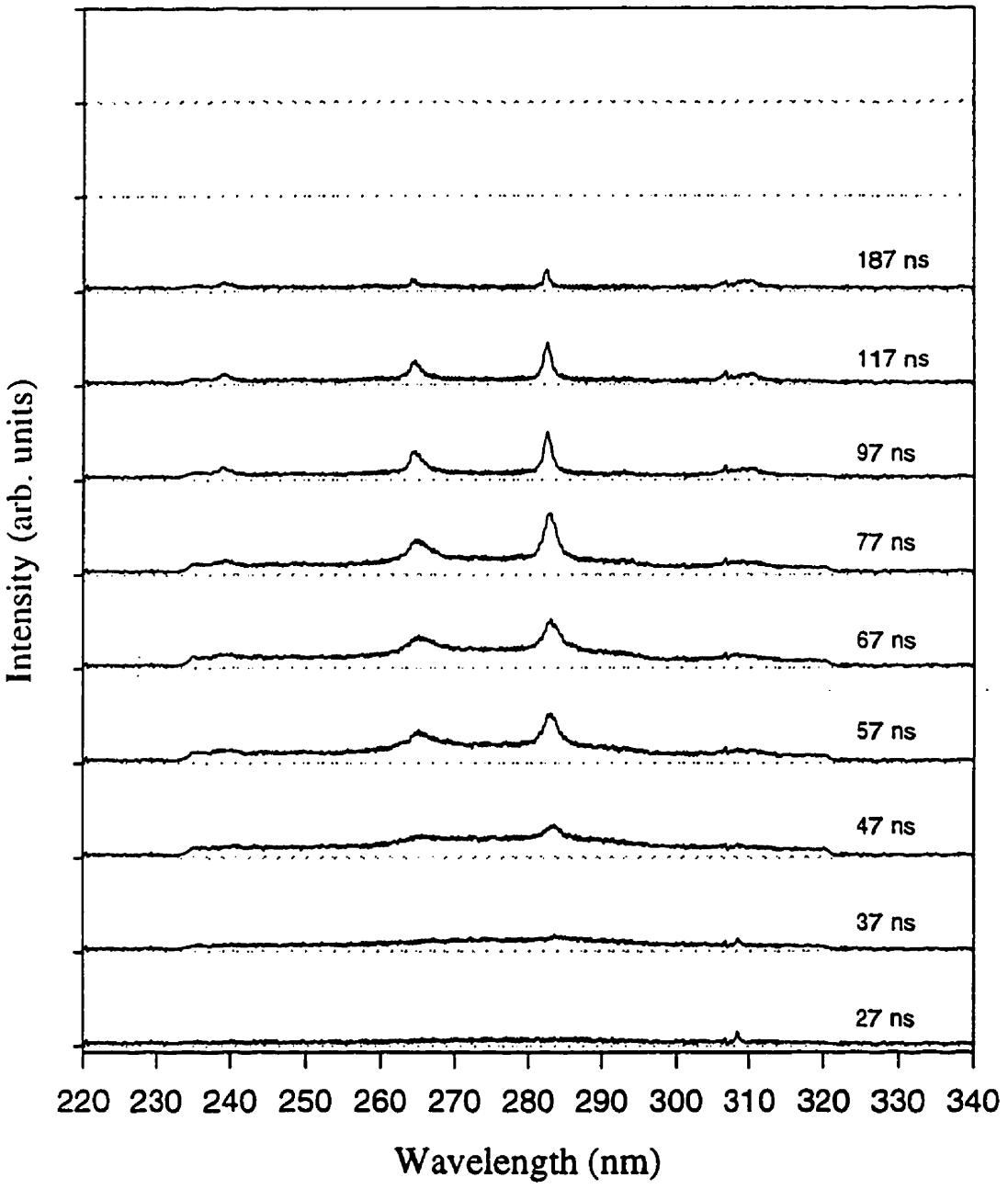

Figure 5.25b. Al plasma emission in the 235 to 325 nm spectral range at a pressure of 1 atm N_2. The laser intensity and wavelength are the same as in figure 5.25a. . Two peaks at 281.6 nm and 263.7 nm are observed. These peaks are due to transitions in Al^+.

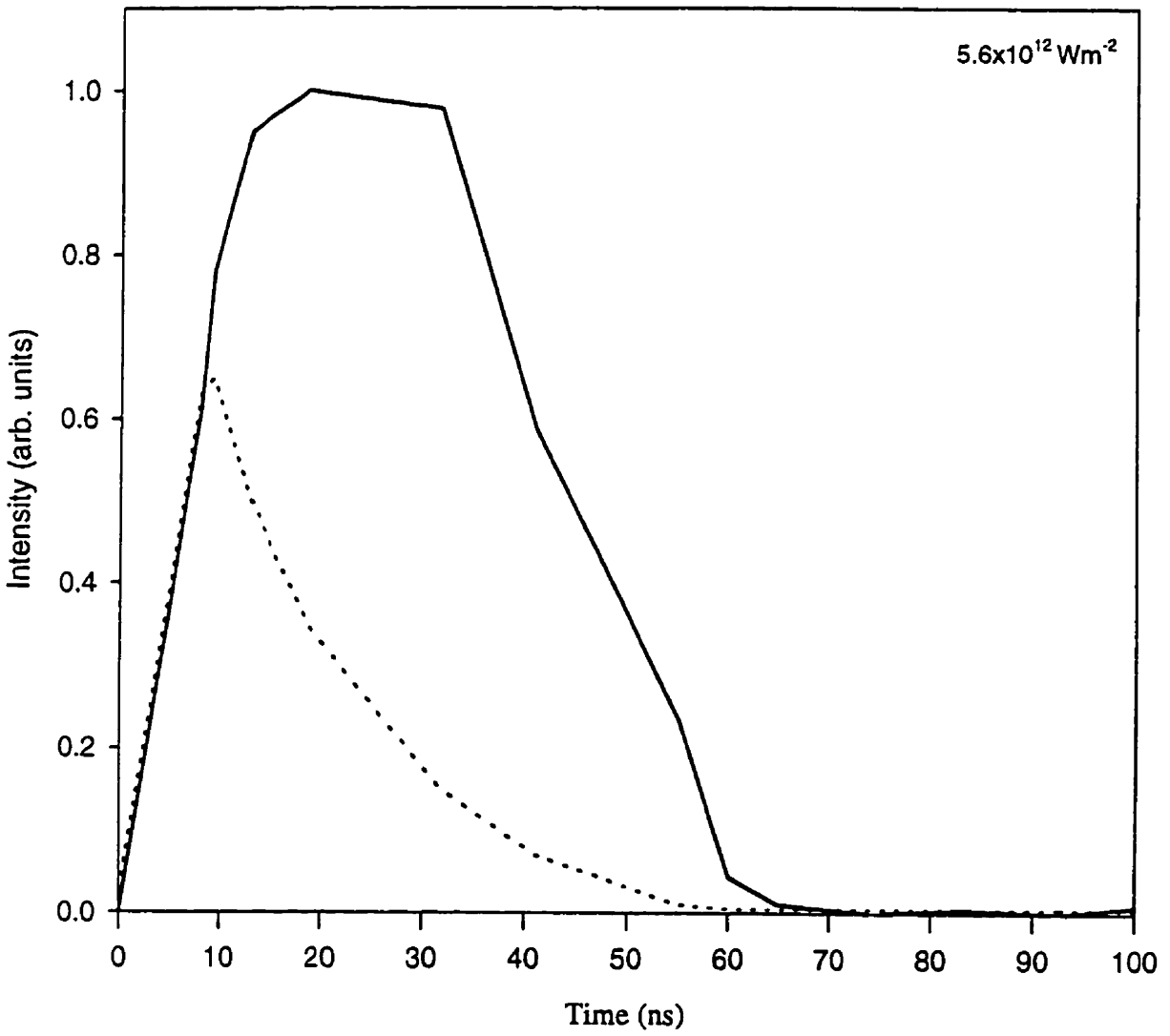

Figure 5.26. Transmission of the laser pulse through the Al plasma plume for an intensity of 5.6×10^{12} Wm^{-2} and wavelength 308 nm. Since there is no overlap with the Al ground state transition at 308.22 nm (Appendix A), the observed transmission must be due to inverse bremsstrahlung absorption. Solid line - unattenuated laser pulse. Dashed line - transmitted laser pulse.

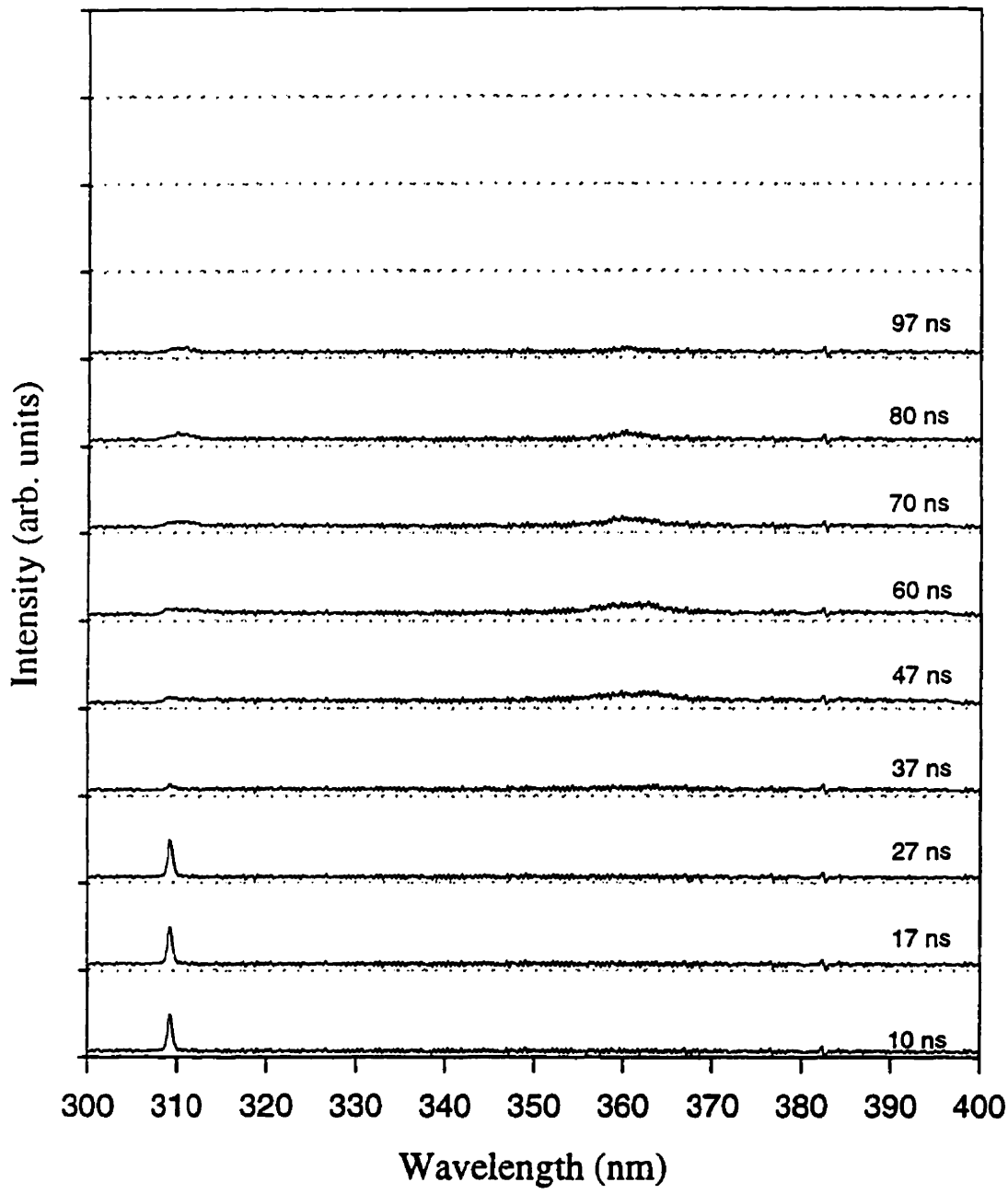

Figure 5.27a. Al plasma emission in the 307 nm to 395 nm range at a pressure of 1 atm N_2. The laser intensity is 2×10^{12} Wm^{-2} and the wavelength is 308 nm. The scattered signal is observed at 308 nm but very little line emission is present.

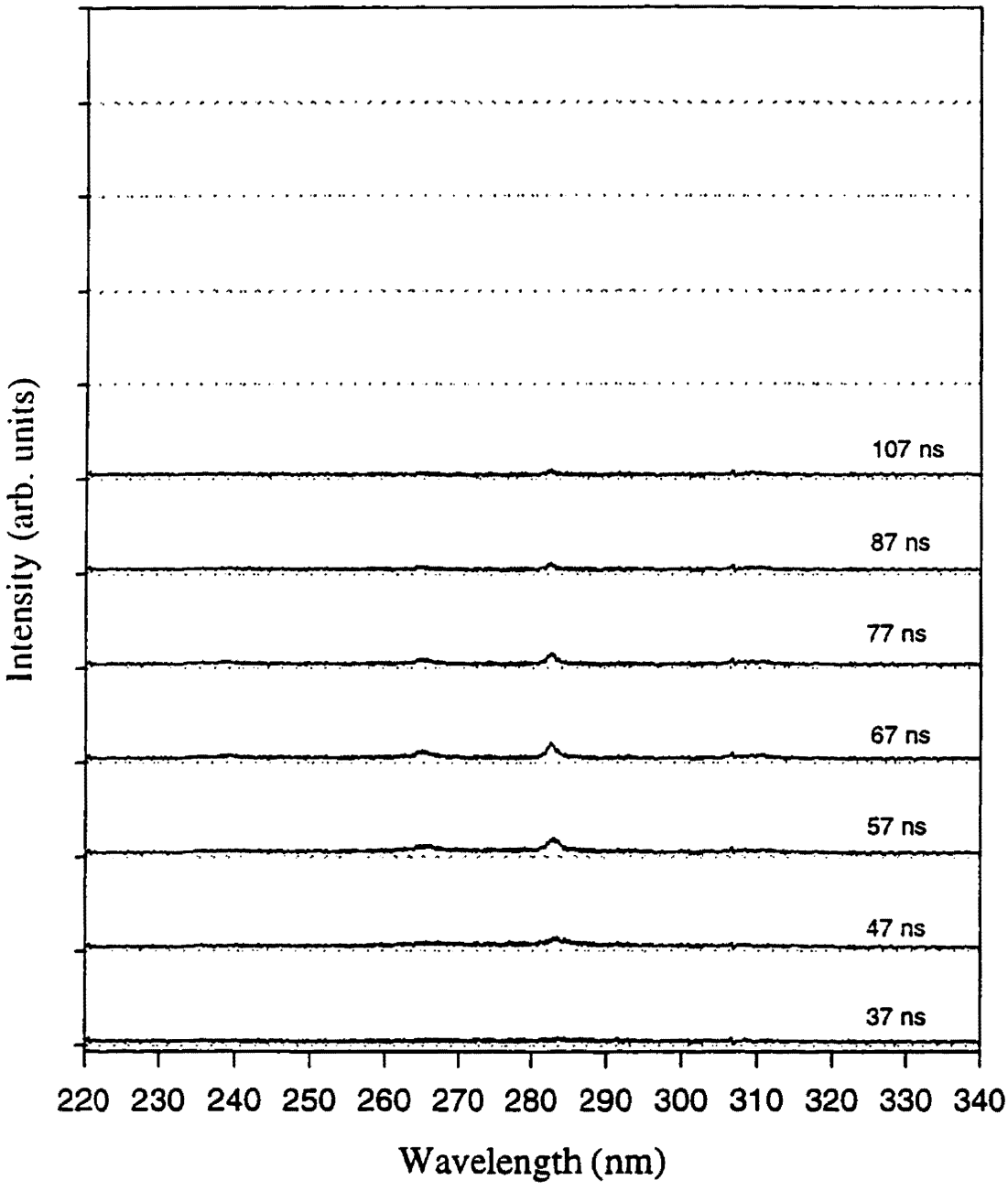

Figure 5.27b. Al plasma emission for the 235 to 325 nm spectral range and pressure of 1 atm N_2. The laser intensity and wavelength are the same as in figure 5.27a. Very little line emission is observed at 281.6 nm and 263.7 nm. These peaks are due to transitions in Al^+.

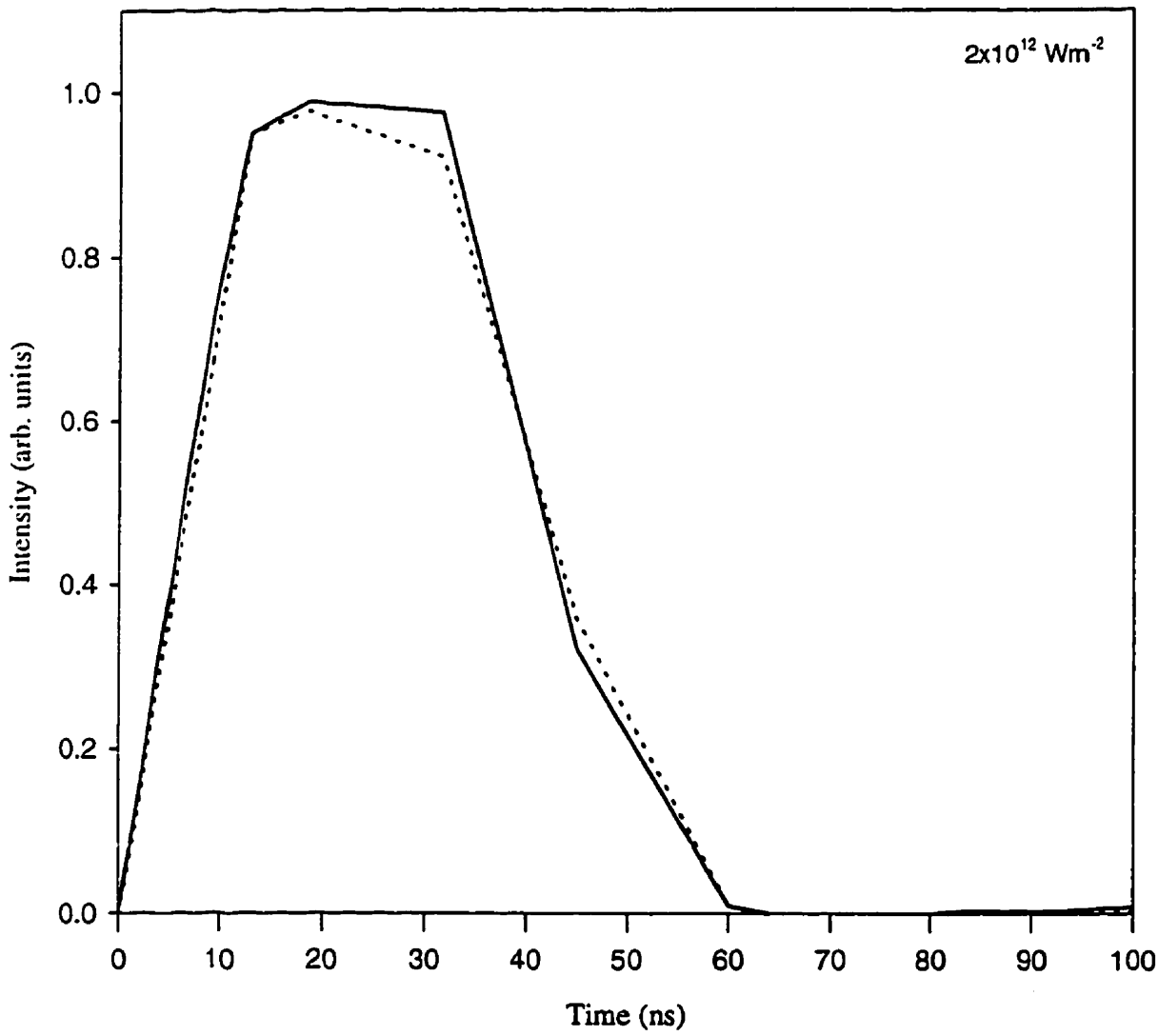

Figure 5.28. Transmission of the laser pulse through the Al plasma plume for a laser intensity of 2×10^{12} Wm^{-2} and wavelength 308 nm. The transmission of the laser pulse is nearly 100% as indicated by the dashed line. The solid line is the unattenuated laser pulse.

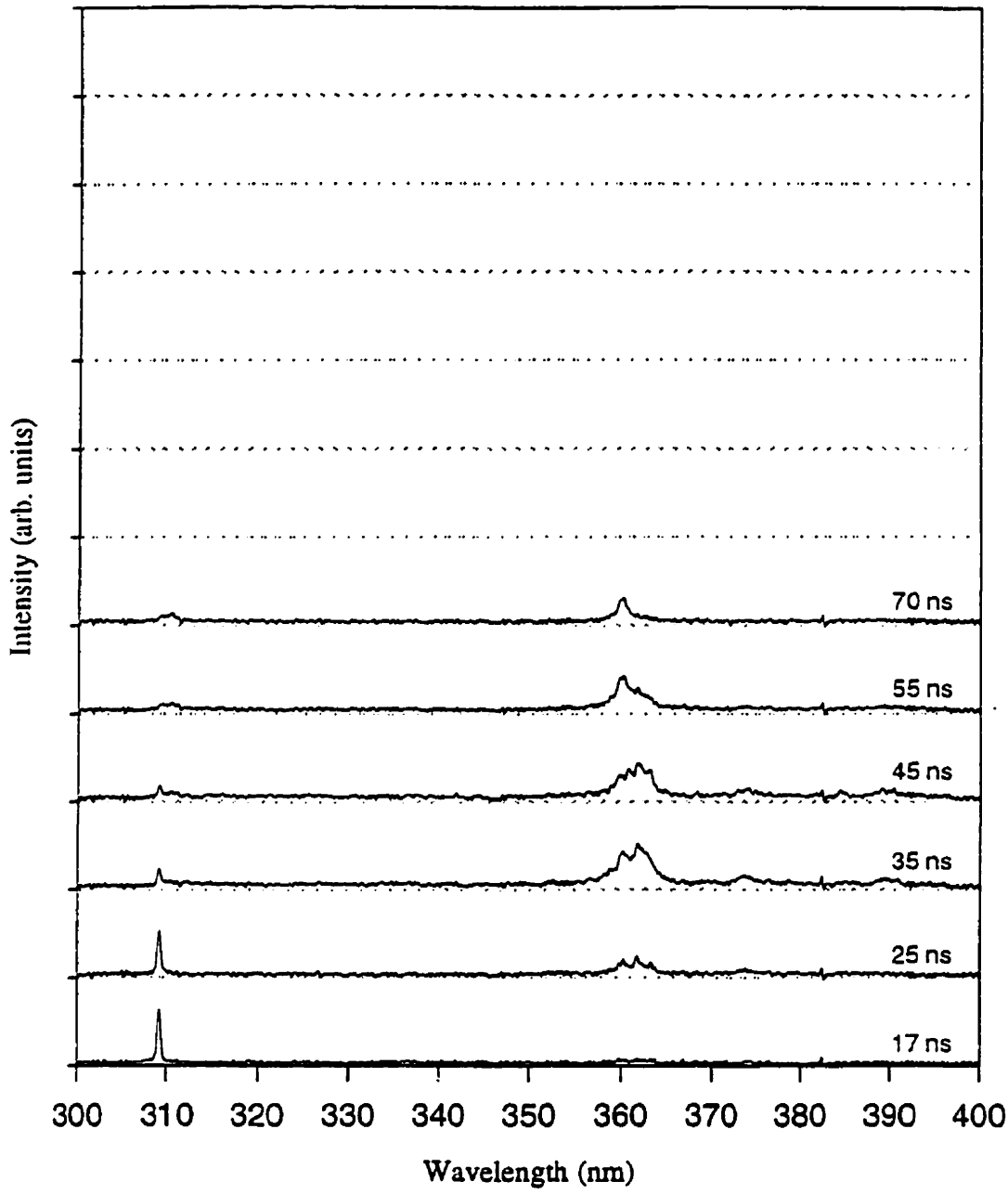

Figure 5.29a. Al plasma emission in the 307 - 395 nm range at a pressure of 10^{-3} atm. The laser intensity is 10^{13} Wm^{-2} and the wavelength is 308 nm. Scattering (308 nm) and line emission from Al^{2+} (360.1 nm) are still observed indicating that the effects of the gas pressure are small.

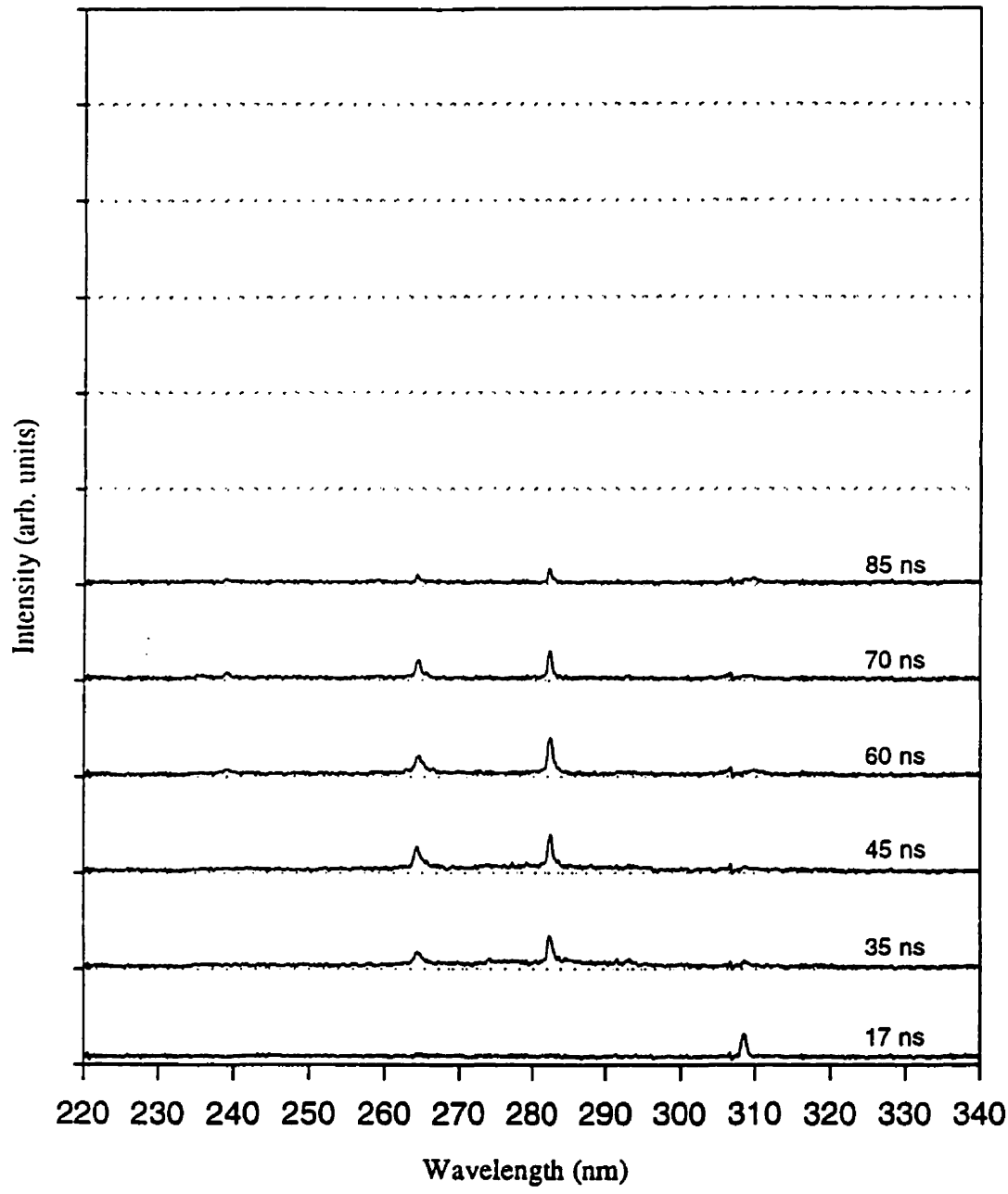

Figure 5.29b. Al plasma emission for the 235 - 325 nm spectral range at a pressure of 10^{-3} atm. The laser intensity and wavelength are the same as in figure 5.29a. Line emission is still observed at 281.6 nm and 263.7 nm due to transitions in Al^{+}.

The effects of gas composition were minimal. The intensity of the lines was higher when Ar was used since the plasma was contained closer to the surface and lower when He was used since the plasma expanded faster , but the effect on the nanoparticles and transmission of the laser pulse were unchanged.

These results demonstrate that small nanoparticles are present in the plume. The nanoparticles appear to be ejected from the surface and quickly ionized resulting in large electron densities capable of absorbing the laser pulse energy. Nanoparticle scattering appears to be an insignificant process in attenuating the laser pulse.

These results assumed that no overlap occurred between the laser line and the resonant Al ground state transition at 308.22 nm (see Appendix A) as was the case for the laser used. It should be noted, however, that using 308 nm radiation to perform such experiments may result in resonant absorption in the Al ground state and that this may contribute to the 308 nm emission observed in the figures. Even if initially, there is no resonant absorption in Al (Appendix A), broadening of the absorption bands once a plasma forms (figure 5.23a), can result in some overlap with the laser line. Plasma heating can then be a result of inverse bremsstrahlung and line absorption in the latter stages of the laser pulse when the vapor is hot and ionized.

Chapter 6

Plasma Forming Mechanisms

6.1 Model of the Laser-Plume Interaction

The results of chapter 5 show that nanoparticles of size ~ 2 - 3 nm and of density ~ 6×10^{20} m^{-3} are present in the plume during laser irradiation. However, the extinction produced by nanoparticles is too small for the size and density calculated. The attenuation of the laser beam through the plume, therefore, appears to be by inverse bremsstrahlung absorption. This requires an electron density of ~ 10^{26} m^{-3} which cannot be produced by photoionization or target heating alone (Chapter 3) indicating a different ionization mechanism exists.

It will be shown in this chapter that such high electron densities are possible by laser heating of nanoparticles in the plume. This results in the thermal emission of electrons and

subsequent ionization of the nanoparticles. However, the ions will also escape due to Coulomb repulsion and so the laser heating of nanoparticles produces free electrons and ions. This process can continue until the nanoparticles completely vaporize.

The density of free electrons and ions depends on the amount of laser heating, number density, and size of nanoparticles. Under the appropriate conditions, the free electron and ion density can reach sufficient levels for inverse bremsstrahlung absorption to occur in the first 10 ns of the laser pulse.

6.2 Laser Heating and Ionization of Metal Nanoparticles

6.2.1 Laser heating

The amount of heating produced in a metal nanoparticle can be calculated by considering a sphere in a uniform electric field where the radius of the sphere is smaller than the wavelength of the field. Ditmire et al. (1996) gives the rate of heating in Wm^{-3} for a nanoparticle as,

$$\frac{dH}{dt} = \frac{9\omega^2\omega_p^2 f_{coll}}{c} \frac{I_{las}}{9\omega^2(\omega^2 + f_{coll}^2) + \omega_p^2(\omega_p^2 - 6\omega^2)} \tag{6.1}$$

where ω is the laser frequency, ω_p is the plasma frequency, f_{coll} is the electron-ion collision frequency, and I_{las} is the laser intensity. The collision frequency is (Zel'dovich and Raizer 1966, p419),

$$f_{coll} = \frac{4}{9}\sqrt{2\pi}\,\frac{Z^2 e^4 N_{ion}}{m_e^{1/2}(k_b T_e)^{3/2}(4\pi\varepsilon_o)^2} \tag{6.2}$$

where N_{ion} is the ion density, Z is the charge on the ions, and T_e is the electron temperature. In using these equations, the density of the nanoparticle is assumed to be that of the metal and can be treated as spherical solid density plasmas with a free electron density determined by the number of valence electrons in the metal. Equation 6.1 then represents inverse bremsstrahlung absorption for a sphere.

The laser energy is deposited in the electron gas and the equilibration time between the electrons and ions should, therefore, be considered. This is given by the solution to (Zel'dovich and Raizer 1966 p 421),

$$\frac{\partial T_e}{\partial t} = -\frac{T_e - T_i}{\tau_{eq}} \tag{6.3}$$

where τ_{eq} is the equilibration time given by (Zel'dovich and Raizer 1966 p 421),

$$\tau_{eq} = \frac{18 m_e m_i \varepsilon_o^2 \pi^2}{\sqrt{2\pi} N_i Z^2 e^4} \left(\frac{k_b T_e}{m_e} \right)^{3/2} \tag{6.4}$$

and is on the order of 10^{-14} s for a plasma at the density of a solid. Since the laser pulse has a FWHM = 30 ns, the heating will be in equilibrium so that a two temperature plasma does not need to be considered.

The heating rate for a nanoparticle can be quite large. For example, an Al nanoparticle initially at 5000 K in a 308 nm field at an intensity of 1.0×10^{13} Wm^{-2} , has a heating rate ~

7×10^{12} °Ks^{-1}. This is nearly the same as the bulk heating rate from equation 2.7 which is ~ 5×10^{12} °Ks^{-1} and indicates that rapid heating of nanoparticles can occur.

6.2.2. Ionization and vaporization of metal nanoparticles

As nanoparticles are heated, they will undergo ionization and vaporization. Nanoparticle ionization can occur from thermal electron emission. To calculate the rate of emission it is assumed that the electrons have a Maxwellian velocity distribution and only those electrons with an energy greater than the work function of the metal and the Coulomb attraction to the nanoparticle can escape. A further constraint is that only electrons within one mean free path of the surface can escape. Applying these conditions and integrating the Maxwellian velocity distribution over the surface of a sphere, the thermal electron emission rate in s^{-1} is (Ditmire et al. 1996),

$$R_{es} = \frac{N_e\sqrt{8\pi}}{(m_e k_b T)^{1/2}}(k_b T_e)\exp(-K_{esc}/k_b T_e)\times\begin{Bmatrix} L_{mfp}(12r^2 - L_{mfp}^2)/4r, L_{mfp} < 2r \\ 4r^2, L_{mfp} > 2r \end{Bmatrix} \quad (6.5)$$

where T_e is the electron temperature, N_e is the free electron density, r is the radius of the nanoparticle, K_{esc} is the energy required for electrons to escape, and L_{mfp} is the mean free path of the electrons. L_{mfp} can be calculated from the electron-electron collision frequency, f_{ee}, and the average thermal speed of the electrons, v_e, (Zel'dovich and Raizer 1966, p 419). Dividing v_e by f_{ee} gives,

$$L_{mfp} = \frac{9}{4\pi} \frac{(4\pi\varepsilon_o)^2 (k_b T_e)^2}{N_e e^4} \tag{6.6}$$

where N_e is the electron density. K_{esc} is the sum of the work function and the Coulomb attraction to the nanoparticle. This can be written as,

$$K_{esc} = K_{WF} + \frac{Qe^2}{4\pi\varepsilon_o r} \tag{6.7}$$

where Q is the charge on the nanoparticle. This also depends on the radius, r, of the nanoparticles. The amount of charge will dramatically affect the thermal electron emission rate and, therefore, the rate of ionization due to the exponential dependence on the Coulomb charge in equation 6.5. This, however, also depends on the rate of heating.

Photoemission also lends to ionization. The rate for a spherical nanoparticle is,

$$R_{pe} = \eta \frac{I}{h\nu} 2\pi r^2 \tag{6.8}$$

where I is laser intensity and η is the quantum efficiency for photoemission. For Al, $\eta \sim 10^{-4}$ at UV laser wavelengths (Kawamura et al. 1984) and R_{pe} is comparable to R_{es} at the intensities considered.

Nanoparticles will also be vaporized reducing the size and the charge on the nanoparticle. The emission rate of atoms or ions can be calculated from the classical Rice-Ramsperger-Kassel (RRK) theory (Jarrold 1994, Haberland 1994),

$$R_{diss} = \nu\left(1 - \frac{D(n)}{sk_b T_e}\right)^{s-1} \tag{6.9}$$

where ν is the vibrational frequency of the atoms in the nanoparticle, $D(n)$ is the dissociation energy that must be overcome for a particular species, atom or ion, to leave the nanoparticle, and $s=3n-6$, where n is the number of atoms in the nanoparticle, is the number of ways of distributing the energy of a particular species in the nanoparticle. This, of course, is a statistical equation derived from classical statistics and requires a large ensemble. Haberland (1994) has shown that for large nanoparticles with $n > 20$, the classical RRK theory is satisfactory. To make use of this equation, the dissociation energy $D(n)$ must be defined. Three cases are considered: (1) vaporization of a neutral atom from a neutral nanoparticle, (2) vaporization of a neutral atom from an ionized nanoparticle, (3) ejection of an ion from an ionized nanoparticle. For (1), the dissociation energy is (Brechignac 1994),

$$D(n,1) = E(X_n) - E(X_{n-1}) - E(X_1) \tag{6.10}$$

where E is the binding energy of the nanoparticle containing n atoms of species X. This just depends on the difference between the binding energy of the nanoparticle and its fragments. For (2), $D(n)$ for a nanoparticle with a charge Q is,

$$D^{Q+}(n,1) = E(X_n^{Q+}) - E(X_{n-1}^{Q+}) - E(X_1) \tag{6.11}$$

For removal of an ion, the dissociation energy is,

$$D_{ion}^{Q+} = E(X_n^{Q+}) - E(X_{n-1}^{(Q-1)+}) - E(X_1^{+}) - E_{Coul} \tag{6.12}$$

where the Coulomb repulsive energy should be included for the separated ion. This lowers the dissociation energy and therefore increases the ion emission rate.

The binding energy $E(X_n)$ associated with equations 6.10 - 6.12 is different from the binding energy in the bulk material due to the finite size of the nanoparticles. Since most of the atoms are contained on the surface of a small nanoparticle (~ 2nm), the lattice constant can have an entirely different value than inside the nanoparticle thus changing such properties as the density of states. This, in turn, affects the binding energy. Skala (1985) has shown by decomposing an infinite crystal into a collection of identical non-interacting nanoparticles that the density states of the nanoparticle system is asymptotically related to the density of states of the bulk as follows,

$$g_{clust}(E) \leq g_{bulk}(E) - \frac{const}{n^{1/d}} \tag{6.13}$$

where n is the number of atoms in the nanoparticle and d is the dimension. The constant depends on the crystal structure. This asymptotic formula shows that as the nanoparticle grows it begins to take on the properties of the bulk. Using equation 6.13, Skala (1985) finds the binding energy per atom for a 3 - dimensional nanoparticle to be,

$$\frac{E_{bind}}{n} = E_{bulk} - \frac{const \times E_{bulk}}{n^{1/3}} \tag{6.14}$$

Using experimental values for binding energies for Al nanoparticles in the size range 2 - 100 atoms (Ray et al. 1989, Jarrold 1994), the constant in equation 6.14 is found to be ~1. For Al, the binding energy of a nanoparticle with n atoms (equation 6.10) is therefore,

$$E(Al_n) = 3.36n - 3.36n^{2/3}(eV) \tag{6.15}$$

where 3.36 eV is the binding energy of the bulk. For a charged nanoparticle, the ionization potential of the nanoparticle as well as the ionization potential of an atom must be included since this affects the binding energy of the atoms. Brechignac (1994) gives the binding energy for a charged nanoparticle as follows,

$$E(Al_n^{Q+}) = 3.36n - 3.36n^{2/3} + 2Q - \frac{e^2}{8\pi\varepsilon_o r_{ws}}\left(Q^2 - \frac{1}{4}Q\right)n^{-1/3}(eV) \tag{6.16}$$

where r_{ws} is the Wigner-Sietz radius (Sugano 1991) = 0.16 nm for Al. Substituting equations 6.15 and 6.16 into 6.10- 6.12 gives for the nanoparticle dissociation energies of atoms and ions,

$$D(n,1) = 3.36(1 + (n-1)^{2/3} - n^{2/3}) \tag{6.17}$$

$$D^{Q+}(n,1) = D(n,1) + (Q^2 - \frac{Q}{4})\frac{e^2}{8\pi\varepsilon_o r_{ws}}((n-1)^{-1/3} - n^{-1/3}) \tag{6.18}$$

$$D_{ion}^{Q+} = \left\{ \begin{array}{l} D(n,1) + \frac{e^2}{8\pi\varepsilon_o r_{ws}}\left(\frac{3}{4} + \left[(Q-1)^2 - \frac{Q-1}{4}\right](n-1)^{-1/3} - \left[Q^2 - \frac{Q}{4}\right]n^{-1/3}\right) \\ -\frac{(Q-1)e^2}{4\pi\varepsilon_o r_{ws}}(n-1)^{-1/3} \end{array} \right\} \tag{6.19}$$

as a function of the number of atoms and the charge in the nanoparticles. These are the energies that must be overcome before an ion or an atom can dissociate from a nanoparticle. Generally, the nanoparticle dissociation energy for atoms increases with nanoparticle size and charge since the binding energy increases. For ions, however, the nanoparticle dissociation energy decreases with increasing charge due to the Coulomb repulsion term but still increases with nanoparticle size.

Substituting equation 6.18 and 6.19 into 6.9 gives the emission rate of atoms and ions from charged nanoparticles. This only depends on temperature, nanoparticle size, and charge. The vibrational frequency of the atoms is assumed to be constant. For ions, this rate will increase with charge and temperature and decrease with increasing nanoparticle size, while for atoms, the rate decreases with an increase in charge.

If the charge is large enough, then the dissociation energy for ions can be negative due to Coulomb repulsion and the ions can dislocate from their equilibrium positions. Equation 6.9 is, therefore, not valid as it assumes that the ions are in equilibrium with a vibrational frequency ν. In this case, the ions can be assumed to have a maxwellian velocity distribution as they are free to leave the nanoparticle. The ion emission rate can, therefore, be calculated from equation 6.5 and is given as,

$$R_{es} = \frac{N_i\sqrt{8\pi}}{(m_a k_b T)^{1/2}}(k_b T_e)\exp(-D_{ion}^{Q+} / k_b T_e) \times \begin{Bmatrix} L_{ion}(12r^2 - L_{mfp}^2) / 4r, L_{ion} < 2r \\ 4r^2, L_{ion} > 2r \end{Bmatrix} \quad (6.20)$$

Here, the dissociation energy for the ions is used. This rate, therefore, depends on the thermal and repulsive energies of the ions. The mean free path of the ions, L_{ion}, is dominated by the collision frequency between ions and atoms and is given by,

$$L_{ion} = \frac{1}{1.256 \times 10^{-19} N_a} \quad (6.21)$$

where the numerical factor is the collision cross-section and N_a is the atomic density of the nanoparticle. The ion-ion collision frequency is much smaller.

6.2.3 Production of free electrons and ions

Since ions are ejected from the nanoparticles, the ionization of a nanoparticle proceeds as a competition between emission of electrons and emission of ions. Initially, thermal and

photo-emission of electrons creates a charge on a nanoparticle. As the charge increases, the thermal electron emission rate decreases, due to Coulomb attraction, while the ion emission rate increases, due to Coulomb repulsion. This, however, reduces the charge on the nanoparticle and the electron emission increases again which in turn increases the ion emission rate. The result is that the competition between emission of electrons and emission of ions generates free electrons and ions.

As nanoparticles are heated, the electron and ion emission rates will increase with temperature (figure 6.1) thus increasing the emission and temperature of free electrons and ions over time. The nanoparticle size, however, decreases due to ejection of atoms and ions. This reduces the dissociation energy (equation 6.19) and results in a faster increase in the ion emission rate (figure 6.2). The electron emission rate also increases due to decreasing charge. As a result, an avalanche type ionization can occur as the electrons and ions are ejected at an increasing rate. This process can produce an exponential increase in the free electron and ion densities as the nanoparticles become smaller. Depending on the size and number of nanoparticles, the number of free electrons and ions can be quite large. For example, Al nanoparticles 2 nm in size with ~ 2000 atoms per nanoparticle and number density 10^{21} m^{-3}, being continuously heated, could conceivably produce an electron and ion density of ~ 2×10^{24} m^{-3} if the nanoparticles completely ionize. If the nanoparticles were 5 nm, the number of atoms increases to ~ 31000 and the free electron and ion densities could reach ~ 3×10^{25} m^{-3}. Atomic vaporization of the nanoparticles will, however, reduce the number of free electrons and ions generated since there would be less atoms in a nanoparticle to ionize.

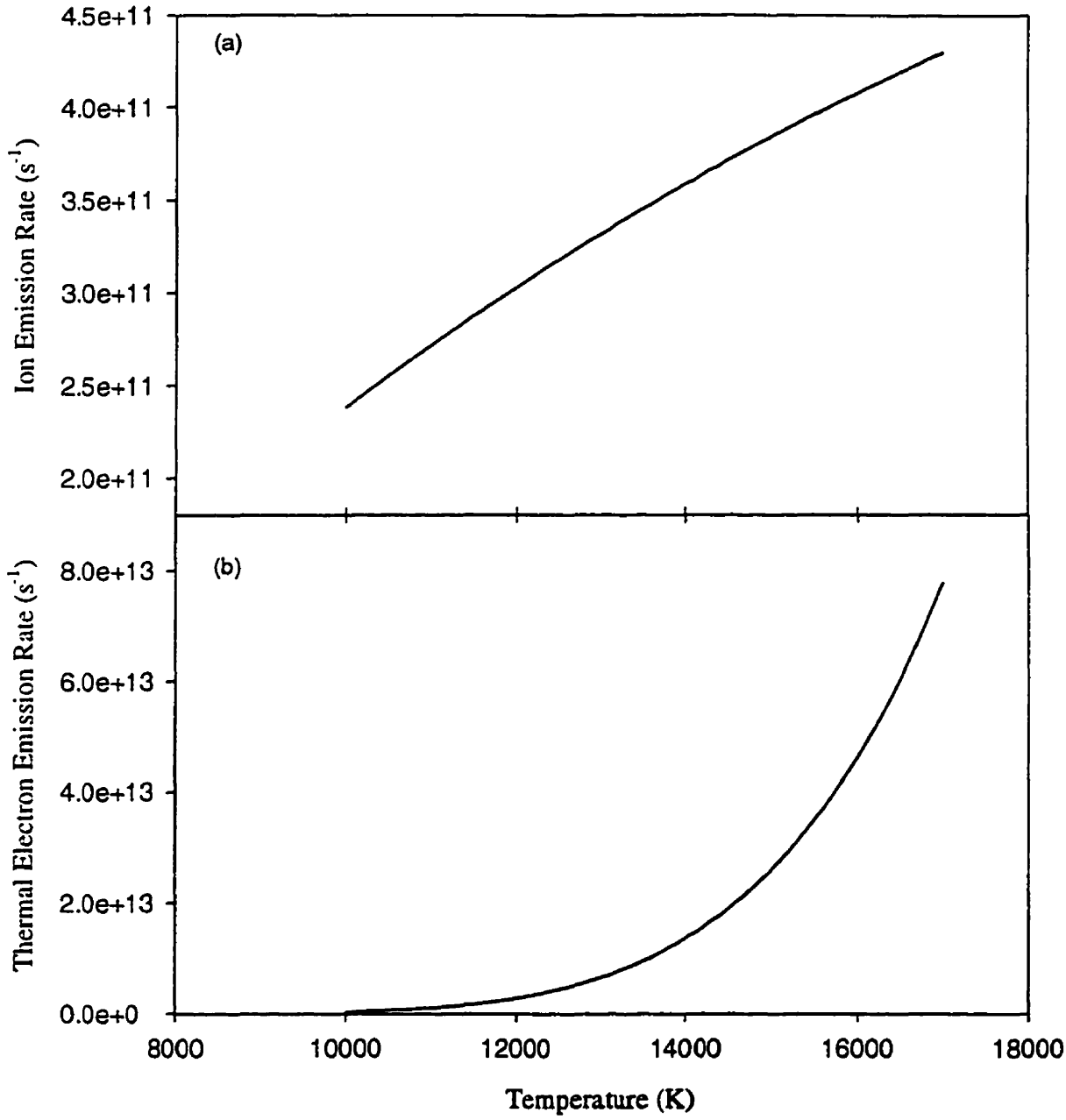

Figure 6.1. a) Ion emission rate as a function of temperature for an Al nanoparticle 5 nm in size with a charge Q = 15. The vibrational frequency for Al is ~ $1\times10^{12}\,s^{-1}$ (Kittel 1986). b) Thermal electron emission for the same conditions as in (a).

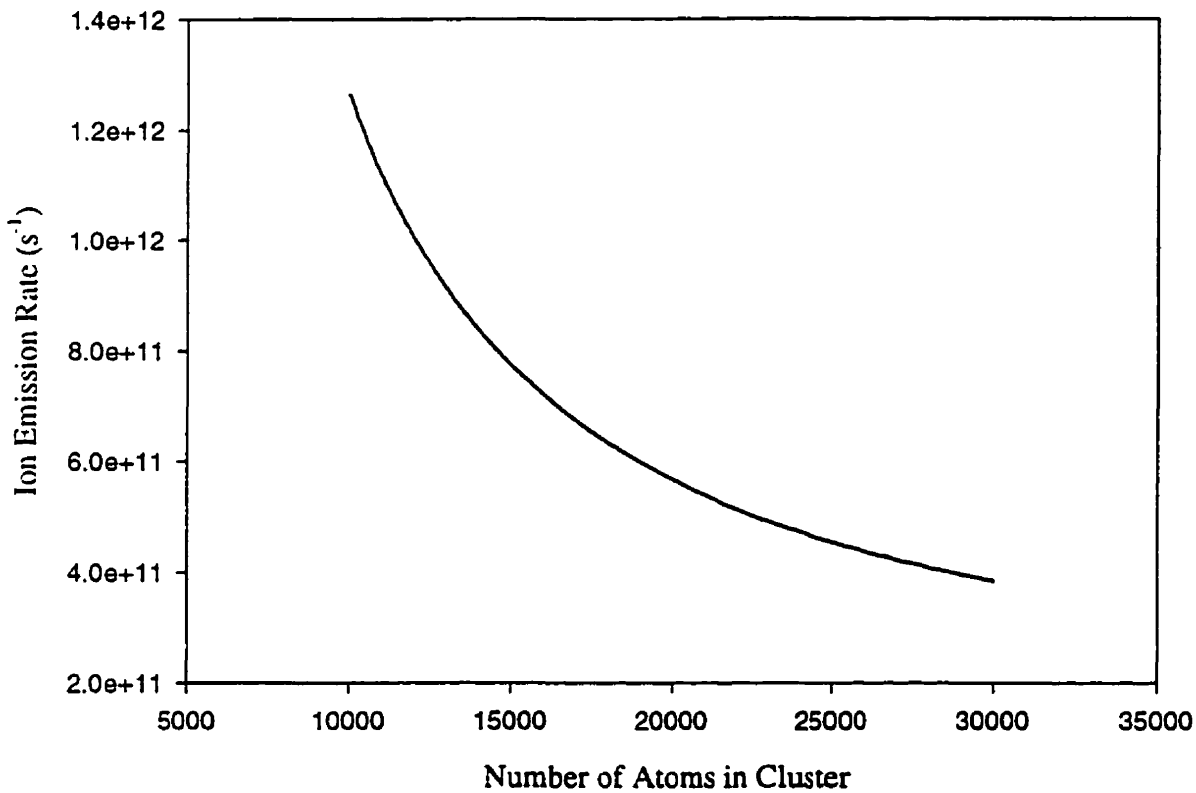

Figure 6.2. Ion emission rate as a function of decreasing nanoparticle size. The temperature is 15000 K and Q = 15.

The ejected electrons and ions can recombine but can also ionize the neutral vapor in the plume as they will normally have higher temperatures than the vapor, due to nanoparticle heating. This can result in larger electron densities than obtained by nanoparticle ionization. The process is governed by three-body recombination and collisional ionization as these are the dominant processes at electron densities $> 10^{23}$ m^{-3} (Zel'dovich and Raizer 1966, p405). For Al, the recombination and ionization rates by electrons in number of electrons per cubic meter per second are given by (Zel'dovich and Raizer 1966, p390),

$$\begin{aligned} Z_{Rec} &= 2.199 \times 10^{-36} \frac{N_e^2 N_i}{T_e} \\ Z_{Ion} &= 4.838 \times 10^{-15} \exp(-2.9e / k_b T_e) N_e N_* T_e^{1/2} \end{aligned} \tag{6.22}$$

where N_e and N_i are the electron and ion densities, and N_* is the density of Al in the first excited state ($3s^2 4s\ ^2S$). These rates are for the reaction,

$$Al^* + e^- + 2.9\ eV \leftrightarrow Al^+ + 2e^-$$

discussed in chapter 2 where Al^* refers to the first excited state in Al. This reaction is used since Al atoms in the first excited state are more abundant than in higher excited states. Collisional ionization and recombination by ions is not considered as this process is relatively weak compared to electron processes (Zel'dovich and Raizer 1966, p399).

Production of free electrons and ions can, therefore, occur by two processes: ionization of nanoparticles and ionization of the plume by the ejected electrons and ions.

6.2.4 Production of high energy ions

Once nanoparticles begin to ionize and ions are ejected, a charge can develop on the nanoparticles since the electron emission rate can be greater than the ion emission rate (figure 6.1). The Coulomb force between the nanoparticles and the ion can, therefore, produce quite a strong acceleration for the ejected ion. This can produce high energy ions as observed in section 5.3. This is often referred to as a Coulombic explosion of nanoparticles (Purnell et al. 1994, Codling and Frasinski 1994). For the nanoparticles examined here one can consider the Coulomb force on an ion outside a charged sphere with charge Q and radius r,

$$F = \frac{Qe^2}{4\pi\varepsilon_o r^2} \tag{6.23}$$

which will impart a net acceleration to the ion given by $a = F/m$. The amount of acceleration and, therefore, energy gained by the ion will depend on the amount of charge on the nanoparticle and the nanoparticle size when the ion is ejected.

6.3 Numerical Calculations and Comparison with Results

6.3.1 Ionization of the plume

Figures 6.3 shows the results for the laser heating and ionization of Al nanoparticles with a size of 5 nm and an initial internal temperature of 5000 K, at 3 different laser intensities. The nanoparticle number density is 10^{21} m^{-3} and the vibrational frequency of the atoms in the nanoparticles is 1×10^{12} s^{-1} (Kittel 1986). The nanoparticles are assumed to be contained in an Al vapor plume with a density ~ 2×10^{26} m^{-3}, from simulations, and irradiated by an excimer laser pulse with a rise time of 10 ns and a fall time of 50 ns. The heating is assumed to begin ~ 3 ns after the start of the laser pulse since this is the time required for an Al surface to reach ~ 5000 K and begin substantial vaporization. At 10^{13} Wm^{-2}, the laser rapidly heats the nanoparticles to ~ 16500 K in 1.8 ns. The nanoparticle size decreases as the electrons and ions are emitted and the free electron and ion densities increase. As the nanoparticle becomes smaller the ion and electron emission rates increase as previously discussed and the nanoparticles rapidly vaporize by ~ 4.8 ns. The maximum electron and ion densities reached are ~ 9.0×10^{24} m^{-3}. This density is not higher because the nanoparticles also experience atomic vaporization which reduces the nanoparticle sizes before they have a chance to generate more electrons and ions. At 5.6×10^{12} Wm^{-2}, the nanoparticles heat at a slower rate, and the electron and ion emission rates are smaller resulting in the nanoparticles lasting for a longer period of time. The free electron and ion densities are less since the nanoparticles will experience more atomic vaporization. At 2×10^{12} Wm^{-2}, the electron and ion emission rates are small due to the low heating of the nanoparticles and the vaporization of the nanoparticles occurs mostly by atomic

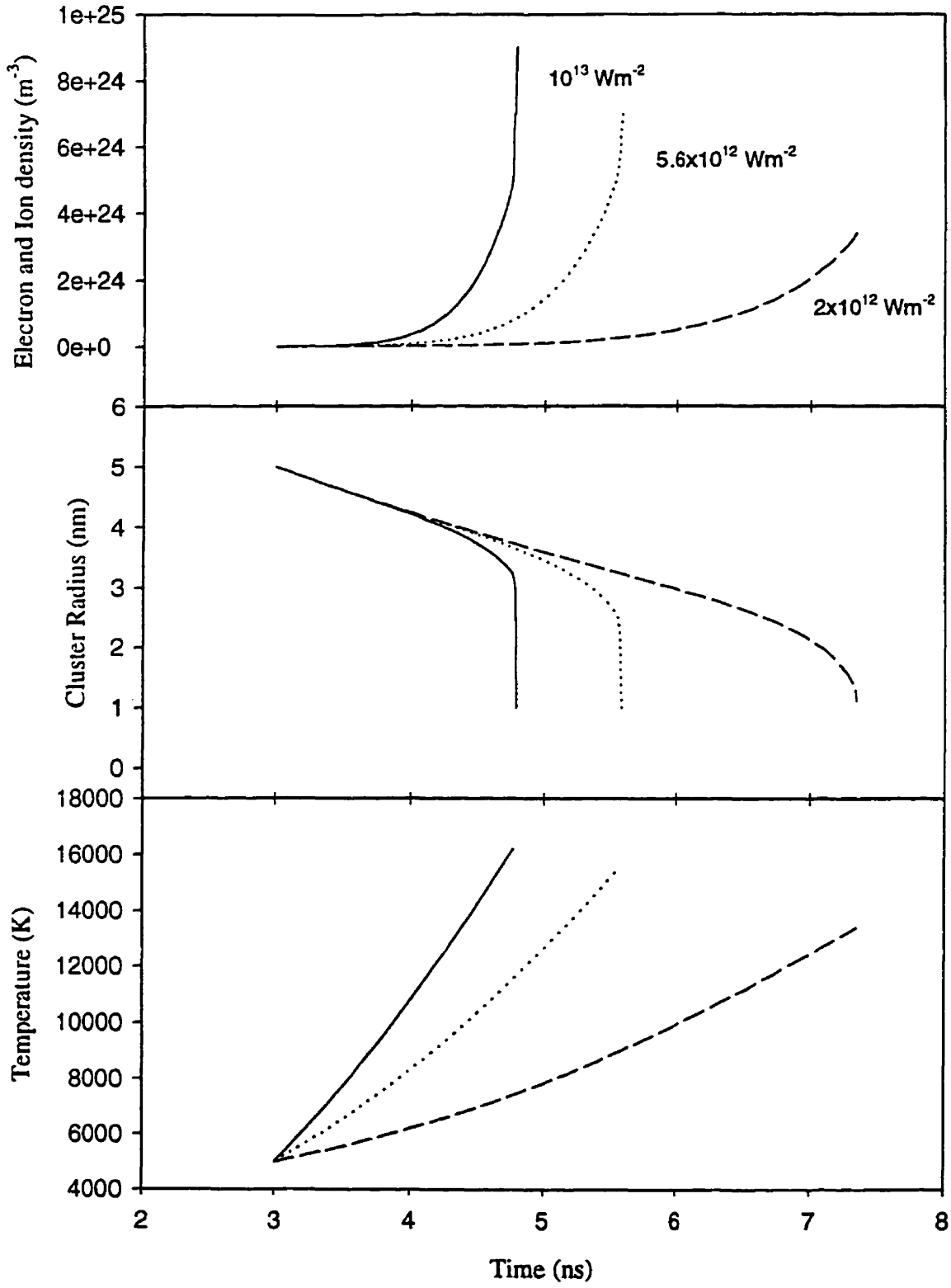

Figure 6.3. Results for the ionization of 5 nm Al nanoparticles in an Al vapor plume, at laser intensities of 10^{13}, 5.6×10^{12}, and 2×10^{12} Wm^{-2}. The laser wavelength is 308 nm.

vaporization. The electron and ion densities produced are $\sim 10^{24}$ m^{-3} and the lifetime of the nanoparticles is ~ 4.5 ns.

These results show that nanoparticles ionize and vaporize within in a few nanoseconds due to rapid laser heating. Even at relatively low laser intensities, the nanoparticles can only survive ~ 4.5 ns. This is an important result since the rates of nanoparticle vaporization, ~ 0.8 to 2.25 nm/ns, are greater than the rates of nanoparticle growth found by Callies et al. (1998) suggesting that nanoparticles cannot form from condensation in the plume during the laser pulse. Since nanoparticles were detected in section 5.4 for ~ 30 ns, the nanoparticles must, therefore, be ejected from the molten surface of the target as this is the only other source of nanoparticles (Kelly and Rothenberg 1985).

These results also indicate that the nanoparticle sizes determined in section 5.4 should actually be larger since the scattered signal was averaged over 10 ns but the nanoparticles are vaporized in under 5 ns. To compare the model to the results, the nanoparticle sizes in figure 6.2 should be averaged over 10 ns. This gives nanoparticle sizes in the range of 2 to 3 nm. This is very close to the experimentally determined sizes and suggests that the nanoparticles emitted from the target are ~ 5 nm in size.

The electron densities generated by nanoparticle ionization are smaller than calculated in section 5.4. However, since nanoparticles are most likely ejected from the target surface, continuous ionization of nanoparticles can occur throughout the laser pulse with the most intense ionization occurring at the peak of the pulse where the intensity is highest as shown in figure 6.4. Here, the electron and ion density can be larger due to an increased heating rate and the nanoparticles survive for a shorter period of time. The free electron

and ion densities can, therefore, increase over time. For example, at 10^{13} Wm^{-2}, the free electron density could rise to ~ 1×10^{26} m^{-3} in 10 ns assuming the number density of nanoparticles remains constant. In addition to the continuous ionization of nanoparticles, these electrons and ions can collisionally heat and ionize the vapor over time as the electron density and temperature increase (figure 6.4). The heating is dominated by ion-atom collisions due to the heavy mass of the ions. Heating by electrons occurs at a much slower rate due to their low mass. This heating rate can be calculated from,

$$\frac{dT}{dt} = \frac{N_i}{N_a}\frac{\Delta T}{\tau_{ion-atom}} \tag{6.24}$$

where N_i is the ion density, N_a is the density of the vapor, ΔT is the temperature difference between the vapor and the ejected ions, and $\tau_{ion\text{-}atom}$ is the time between collisions given as (Zel'dovich and Raizer, p 421 1966),

$$\tau_{ion-atom} = \frac{1}{1.256\times10^{-19}N_a}\sqrt{\frac{\pi m_a}{8k_b T_i}} \tag{6.25}$$

The heating rate can be quite large. For example, from figure 6.3 at a laser intensity of 10^{13} Wm^{-2}, the average ion density over the vaporization period is ~5×10^{23} m^{-3}. Substituting into equation 6.24 with a vapor density of 2×10^{26} m^{-3} and using an average temperature difference between the vapor and the ejected ions of ~ 6000 K gives dT/dt ~ 1.2×10^{12} Ks^{-1}. This heating rate will increase as the temperature and number of ejected

ions increases. The vapor temperature can, therefore, rise very quickly over time and in ~ 7 ns can reach ~ 13500 K, assuming continuous ionization of nanoparticles so that a fresh supply of ions exists. As the vapor heats, cooling electrons can collisionally ionize excited atoms as shown in figure 6.5 assuming a vapor density of 2×10^{26} m^{-3} and temperature of ~ 7000 K from heating. The recombination rate of the ejected electrons and ions is also shown. These were calculated using the values in figure 6.3. As can be seen, initially little ionization occurs but as the electron density and temperature increases, the ionization rate of the plume rises exponentially. The recombination rate between electrons and ions is much smaller. This indicates that ionization of the plume by the ejected electrons can be important in increasing the electron density. For example, at 10^{13} Wm^{-2}, the average ionization rate over the 1.7 ns that nanoparticles are ionized is ~ 2×10^{34} $m^{-3}s^{-1}$. If this rate is maintained over time which can occur if nanoparticles are continuously ionized (figure 6.4) and the vapor is heated, then the electron density in the plume with the ionization beginning at 3 ns could reach ~ 1.4×10^{26} m^{-3} 10 ns after the start of the laser pulse which is greater than that produced by nanoparticle ionization. The recombination between electrons and ions will be limited because of collisional vapor heating by ions and plasma heating that occurs by inverse bremsstrahlung absorption at a density ~ 3×10^{25} m^{-3} (figure 2.9). As the intensity is lowered, the ionization rate will decrease. At 5.6×10^{12} Wm^{-2}, the average rate is ~ 1.2×10^{34} $m^{-3}s^{-1}$ and by 10 ns the electron density in the plume can rise to ~ 8.4×10^{25} m^{-3} whereas nanoparticle ionization alone would produce ~3×10^{25} m^{-3} while at 2×10^{12} Wm^{-2}, the average electron density in the plume at 10 ns would be ~ 1.4×10^{25} m^{-3}.

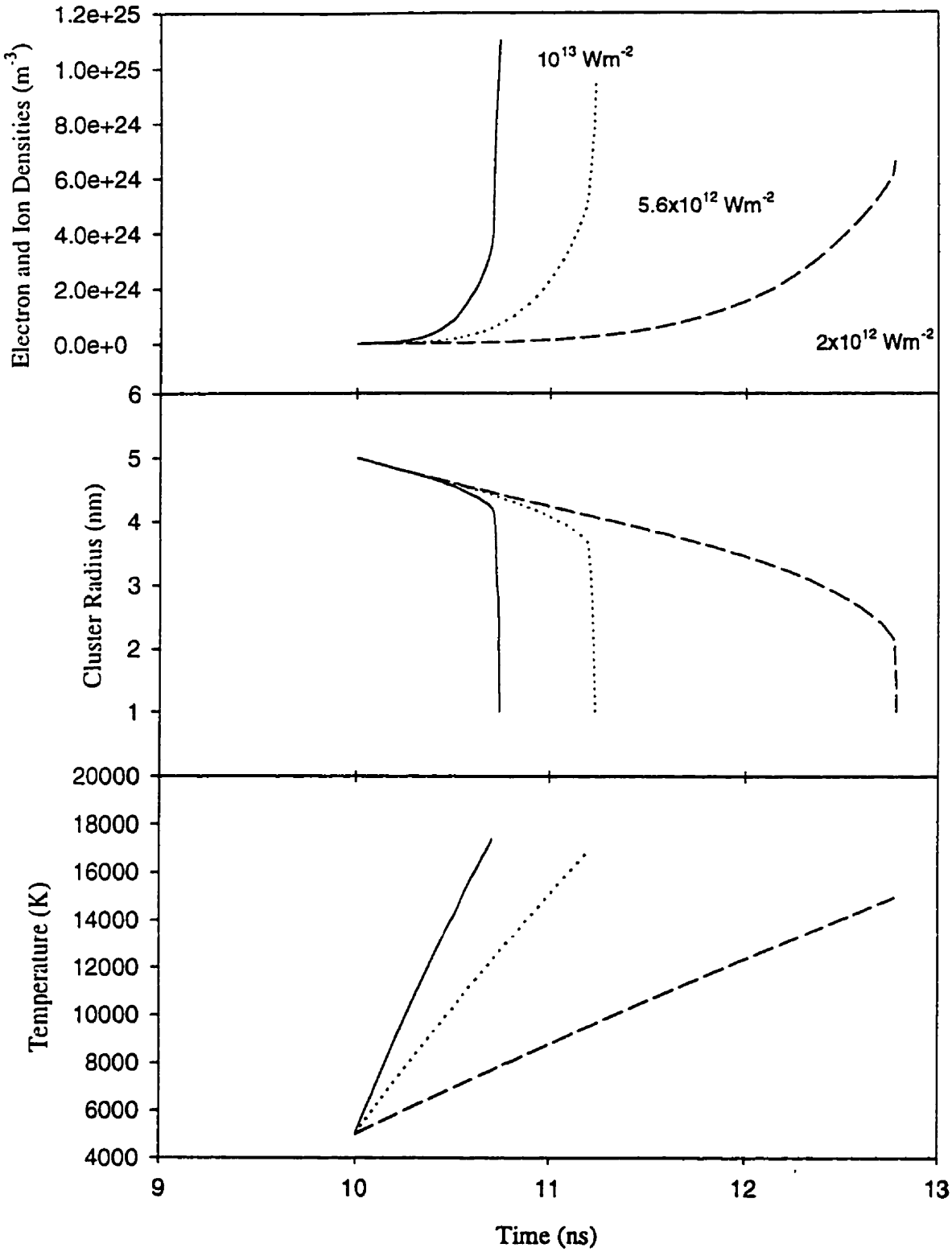

Figure 6.4. Results for the ionization of 5 nm Al nanoparticles in an Al vapor plume, for the same conditions as in figure 6.3. Ionization starts at 10 ns.

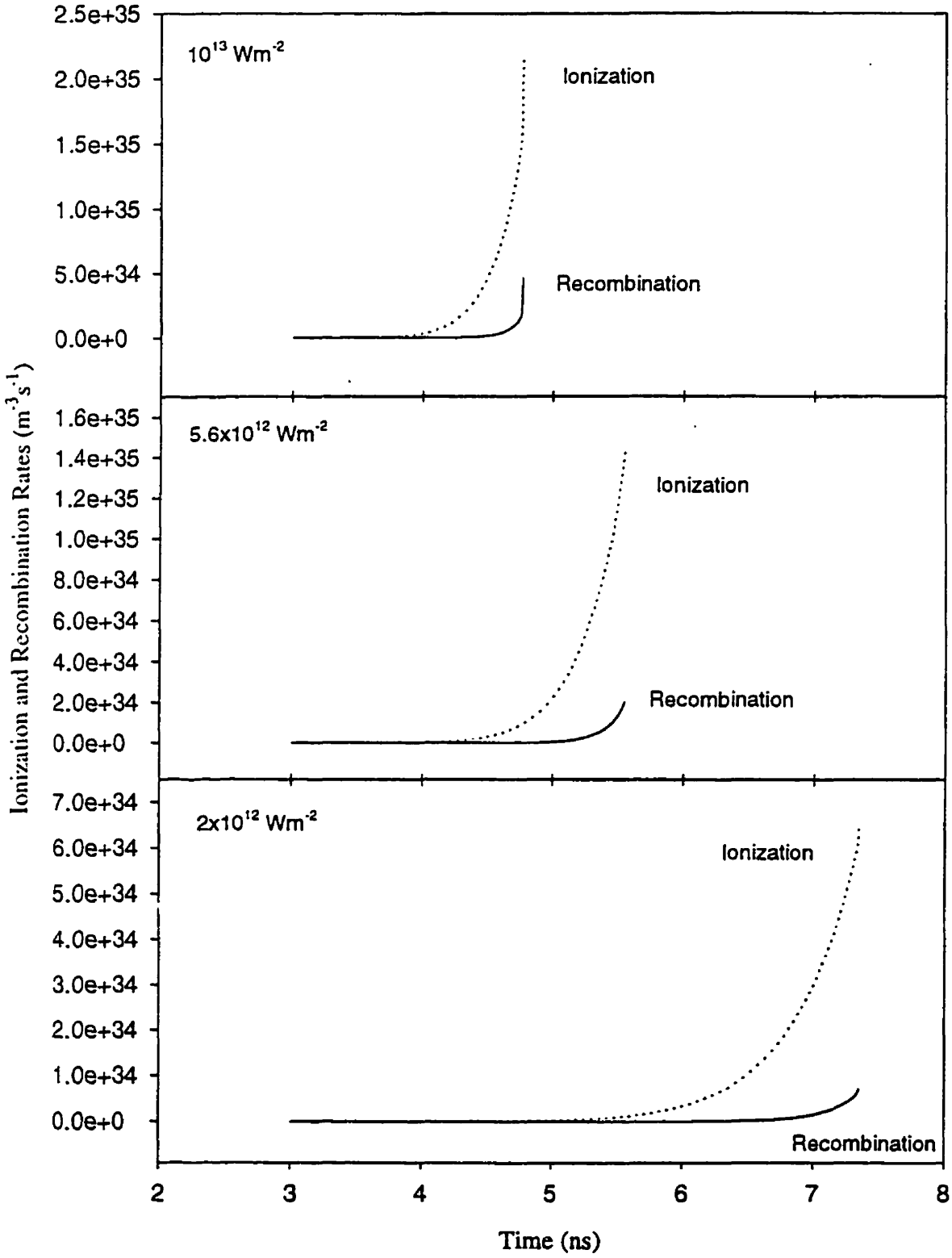

Figure 6.5. Ionization rates of the vapor by ejected electrons, and recombination rates of the ejected electrons and ions using the values in figure 6.3.

Comparison between the electron densities generated by this process at 10 ns with the electron densities measured in section 5.4 for inverse bremsstrahlung absorption is shown in table 6.1. Good agreement exists between theory and experiment. The calculated electron density may be slightly lower due to using average values but should still be comparable.

This result shows that the ionization of nanoparticles can be very important in increasing the electron density in the plume when no resonant ground state transitions occur. However, ionization of nanoparticles alone is not sufficient. It is necessary that the ejected electrons and ions collisionally ionize the vapor to further increase the electron density.

Table 6.1. Comparison of electron densities generated by nanoparticle ionization with the electron densities inferred in section 5.4

Laser intensity Wm^{-2} ($\times 10^{12}$)	Calculated electron density (m^{-3}) ($\times 10^{25}$)	Inferred electron density (m^{-3}) ($\times 10^{25}$)
10	14	15
5.6	8.4	10
2	1.4	<3

The good agreement obtained suggests that the ionization of the plume can occurs as follows: nanoparticles of size ~ 5 nm and number density ~ 10^{21} m^{-3} are ejected from the molten metal surface. This starts ~ 3 ns after the start of the laser pulse to give enough

time for the target to sufficiently heat and vaporize. The nanoparticle are then strongly heated by the laser and ionization begins and competes with ion emission. As the nanoparticles continue to heat the electron and ion emission rates increase exponentially, and greater numbers of electrons and ions are emitted with increasing temperature. Eventually, the nanoparticles vaporize and the emission stops. However, the electrons and ions have higher temperatures than the vapor and will therefore, collisionally heat and ionize the vapor. This process can continue over time since nanoparticles are being continuously ionized thus supplying more electrons and ions. As a result, the electron and ion densities can reach sufficient levels for inverse bremsstrahlung absorption at 10^{13} and 5.6×10^{12} Wm^{-2} assuming that the plasma expands to ~ 50 μm by 10 ns, but not at 2×10^{12} Wm^{-2} since the heating rate is slower and insufficient electron density is produced.

Once the electron density is sufficient for inverse bremsstrahlung absorption to occur at 10^{13} and 5.6×10^{12} Wm^{-2}, nanoparticles emitted from the surface can continue to be ionized, but the laser intensity will be lower because of absorption in the plasma. The electron densities produced by nanoparticle ionization will, therefore, substantially decrease to levels similar to the ionization produced at 2×10^{12} Wm^{-2} but the nanoparticles will still vaporize. Further ionization in the plume will be the result of inverse bremsstrahlung absorption alone. At 2×10^{12} Wm^{-2}, the electron density is too low for substantial inverse bremsstrahlung absorption at 10 ns. The ionization of the nanoparticles and plume will not produce enough electrons until late in the laser pulse, ~ 40 ns.

6.3.2 High energy ions

As nanoparticles are being ionized, a charge can develop on the nanoparticles since the electron emission rate from thermal and photon processes is larger than the ion emission rate. Figure 6.6 shows the charge that develops on the nanoparticles from figures 6.3 and 6.4. The small initial oscillation in the charge occurs since the nanoparticles start off with no charge and the thermal electron emission rate is much larger than the ion emission rate. As the charge increases, the thermal electron emission rate decreases below the ion emission rate and this decreases the charge. But once the temperature rises sufficiently the electron emission rate will again increase. The charge then increases until the ion emission rate finally becomes larger than the thermal and photoelectron emission rates (due to decreasing nanoparticle size and increasing charge) and the charge subsequently decreases to zero.

This charge creates a Coulomb repulsion between ejected ions and the charged nanoparticle which can produce a strong acceleration on the ions as they leave thus increasing their velocities. From equation 6.23, the Coulomb force and, therefore, the acceleration of the ions can be calculated. Most of the ions will gain little energy because of repulsion from neighboring charged nanoparticles. For example, at a nanoparticle density of 10^{21} m^{-3}, the nanoparticles are ~ 126 nm apart. An ion can, therefore, only be accelerated for ~ 63 nm before it is decelerated by a neighboring charged nanoparticle. However, ions that are produced near the interface between nanoparticles and the plume experience no such deceleration and are subjected to Coulomb repulsion from all the nanoparticles behind them thus producing a large acceleration (this occurs since the

electrons have much higher velocities than the ions and can, therefore, escape from the region of nanoparticle ionization leaving behind a charged "cloud" of particles). For example, nanoparticles with a charge Q = 18 and number density 10^{21} m^{-3}, contained in a spherical volume ~ 50 μm in diameter near the surface of the target can produce an initial ion acceleration equal to ~ 1.0×10^{16} ms^{-2}! This can create very high ion velocities in ~ 5 ps. The results corresponding to the maximum charges in figure 6.6 are shown in table 6.2. This was calculated assuming that nanoparticles with number density

Table 6.2 Maximum ejection velocities of ions escaping nanoparticles from figures 6.5

Intensity (Wm^{-2}) ($x10^{12}$)	Maximum Velocity (fig 6.5a) (Kms^{-1})	Maximum Velocity (fig 6.5b) (Kms^{-1})
10	28	38
5.6	24	33
2	16	23

10^{21} m^{-3} are contained in a spherical volume 50 μm in diameter which corresponds to the extent of the nanoparticles from the surface (Callies et al 1998) and that the ions are ejected from the nanoparticles at the interface between nanoparticles and the plume. The ions were accelerated for ~3 ps which is the time between ion-atom collisions in the plume assuming a vapor density of ~ 10^{26} m^{-3}.

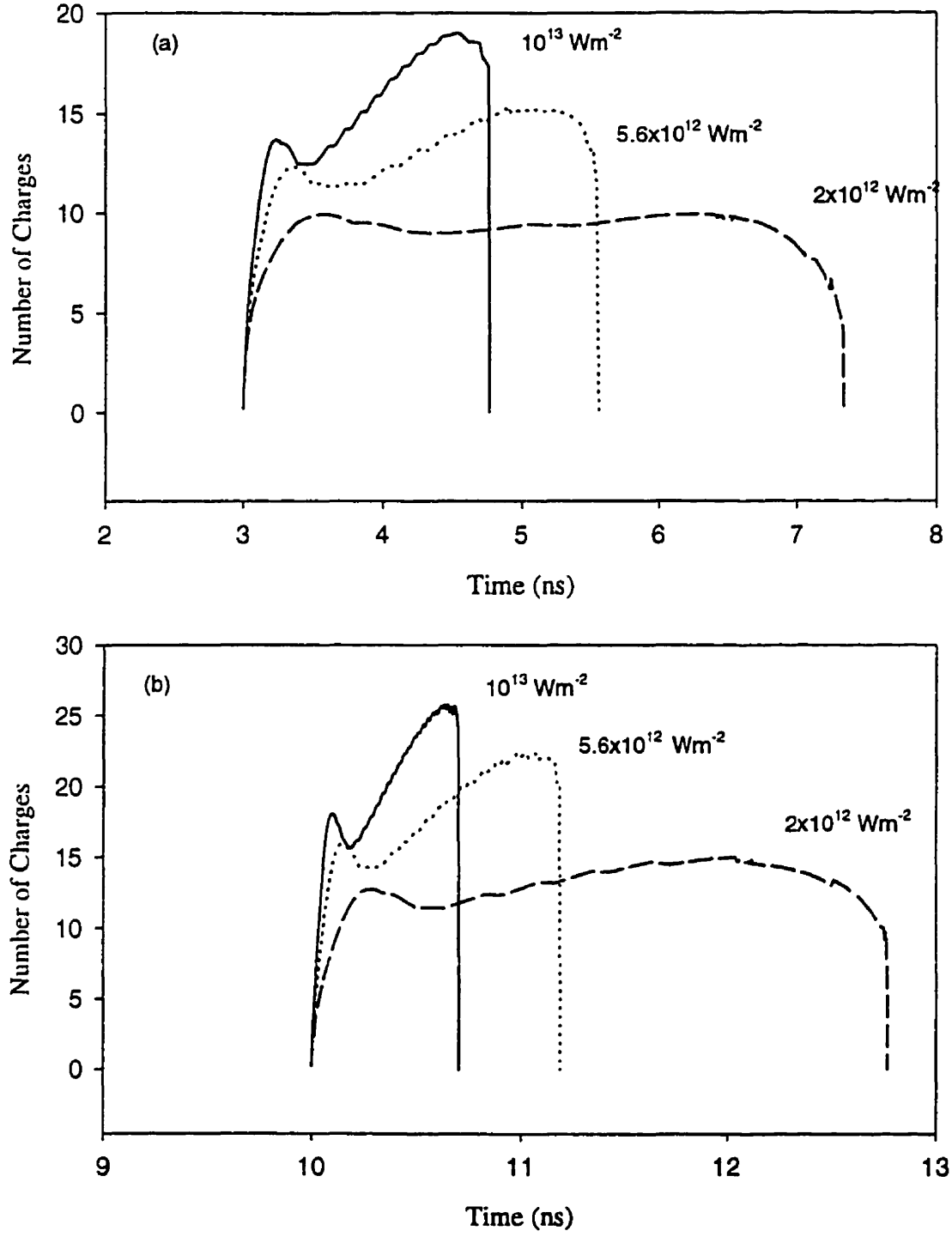

Figure 6.6. (a) Charge on nanoparticles that begin ionization at 3 ns. (b) Charge on nanoparticles that begin ionization at 10 ns. These results were obtained form the simulations in figures 6.3 and 6.4.

The ion velocities are greater for the results of figure 6.5b due to the larger charge caused by the stronger heating. These high velocities compare well to the velocities calculated from the TOF measurements as shown in table 6.3. for similar laser intensities.

Table 6.3. Measured ion velocities for the TOF results

Intensity (Wm^{-2}) ($x10^{12}$)	Measured Ion Velocity (Kms^{-1})
9.7	34
6.3	30
2.4	10

It appears that the nanoparticles that are ionized early in the laser pulse result in slightly lower ion velocities except at 2×10^{12} Wm^{-2} where the ion velocity is larger. For the nanoparticles ionized at the peak of the laser pulse, the calculated and measured ion velocities are in better agreement but the discrepancy is greater for 2×10^{12} Wm^{-2}. The reason for differences between experiment and theory is that nanoparticles are ionized continuously so that the ion velocities will be an average over a large number of ionization events with the highest velocities produced near the peak of the laser pulse where the intensity is highest. Better agreement can, therefore, be obtained by averaging the calculated velocities in table 6.2. This gives 33, 28.5, and 19.5 Kms^{-1}. The first two are closer to the measured velocities, but the last velocity corresponding to 2×10^{12} Wm^{-2} is about twice as large. This may be due to using nanoparticles that were too large in the calculations. Smaller nanoparticle would produce less charge (since the electron emission

rate would be smaller) and, therefore, less acceleration of ions. For example using nanoparticles with an initial size of 3 nm creates a charge of Q = 5 when the heating starts at 3 ns and a charge of Q = 7 when the heating starts at 10 ns. The maximum velocity of ejected ions for nanoparticles with a density of 10^{21} m^{-3} contained in a spherical region 50μm from the target would be 6.1 and 9.3 Kms^{-1} which are in much better agreement with the TOF measurements.

These results are also applicable to the doubly charged ions observed in section 5.3 since it is possible for a doubly charged ion to be ejected from a nanoparticle. This can happen by collisions as an ion is being ejected. In this case, the double charge on the ion can double the initial acceleration and thus increase the velocity to values higher than calculated in table 6.2 and indicated in table 5.1. Calculation of the velocities for the doubly charged ions, however, is not possible since the charge on the nanoparticles when doubly charged ions are created is not known.

For expansion into a background gas, such high ion velocities cannot be observed due to the shorter collision time, $\sim 5\times10^{-13}$ s, between the ions and the vapor resulting from the higher vapor density and the background gas. However, the amount of energy transfer in the collisions can explain the acceleration and the high plume propagation velocities observed in section 5.2 which are much greater than calculated in the simulations.

The good agreement found between theory and experiment confirms that high energy ions in laser induced plasmas are the result of acceleration of ions ejected from nanoparticles which are ionized in the plume and not from recombination or space-charge effects.

This final result is a good test of the model and shows the significance of nanoparticles in UV laser induced plasmas not only for plasma formation but for generation of high energy ions.

6.3.3 Discussion

The results presented here for the ionization of nanoparticles show that this is an efficient process for quickly generating large electron and ion densities in the plume when no resonant ground state transitions are present in the vapor. This is the case for the 248 nm laser irradiation of Al. At 308 nm, one should consider the resonant ground state Al transition at 308.22 nm.

The nanoparticle dissociation occurs as a result of strong laser heating with rapid electron and ion emission from nanoparticles which exponentially rise with temperature resulting in nanoparticle vaporization. These emitted electrons and ions can then ionize the vapor in the plume and generate sufficient electron densities for inverse bremsstrahlung absorption, the dominant energy transfer mechanism in UV laser-induced plasmas (assuming no resonant ground state transitions in the vapor). This depends on the laser intensity which controls the rate of heating and, therefore, the numbers of ejected electrons and ions. This can explain the initial ionization that occurs near the target surface in figure 5.10 at 248 nm.

The results also show that nanoparticles can develop a substantial charge. This causes an acceleration of ejected ions producing ions with high velocities which can be observed for laser ablation of Al into vacuum at 308 nm in which the plasma has a low density and

no shock wave is present. For laser ablation of Al into a background gas, the high ion velocities can explain the much higher plume velocities found in section 5.2. This is due to high energy ions "pushing" against the background gas causing the acceleration observed.

For the UV laser ablation of Al (see Appendix A), the good agreement found between the theoretical and experimental electron densities as well as the ion velocities shows that the plasma formation in the plume occurs as the result of the ionization of nanoparticles with an initial size of 5 nm and a number density of 10^{21} m^{-3}. These nanoparticles are ejected from the molten surface since they are rapidly vaporized and, therefore not capable of being formed in the plume. The ionization process begins as soon as substantial vaporization of the Al occurs, ~ 3 ns after the start of the laser pulse. The nanoparticles are then continuously ionized throughout the laser pulse as new nanoparticles become available from the surface. The electron densities generated by the ejected electrons are sufficient for inverse bremsstrahlung to become active and absorb the laser pulse energy. Once the electrons begin to absorb the laser pulse, rapid plasma expansion can occur as the plasma is heated. This creates an avalanche ionization (chapter 2) and the entire vapor can become ionized in ~ 30 ns as observed in section 5.2.

Nanoparticle ionization is the most likely mechanism of forming an Al plasma using 248 nm laser radiation since no resonant ground state transitions occur near 248 nm. At 308 nm, nanoparticle ionization is also important as it explains the high energy ions observed, but one should also consider the resonant ground state Al transition at 308.22 nm (see Appendix A).

Chapter 7

Conclusions

The excimer laser ablation of metals is a very complex process. Inverse bremsstrahlung absorption and cluster scattering are two competing mechanisms that can attenuate the laser pulse in the plume when no resonant ground state transitions exist in the vapor. However, neither mechanism alone is capable of explaining how the laser beam is attenuated.

The work presented in this thesis explored theoretically and experimentally the energy transfer mechanism present in the plume for the excimer laser ablation of Al with laser intensities 2×10^{12} to 10^{13} Wm^{-2} at 248 nm and 308 nm. Simulations of laser ablation at 308 nm (assuming no resonant ground state transitions, see Appendix A) indicated that the ionization level remained quite low and was insufficient for absorption of the laser pulse. The effect of

different ambient gases was minimal in increasing the level of ionization in the plume and absorption was found to only occur for intensities greater than 10^{13} Wm^{-2}.

Experimentally, the results were different. Dye laser resonance absorption indicated that the plume was strongly ionized forming a plasma at 248 nm. The plasma appeared to develop near the target under 30 ns and quickly spread throughout the entire vapor. By 40 ns, most of the vapor was ionized.

Time of flight experiments were performed to test for clusters in the plume at 308 nm. No clusters were observed. However, the ions had very high kinetic energies, > 100 eV. No mechanism was found to account for these observations. It was hypothesized that the ions might be produced by laser heated clusters that when vaporized might release high energy ions. To confirm this, optical spectroscopy performed in conjunction with scattering at 308 nm showed that clusters formed in the first 30 ns of the laser pulse. The cluster sizes were in the range of 2 - 3 nm and of density ~ 10^{21} m^{-3}. The cluster sizes decreased as the plasma began to form near 30 ns. In the latter part of the laser pulse no cluster formation was observed. Attenuation of the laser beam was found to begin ~ 10 ns after the start of the laser pulse. The clusters sizes and densities calculated showed that cluster scattering was insufficient for the observed transmission of the laser pulse through the plume. This leaves only inverse bremsstrahlung absorption as the dominant energy transfer mechanism in the plume since no resonant ground state Al transitions occurred for the 308 nm laser used (see Appendix A). The electron densities required for this were found to be ~1.5×10^{26}, 1×10^{26}, and < 3×10^{25} m^{-3} for laser intensities 10^{13}, 5.6×10^{12}, and 2×10^{12} Wm^{-2} respectively. Generation of such high electron densities early in the laser pulse were determined to not be possible by

target heating and photoionization at 248 nm. This was also the case for the 308 nm laser used (see Appendix A). This indicates that cluster ionization may be a possible mechanism of ionizing the plume.

To verify the results, a model of cluster heating and ionization was developed. In the model, laser heating of clusters produces ionization since the rate of ejection of electrons is greater than the rate of ejection of ions. As clusters continue to heat, the charge increases increasing the dissociation rate of the ions and atoms from the clusters. Once the ionic emission rate becomes large enough the clusters rapidly vaporize as the electron and ion emission rates compete thus releasing large numbers of electrons and ions with high temperatures. The ejected electrons and ions can then ionize the vapor in the plume and this can increase the electron density in the plume to levels sufficient for inverse bremsstrahlung absorption.

The model showed that 5 nm clusters with a number density $\sim 10^{21}$ m^{-3} ionized very rapidly, < 5 ns, indicating that cluster growth in the plume was not possible. Comparison with the experimental results showed that the clusters must be ejected from the molten surface of the Al with sizes ~ 5 nm. This was also confirmed by the electron densities produced by cluster ionization which agreed with measured electron densities at comparable laser intensities.

Since the clusters become ionized it was found that the high energy ions produced in the TOF results were caused by the large charge on the clusters which accelerated ejected ions by Coulomb repulsion. The calculated ion velocities were very similar to the measured ion velocities providing a good test of the model, and explaining the high propagation speeds of the plume in section 5.2.

In summary, the excimer laser ablation of Al initially produces clusters with sizes up to ~ 5 nm and densities of ~ 10^{21} m^{-3}. The clusters originate in the molten Al surface. Once the clusters are ejected into the plume laser heating strongly heats and ionizes the clusters. The ejection of the electrons and ions increases as the cluster temperature increases until the cluster vaporizes. The ions are ejected and accelerated away by Coulomb forces producing high energy ions. The electrons and ions produced are of sufficient number and have a high enough temperature that they can ionize the vapor. The ionization occurs within 10 ns and is near the target surface. Once the laser pulse energy begins to be absorbed by inverse bremsstrahlung absorption, an avalanche ionization can occur eventually ionizing the rest of the vapor.

This process is not restricted to Al. Any metal will strongly absorb UV radiation. Therefore, with excimer lasers, ablation of metals should produce clusters which are then ionized creating an absorbing plasma and high energy ions. One should, however, consider any resonant ground state transitions in the metal which can also efficiently absorb laser radiation. In this case, clusters can also be formed and high energy ions generated but the ionization process in the plume may follow a different mechanism.

APPENDIX A: XeCl Laser Emission

The wavelength and bandwidth of the 308 nm excimer laser used in the experiments is shown in figure A.1. The mercury calibration spectrum for the spectrometer is also shown in figure A.2. These spectra were obtained with a UV-VIS spectrometer of resolution 0.11nm. The XeCl emission line appears at 307.65 nm and does not overlap with the 308.22 nm ($3s^23p\ ^2P$ - $3s^23d\ ^2D$) (Reader et al. 1980) absorption line of ground state Al. Only one line is present as can be seen. This is due to the use of dielectric mirrors and the fact the laser is ~ 13 years old. Also, numerous changes have been made to the electrode assembly in the past and the gas mixture has been altered to accommodate the age of the laser. As well, the laser suffers from an alignment problem, which affects the power. A normal XeCl excimer will produce emission near 308.2 nm as discussed by McKee (1988). Substantial overlap will then occur between the laser line at 308.2 nm and the Al absorption line at 308.22 nm that ionization of Al by a 308 nm excimer laser can proceed directly from the ground state via a two-photon process.

The amount of overlap can be calculated by assuming the pulse to be Gaussian. From figure A.1 the pulse width is ~ 0.18 nm at half the maximum. The gives an intensity profile,

$$\frac{I}{I_o} = e^{-(\lambda-307.65)^2/0.011} \qquad \text{A.1}$$

The amount of collisional broadening for the absorption line can be calculated from,

$$\Delta\nu = \sqrt{\frac{3}{2}}\frac{8Pa^2}{(mkT)^{1/2}} \qquad \text{A.2}$$

Assuming a vapor pressure of ~ 1000 atm, T=6000 K, gives $\Delta\lambda = 0.1$ nm. The edge of the absorption line can, therefore, broaden to 308.17 nm. From the intensity profile, the laser intensity at 308.17 nm is,

$$I = 2.1\times10^{-11} \times 10^{13}\ \mathrm{Wm^{-2}} = 211\ \mathrm{Wm^{-2}}$$

The absorption cross-section, σ, for the Al absorption line claculated from the radiation bandwidth of the line and the oscillator strength (Reader et al. 1980) is ~ 10^{-20} m^2. Assuming a vapor density, ρ, of ~ 10^{27} m^{-3}, the amount of power absorbed per cubic meter of material is

$$P = I*\sigma*\rho = 2.1\mathrm{x}10^{9}\ \mathrm{Wm^{-3}}$$

With a laser pulse width of 30 ns, this corresponds to a photon density of $9.9\mathrm{x}10^{19}$ m^{-3} which is the density of Al atoms excited by the laser to the 3d state. Ionization of the excited state will, therefore, be limited to no more than $1\mathrm{x}10^{20}$ electrons per cubic meter which is negligibly small compared to the vapor density and not enough for inverse bremsstrahlung absorption. The actual vapor density and pressure in the plume may be much lower and this can drive the amount of ionization well below 10^{20} electrons per cubic meter.

This result demonstrates that insufficient overlap occurs between the XeCl laser line and the Al absorption band to create enough electrons to cause ionization of the vapor. It should be noted that this is a special case for the excimer laser used in the experiments. Therefore, any Al ablation experiments performed with a 308 nm excimer laser should take into account the 308.22 nm Al ground state transition.

At 248 nm, there are no resonant Al absorption lines present. Ionization of Al Vapor for KrF laser radiation should, therefore, proceed from excited states.

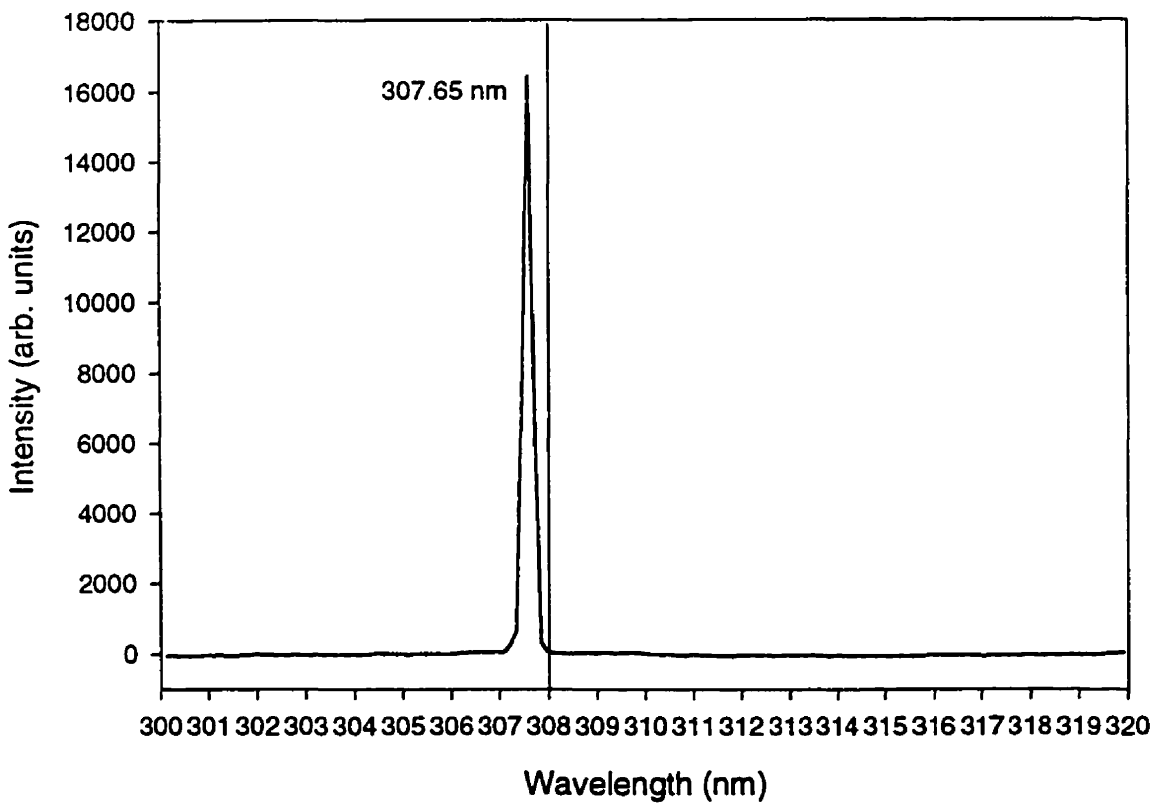

Figure A.1. XeCl laser emission measured using a UV-VIS spectrometer with a resolution of 0.11 nm.

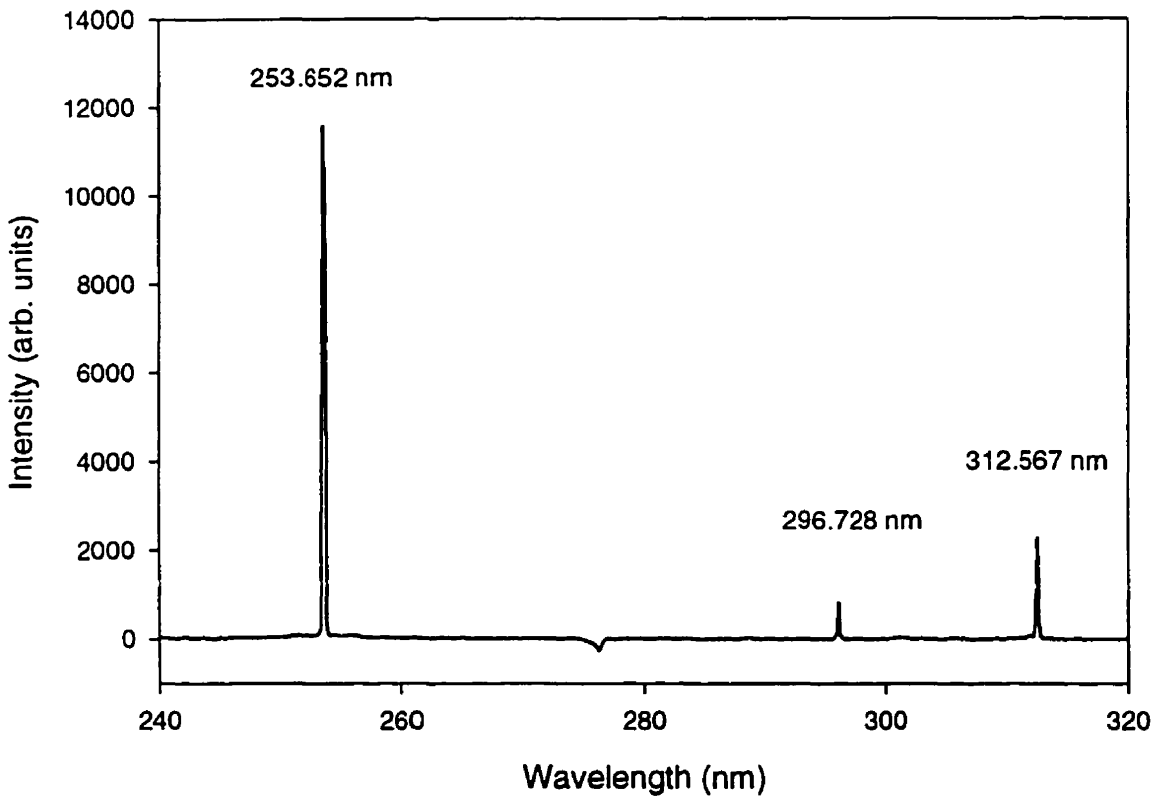

Figure A.2. Mercury calibration spectrum used to calibrate the UV-VIS spectrometer used in Figure A.1.

APPENDIX B: Riemann Problem

To solve the Riemann problem, it is best to work in Lagrangian coordinates in which the spatial variable, dx, is transformed to a mass coordinate dm=ρdx. The Euler equations can then be rewritten as (Zel'dovich and Raizer 1966, p 5),

$$\begin{aligned} &\frac{\partial V}{\partial t} - \frac{\partial u}{\partial m} = 0 \\ &\frac{\partial u}{\partial t} + \frac{\partial P}{\partial m} = 0 \\ &\frac{\partial E}{\partial t} + \frac{\partial uP}{\partial m} = Q \end{aligned} \tag{B.1}$$

where E is the total energy. Across a discontinuity such as a shock wave, equations B.1 can be integrated to give the following jump conditions (van Leer 1978),

$$\pm W(V^* - V_\pm) + (u^* - u_\pm) = 0 \tag{B.2}$$

$$\pm W(u^* - u_\pm) - (P^* - P_\pm) = 0 \tag{B.3}$$

$$\pm W(E^* - E_\pm) - (u^* P^* - u_\pm P_\pm) = 0 \tag{B.4}$$

where W is referred to as the Lagrangian shock speed dm/dt. The sign indicates the direction of propagation of the wave. Combining equation B.2 and B.3, and B.2 with A.4, W can be obtained in terms of the pressure,

$$W_{\pm} = C_{\pm}\left[1 + \frac{\gamma+1}{2\gamma}\frac{P^{*} - P_{\pm}}{P_{\pm}}\right]^{1/2} \tag{B.5}$$

where C is the Lagrangian sound speed which equals the sound speed multiplied by the density. This equation has exactly the same form as equation 3.3.

To resolve the discontinuities, Colella (1982) takes the direction of the wave in equations B.2 - B.4 as representing the left and right states at the boundaries of the cells to give,

$$W_{L,R} = C_{L,R}\left[1 + \frac{\gamma+1}{2\gamma}\frac{P^{*} - P_{L,R}}{P_{L,R}}\right]^{1/2} \tag{B.6}$$

The idea is then to find P^{*}, u^{*}, and V^{*}, the post shock values. The iteration procedure derived from equations B.2 - B.4 is as follows (Colella 1982),

$$P^{*,0} = \frac{C_L P_R + C_R(P_L - C_L(u_R - u_L))}{C_L + C_R} \tag{B.7}$$

$$\downarrow$$

$$W^{l}_{L,R} = W_{L,R}(P^{*,l-1}) \tag{B.8}$$

$$\downarrow$$

$$Z_{L,R} = \frac{2(W^{l}_{L,R})^3}{C^2_{L,R} + (W^{l}_{L,R})^2} \tag{B.9}$$

$$\downarrow$$

$$u^{*,l}_{L,R} = u_{L,R} \mp \frac{P^{*,l-1}_{L,R} - P_{L,R}}{W^{l}_{L,R}} \tag{B.10}$$

$$\downarrow$$

$$P^{*,l} = P^{*,l-1} - \frac{Z_L Z_R (u^{*,l}_R - u^{*,l}_L)}{Z_L + Z_R} \tag{B.11}$$

First an estimate of the pressure is made by replacing the lagrangian shock speed with the lagrangian sound speed which is known. This is used to estimate the post shock particle speed for the left and right states. The pressure is then adjusted depending on the particle speeds using a form similar to B.7 and the lagrangian shock speed is reevaluated. The iteration is continued until a predetermined tolerence ε given by,

$$\frac{\left|P^{*,l} - P^{*,l-1}\right|}{P^{*,l}} < \varepsilon \tag{B.12}$$

Having obtained P^*, u^*, is calculated from equation B.3 as (van Leer 1978, Colella 1982)),

$$u^* = \frac{P_L - P_R + u_L W_L + u_R W_R}{W_L + W_R} \tag{B.13}$$

Equations B.2 and B.3 are then used to obtain the density using either the left or right state depending on where the contact discontinuity is located,

$$\rho^* = \left(\rho_L^{-1} - \frac{\left(P^* - P_{L,R}\right)}{W_{L,R}^2}\right)^{-1} \tag{B.14}$$

This method of "averaging" the left and right states completely resolves the discontinuities and ensures that a smooth flow exists across shock waves.

REFERENCES

Aden, M., Kreutz, E. W., and Voss, A., *J. Phys. D: Appl. Phys.*, **26**, 1545, 1993.

Anisimov, S. I., *Soviet Phys. JETP*, **27**, 182, 1968.

Bohren C. F., and Huffman D. R., "Absorption and Scattering of Light by Small Particles", John Wiley and Sons, Inc., New York, 1983.

Bransden A.S., Megaw J. H. P. C, Balkwill P. H., Westcott C., *J. Mod. Optics*, **37**, 813, 1990.

Brechignac C., in "Clusters of Atoms and Molecules I", ed. H. Haberland, Springer-Verlag, New York, 1994.

Brosda B., Castell-Munoz R., and Kunze H-J., *J. Phys. D: Appl. Phys.*, **23**, 735, 1990.

Bykovskii Yu. A., Sil'nov S. M., Sotnichenko E. A., and Shestakov B. A., *Sov. Phys. JETP*, **66**, 285, 1988.

Callies, G., Schittenhelm, H., Berger, P., Dausinger, F., and Hugel, H., *Proc. SPIE*, **2246**, 126, 1994.

Callies, G., Berger, P., and Hugel, H., *J. Phys. D: Appl. Phys.*, **28**, 794, 1995.

Callies G., Schittenhelm H., Pinho G. P., Berger P., and Hugel H., *Proc. SPIE.*, **3092**, 398, 1997

Callies G., Schittenhelm H., Berger P., and Hugel H., in "Laser Ablation", *Proc. of the fourth International Conf. on Laser Ablation*, eds. R. E. Russo, D. B. Geohegan, R. F. Haglund Jr., and K. Murakami. p 134, 1998.

Cappelli, M. A., Paul, P. H., and Hanson, R. K., *Appl. Phys. Lett.*, **56**, 1715, 1990.

Carslaw, H. S. and Jaeger, J. C., "Conduction of Heat in Solids", 3rd edition, Oxford

University Press, London 1976.

Cercignani, C., "Rarefied Gas Dynamics", Progress in Astronautics and Aeronautics, 1981, p 305.

Cheung, N. H., Ying, Q. Y., Zheng, J. P., and Kwok, H. S., *J. Appl. Phys.*, **69**, 6349,1991.

Codling K., and Frasinski J., *Contemporary Phys.*, **35**, 243, 1994.

Colella, P., *SIAM J. Sci. Stat. Comput.*, **6**, 104, 1985.

Colella, P., *SIAM J. Sci. Stat. Comput.*, **3**, 76, 1982.

Ditmire, T., Donnely, T., Rubenchik, A. M., Falcone, R. W., and Perry M. D., *Phys. Rev. A.*, **53**, 3379, 1996.

Dreyfus, R. W., *J. Appl. Phys.*, **69**, 1721, 1991.

Dreyfus, R. W., Kelly, R., and Walkup, R. E., *Appl. Phys. Lett.*, **49**, 1478, 1986.

Duley, W. W., "UV Lasers: Effects and Applications in Materials Science", Cambridge University Press, Cambridge, 1996.

Duley, W. W., "CO2 Lasers: Effects and Applications", Academic Press, New York, 1976.

Dyer P. E., *Appl. Phys. Lett.*, **55**, 1630, 1989.

Estler R. C., and Nogar N. S., *J. Appl. Phys.*, **69**, 1654, 1991.

Frezotti, A., "Rarefied Gas Dynamics", Progress in Astronautics and Aeronautics, 1986, p 313.

Fukushima K., Kanke Y., and Morishita T., *J. Appl. Phys.*, **74**, 6948, 1993.

Geohegan, D. B., *Appl. Phys. Lett.*, **60**, 2732, 1992.

Georgiou S., Zafiropulos V., Anglos D., Balas C., Tornari V., and Fotakis C. in "Laser Ablation", *Proc. of the fourth International Conf. on Laser Ablation,* eds. R. E. Russo, D. B. Geohegan, R. F. Haglund Jr., and K. Murakami. p 738, 1998

Gilgenbach, R. M. and Ventzek, P. L. G., *Appl. Phys. Lett.*, **58**, 1597, 1991.

Gilton T. L., Cowin J. P., Kubiak G. D., and Hamza A. V., *J. Appl. Phys.*, **68**, 4802, 1990.

Grun, J., Stamper, J., Manka, C., Resnick, J., Burris, R., and Ripin, B. H., *Appl. Phys. Lett.*, **59**, 246, 1991.

Guo, H., Lou, Q., Chen, S. C., Cheung, N. H., Wang, Z. Y., and Lin, P. K., *Opt. Comm.*, **98**, 220, 1993.

Gupta, A., Braren, B., Casey, K. G., Hussey, B. W., and Kelly, R., *Appl. Phys. Lett.*, **59**, 1302, 1991.

Haberland H., in "Clusters of Atoms and Molecules I", ed. H. Haberland, Springer-Verlag, New York, 1994.

Habermeier H. -U., "Laser Ablation of Electronic Materials", eds. E. Fogarassy and S. Lazare, Elsevier Science Publishers, The Netherlands, p 281, 1992.

Hansen W. W., Janson S. W., and Helvajian H., *Proc. SPIE*, **2991**, 104, 1997.

Hayashi H., and Miyamoto I., *Proc. Laser Materials Processing Conf., (ICALEO '95)* p 391, 1995.

Herziger G., and Kreutz E. W., "Laser Processing and Diagnostics", ed. D. Bauerle, Springer-Verlag, Berlin, 1984, p. 90.

Izumi H., Ohata K., Sawada T., Morishita T., and Tanaka S., *Appl. Phys. Lett.*, **59**, 597, 1991.

Jarrold M. F., in "Clusters of Atoms and Molecules I", ed. H. Haberland, Springer-Verlag, New York, 1994.

Kawamura Y, Toyoda K, and Kawai M. *Appl. Phys. Lett.* **45**, 308, 1994.

Kelly, R. and Rothenberg, J. E., *Nucl. Instrum. Methods*, **B7/8**, 755, 1985.

Kelly, R. and Dreyfus, R. W., *Surf. Sci.*, **198**, 263, 1988.

Kelly R., Miotello A., Braren B., and Otis C. E., *Appl. Phys. Lett.*, **60**, 2980, 1992.

Kinsman, G. PhD Thesis. York University, 1991.

Kitagawa A., Inoue T., Komura A., Suzuki M., Nakajima H., Takemoto T., and Matsunawa A., *Proc. Laser Materials Processing Conf., (ICALEO'95)* p 211, 1995.

Kittel C., "Introduction to Solid State Physics", sixth ed., John Wiley and Sons, Inc., New York, 1986, p 98.

Knight, C. J., *AIAA*, **17**, 519, 1979.

Kuper S., and Brannon ., *Appl. Phys. Lett.*, **60**, 1633, 1992.

Landau L. D., and Lifshitz E. M., "Electrodynamics of Continuous Media", Pergamon Press, New York, 1960, p 11.

Lubben D., Barnett S. A., Suzuki K., Gorbatkin S., and Greene J. E., *J. Vac. Sci. Technol. B.*, **3**, 968, 1985.

"Lumonics HyperEX-400 excimer laser manual", Lumonics, Inc., Kanata, Ont., 1985.

McKee, T. J., *Can. J. Phys.*, **66**, 859, 1988.

Miyamoto, I., Ogawa, T., Marou, H., and Konno, D., *Proc. Laser Materials Processing*

Conf., (ICALEO'94), p 240, 1994.

Miyamoto, I., Maeda, A., and Marou, H., *Proc. Laser Materials Processing Conf., (ICALEO'94)*, p 249, 1994.

Mulser, P., Sigel, R., and Witkowski, S., *Physics Reports*, **6**, 187,1973.

Murnane M. M., Kapteyn H. C., Gordon S. P., Boker J., Glytsis E. N., and Falcone R. W., *Appl. Phys. Lett.*, **62**, 1068, 1993.

Noorbatcha, I., Luchese, R. R., and Zeiri, Y., *J. Chem. Phys.*, **86**, 5816, 1987.

Orlando T. M., Cowin J. P., and Barlow S. E. "Laser Ablation: Mechanisms and Applications -II", eds. J.C. Miller and D.B. Geohegan, pg 341, 1994.

Otis, C. E., Braren, B., Thompson, M. O., Brunco, D., and Goodwin, P. M., *Proc. SPIE*, **1856**, 132, 1993.

Palik, E. D. (ed.), "Handbook of Optical Constants of Solids", Academic Press, New York, 1985.

Phipps, C. R., Turner, T. P., Harrison, R. F., York, G. W., Osborne, W. Z., Anderson, G. K., Corlis, X. F., Haynes, L. C., Steele, H. S., and Spicochi, K. C., *J. Appl. Phys.*, **64**, 1083, 1988.

Pinho, G. P., Callies, G., Schittenhelm, H., Mueller, R. E., Berger, P., Duley, W. W., and Hugel, H., *Proc. SPIE.*, **2991**, 21, 1997.

Pirri, A. N., Root, R. G., and Wu, P. K. S., *AIAA*, **16**, 1296, 1977.

Poprawe, R., Beyer, E., and Herziger, G., *Inst. Phys. Conf.*, **72**, 67, 1985.

Puell H., *Z. Naturforsch*, **25a**, 1807, 1970.

Purnell J., Snyder E. M., Wei S., and Castleman Jr. A. W., *Chem. Phys. Lett.*, **229**, 333,

1994.

Ray U., Jarrold M. F., Bower J. E., and Kraus J. S., *J. Chem. Phys.*, **91**, 2912, 1989.

Reader J., Corliss C. H., Wiese W. L., and Martin O. A., "Wavelength and Transition Probabilities for Atoms and Atomic Ions", National Standard Reference Data System-NBS 68. US Government Printing Office, 1980.

Rosen, D. I., Mitteldorf, J., Kothandaraman, G., Pirri, A. N., and Pugh, E. R., *J. Appl. Phys.*, **53**, 3190, 1982

Saenger K. L., *J. Appl. Phys.*, **66**, 4435, 1989.

Sappey, A. D., and Gamble, T. K., *J. Appl. Phys.*, **72**, 5095, 1992.

Sappey, A. D., and Gamble, T. K., *Appl. Phys. B.*, **53**, 353, 1991.

Schittenhelm, H., Callies, G., Berger, P., and Hugel, H., *J. Phys. D: Appl. Phys.*, **29**, 1564, 1996.

Schittenhelm H., Callies G., Berger P., and Hugel H. in "Laser Ablation", *Proc. of the fourth International Conf. on Laser Ablation*, eds. R. E. Russo, D. B. Geohegan, R. F. Haglund Jr., and K. Murakami. p 922,1998.

Sedov, L. I., "Similarity and Dimensional Methods in Mechanics", Cleaver Hume Press, 1959.

Sell, J. A., Henelfinger, D. M., Ventzek, P. L. G., and Gilgenbach, R. M., *J. Appl. Phys.*, **69**, 1330, 1991.

Singh, R. K., Bhattacharya, D., and Narayan, J., *Appl. Phys. Lett.*, **57**,2022,1990.

Sod., G. A., *J. Comp. Phys.*, **27**, 1, 1978.

Spitzer L., "Physics of Fully Ionized Gases", Interscience, New York, 1967.

Sugano S., "Microcluster Physics", Springer-Verlag, New York, 1991, p 39.

Sussman, M. V., "Elementary General Thermodynamics", Addison-Wesley, Reading Massachusetts, 1972.

Tozer, B. A., *Phys. Rev.*, **137**, 1665, 1965.

van Leer, B., *J. Comp. Phys.*, **32**, 101, 1979.

Ventzek, P. L. G., Gilgenbach, R. M., Ching, C. H., and Lindley, R. A., *J. Appl. Phys.*, **72**, 1696, 1992.

Ventzek, P. L. G., Gilgenbach, R. M., Ching, C. H., Lindley, R. A., and Lash, J. S., *Proc. SPIE*, **1856**, 82, 1993.

Ventzek, P. L. G., Gilgenbach, R. M., Heffelfinger, D. M., and Sell, J. A., *J. Appl. Phys.*, **70**, 587, 1991.

von Gutfled R. J., and Dreyfus R. W., *Appl. Phys. Lett.*, **54**, 1212, 1989.

Wang H., Salzberg A. P., and Weiner B. R., *Appl. Phys. Lett.*, **59**, 935, 1991.

Wiedeman L., and Helvajian H., *J. Appl. Phys.*, **70**, 4513, 1991.

Wiese W. L., Smith M. W., and Miles B. M., "Atomic Transition Probabilities Vol II Sodium through Calcium", National Standard Reference Data System-NSB 22. US Government Printing Office, 1969.

Weyl, G., Pirri, A. N., and Root, R., *AIAA*, **19**, 460, 1980.

Ytrehus, T. "Rarefied Gas Dynamics", Progress in Astronautics and Aeronautics, 1976, p 1197.

Zel'dovich, Ya. B., and Raizer, Yu. P., "Physics of Shock Waves and High Temperature

Hydrodynamic Phenomena", Academic Press, New York, Vol 1, 1966, p5.

Zel'dovich, Ya. B., and Raizer, Yu. P., "Physics of Shock Waves and High Temperature Hydrodynamic Phenomena", Academic Press, New York, Vol 1, 1966, p383.

Zel'dovich, Ya. B., and Raizer, Yu. P., "Physics of Shock Waves and High Temperature Hydrodynamic Phenomena", Academic Press, New York, Vol 1, 1966, p407.

Zel'dovich Ya B., and Raizer, Yu P., "Physics of Shock Waves and High Temperature Hydrodynamic Phenomena", Academic Press, New York, Vol 1, 1966, pg 43.

Zel'dovich Ya B. and Raizer, Yu P., "Physics of Shock Waves and High Temperature Hydrodynamic Phenomena", Academic Press, New York, Vol 1, 1966, pg 53.

Zel'dovich Ya. B., and Raizer Yu. P., "Physics of Shock Waves and High Temperature Hydrodynamic Phenomena", Academic Press, New York, Vol 1, 1966, p 419.

Zel'dovich Ya. B., and Raizer Yu. P., "Physics of Shock Waves and High Temperature Hydrodynamic Phenomena", Academic Press, New York, Vol 1, 1966, p 421.

Zel'dovich Ya. B., and Raizer Yu. P., "Physics of Shock Waves and High Temperature Hydrodynamic Phenomena", Academic Press, New York, Vol 1, 1966, p 390.

Zheng X. -Y., Lowndes D. H., Shen Z., and Warmack R. H., "Laser Ablation: Mechanisms and Applications II" eds. J. C. Miller and D. B. Geohegan, *AIP Conf. Proc.*, **288**, 262, 1994.

Znotins T. A., *Laser Focus/Electro-optics*, 1987, p. 54.